Modeling Io's and Europa's Plasma Interaction with the Jovian Magnetosphere: Influence of Global Atmospheric Asymmetries and Plumes

Inaugural-Dissertation

zur

Erlangung des Doktorgrades

der Mathematisch-Naturwissenschaftlichen Fakultät

der Universität zu Köln

vorgelegt von

Aljona Blöcker

aus Lobanowo

Köln 2017

Berichterstatter: Prof. Dr. Joachim Saur

Prof. Dr. Bülent Tezkan

Tag der mündlichen Prüfung: Montag, 03. Juli 2017

Abstract

We apply a three-dimensional (3D) magnetohydrodynamic (MHD) model to study the influence of inhomogeneities in Europa's and Io's atmospheres, as, for example, water vapor plumes and volcanic plumes, on the plasma interaction with the Jovian magnetosphere. The ideal MHD equations have been extended in order to account for the effects of the moons' atmospheres and plumes on the plasma interaction. We have included collisions between ions and neutrals, plasma production and loss due to electron impact ionization and dissociative recombination. Moreover, electromagnetic induction in a subsurface water ocean was also considered by the model in modeling of Europa's plasma interaction. In addition to the MHD model we apply an analytic model based on the model of Saur et al. (2007) to understand the role of steep gradients and discontinuities in Europa's interaction. We find that Europa's global atmosphere weakens the effect of the hemisphere coupling and generates steep gradients in the magnetic field.

Volcanic eruptions on Io and water vapor plumes on Europa locally enhance the neutral density of the atmosphere and thus modify the plasma interaction. We show that an inhomogeneity near the north or south pole affects the plasma interaction in a way that a pronounced north-south asymmetry is generated. We find that an Alfvén winglet develops within the main Alfvén wing on that side where the inhomogeneity is located. Since Europa's atmosphere is much thinner (by a factor of $\sim$100 compared to Io's atmosphere) we show that dense atmospheric inhomogeneities affect the Alfvénic far-field much stronger compared to Io. At Europa the plasma velocity experiences a decrease up to 95% of the upstream velocity in the Alfvén winglet and a decrease up to 60% of the upstream velocity in the ambient Alfvén wing. Whereas at Io the plasma flow is decelerated by up to 93% in the Alfvén winglet and by more than 80% in the ambient Alfvén wing. Simultaneously, the Alfvén waves perturb also the magnetic field in the Alfvénic far-field so that the magnetic field perturbations are stronger in the Alfvén winglet than in the ambient Alfvén wing. The global form of the Alfvén wings is unchanged because the Alfvén velocity in the far-field is uninfluenced by the distribution of the neutral density in the atmosphere.

Additionally to the effect of volcanic plumes on Io's plasma interaction, we analyze the role of volcanic plumes on the supply rate of the Io plasma torus. We estimate that the contribution to the mass loading by the volcanic plumes is nearly negligible compared to the total mass loading rate of the global atmosphere and that the ejected neutrals, associated with the plume, contribute by less than 7 % to the total atmospheric sputtering rate. Furthermore, we apply our MHD model to analyze the effects of an asymmetric atmosphere on the plasma interaction. Therefore, we use different atmosphere models with longitudinal and latitudinal dependencies. We compare our model results with Io's plasma environment measured with the instruments of the Galileo spacecraft during two Io passes: I24 and I27. We demonstrate that parts of the magnetic field perturbations, linked to the induction signals of a subsurface magma ocean (Khurana et al., 2011) can alternatively be explained by considering a global asymmetric atmosphere without considering induced fields from a subsurface magma ocean.

Our analytic model results show that the resultant discontinuities for a plume that contains 50% of the mass content of Europa's atmosphere would only contribute to about 5% for the magnetic field amplitudes generated by the global atmosphere. Furthermore we compare our model results with the measured magnetic field data from three flybys of the Galileo spacecraft at Europa which included Alfvén wing crossings: E17, E25A, and E26, to investigate if signals of plumes are visible in the magnetic field measurements. Our analysis suggests that the magnetic field perturbations measured along the E26 trajectory could be consistent with a plume on the southern hemisphere.

Zusammenfassung

Die vorliegende Dissertation beschäftigt sich mit der lokalen Plasmawechselwirkung der Jupitermonde Io und Europa mit der umgebenden Jupitermagnetosphäre. Die treibende Kraft dieser Plasmawechselwirkung ist die fortdauernde Anströmung der beiden Satelliten, die sich in der inneren Magnetosphäre von Jupiter befinden, von dem korotierenden, magnetosphärischen Plasma, das stark von Jupiters Magnetfeld beeinflusst wird. Die Atmosphären der Satelliten wechselwirken mit den geladenen Teilchen und verursachen Störungen in der Plasmaumgebung des Satelliten. Insbesondere Io gilt als das Paradebeispiel für die Betrachtung der sub-Alfvénischen Plasmaströmung, die auf eine Satellitenatmosphäre trifft. Die Stöße der magnetosphärischen Teilchen mit den Neutralgasteilchen der Satellitenatmosphäre erzeugen elektromagnetische Störungen, die sich in Form von Alfvénwellen parallel und antiparallel zu Jupiters Magnetfeldlinien ausbreiten. Im Ruhesystem des Satelliten betrachtet, formen die Störungen die sogenannten Alfvén Flügel im Fernfeld des Mondes (ab ungefähr zwei Satellitenradien Entfernung vom Satelliten). Vornehmlich durch Elektronenstoßionisation und Stößen zwischen dem Plasma und dem Neutralgas bildet sich in der nahen Umgebung des Satelliten eine leitfähige Ionosphäre mit einem starken ionosphärischen Stromsystem aus. Dieses Stromsystem wirkt sich stark auf das elektrische Feld im anströmenden Plasma aus, indem es das elektrische Feld in der Ionosphäre kurzschliesst und modifiziert. Die Plasmaströmung auf den Satelliten und das umgebende Magnetfeld, die vom elektrischen Feld beeinflusst sind, werden ebenfalls modifiziert.

Die Wechselwirkung sowie die Eigenschaften der Satelliten wurden in den vergangenen Jahrzehnten mehrfach durch Raumsonden Vorbeiflüge und Hubble Space Teleskop (HST) Fernbeobachtungen untersucht und sind immer noch Gegenstand aktueller Forschung. Die Satelliten besitzen einzigartige Eigenschaften, die noch teilweise unerforscht sind. Mit seinen heftigen Vulkaneruptionen gilt Io als der vulkanisch aktivste Körper in unserem Sonnensystem und besitzt wahrscheinlich einen unterirdischen, stark leitfähigen Magma Ozean. Ios Atmosphäre wird durch dynamische vulkanische Ausgasungen und durch Sublimation von Ablagerungen von Schwefeldioxid auf der Oberfläche gespeist. Die Atmosphäre ist nicht homogen und zeigt starke Variationen mit der Länge und Breite. Ios Nachbarmond Europa hat kürzlich das Interesse vieler Forscher auf sich gezogen als HST Beobachtungen am Südpol Wasserfontänen zeigten (Roth et al., 2014b, Sparks et al., 2016), die offenbar bis zu 200 Kilometer in die Höhe schießen. Mit seinen Wasserfontänen, seiner dünnen Sauerstoffatmosphäre und dem unterirdischen Wasser Ozean zählt Europa zu einem der vielversprechendsten Orte für die Suche nach außerirdischem Leben erklärt.

Der Fokus dieser Arbeit liegt auf der Beantwortung der Fragestellung wie globale und lokale Asymmetrien, wie zum Beispiel vulkanische Fontänen oder Wasserfontänen, in den Statellitenatmosphären sich auf ihre Plasmaumgebung auswirken. Die Fontänen werden auch Plumes genannt. Eine generelle Untersuchung der Auswirkungen von Plumes auf das Alfvénische Fernfeld wurde bei Io und Europa zuvor noch nicht durchgeführt. Dazu präsentieren wir eine systematische Studie der Plasmawechselwirkung wenn sich eine lokale atmosphärische Inhomogenität, d.h. ein Plume, in der globalen

Atmosphäre der Satelliten befindet.

Dazu verwenden wir ein dreidimensionales Ein-Fluid magnetohydrodynamisches (MHD) Modell, das die Plasmawechselwirkung selbstkonsistent sowohl lokal als auch im Alfvénischen Fernfeld beschreibt. Wir modifizieren die idealen MHD Gleichungen indem wir zusätzliche Terme für die Elektronenstoßionisation, elastische Stöße zwischen Ionen und Neutralgasteilchen, die zusätzlich den Prozess des Ladungsaustausches beinhalten, und dissoziative Rekombination einfügen. Der Einfluss von Induktionssignalen aus einem unterirdischen Wasserozean bei Europa wurde ebenfalls in dem Modell berücksichtigt. Zusätzlich zu dem MHD Modell leiten wir ein analytisches Modell ab für die Betrachtung von Europas elektrodynamischer Wechselwirkung mit einer globalen Atmosphäre, die einen Plume beinhaltet. Das Modell basiert auf dem Hemisphärenkopplungsmodell entwickelt von Saur et al. (2007) für Enceladus elektrodynamische Wechselwirkung und beinhaltet Aspekte der Plasmawechselwirkung mit einer atmosphärischen Inhomogenität, die in unserem MHD Modell nicht beschrieben werden (z.B. Magnetfelddiskontinuitäten).

Wir zeigen, dass ein Plume sich nicht nur auf die nahe Umgebung des Satelliten auswirkt sondern auch das Alfvénische Fernfeld modifiziert. Der Plume ist dichter als die umgebende Atmosphäre und bewirkt somit eine lokale Verstärkung der Stöße zwischen Ionen und Neutralgasteilchen und der Plasmaproduktion. Diese lokal verstärkte Wechselwirkung wird dann entlang der Magnetfeldlinien in die Alfvén Flügel abgebildet. Der Plume hat eine starke Nord-Süd Asymmetrie in den Alfvén Flügeln zur Folge, sodass sich innerhalb des Flügels, der in Verbindung mit der Hemisphäre steht, die den Plume beinhaltet, ein weiterer kleinerer Alfvén Flügel ausbildet. Innerhalb dieses kleineren Alfvén Flügels sind das Magnetfeld und Geschwindigkeitsfeld stärker gestört als im umgebenden Alfvén Flügel.

Bei der Anwendung des Modells auf Ios Atmosphäre und dessen vulkanische Plumes, haben wir uns auf Positionen von drei verschiedenen Vulkanen beschränkt. Die Vulkane Pele, Tvashtar und Thor sind bekannt für ihre hohen Plumes und große Ausdehnung. Die Plumes werden als eine Inhomogenität in der globalen Atmosphäre analytisch eingefügt und sind charakterisiert durch ihre Dichte and der Oberfläche, ihre Ausdehnung und ihre Skalenhöhe in unserem Modell. Während Pele sich in der dichten Äquatoratmosphäre von Io befindet, liegen die anderen beiden Vulkane in Ios hohen Breiten nahe des Nordpols, wo die umgebende Atmosphäre deutlich dünner ist (ungefähr 2 % der Äquatoratmosphärendichte). Wir zeigen, dass der Tvashtar Plume lokale Signale im Magnetfeld und Geschwindigkeitsfeld in den Alfvén Flügeln verursacht. Der Pele Plume dagegen verursacht nahezu keine Signaturen im Fernfeld, da sein Effekt durch die starke Plasmawechselwirkung mit der umgebende Äquatoratmosphäre stark geschwächt wird. Der Effekt der Plumes im Nahfeld wird vor allem durch die Erhöhung der Plasmadichte sichtbar. Ein oft diskutierter Punkt ist der Einfluss von Vulkanausbrüchen auf den Io Plasma Torus. Io gilt als die Hauptquelle für das magnetosphärische Plasma in der Jupitermagnetosphäre. Pro Sekunde entweicht ungefähr eine Tonne Masse in Form von ionisierten und neutralen Teilchen aus Ios Atmosphäre (Broadfoot et al., 1979). Mithilfe der Modellergebnisse konnten wir abschätzen, dass ein vulkanischer Plume auf Io einen sehr geringfügigen Anteil zur Plasmaproduktion beiträgt und somit ein starker Einfluss auf den Torus durch einen Vulkanausbruch nicht zu erwarten ist.

Eine weiterer, wichtiger Punkt dieser Dissertation ist die Betrachtung der Auswirkungen verschiedener Asymmetrien in Ios Atmosphäre auf Ios Plasmaumgebung zur Zeit der beiden Vorbeiflüge I24 und I27 der Raumsonde Galileo. Eine seit Jahren diskutierte Frage ist die Existenz einer globalen, leitfähigen Magmaschicht im Untergrund von Io. Khurana et al. (2011) haben mithilfe von MHD Modellen gezeigt, dass für die Störungen in den Magnetfelddaten der Vorbeiflüge I24 und I27 Induktionssignale eines unterirdischen, leitfähigen Magma Ozeans verantwortlich sind. Widersprüchlich dazu haben Roth et al. (2017) kürzlich gezeigt, dass die Existenz eines solchen leitfähigen Ozeans, die von Khurana et al. (2011) postuliert wurde, inkonsistent mit den Hubble Space Teleskop Beobachtungen der Aurora bei Io wäre. Mit der Betrachtung verschiedener Asymmetrien in Ios Atmosphäre auf Ios Plasmaumgebung während der Vorbeiflüge I24 und I27 können wir zeigen, dass die Magnetfelddaten alternativ auch mit einer komplexen Atmosphäre erklärt werden können ohne Induktionssignale aus einer leitfähigen, unterirdischen Schicht in Betracht zu ziehen. Zur Unterstützung unserer Analyse der Einflüsse der Asymmetrien in der Atmosphäre verwenden wir Messungen während der Vorbeiflüge der Dichte, Ionentemperatur und Geschwindigkeit.

Bei der Anwendung unseres MHD Modells auf Europa können wir zeigen, dass der Einfluss der Wasserfontänen auf die Plasmaumgebung deutlich stärker ist als der Einfluss von Vulkanplumes bei Io. Die deutlich dünnere Atmosphäre (um einen Faktor 100) als bei Io und der dichte Plume nahe dem Südpol bewirken starke Störungen im Magnet- und Geschwindigkeitsfeld im Alfvénischen Fernfeld. Für einen Plume am Südpol mit einem ähnlichen Ausmass wie der beobachtete Plume von Roth et al. (2014b) zeigen wir, dass die anströmende Plasmaströmung ein Abbremsen um bis zu 95% im kleinen Alfvén Flügel und ein Abbremsen um 60% im umgebenden, südlichen Alfvén Flügel aufgrund der globalen Atmosphäre erfährt. Das Magnetfeld zeigt ebenfalls starke Störungen im kleinen Alfvén Flügel aufgrund des Plumes. Mit unserem analytischen Modell können wir zusätzlich zeigen, dass Europas globale Atmosphäre den Effekt der Hemisphärenkopplung schwächt und wie die Plumes ebenfalls starke Gradienten im Magnetfeld produziert. Somit ist eine direkter Nachweis auf einen Plume bei Europa aus beobachteten Gradienten im Magnetfeld im Alfvénischen Fernfeld wie es bei Enceladus durchgeführt wurde (Simon et al., 2014) nicht möglich.

Darüber hinaus befassen wir uns mit den gemessenen Magnetfelddaten von drei Europa Vorbeiflügen der Galileo Raumsonde: E17, E25A und E26. Bei den drei Vorbeiflügen durchquerte Galileo die Alfvén Flügel. Mithilfe des analytischen und numerischen Modells analysieren wir die gemessenen Magnetfeldstörungen mit Hinblick auf mögliche Plume Signaturen in den Daten. Unsere Analyse der Magnetfelddaten des Vorbeiflugs E26 zeigt, dass Signale eines Plumes auf Ios südlichen Hemisphäre mit den gemessenen Störungen in den Daten konsistent sind. Eine eindeutige Schlussfolgerung auf den Einfluss von Plumes während des E26 Vorbeiflugs ist jedoch nicht möglich, da weitere Effekte wie eine asymmetrische Atmosphäre oder magnetosphärische Effekte, die wir nicht in unserem Modell beschrieben haben, das Magnetfeld ebenfalls beeinflussen können. Für eine genauere Aussage über mögliche Plumesignale in den Daten ist die Betrachtung weiterer unabhängiger, hochaufgelöster Messungen, wie z.B. Plasmadichte und Geschwindigkeit notwendig, die uns zur Zeit dieser Studie nicht zur Verfügung standen.

Mit unserer Studie haben wir zu einem erweiterten Verständnis der Auswirkungen von Inhomogenitäten in den globalen Atmosphären der beiden Jupitermonde Io und Europa auf die Plasmaumgebung beigetragen. Die Schlussfolgerungen in dieser Arbeit liefern Ideen wie zukünftige Raumfahrtmissionen Plumes detektieren können oder wie Plumesignale in den Messungen erkannt werden können.

Contents

1. Introduction

The beginning of the exploration of the Galilean moons dates back to the 7th day of January in 1610 when Galileo Galilei pointed his telescope skyward in direction of the large Jovian satellites. Galilei's discovery of the Galilean moons was reported in his short astronomical treatise *Sidereus Nuncius* in March of the same year. Around the same time, the Bavarian astronomer Simon Marius (Mayr) asserted that he discovered the four moons before or at least contemporaneously with Galilei (Johnson, 1931). However, Marius failed to communicate his findings and did not publish his observations until 1612. Although he did not receive the credit for the first detection of the moons, he suggested to call each satellite by one mythological name, after the lovers of Zeus, the highest god in the ancient Greek mythology, i.e., Io, Europa, Ganymede and Callisto (Lynn, 1903). Followed by their discovery, the motion of the four Galilean moons drew attention of a number of scientists. The Danish astronomer Olaus Rømer discovered in 1676 that light propagates at a finite velocity while studying the timing of eclipses of Io and made the first quantitative measurement of the speed of light. In 1788, the French mathematician Pierre-Simon Laplace published his mathematical theory of the orbits where he concluded that the orbital periods of Io, Europa, and Ganymede are nearly in a perfect 1:2:4 ratio.

Detailed investigations of the moons began with the first hint for an electrodynamic connection between Io and Jupiter by Bigg (1964). He discovered that Jovian radio emissions are controlled by Io's position in the Jovian magnetosphere. These observations led to the idea that the plasma near Io is coupled electrodynamically with the Jovian ionosphere through field-aligned currents and were followed by first theoretical models of the linkage of Io to Jupiter's ionosphere, e.g., by Piddington and Drake (1968) and Goldreich and Lynden-Bell (1969). It was Drell et al. (1965), who stated the idea to apply the mechanism of the generation of the Alfvén waves to the analysis of Io's orbit and presented the linear Alfvén wave model. They showed that the Alfvén perturbation extends out in wings in the rest frame of an idealized conductor moving through a collisionless plasma in a direction perpendicular to the magnetic field lines.

In the past four decades, starting with the Pioneer 10 and 11 observations in 1973 and 1974 and followed by the Voyager 1 and 2 observations in 1979, detailed studies and extraordinary findings were obtained by several spacecraft missions and both space and ground based telescope observations. The Galileo mission, a spacecraft in orbit

around Jupiter between December 1995 and September 2003, offered for the first time long-term observations of Jupiter and the Galilean moons. The Hubble Space Telescope (HST) provided detailed observations of Jupiter's and the satellite's atmospheres, aurora and surfaces. Simultaneous spacecraft and telescope observations were made with HST, when the Cassini or the New Horizon spacecraft flew-by the Jovian System on their flight to Saturn and Pluto and the outer solar system. All these missions revolutionized our understanding of the properties and the plasma environment of the Galilean satellites.

To mention some of the unique properties of the Galilean moons: The outermost moon, Callisto, orbiting Jupiter in a distance of about 26 Jupiter radii, may hide a salty ocean under its icy, cratered surface (Khurana et al., 1998). Ganymede, the largest moon of Jupiter and in the solar system is located in a distance of about 15 Jupiter radii to Jupiter. The moon possesses an intrinsic magnetic field and probably a subsurface ocean (Saur et al., 2015). The surface of Ganymede's neighboring satellite, Europa, is covered with ice and it is the smoothest surface in our solar system (e.g., Pappalardo et al., 2009). Europa harbors a water ocean under its icy crust (e.g., Zimmer et al., 2000) and water vapor plumes were spotted jetting from its surface (Roth et al., 2014b). The satellite possesses a tenuous atmosphere composed primarily of oxygen (Hall et al., 1995, 1998). Recently, NASA gave Europa (besides Saturn's moon Enceladus) the top priority in future exploration as Europa is believed to harbor the key ingredients for life in its ocean. In particular, the investigations of Europa's water vapor plumes are laying the groundwork for NASA's Europa Clipper mission, which is planned for launch in the 2020s. The surface of the innermost moon, Io, shows a variety of volcanic activity with lava flows and enormous volcanic eruptions (e.g., Lopes-Gautier et al., 1999). Its mantle might be partially molten (e.g., Khurana et al., 2011). The volcanic plumes and the sublimation of sulfur dioxide (SO_2) frost originating from these eruptions are the origin of Io's atmosphere which shows strong longitudinal and latitudinal variations (e.g., Lellouch et al., 2007).

The case of magnetospheric plasma flowing with sub-Alfvénic velocities past a moon with a tenuous atmosphere is a very common interaction scenario in the outer solar system and was frequently studied (see, e.g., Kivelson et al., 2004, Neubauer, 1998). The Galilean moons also experience such a sub-Alfvénic flow as they are embedded in Jupiter's magnetospheric plasma, which constantly overtakes the moons. Ionization and collisions within the atmosphere and induced fields in subsurface oceans modify the plasma environment and drive large currents through the moons' ionosphere. A key feature of the sub-Alfvénic flow past the moon's atmosphere is the development of Alfvén wings. In the rest frame of the moons, standing Alfvén waves are generated which perturb the fields and form a tube-shaped region referred to as the Alfvén wing (see, e.g., Neubauer, 1980, Goertz, 1980). The Alfvén mode is of particular interest for the understanding of the sub-Alfvénic plasma interaction because it carries field-aligned

currents and energy along Jupiter's background magnetic field at the Alfvén velocity in the rest frame of the plasma. The perturbations which occur in the vicinity of the moons map out along the Alfvén characteristics, i.e., along the direction of the group velocity of the Alfvén waves. The atmospheres of the moons are the root causes for the generation of the Alfvén wings and, thus, decisively influence the plasma interaction. Therefore, the Alfvénic far-field is diagnostic of the moons' atmospheric properties and provides the opportunity to draw conclusions about Io's and Europa's atmospheres by studying the velocity and magnetic field in the Alfvén wings.

The present thesis focuses on Io's and Europa's plasma interaction. With our study, we in particular aim to show how features such as Europa's water vapor plumes, Io's volcanic plumes and atmospheric asymmetries affect the satellites' interaction with the Jovian magnetosphere. In the dense local plume regions in Europa's and Io's global atmosphere, ionization and collisions between the magnetospheric and neutral particles are enhanced and, therefore, stronger perturbations are generated which propagate along the magnetic field lines and map out into the Alfvén wing as well. A consequence of the localized region of increased perturbations is the development of a small Alfvén wing within the main Alfvén wing. We will refer to this smaller Alfvén wing as **Alfvén winglet**. Alfvén wings have been introduced and studied in detail dating back to, e.g., Neubauer (1980), Southwood et al. (1980), Goertz (1980). However, the formation of Alfvén winglets within the Alfvén wings has not been systematically studied before. We provide the first systematic study of Alfvén winglets and how they are shaped by local atmospheric inhomogeneities at Io and Europa.

Io's atmosphere is supported by sublimation of SO_2 surface frost and by direct volcanic outgassing of SO_2, where the detailed longitudinal and latitudinal structure is not fully known. We apply our MHD model to analyze the effects of an asymmetric atmosphere and the role of volcanic plumes on the plasma interaction. Therefore, we use different atmosphere models with longitudinal and latitudinal dependencies. Additionally, we compare our model results with the Galileo MAG data of the flyby I31 in order to investigate whether perturbations in the measurements can be explained by a volcanic plume. Previously, Khurana et al. (2011) stated the existence of Io's global subsurface magma ocean by modeling and analyzing magnetic field measurements during the Galileo flybys I24 and I27. We analyze the measurements of the same flybys and find an alternative explanation for the observed magnetic field perturbations. We suggest, that the perturbations are likely caused by asymmetries in Io's atmosphere rather than induction effects in a subsurface magma ocean.

As the density and the extent of Europa's water vapor plumes are not well known at the time of our studies, we will perform a parameter study with different plume densities within Europa's global atmosphere to study the effects on the local plasma

interaction, the Alfvén wings, and the Alfvén winglets. We present both magnetohydrodynamical (MHD) and analytic investigations in comparison with the magnetic field during three flybys of the Galileo spacecraft: E17, E25A, and E26. During these flybys, the Galileo spacecraft crossed Europa's Alfvén wings and the measurements, thus, can be used to investigate atmospheric properties propagated along the wings. The comparison of our simulation results with the Galileo Magnetometer (MAG) data along the trajectories of these three flybys allows us to investigate whether perturbations in the measurements can be explained by any local atmospheric inhomogeneity. Our work provides ideas on how to detect plumes in the plasma measurements during future missions.

The thesis is organized as follows: In Chapter 2, we give an overview of the properties of the interiors, atmospheres and plasma environments of Io and Europa as well as previous models of their plasma interaction. We then give a description of the plasma interaction models by Saur et al. (1999, 2007) to describe the effects of the moon's local electrodynamic interaction. Both models models are basis of our analytic studies of the effect of atmospheric inhomogeneities on Europa's plasma interaction. In Chapter 3, we present our numerical model of Io's and Europa's local interaction with the magnetospheric plasma and describe the dominant processes which occur in the vicinity of the moons. In Chapter 4, we derive the analytic model of Europa's electrodynamic interaction which accounts for the effect of an atmospheric inhomogeneity in Europa's global atmosphere on its plasma environment. In Chapters 5 and 6, we present the results of the modeling of Io's and Europa's plasma interaction, respectively. We also compare our model results with the Galileo measurements from several flybys. The last Chapter summarizes the proceedings and the main conclusions of our studies.

Parts of this thesis were already published in Blöcker et al. (2016).

2. Observations and Previous Models

This Chapter summarizes the current understanding of the interiors, the atmospheres and the plasma environments of Io and Europa and gives a description of their plasma interaction.

2.1. Io's Physical Properties and Plasma Environment

2.1.1. Io's Interior and Surface Structure

Io and the other Galilean moons are embedded in Jupiter's strong magnetic field. The orbital and rotational period of the Galilean moons are equal implying that each moon is in synchronous rotation and is always facing into the same direction toward Jupiter. During Io's rotation, the moon is exposed to a centrifugal force that acts to flatten its shape. At the same time, a steady tidal force acts on Io and elongates the moon along the line from Io to Jupiter. Io's orbit is additionally influenced by a strong 1:2:4 Laplace resonance with Europa and Ganymede. The consequence of this resonance is enhanced eccentricity of Io's orbit which, in combination with the synchronous rotation, lead to strong tidal forces affecting its interior and surface. The Galileo measurements of the tidally and rotationally influenced gravitational field of Io yielded constraints on interior models of the satellite. Io is a differentiated body consisting of a metallic core and a silicate mantle overlying by a global crustal layer. The core is thought to represent 10% to 20% of the total mass (with 10–14% iron in the core), depending on the composition of iron and silicate (pure iron (Fe) or an iron-iron sulfide (Fe–FeS) mixture) which is not exactly known. The core radius ranges from 0.35 R_{Io} for pure Fe to about 0.5 R_{Io} for Fe–FeS with Io's radius R_{Io}=1821 km and is mostly depending on its density. The rigid crust is required to be thicker than 15 km to keep up Io's topography with high mountains (Schenk et al., 2001). Several internal structural models suggest that parts of the hot interior material below the crust are partially molten. The observed temperatures of most eruptions on Io (1200–1400 K) support melt fractions of 10–20% for thermal equilibrium reasons (Moore, 2001). The estimated total heat flux from the interior to the surface is 1.5–4 Wm^{-2} with the main contribution from volcanic hot spots (Moore et al., 2007). Furthermore, Keszthelyi et al. (2004) concluded that the highest temperatures with values up to 1870 K observed from surface eruptions on Io (McEwen et al., 1998) are consistent with very high melt fractions above 50% in the mantle.

A review about Io's interior in more detail is given in, e.g., Moore et al. (2007).

Io's surface shows the absence of craters implying that Io has a young surface which is encompassed by high and steep mountains and low relief volcanic centers separated by extensive plains (Jaeger et al., 2003). Most of the mountains are rugged, isolated peaks whose distribution is randomly across the surface (Carr et al., 1998). Their heights range from a few kilometers to approximately 18 kilometers (Schenk et al., 2001) and extend laterally for a few hundreds of kilometers. A few mountains are thought to be volcanic in origin (Moore et al., 1986) due to caldera-like depressions abutting the mountains. Most of them are assumed to be fault-bounded tectonic massifs (Schaber, 1982, Nash et al., 1986, McEwen et al., 1989). However, no obvious tectonic patterns has been identified in the global mountain distribution (Schenk et al., 2001, Kirchoff and McKinnon, 2005). In the plain regions, a substantial vertical structure is absent. These regions coincide with the regions of low-viscosity sulfur flows.

Io's volcanic activity has been observed by different spacecrafts and ground based telescopes (e.g., Veeder et al., 1994, Goguen et al., 1988, Spencer et al., 1997). The results from the Galileo spacecraft mission made a major progress in understanding Io's volcanic activity. During several Io flybys, Galileo obtained numerous observations in visible and infrared wavelengths that revealed Io's volcanic features and how magma erupts on Io's surface. Io is extremely geologically active and a wide range of volcanic phenomena were observed on Io's surface. These volcanic features include more than 400 volcano-tectonic depressions called *paterae* and over 150 active hot spots (e.g., Geissler and Goldstein, 2007). Of these volcanoes, up to 400 km high gas and dust plumes from 16 different volcanic centers have been observed (e.g., Williams and Howell, 2007, Geissler and Goldstein, 2007, and references therein). The volcanic eruptions consist of effusions of lava as long lava flows, as lava lakes confined within Io's many paterae, and as fire fountains, as well as explosive gas and dust plumes (Williams and Howell, 2007). Active hot spots are randomly distributed (Lopes-Gautier et al., 1999). The distribution of mountains and paterae is concentrated toward Io's equator.

From observations of the plumes and their deposits two distinct classes of plumes on Io have been introduced exemplified by the two volcanoes Pele and Prometheus (McEwen and Soderblom, 1983). The Prometheus-type plumes are smaller, typically reaching heights of less than 100 km and are most common on Io. These long-lived plumes are created over ends of compound lava flow fields. The dust-rich plumes produce SO_2-rich deposits with a radius smaller than 200 km and are white or yellow in color unless contaminated with silicates (Geissler and Goldstein, 2007). The largest Prometheus-type plume is erupted by Thor. During the Galileo flyby I31, a 500 km high dust plume was observed producing white deposits in form of a circular ring of 300 km in radius. The plume is not as long-lived as the usual Prometheus-type plume of other volcanos. Reasons for this are still unclear. Pele-type plumes are giant, short-lived

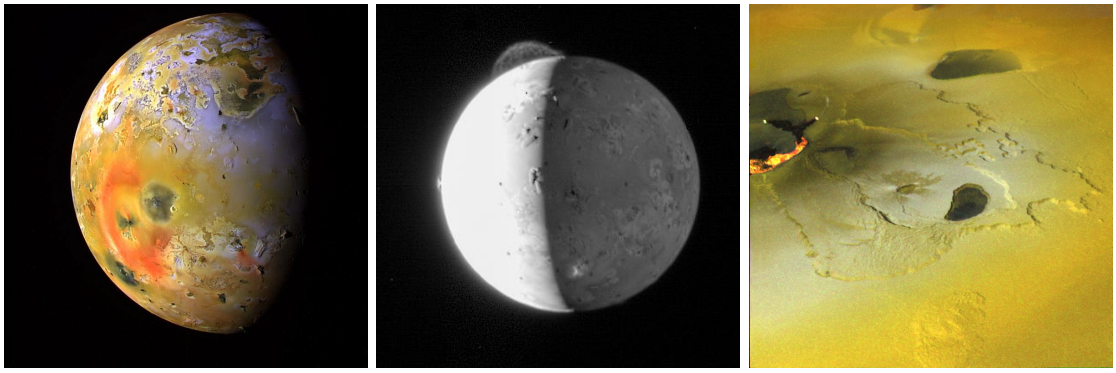

(a) (b) (c)

Figure 2.1. – (a) Enhanced color composite of Io's Pele hemisphere was obtained by the Galileo Solid-State Imaging (SSI) experiment on September 19, 1997. Bright red materials surrounding Pele, and black spots with low brightness mark areas of recent volcanic activity and are usually associated with high temperatures and surface changes. (b) This image of Io was taken by the Long Range Reconnaissance Imager (LORRI) on New Horizons on February 28, 2007. The image shows the 290-kilometer high plume from the volcano Tvashtar near Io's north pole and about 60-kilometer high plume from the Prometheus volcano near the equator. (c) Active eruption and lava flows at the Tvashtar Catena obtained by Galileo in February 2000. This picture represents a horizontal length of about 180 km. (Courtesy of NASA)

(lasting only weeks or months), high-temperature eruptions. They produce enormous red rings with a radius of up to 600 km that are poor in SO_2 and may dominantly consist of condensed sulfur (Geissler and Goldstein, 2007). The Pele volcano is unique because its plume is long-lived and stayed active throughout the Galileo era (McEwen et al., 2004). Pele is located near Io's equator and is shown in Figure 2.1a. Another prominent example of a Pele-type plume is Tvashtar which is located nearer to Io's north pole than Pele (see Figure 2.1b). Figures 2.1b and 2.1c display a high volcanic plume that was seen to emanate from the Tvashtar volcano and a fresh eruption from the Tvashtar Catena volcanic area, respectively. Tvashtar is exposed to variations in its volcanic activity and its eruption is sporadic.

2.1.2. Io's Atmosphere

The first detection of Io's atmosphere was obtained during the Voyager mission in 1979. The Voyager Infrared Interferometer Spectrometer (IRIS) experiment achieved the detection of a localized volcanic plume atmosphere consisting of gaseous SO_2 over the volcanic center Loki Patera (Pearl et al., 1979). The simultaneous findings of Io's volcanism (Morabito et al., 1979) and the S^+ and O^+ ion composition in the Io plasma torus (Bridge et al., 1979) supported the idea of an atmosphere around Io with SO_2 as the dominant atmospheric species (Ballester et al., 1990). In addition to SO_2 minor compounds, such as SO, S_2, NaCl, S, O, K, Cl, and Na, have been detected in Io's atmosphere (see Lellouch et al., 2007). After the detection of Io's atmosphere, the question was raised whether Io's atmosphere is primarily maintained by strong volcanic outgassing or sublimation of SO_2 frost from Io's surface by sunlight. Though

it is understood that the SO_2 in Io's atmosphere originates from the volcanoes, it is unclear to what extent each process contribute to maintain the atmosphere. Sputtering from SO_2 surface frosts has been ruled out as a dominant source. But the process may still be the dominant source of the atmosphere in some specific locations, e.g., at high latitudes or on the nightside (see Lellouch et al., 2007). An atmosphere supported by sublimation could collapse during eclipses by Jupiter, as the SO_2 vapor pressure is strongly coupled to the temperature of the surface frost (Saur and Strobel, 2004). Whereas, an atmosphere supported by outgassing of volcanic plumes depends on the number of simultaneously large active volcanoes and should be temporally variable (Wong and Smyth, 2000). Sublimation-driven and volcanic atmospheres would have different vertical structures: The sublimation atmosphere should be hydrostatic and the volcanic atmosphere more plume-like or localized with significant gas horizontal and vertical velocities (Lellouch et al., 2007).

Io's atmosphere has been studied for many years through its emission and absorption features at ultraviolet (UV), infrared (IR), millimeter wavelengths, and from surface reflected solar Lyman-α intensity data (see Lellouch et al., 2007). Io's atmosphere is still an unresolved issue but the numerous observations and models, although sometimes contradictory, permanently improve our understanding of the nature of Io's atmosphere.

The atmospheric column density varies spatially with latitude, longitude (see Lellouch et al., 2007) and probably also with time (Trafton et al., 1996, Jessup, 2002). Persistent hot spots and active plumes are concentrated toward lower latitudes at Io (Lopes-Gautier et al., 1999). The abundance of SO_2 frost coincides with the locations of active volcanoes (e.g., Douté et al., 2001). The observed longitudinal variability in atmospheric density correlates with the longitudinal variability in the abundance of SO_2 frost. However, from the observed correlations of Io's atmosphere with the positions of volcanoes as well as the longitudinal distribution of SO_2 frost alone it is not possible to distinguish between sublimation or direct outgassing as the dominant source of the atmosphere (Feaga et al., 2009, Spencer et al., 2005). Millimeter-wave observations of SO_2 rotational lines by Lellouch et al. (1990, 1992) are argued to be consistent with dynamical atmospheric models with volcanic sources, an areal coverage of 2–20%, column density of 6×10^{21} m^{-2}, and temperatures of 500–600 K at 40 km altitude. The assumption of a localized atmosphere is supported by the interpretation of observations of SO_2 gas absorption at UV wavelengths by the HST Faint Object Spectrograph (FOS) (Ballester et al., 1994) and the Galileo UV spectrometer (Hendrix et al., 1999). The interpretation of the observations of far ultraviolet atomic emissions from Io's near-surface and extended atmosphere favors sublimation as the main mechanism (Clarke et al., 1994, Wolven et al., 2001, Retherford et al., 2007, Roth et al., 2011). Tsang et al. (2012, 2013) found that a combination of both, a sublimation-driven and a time-invariant volcanic component, is required to explain the influence of the variations in sunlight

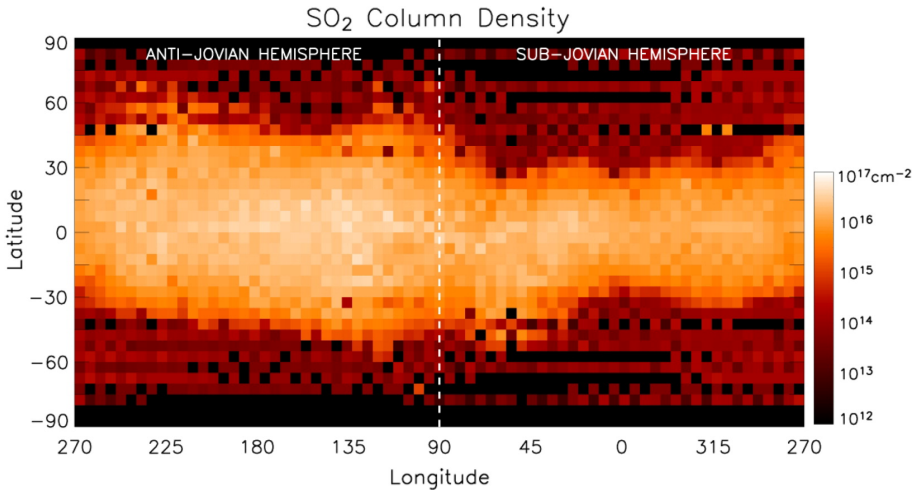

Figure 2.2. – Average distribution of Io's daytime SO_2 atmosphere derived from Lyman-α observations. The cylindrical projection shows the obvious difference in abundance between anti- and sub-Jovian hemispheres (Feaga et al., 2009).

on the atmospheric density throughout an entire Jupiter year. The increase of 25% in insolation at perihelion compared to aphelion due to the orbital eccentricity of Jupiter effects a seasonal increase in atmospheric density on Io (Tsang et al., 2012, 2013). Recently, Tsang et al. (2016) have shown that sublimation is the dominant producer of Io's atmosphere. They presented the first high-resolution spectra at 19 μm of Io's SO_2 atmosphere in Jupiter eclipse from the ground based Gemini telescope. Their modeling study demonstrated that the atmosphere has collapsed by a factor of 5 ± 2 (from 2.0–2.5 $\times$ 10^{20} m^{-2} to $\sim$0.5 $\times$ 10^{20} m^{-2}) shortly after eclipse ingress, implying that the atmosphere is strongly sublimation-driven. Furthermore, from their modeling and previous UV observations they infer that at ingress longitudes (eclipse ingress longitudes at $\sim$340° W), the atmosphere is mostly maintained by sublimation, while at egress longitudes (eclipse egress longitudes at $\sim$20° W), where a larger number of volcanic centers is located, the atmosphere is dominated by volcanic outgassing.

Observations of surface reflected solar Lyman-α intensity by the Hubble Space Telescope imply a latitudinal variation of the SO_2 atmosphere (Roesler et al., 1999, Feldman et al., 2000, Strobel and Wolven, 2001) as shown in Figure 2.2. A sharp decrease of the SO_2 density ($with$ $\sim$2% of the equatorial SO_2 column density at the poles) poleward of 30° is expected in order to explain the observations (Strobel and Wolven, 2001). Studies showing that the latitudinal dependence is due to a sublimation-dominated atmosphere have been inconclusive (Lellouch et al., 2007). Although the latitudinal variations of the atmosphere observed by HST Imaging Spectrograph (STIS) can be interpreted as an atmosphere at vapor pressure equilibrium varying with frost temperature (Jessup et al., 2004, Jessup and Spencer, 2013), the variations can also be attributed to more volcanoes near the equator (Strobel and Wolven, 2001, Feaga et al., 2009). The inferred latitudinal and seasonal variations in the SO_2 density are also

consistent with a sublimation-driven atmosphere with a SO_2 frost albedo of $\sim$0.5 $\pm$ 0.09 (Tsang et al., 2012, Walker et al., 2012) and an inferred volcanic component that is $\sim$20–30% of the sublimated gas density (Jessup and Spencer, 2015). Besides the latitudinal variability, the atmospheric density varies with longitude, with the densest atmosphere located on the anti-Jovian hemisphere. Feaga et al. (2009) derived a global map of the SO_2 column density from HST STIS observations of the reflected Lyman-α radiation (see Figure 2.2), which shows a denser and more extended atmosphere on the anti-Jovian hemisphere (with a maximum column density of 5×10^{16} cm^{-2}). These findings are also supported by the studies of Jessup et al. (2004), Spencer et al. (2005), Moullet et al. (2010) and Tsang et al. (2012). Additionally, Saur et al. (2002) suggest an upstream-downstream asymmetry of Io's surface density and scale height, which are smaller on the upstream side (by a factor of two difference) than on the downstream side due to the drag force of the flowing plasma on Io's atmosphere.

The mentioned variations of the atmosphere, different measurement techniques, and data analysis models, leads to partly inconsistent values for the SO_2 column density obtained over the years. The observations of Io's atmosphere indicate that Io's equatorial dayside SO_2 column density ranges from 1.5 to 22 $\times$ 10^{20} m^{-2} depending on the observed longitude and heliocentric distance of Io at the time of observation (McGrath et al., 2000, Jessup et al., 2004, Spencer et al., 2005, Jessup and Spencer, 2015, Feaga et al., 2009, Tsang et al., 2012). Lellouch et al. (2007) inferred in their review a mean vertical column density of (1–5) $\times$ 10^{20} m^{-2} for Io's atmosphere and a coverage of 50–70% of the dayside hemisphere. Io's dayside surface temperature varies between 110–120 K (e.g., Strobel et al., 1994, Wong and Smyth, 2000). Spencer et al. (2000) provide a lower surface temperature of about 90 K on the night side from Galileo radiometer measurements.

Earth-based high-resolution optical spectroscopic studies by Brown and Chaffee (1974a,b) revealed emission by free sodium (Na) atoms at Io which Trafton et al. (1974) showed to come from extended neutral clouds. Following observations have shown the presence of clouds of neutral potassium (K), oxygen (O), and sulfur (S) near Io (Trafton, 1975, Brown and Ip, 1981, Pilcher and Strobel, 1982, Durrance et al., 1983). Kupo et al. (1976) reported the detection of ionized sulfur implying that the Jovian magnetosphere contains heavy ion plasma (O^{++}, S^{+++}, O^{+}, S^{++}, and S^{+} (Bagenal et al., 2016)) in addition to hydrogen plasma (Frank et al., 1975).

The loss of Io's atmosphere into the Jovian magnetosphere has a strong impact on the entire Jovian system. This atmosphere is permanently being lost to Jupiter's magnetosphere due to primarily sputtering, ionization and charge exchange. The lost particles are partly ionized and partly neutral. The neutrals are finally ionized by UV radiation or electron impact (Saur et al., 2004). The ions are then picked-up by Jupiter's

Table 2.1. – Physical properties of Io and Europa and their local plasma environment (Neubauer, 1998, Schubert et al., 2004, Weiss, 2004, Kivelson et al., 2004, and references therein). The ion/electron cyclotron frequency is calculated by $\Omega_{i,e} = \frac{|q|B_0}{2\pi m_{i,e}}$ and the ion gyroradius by $r_{g,i} = \frac{v_{th}}{2\pi\Omega_i}$ with the thermal velocity $v_{th} = \sqrt{\frac{2k_BT_i}{m_i}}$ and the charge q.

	Io	Europa
Satellite's radius	1821 km (R_{Io})	1569 km (R_E)
Semi-major axis	5.9 R_J	9.4 R_J
Mass density	3.5 g cm^{-3}	3.014 g cm^{-3}
Relative plasma velocity v_0	57 km s^{-1}	104 km s^{-1}
Average Jovian magnetic field B_0	2000 nT	450 nT
Electron number density n_e	1200–3800 cm^{-3}	18-250 cm^{-3}
Temperature of the thermal electrons k_BT_e	5 eV	100 eV
Temperature of the ions k_BT_i	20–90 eV	50–400 eV
Mean ion mass m_i	22 amu	18.5 amu
Ion cyclotron frequency Ω_i	1.5 Hz	0.5 Hz
Electron cyclotron frequency Ω_e	48 kHz	10 kHz
Thermal ion gyroradius $r_{g,th}$	1.8 km	8 km
Pickup ion gyroradius $r_{g,pu}$	3 km	19 km
Alfvén velocity v_A	27–53 km s^{-1}	76–330 km s^{-1}
Alfvén Mach number M_A	0.3	0.39
Sound velocity c_S	150–340 km s^{-1}	145–700 km s^{-1}
Sonic Mach number M_S	1.65	1.75
Plasma beta β	0.04	0.06
Alfvén conductance Σ_A	2.4–5.4 S	1.1–5.5 S
Pedersen conductance Σ_P	200 S	30 S
Hall conductance Σ_H	100-200 S	10 S

rotating magnetic field and form the so-called Io torus or plasma torus as shown in the sketch of Figure 2.3. Saur et al. (2003) investigated the relative importance of elastic and inelastic collisions in Io's atmosphere and found that at least 80 % of the material leaves the atmosphere as neutrals accelerated by elastic collisions with the corotating plasma. The total mass that is fed into the magnetosphere is assumed to be as much as 1 ton per second (Broadfoot et al., 1979).

2.1.3. Concepts of Io's Plasma Interaction

Io is located at a distance of about 5.9 R_J (where R_J =71492 km is the radius of Jupiter) deep within Jupiter's huge magnetosphere which is thought to extend up to the orbit of Saturn (4.3 AU from Jupiter) on the nightside. In the inner magnetosphere (<10 R_J), the plasma is influenced by the planet's strong magnetic field and corotates almost rigidly with the planet's period (Hill, 1979). Io rotates around Jupiter with a Keplerian velocity of 17 km s^{-1} whereas the magnetospheric plasma moves with Jupiter's magnetic field lines with a velocity of about 74 km s^{-1} in the same direction. As Io's orbital period is larger (42 h 28 min) than Jupiter's rotation period (9 h 55m), the magnetospheric

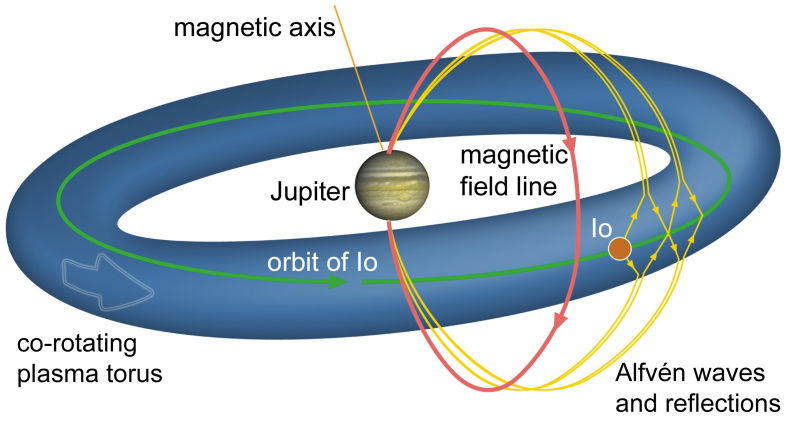

Figure 2.3. – Sketch of the far-field interaction of Io with the Jovian magnetosphere. The Alfvén wings are displayed by the yellow lines. The plasma torus is inclined with respect to Io's orbit (green line) due to the tilt of Jupiter's magnetic axis. The Alfvén waves are partly reflected at the torus edges (Jacobsen et al., 2007).

plasma constantly overtakes the moon and impinge onto Io's atmosphere with a relative velocity of 57 km s^{-1}. Due to the local perturbation of the plasma flow, several plasma wave modes are excited. The Alfvén wave is the most important for our studies as it carries the electric currents almost lossless parallel and anti-parallel to the magnetic field (Neubauer, 1980). The geometry of Io's interaction with the Jovian magnetosphere and the Alfvén wave propagation are sketched in Figure 2.3.

In several previous studies of the moon-plasma interaction the plasma is described by a fluid approach (e.g., Linker et al., 1988, Neubauer, 1998, Saur et al., 1999). Our models of Io's and Europa's plasma interaction are also based on the fluid approach. This description is convenient but it neglects the small-scale kinetic effects in the theoretical concept of the interaction (see, e.g., Saur et al., 2004). The characteristic microscopic length and time scales, e.g., ion gyroradii and gyroperiods (see Table 2.1), are considerably smaller than the global scales of Io, i.e. its radius, and plasma convecting times (at Io, a given plasma velocity of 57 km/s and Io's diameter of 3642 km give a typical convecting time of one minute). Therefore, the fluid approach is valid for the treatment of Io's plasma interaction. Furthermore, several characteristic parameters qualitatively constraint Io's plasma interaction. For instance, the plasma beta β (ratio of thermal pressure to magnetic field pressure), which is considerably smaller than one (see Table 2.1), and the Alfvénic Mach number (ratio of the unperturbed plasma bulk velocity to the velocity of the Alfvén waves) of M_A=0.3 imply that the influence of Jupiter's strong magnetic field is the dominant component in modifying the topology of the interaction

These properties make the interaction essentially anisotropic (Saur et al., 2004). The low M_A, the sonic Mach number M_s =1.65, and the fast Mach number, which is smaller than one, indicate that no bow shock forms at Io and that the interaction is sub-Alfvénic.

Io's orbit is embedded in the Io plasma torus (see Figure 2.3). Thus, Io's atmosphere is constantly bombarded by magnetospheric particles. As we treat the plasma as a fluid, we consider the plasma interaction in the magnetohydrodynamical framework. There are two different approaches within the MHD approach to describe the plasma interaction (see, e.g., Saur et al., 2004, and references therein): the B, v picture (with the magnetic field B and the bulk velocity v as fundamental variables) and the E, j picture (with the electric field E and the current density j as fundamental variables). The analytic interaction model which we apply to calculate the influence of plumes at Europa on the Alfvénic far-field is based on the model developed by Saur et al. (1999, 2007) and is for the most part formulated in the E, j approach. We will begin the explanation of the physics of Io's plasma interaction in the E, j concept.

The continuous flow of the magnetospheric particles past Io's atmosphere generates local perturbations. Due to electron impact ionization, elastic collisions between the torus particles and the atmospheric particles, and, to a lesser extent, photoionization (Saur et al., 1999), a highly conducting ionosphere within Io's atmosphere is formed. Assuming that the magnetic field lines are frozen into the fluid, the electric field in the rest frame of the magnetospheric plasma is required to be zero. In the rest frame of Io, the atmospheric gas and the ionospheric plasma are at rest with respect to the corotating torus plasma. Thus, the ionospheric plasma undergoes a motional electric field $\underline{E}_0 = -\underline{v}_0 \times \underline{B}_0$, which permits an electric current to flow through Io's ionosphere. $\underline{B}_0$ and $\underline{v}_0$ are the background magnetic field and the undisturbed relative plasma velocity, respectively. The ionospheric current flows mostly from the Jupiter-facing side of Io to the anti-Jupiter side as shown in Figure 2.4 and carries a total electric current of about 10 million A through Io's ionosphere (Saur et al., 1999). The electric conductivity parallel to the magnetic field direction is generally very high everywhere. In the ionosphere the electric conductivity perpendicular to the electric field becomes large while it is almost zero elsewhere. The ionospheric current system essentially short circuits and modifies the corotational electric field as seen in the rest frame of Io by generating polarization charges. The modification of the electric field effects the local Lorentz forces resulting in an acceleration or deceleration of the plasma in the vicinity of Io. The plasma flow is strongly diverted around Io and significantly reduced inside the ionosphere. The neutral atmosphere becomes dilute with increasing distance from Io. Hence, the ionospheric current perpendicular to the magnetic field cannot be maintained outside the ionosphere because of the vanishing conductivity perpendicular to the magnetic field and the current system is continued along the magnetic field lines carried by Alfvén waves.

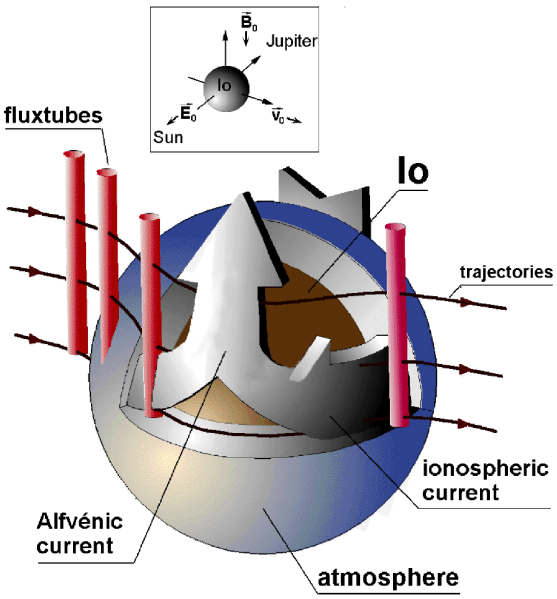

Figure 2.4. – Sketch of the local plasma interaction in Io's close vicinity. The coordinate system of the sketch and the model by Saur et al. (1999) presented in Section 2.1.3.1 is illustrated in the small box. The wide, grey arrows represent the current system and the black lines show the trajectories of the flux tubes (red) (Saur et al., 2000).

In the v, B picture momentum is exchanged through mass loading and collisions between the plasma and the atmosphere. These processes are balanced by the $\underline{j} \times \underline{B}$ force in the momentum equation and lead to a deceleration of the plasma flow. This deceleration implies a pile up of the magnetic field lines in the upstream region of the moon and a draping of the field lines around the moon sketched in Figure 2.5. The magnetic field lines slowly convect through the ionosphere bending around it (Saur et al., 2004). The pile up of the magnetic field lines results in an enhanced magnetic field magnitude upstream of the moon. Farther away from Io's ionosphere, the magnetic field lines move with the corotating plasma. Mass loading and collisions vanish and the inertia of the plasma becomes important and is balanced by the $\underline{j} \times \underline{B}$ force. The incident plasma flow is diverted around Io resulting in an increase of the plasma velocity at the flanks of the moon. Downstream of the moon, the magnitude of the magnetic field decreases and the plasma flow is accelerated to its unperturbed velocity due to the magnetic tension which straightens out the field lines. The local perturbation produced in the ionosphere excites different wave modes. In particular, the Alfvén wave plays the main role carrying field-aligned electric current $\underline{j}_{C_A^{\pm}}$ as indicated in Figure 2.5.

For the coupling of the current system in the far-field (outside Io's atmosphere) for a sub-Afvénic interaction, two standard models exist:

1. The unipolar inductor model describes the electric currents with Birkeland currents and assumes an infinite conductivity along the magnetic field direction (Piddington and Drake, 1968, Goldreich and Lynden-Bell, 1969).

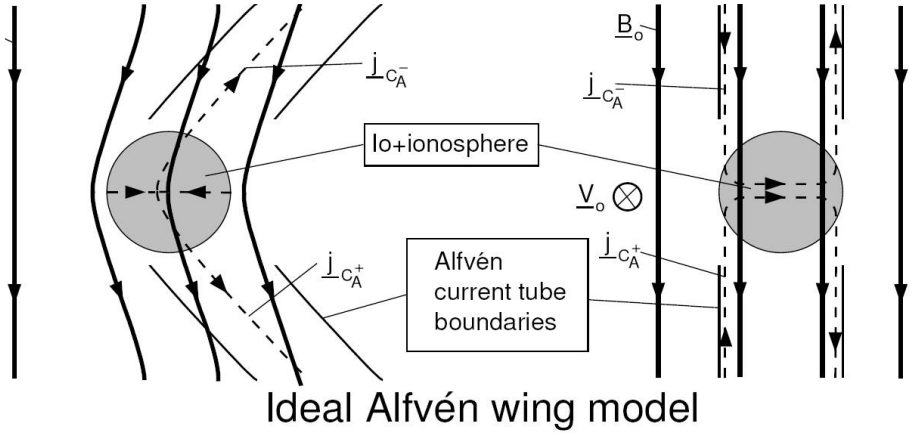

Figure 2.5. – Sketch of the ideal Alfvén wing model applied to Io in a side view (left, Jupiter is located behind Io) and in a front view along the flow direction (right, with Jupiter to the far left). The current system is shown by dashed lines and the magnetic field lines are represented by solid lines with arrows. Ionospheric currents are connected to Alfvén wing currents along the Alfvén characteristics $C_A^{\pm}$. The boundaries of the current tubes are shown as solid lines (Kivelson et al., 2001a, Saur et al., 2004).

2. The Alfvén wing model describes Io's interaction independent of Jupiter's ionosphere and characterized by the Alfvén conductance in the far-field (Neubauer, 1980, Goertz, 1980).

The currents in the unipolar inductor model close in Jupiter's ionosphere which is specified by the Jovian Pedersen and Hall conductances (Piddington and Drake, 1968, Goldreich and Lynden-Bell, 1969). This model neglect the plasma inertia, because a low-density plasma is assumed. Therefore, the validity of this model is limited to high magnetic latitudes and is not given in the high density Io plasma torus (see, e.g., Saur et al., 2004). The Alfvén wing model takes into account reflected Alfvén waves at the boundaries of the torus or the Jovian ionosphere (see Figure 2.3) (e.g., Neubauer, 1998, Jacobsen et al., 2007). The unipolar inductor model is seen as the extreme case of an infinite number of overlapping reflected wings (Neubauer, 1998, and references therein). The importance of the current loop model (unipolar inductor) and the Alfvén wing model depends on the relative values of the Alfvén wave time to Jupiter's ionosphere and the time for the plasma to convect through Io. For our studies, the plasma interaction is described with the pure Alfvén wing model so that Jupiter's ionosphere and reflected Alfvén waves reaching the moon again and modifying its electric field are neglected. The ideal Alfvén wing model is a good approximation for Io's local plasma interaction (for further details see, e.g, Saur et al., 2004) and has already been applied, e.g., in the work of Linker et al. (1998), Combi et al. (1998), Saur et al. (1999). In the following, we further describe the ideal Alfvén wing model.

The Alfvén waves propagate with the Alfvén velocity $\underline{v}_A$ which is always larger than the plasma bulk velocity $\underline{v}_0$ at Io (see Table 2.1). Based on the linear Alfvén wing model of Drell et al. (1965), Neubauer (1980) derived a nonlinear analytic model of the Alfvénic

current system. He showed that the perturbations of the moon's plasma environment can be described as the interaction of MHD nonlinear waves in the framework of the method of characteristics (e.g., Neubauer, 1980, 1998). As illustrated in Figure 2.5, the Alfvén waves travel along characteristics which are inclined at the angle $\tan\Theta_A = M_A$ with respect to the Jovian field lines (see Figure 2.5). The Alfvén characteristics are presented by lines along the total group velocities (Neubauer, 1980). The region where the perturbation currents flow is called the *Alfvén wing* or flux tube. These transverse waves disturb consecutively the magnetic and the velocity field in the moon's plasma environment. The Alfvén wave intensity is constant along the Alfvén characteristics at an arbitrary distance from Io's atmosphere (Neubauer, 1998). The Alfvén wing model is sketched in Figure 2.5.

Apart from Alfvén waves, compressional slow and fast mode magnetosonic waves are generated by the plasma interaction. Slow mode waves can also generate wing structures along their characteristics (Neubauer, 1998) tilted at $\arctan M_S$ to the background magnetic field. Along the magnetic field, the slow mode group velocity is the sound speed which is not limited to propagation strictly parallel to the magnetic field as it is the case for Alfvén waves (Linker et al., 1988). However, the perturbations associated with the slow mode waves are generally much weaker than the Alfvén perturbations (Neubauer, 1998). Unlike the amplitude of the Alfvén wave, the amplitude of the slow mode decreases with distance to Io (Neubauer, 1998). The magnetic field diffuses through Io and, hence, the magnetic field downstream of the moon is much weaker then upstream resulting in a decrease of the magnetic pressure and in an increase of the plasma pressure. The slow mode restores the pressure balance, where the plasma and magnetic pressures are anti correlated (Linker et al., 1988). The disturbances associated with the fast mode propagate away from the moon in an approximately isotropic manner and decrease in amplitude with the distance from the moon (Neubauer, 1980). As Io moves with a velocity smaller than the fast magnetosonic mode, no characteristics exist for the fast mode (Saur et al., 2004). There exists another degenerated wave mode corresponding to entropy waves with the group velocity $\underline{v}_0$ extending to infinity like the Alfvén mode. This wave mode is associated with density and temperature variations in ideal MHD and is often neglected (Neubauer, 1998).

The strong electromagnetic interaction between Jupiter's magnetic field and Io's ionosphere is illustrated in the infrared (Connerney et al., 1993) and UV (Clarke et al., 1996) images of an intense spot of the magnetic flux tube connected to Io and a trailing wake-like structure on Jupiter's upper atmosphere. The spot is called the Io *footprint* and is shown in Figure 2.6. Footprints in the far UV (FUV) emissions of Europa and Ganymede (see Figure 2.6) have also been identified by Clarke et al. (2002).

A further visible effect of Io's plasma interaction is Io's aurora which appears as two bright spots near Io's magnetic equator (Roesler et al., 1999, Geissler et al., 1999).

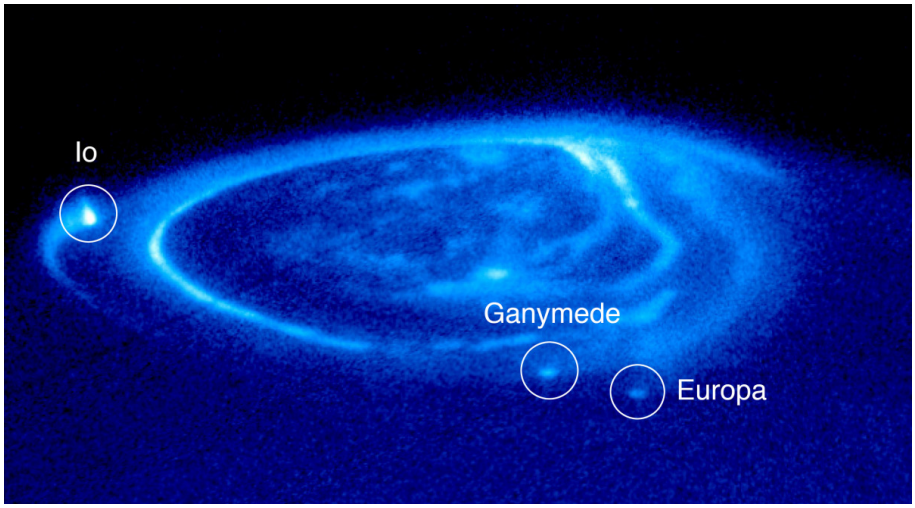

Figure 2.6. – Aurorae seen in a UV image of Jupiter taken with the Hubble Space Telescope Imaging Spectrograph (STIS) on November 26, 1998. The annotations mark the Io, Ganymede, and Europa footprints. (Courtesy of NASA and the Hubble Heritage Team)

Saur et al. (2000) explained the morphology of the aurora with the diversion of the incident electrons into the atmosphere. While upstream of the moon only a small fraction of the hot torus electron flux tubes can reach Io's atmosphere, at the flanks the streamlines are less divergent and hot electrons can easily enter the atmosphere producing bright emissions. The primary source of the auroral glow is electron impact excitation (Saur et al., 2000, Shaposhnikov et al., 2013). As Jupiter's background magnetic field changes with time at the location of Io, the spots oscillate so that they stay in approximate correlation with Io's magnetic equator (Roesler et al., 1999, Geissler et al., 1999). Retherford et al. (2000) have shown that the spot locations in HST FUV images only coincide to $\sim$80% with the tangent magnetic field points. The attenuation of the spot oscillation could originate from a modification of the magnetic field near Io (Roth et al., 2017).

In the following section, we will focus on the ionospheric interaction and describe the basic ideas of the theoretical description of the ionospheric currents and electric field in the models of Saur et al. (1999, 2007). These models are also the basis for our analytic studies of the influence of atmospheric inhomogeneities on Europa's plasma interaction. Europa's sub-Alfvénic plasma interaction is similar to the interaction scenario at Io (see Section 2.2.4). Therefore, the theoretical description of the ionospheric currents is analogous.

2.1.3.1. Overview of the Models by Saur et al. (1999, 2007)

Considering the satellite's plasma interaction, Saur et al. (1999) develop a three-dimensional, stationary, two-fluid plasma model for electrons and one ion species. The model was also previously applied to Europa in Saur et al. (1998). In the following,

we outline the main steps of the derivation of the model, its analytic solution, and the implications of the ionospheric Hall effect on the plasma interaction at Io.

As mentioned above, Io's ionosphere has an electromagnetic influence on the unperturbed magnetospheric plasma flow producing a current system consisting of ionospheric currents and Alfvén wing currents. Saur et al. (1999) begin with the momentum equations for electrons and one ion species and derive an equation for the electric potential in Io's ionosphere. Due to the very large electric conductivity parallel to the magnetic field lines, the background magnetic field lines are isolines of the electric potential (e.g., Neubauer, 1998, Saur et al., 1998, 1999). Consequently, the electric potential is reduced to two coordinates (in the xy plane) perpendicular to the background field. An Io-centered coordinate system is used in the derivation: the z axis is antiparallel to the background magnetic field, the y axis points in direction opposite to the unperturbed motional electric field $\underline{E}_0$, and the x axis points into the direction of the corotational flow (see small box in Figure 2.4). Plasma flow, electric current and the resultant magnetic field perturbations can be calculated from the electric potential. The electric potential is related through $\underline{E} = -\nabla\Phi$ to the electric field $\underline{E}$. The derivation of the electric potential is similar to previous derivations, e.g., by Wolf-Gladrow et al. (1987) or Neubauer (1980, 1998). Saur et al. (1999) derive a two-dimensional elliptic differential equation for the electric potential Φ. The magnetic field is not treated self-consistently and is given by the constant homogeneous background magnetic field $\underline{B}_0$ with the magnitude B_0. Thus, only the electric field is calculated. The magnetic field can be determined as a perturbation field based on the calculated electric current. The magnetic field components in the Alfvén wings are then directly calculated from the electric potential (Neubauer, 1980).

The motional electric field induces currents inside Io's ionosphere. The currents which are driven in the moon's ionosphere are the Pedersen and Hall currents and are described by the anisotropic Ohm's law:

$$\underline{j}_\perp = \sigma_P \underline{E}_\perp + \sigma_H \frac{\underline{B} \times \underline{E}_\perp}{B_0} \tag{2.1}$$

with the Pedersen and Hall conductivities σ_P and σ_H and the electric field $\underline{E}_\perp$ perpendicular to the background magnetic field. These conductivities depend on the elastic ion-neutral collision frequencies and mass loading processes:

$$\sigma_P = \frac{en}{B_0} \frac{\omega_{\mathsf{ci}} \tilde{\nu}_{\mathsf{in}}}{\omega_{\mathsf{ci}}^2 + \tilde{\nu}_{\mathsf{in}}^2} \tag{2.2}$$

$$\sigma_H = \frac{en}{B_0} \frac{\tilde{\nu}_{\mathsf{in}}^2}{\omega_{\mathsf{ci}}^2 + \tilde{\nu}_{\mathsf{in}}^2}\,, \tag{2.3}$$

where n is the neutral number density of the plasma (densities of the electrons and the ions are equal for quasi-neutrality), e is the electron charge, $\tilde{\nu}_{\text{in}}$ is the effective ion-neutral collision frequency, and ω_{ci} is the ion gyro frequency. Neubauer (1998) has shown that the electron gyro frequency exceeds the effective electron collision frequency in Io's and Europa's vicinity. Consequently, the ionospheric conductivities depend only on the gyro frequency and the effective collision frequency. Since the conductivities become very small outside of the ionosphere, the perpendicular ionospheric currents $\underline{j}_\perp$ need to be continued along the magnetic field lines and coupled to the field-aligned currents $\underline{j}_\parallel$ that are driven in the Alfvén wings. This is based on charge conservation given by $\nabla \cdot \underline{j} = \nabla \cdot (\underline{j}_\perp + \underline{j}_\parallel) = 0$ within the MHD approximation. The Alfvénic current

$$j_A = \pm \Sigma_A \nabla \cdot \underline{E} \tag{2.4}$$

flows along the Alfvén characteristics and is described by the Alfvén conductance Σ_A. Using the condition of charge conservation allows us to derive the differential equation for the electric potential (e.g., Neubauer, 1998)

$$(\Sigma_P + \Sigma_A)\Delta\Phi + \left(\frac{\partial \Sigma_P}{\partial x} - \frac{\partial \Sigma_H}{\partial y}\right)\frac{\partial \Phi}{\partial x} + \left(\frac{\partial \Sigma_P}{\partial y} + \frac{\partial \Sigma_H}{\partial x}\right)\frac{\partial \Phi}{\partial y} = 0\,. \tag{2.5}$$

$\Sigma_{P,H}$ are the height-integrated conductivities, which are called conductances. The integration is performed along the field lines (along z because $\underline{B}_0 \parallel \underline{e}_z$) from the moon's surface out to a distance where the conductivities vanish. In regions of constant conductances, Equation (2.5) reduces to a two-dimensional Laplace equation for the electric potential:

$$\Delta\Phi(x, y) = 0\,. \tag{2.6}$$

Saur et al. (1999) present an analytic solution of Equation (2.5) for a cylindrical homogeneously conducting body. The electric field has to fulfill the boundary conditions that the electric potential is continuous over the boundary and the electric perturbation vanishes at infinity. Additionally, the electric field can jump across the flux tube boundary due to jumps in the conductances (see equation (A2) in Saur et al., 1999). The solution for the ionospheric electric field is then given by

$$\underline{E}^i = -E_0 \frac{2\Sigma_A}{\Sigma_H^2 + (\Sigma_P + 2\Sigma_A)^2} \begin{pmatrix} -\Sigma_H \\ \Sigma_P + 2\Sigma_A \\ 0 \end{pmatrix} = \underline{E}_0 + E_P \begin{pmatrix} \sin\theta_P \\ \cos\theta_P \\ 0 \end{pmatrix} \tag{2.7}$$

where the magnitude of the perturbation electric field is given by

$$E_P = E_0 \sqrt{\frac{\Sigma_H^2 + \Sigma_P^2}{\Sigma_H^2 + (\Sigma_P + 2\Sigma_A)^2}}\,. \tag{2.8}$$

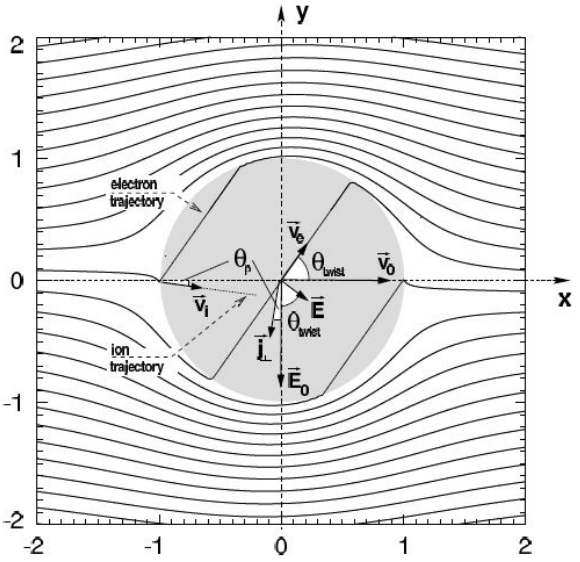

Figure 2.7. – Basic properties of Io's local plasma interaction in the xy plane perpendicular to the background magnetic field derived from the analytic solution of the electric potential equation for constant ionospheric conductances inside the circle with radius $R = 1$ indicating Io's ionosphere. The isocontours show the electric potential and are also the trajectories of the electrons. The plasma velocity is strongly reduced inside the grey shaded circles, which indicates the interaction region. Due to the ionospheric Hall effect, the electron flow is rotated towards Jupiter and the ion flow is slightly rotated away from Jupiter. Most of the plasma is directed around the moon so that it is accelerated on the flanks with respect to the upstream velocity (Saur et al., 1999).

The angle θ_P describes the slight deviation of the ionospheric currents and the ion velocity from the negative y-direction due to the Hall currents:

$$\tan\theta_P = \frac{2\Sigma_A\Sigma_H}{\Sigma_H^2 + \Sigma_P(\Sigma_P + 2\Sigma_A)}\,. \tag{2.9}$$

The deviation is visible in Figure 2.7. The electric field and the velocity field of the electrons perpendicular to the background magnetic field (which is well approximated to first order by the $\underline{E} \times \underline{B}$ drift) are twisted by the angle

$$\tan\theta_{\text{twist}} = -\frac{E_x^i}{E_y^i} = \frac{\Sigma_H}{\Sigma_P + 2\Sigma_A}\,. \tag{2.10}$$

Figure 2.7 shows the deviation of the electromagnetic fields and the break of the anti-sub-Jovian symmetry in the ionosphere (and the Alfvénic far-field). This effect is the result of the ionospheric Hall currents and is called the *ionospheric Hall effect*. Note that for very small Hall conductances the fields are symmetric with respect to the xy plane in the ionosphere. Estimated values for the ionospheric and Alfvén conductances in Table 2.1 indicate that the Hall and Pedersen conductances are of the same order resulting in a significant influence on the electromagnetic fields in Io's ionosphere. Figure 2.7 illustrates the isolines of the analytical solution and the flow pattern. For example, the electron flow is strongly twisted as it is convected across Io's ionosphere. This twist

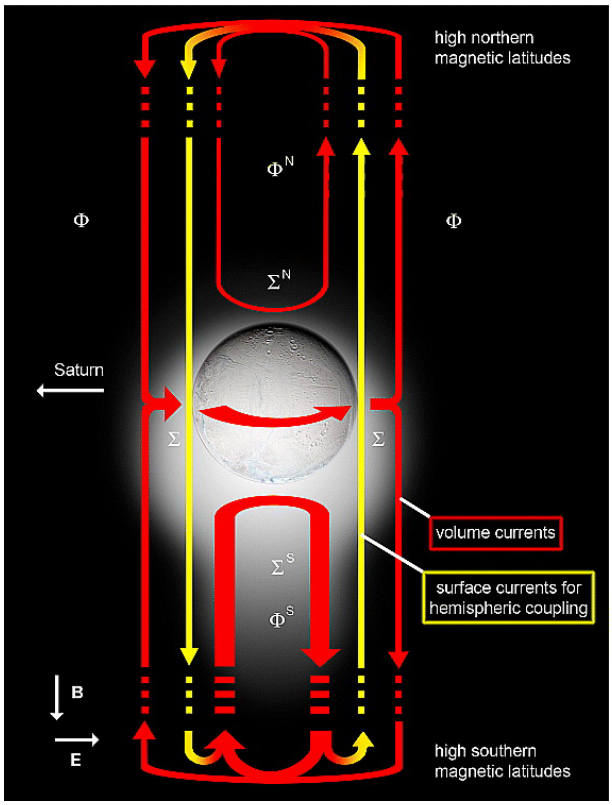

Figure 2.8. – Sketch of the electric current system for a non symmetric plasma interaction due to a south polar plume at Enceladus (Saur et al., 2007).

angle can easily exceed 45° (Saur et al., 1999).

The basis of our analytic studies of the influence of plumes on the plasma interaction is a model for sub-Alfvénic asymmetric magnetospheric interaction developed for Saturn's moon Enceladus by Saur et al. (2007), which we modify and expand for Europa's plasma interaction. The model is based on the perturbation theory for Alfvénic Mach numbers $M_A \ll 1$. For a given electrical conductivity distribution exhibiting a north-south asymmetry, Saur et al. (2007) derive an equation for the electric potential on the assumption that the magnetic field perturbations are significantly smaller than the background magnetic field. Therefore, the magnetic field is assumed to be spatially constant. The derivation of the electric potential is very similar to previous derivations, e.g., of Wolf-Gladrow et al. (1987), Neubauer (1980, 1998), and Saur et al. (1999), with the exception that on the field lines tangent to the non-conducting body a new jump condition for the electric field due to the north-south asymmetry had to be introduced (equation (9) in Saur et al., 2007). Saur et al. (2007) show that both hemispheres of Enceladus, that are not directly linked together due to the blockage of the solid body, are electromagnetically coupled through field-aligned currents, that flow tangent to the solid body. The hemisphere coupling system for Enceladus is illustrated in Figure 2.8. The coupling is due to the fact that the field lines intersecting the moon lie on different potentials of the northern (Φ^N in Figure 2.8) and southern hemisphere (Φ^S) of the moon

while field lines not intersecting the moon lie on the same potential in both hemispheres. This results in the generation of a hemisphere coupling system confined to surface currents along field lines tangent to the solid body (yellow lines). The hemisphere coupling is accompanied by magnetic field discontinuities across the flux tube as predicted and observed at Enceladus (Saur et al., 2007, Simon et al., 2011, 2014). The hemisphere coupling currents are delta currents, i.e., an infinitely thin sheet of current, within the MHD framework and, thus, lead to sharp rotational discontinuities. These delta currents are generated because the electric fields on field lines north and south of the moon differ and, hence, the electric fields jump across the flux tube enveloping the moon. In the region outside the flux tube, the field lines are isopotential lines, the currents are symmetric in the northern and southern far-field for identical Alfvén conductance Σ_A, and no hemisphere coupling currents can be driven.

2.1.3.2. Previous Models of Io's Local Plasma Interaction

In this section, we focus on numerical models for describing Io's local plasma interaction and discuss the relevant results of several authors. Wolf-Gladrow et al. (1987) developed one of the first numerical models which calculates the electric fields, magnetic fields, and current density distributions for given ionospheric conductivities and densities by using Euler potentials and poloidal and toroidal fields for the current density. The model is a three-dimensional self-consistent model of the interaction between Io and the plasma torus in the E, j framework. The authors discuss the results for different sets of densities of spherical atmosphere models and upstream plasma conditions and compare their results with Voyager measurements. This model was followed by the models by Linker et al. (1988, 1989, 1991, 1998) which self-consistently solve the full set of three-dimensional resistive MHD equations for a one-fluid plasma in the B, v framework. These models provided the possibility to study the effects of the three MHD wave modes, the Alfvén mode, the slow and the fast mode, on Io's plasma environment. Combi et al. (1998) used a three-dimensional ideal one-fluid MHD code. Both models, the models of Linker et al. (1998) and Combi et al. (1998), include the ionization and charge exchange by describing the rates of both processes in a spherical cloud around Io. The ionization rates were parameterized by the lifetime of each reaction. For the neutral density, Linker et al. (1998) and Combi et al. (1998) adopted a spherically symmetric cloud falling off as $r^{-3.5}$ based on the findings of Schneider et al. (1991) from sodium observations with a large resolution of 0.1 R_{Io}. Linker et al. (1998) considered the cases where Io is a finite conducting body, as well as cases where Io is intrinsically magnetized. Their model results match the gross features of the interaction of the Galileo I0 flyby but the results are ambiguous for the two cases. The debated issue of an internal magnetic field at Io was resolved with the magnetic field measurements along the Galileo polar passes I30 and I31. The existence of an internal magnetic field was ruled out (Kivelson et al., 2001b). Combi et al. (1998) considered only the scenario of the plasma interaction without an internal magnetic field. The authors were also able to reproduce the general

perturbations of the plasma density, magnetic field and ion pressure and temperature along the I0 trajectory. Since their boundary conditions do not provide a consistent description for the boundary conditions at electrically nonconductive and plasma-absorbing surfaces, the treatment of the surface boundary is problematic in their models. Kabin et al. (2001) improved Combi et al.'s model by including a day-night asymmetry, changes in the description of the ion pickup terms, and the tilt of the upstream magnetic field. With this modified model, it was possible to fit all qualitative perturbations of the Galileo magnetic field measurements of the I0 flyby. Khurana et al. (2011) modified the model by Linker et al. (1998) by improving the inner boundary conditions based on the work of Jia et al. (2009) and the local atmospheric environment. However, in order to reproduce the observed magnetic field perturbation along the Galileo flybys I24 and I27, the Khurana et al. (2011) model requires a global subsurface magma ocean. We discuss their model results in more detail in Chapter 5.2.

Another class of interaction models is provided by the models of Saur et al. (1999, 2002, 2003). These authors developed a two-fluid plasma model for electrons and one ion species in the E, j framework (see Section 2.1.3) and included a self-consistent calculation of Io's aeronomic processes. For simplified assumptions, some properties of Io's interaction can be calculated analytically and provide interesting results of the anisotropic nature of Io's interaction as shown in the previous Section. The main restriction of their model is that they do not self-consistently compute the magnetic field perturbations. Furthermore, they argue that they use realistic boundary conditions, i.e., when a flow line intersects Io's surface, the plasma is absorbed and the flow trajectory ends up empty of plasma.

While the presented models only consider the interaction with only one type of neutrals and without explicit chemistry, Dols et al. (2008, 2012) focus on the multi species chemistry of the interaction in Io's corona, outside of the collision-dominated ionosphere. The authors argue that the torus plasma is composed of multiple ionization states of S and O and interacts with Io's neutral corona that is composed of S, O, SO_2, and SO. This multi species interaction is able to considerably alter the composition and the energy of the plasma of the torus close to Io. The authors combine a model of the plasma flow around Io with a multi species chemistry model and compare the model results to the plasma and magnetic field measurements obtained during five Galileo flybys (I0, I24, I27, I31, and I32). Due to the complexity of the chemical reactions assumed in their model, they simplify the electrodynamic description of the interaction.

Lipatov and Combi (2006) presented the first hybrid simulations for Io's interaction with a particle approach for the ions and a fluid description for the electrons and neutrals. They claim that their model provides an accurate description for the ion dynamics and accounts for the realistic anisotropic ion velocity distribution. Therefore, the model

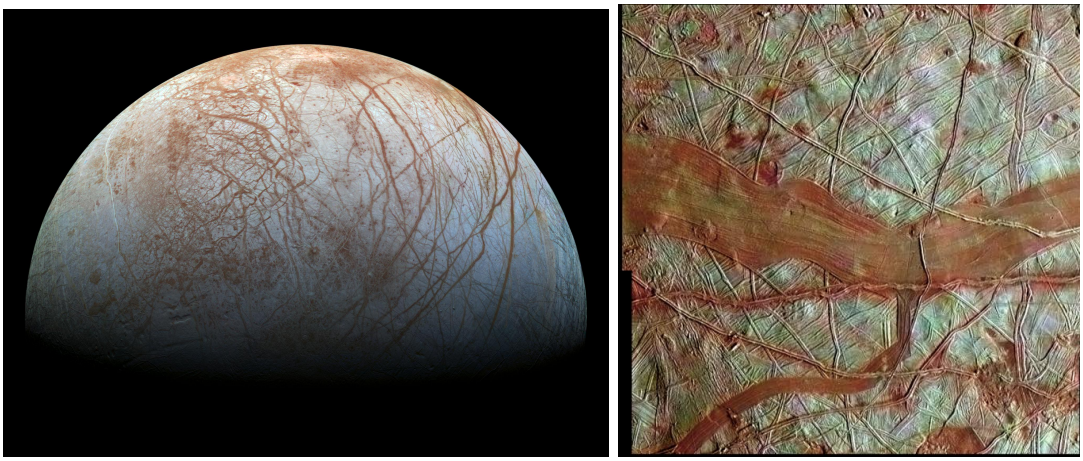

(a) (b)

Figure 2.9. – (a) Global color view of Europa consisting of images acquired by the Galileo Solid-State Imaging (SSI) experiment in 1995 and 1998. Image scale is 1.6 km per pixel. North on Europa is at right. (b) Zoom-in on Europa's surface: The blue-white terrains indicate relatively pure water ice, whereas the reddish areas contain water ice mixed with hydrated salts, potentially magnesium sulfate or sulfuric acid. The reddish material is associated with the broad band in the center of the image, as well as some of the narrower bands, ridges, and disrupted chaos-type features. The image area measures approximately 163 km by 167 km and was obtained on November 6, 1997, by the Galileo spacecraft. (Courtesy of NASA)

includes the effects of anisotropy of the ion pressure that cannot be considered in fluid simulations with isotropic temperatures.

2.2. Europa's Physical Properties and Plasma Environment

In this section, we give an overview of Europa's interior, surface features, atmosphere and its plasma interaction with the Jovian magnetosphere. Afterwards, we summarize previous theoretical and numerical models of Europa's plasma interaction which are most relevant for our study. Parts of this section were already published in Blöcker et al. (2016).

2.2.1. Europa's Interior and Surface Structure

From Galileo gravitational field measurements and modeling, it is known that Europa is a differentiated moon consisting of a metallic core, a silicate mantle and an icy outer shell of 80-170 km (Anderson et al., 1997, 1998, Sohl et al., 2002, Schubert et al., 2004). The geological young icy surface of Europa is sparsely cratered and gives indications that this moon is geologically active. Evidence for a current geological activity at Europa, on the other hand, is not supported by recent studies (Pappalardo et al., 1999, Phillips et al., 2000, Fagents, 2003). The surface is assumed to be 40–90 million years old (Bierhaus et al., 2009). Unlike Io, Europa shows only small elevations on its surface.

High resolution data obtained by the Solid State Imaging experiment of the Galileo

spacecraft provided numerous close-ups of Europa's surface. It was shown that Europa's surface is covered with a series of dark streaks crisscrossing the entire globe called *lineae* shown in Figure 2.9a. Cassen et al. (1979, 1980) showed that tidal stressing caused by the three-body Laplace resonance with Io and Ganymede and the subsequent eccentricity of Europa's orbit provide a significant internal heat source for Europa. This brought up the possibility of a liquid ocean in its icy crust. The geological analysis of long lineaments (Greeley et al., 1998), chaotic terrain (see Figure 2.9b) (Carr et al., 1998), and lenticulae (round, dark spots) (Pappalardo et al., 1998) favor the existence of a liquid ocean. Geissler et al. (1998) suggest that the explanation for the reorientation of the lineaments is non-synchronous planetary rotation of an icy crust which is decoupled from the mantle due to a subsurface liquid ocean. Thermal models also supported the existence of subsurface water layer (e.g., Spohn and Schubert, 2003).

Another technique to identify a conductive, subsurface, liquid layer is to study the induction signals in the magnetic field measurements in Europa's close environment (e.g., Khurana et al., 1998, Kivelson et al., 2000, Zimmer et al., 2000, Schilling et al., 2007) and is described in Section 2.3.2. Zimmer et al. (2000) and Schilling et al. (2007) conclude the existence of a subsurface ocean with conductivities comparable to or less than that of terrestrial seawater.

2.2.2. Europa's Atmosphere

Hubble Space Telescope observations of ultraviolet oxygen emission demonstrated the existence of a tenuous molecular oxygen atmosphere around Europa with column densities in the range of (2–14) $\times$ 10^{18} m^{-2} (Hall et al., 1995, 1998). The atmosphere is mostly produced by sputtering processes of the moon's icy surface and radiolysis driven by the energetic particle flux (Johnson et al., 2004, Paranicas et al., 2001, 2002) and primarily lost by thermal ion sputtering (Saur et al., 1998, Dols et al., 2016). A sketch of the formation of Europa's atmosphere is shown in Figure 2.10. It illustrates the incident charged particles which lead to sputtering and radiolysis of the ices on the surfaces. Sputtering then directly release H_2O molecules and products of H_2O decomposition. Using atomic oxygen emission, McGrath et al. (2004) suggested that the surface is not icy everywhere and that the composition changes with longitude. Besides atomic oxygen, other minor species such as sodium, potassium and variations of hydrogen were detected above the surface (Brown and Hill, 1996, Brown, 2001, Leblanc et al., 2002, 2005). The detailed understanding of Europa's oxygen emissions and its generation process is still an open issue. Numerical, analytic, and kinetic studies on the generation mechanism of the atmosphere have been done by several authors, e.g., Ip (1996), Shematovich and Johnson (2001), Shematovich et al. (2005), Smyth and Marconi (2006), Plainaki et al. (2010, 2013), and Cassidy et al. (2009).

Saur et al. (2011) discussed the possibility of water vapor plumes to explain asym-

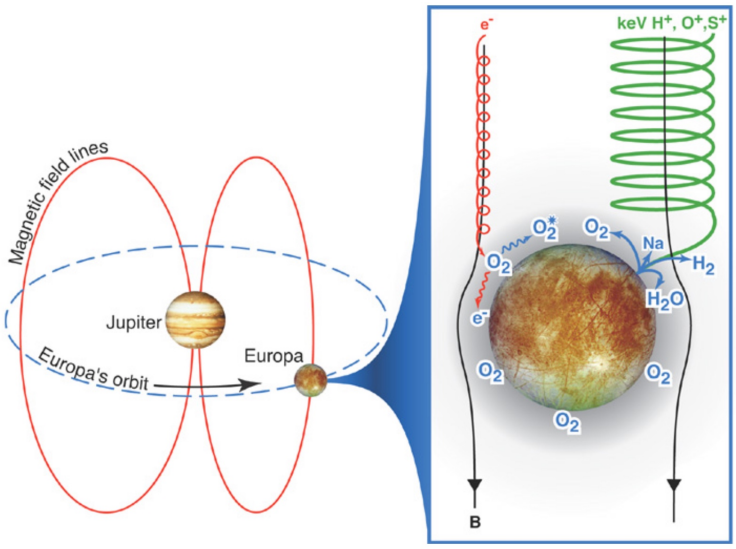

Figure 2.10. – Schematic of the formation of Europa's neutral gas environment. Ions (green) and electrons (red) trapped by Jupiter's magnetic field and erode the surface, producing a tenuous atmosphere composed mostly of O_2. Primarily H_2 and Na and other trace species form an extended neutral torus (Johnson et al., 2004).

metries or inhomogeneities in Europa's UV oxygen emission. Alternatively, emission asymmetries can also be caused by inhomogeneous surface properties (Cassidy et al., 2007), inhomogeneous solar illuminations (Plainaki et al., 2012, 2013), and by Europa's complex plasma interaction with Jupiter's magnetosphere. Roth et al. (2016) analyzed a large set of HST observations providing further details on Europa's UV emissions. They showed that the plasma interaction plays an important role in shaping the morphology of Europa's UV emission. The UV emission is brightest near its poles and dimmest near the equator.

Europa's ionosphere was detected during five Galileo spacecraft radio occultation measurements by Kliore et al. (1997). These measurements revealed an asymmetric ionosphere with electron densities reaching values on the order of 1×10^4 cm^{-3} near the surface and a plasma scale height of 240 $\pm$ 40 km from the surface up to 300 km and of 440 $\pm$ 60 km above 300 km. Saur et al. (1998) showed that electron impact ionization is the main source for the generation of Europa's ionosphere. The newly ionized particles are then accelerated to the velocity of the flowing plasma. Europa's ionosphere is not in chemical equilibrium, but strongly advection-dominated.

2.2.3. Water Vapor Plumes

In December 2012, images of Europa's UV aurora by the HST STIS, shown in Figure 2.11, revealed local hydrogen and oxygen emissions with intensity ratios, which are consistent with electron impact excitation of water molecules, considered as water vapor plumes Roth et al. (2014b). Roth et al. (2014b) show that the two water vapor

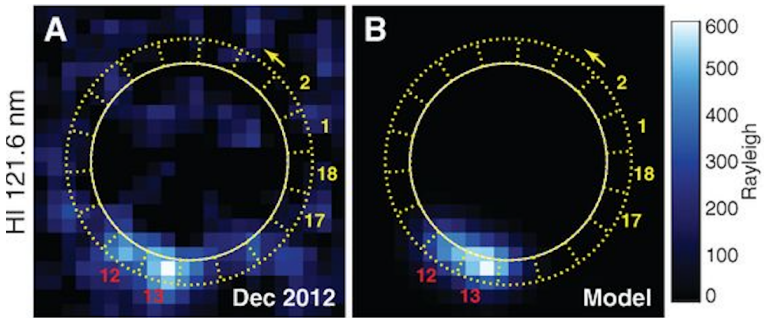

Figure 2.11. – (A) STIS H Lyman-α image of the plume detection by Roth et al. (2014b) and (B) aurora model image based on a Gaussian distribution for an H_2O plume yielding an average column density of $\sim$1.5 $\times$ 10^{20} H_2O/m^2 over a region of $\sim$300 $\times$ 300 km^2 (Roth et al., 2014b).

plumes with a scale height of 200 $\pm$ 100 km and line-of-sight column densities of $\sim$1.5 $\times$ 10^{20} m^{-2} quantitatively fit the HST/STIS observations (see Figure 2.11). Such large plumes would require large super-sonic eruption velocities of $\sim$700 m/s (Roth et al., 2014b). Europa was around the apocenter of its orbit during the detection of plumes. The positive correlation of plume activity with Europa's proximity to the apocenter would be similar to the same correlation established at Saturn's moon Enceladus by Hedman et al. (2013). However, observations from previous and further HST campaigns (more than 20 HST visits) also covering the orbital phase when tensile stresses on south polar fractures are expected to be strongest did not reveal any signatures from plumes in the observations (Roth et al., 2014a). Roth et al. (2014a), therefore, suggest that Europa's orbital position is not a sufficient condition for detecting the plumes. Reasons for the non-detection of the plumes in the other HST observations could be that the eruptive activity is highly time-variable and individual like the volcanoes on Io (Roth et al., 2014a). Additional reasons could be that the line-of-sight geometry for the detection of south polar plumes or the local plasma environment (electron density and energy environment) for the detection of plume signals in Europa's aurora was not suitable (Roth et al., 2014a).

Recently, Sparks et al. (2016) confirmed the existence of water vapor plumes near Europa's south pole from limb anomalies detected in three STIS FUV transit images. In three of ten HST FUV observations the authors found indications for plume activity. Surprisingly, the derived line-of-sight H_2O column densities in the range of (7–33) $\times$ 10^{20} m^{-2} by Sparks et al. (2016) are 5–20 times higher than the one derived by Roth et al. (2014b).

The discovery of transient water vapor plumes near Europa's south pole might open up a direct mean to probe water from a subsurface ocean in order to derive possibly important astrobiological conclusions on the exploration of a potentially habitable environment. Further observations could provide better constraints about e.g., their abundances and time-varying activity and thus give more information about the composition of the subsurface water ocean and the interior physical processes of the moon.

2.2.4. Europa's Plasma Interaction

The comparison of Europa's plasma beta and Mach numbers in Table 2.1 imply that Europa's plasma interaction with the Jovian magnetosphere is similar to Io's plasma interaction as discussed in Section 2.1.3. Europa also experiences a sub-Alfvénic flow as it is embedded in Jupiter's magnetospheric plasma, which constantly overtakes the moon. Ionization and collisions within the atmosphere and induced fields in Europa's interior modify the plasma environment and drive large currents through the moon's ionosphere which are coupled by Alfvén wing currents. Since the source of Europa's atmosphere is surface sputtering the interaction is expected to be much more coupled to the atmosphere as it is the case at Io. Furthermore, the interaction is weaker than at Io. For instance, the atmospheric densities are lower at Europa leading to smaller ionospheric conductances (see Table 2.1). Saur et al. (1998) calculated a smaller total current of 7×10^5 A through the Alfvén wing for Europa which is about a factor of 7 smaller than for Io. As shown in Table 2.1 the Pedersen conductance dominates the Hall conductance implying that the influence of the ionospheric Hall effect is very small (Saur et al., 1998).

The findings of Intriligator and Miller (1982) identified Europa as a source of plasma in Jupiter's middle magnetosphere. The mass outflow probably occur in form of a transported plasma plume (Russell et al., 2000, Eviatar and Paranicas, 2005). Additionally, Volwerk et al. (2001) analyzed ion cyclotron waves driven by positively charged pickup ions in Europa's vicinity showing that, similar to Io, Europa provides mass to Jupiter's magnetosphere. From the detection of a Jupiter-surrounding neutral gas torus in the vicinity of Europa's orbit, Mauk et al. (2003) and Lagg et al. (2003) inferred that Europa is a source of neutral gas in Jupiter's magnetosphere.

2.2.5. Previous Models of Europa's Local Plasma Interaction

In situ measurements by the Galileo spacecraft were obtained during a total of 12 flybys which were extensively studied and modeled focusing on different aspects which modify the plasma interaction with Europa's global atmosphere such as induced fields from a subsurface ocean (see, e.g., Kivelson et al., 1997, Khurana et al., 1998, Kivelson et al., 1999, Zimmer et al., 2000, Schilling et al., 2004, 2007, 2008) and influence of pickup ions (see, e.g., Paterson et al., 1999, Rubin et al., 2015). Different models have been used in the past to describe the interaction between Europa's global atmosphere and the magnetospheric plasma: a two-fluid plasma model (Saur et al., 1998), a multi species chemistry model (Dols et al., 2016), several MHD models (Kabin et al., 1999, Liu et al., 2000, Schilling et al., 2007, 2008, Rubin et al., 2015), and a hybrid kinetic approach (Lipatov et al., 2010, 2013).

Saur et al. (1998) show that the neutral atmosphere and the plasma interaction

are strongly coupled. The model treats the feedback mechanism between the atmosphere and the plasma interaction self-consistently, but assumes a homogeneous Jovian magnetic field. The model of Schilling et al. (2007, 2008) includes electromagnetic induction from a subsurface water ocean from time varying magnetic fields and Europa's interaction with the magnetospheric plasma and their mutual feedback. The authors show that the effect of the fields induced by the time variable plasma interaction is small compared to the induction caused by Jupiter's time varying magnetic field (Schilling et al., 2007). Rubin et al. (2015) study the effect of the magnetospheric and the pick-up ion populations on Europa's plasma environment. Their model calculates self-consistently the electron temperature that is crucial for the electron impact ionization.

Although these models are able to reproduce the overall structure of the measured magnetic field perturbations, some features in the data are still not understood. For example, neither the model results of Schilling et al. (2007) nor those of Rubin et al. (2015) are able to reproduce some prominent structures such as the double-peak structure in the B_x component in the Galileo Magnetometer (MAG) data during the Alfvén wing crossing of the E26 flyby.

2.3. Induction Effects at the Galilean Moons

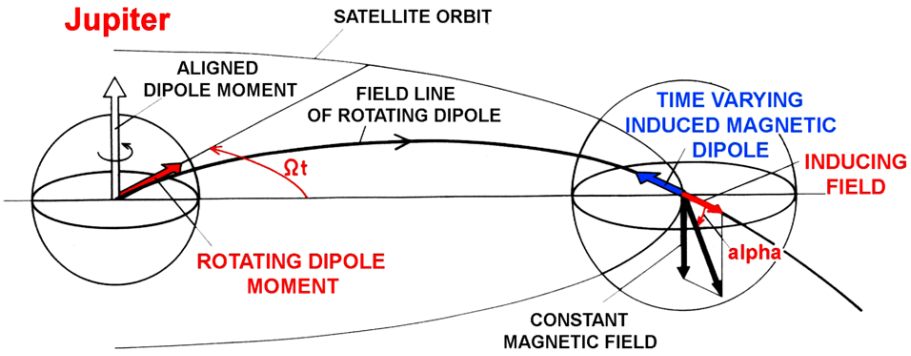

Figure 2.12. – Illustration of the varying magnetic field direction at a satellite due to Jupiter's rotating tilted dipole moment (Neubauer, 1999, Saur et al., 2010).

Electromagnetic induction in the interiors of the moons due to Jupiter's time-varying external magnetic field in the orbit of the moons possibly influence the local magnetic environment of the moons and may play an important role in the plasma interaction (e.g., Neubauer, 1999). In first-order, Jupiter's magnetic field can be approximated by a tilted dipole magnetic field (Connerney et al., 1998). The dipole moment is tilted by 9.6° against Jupiter's spin axis towards longitude 201° in Jovian System III coordinates (λ_{III}) as defined by Seidelmann and Divine (1977). The average inclination of the moons' orbits to Jupiter's equatorial plane is very small implying that the orbits are in Jupiter's equatorial plane. Thus, the moons are faced to a time-varying magnetic field during a synodic rotation period of Jupiter (see Figure 2.3).

The Jovian dipole field can be considered as the superposition of an aligned dipole field (parallel to Jupiter's spin axis) and a field due to a dipole moment perpendicular to the spin axis (Neubauer, 1999) as sketched in Figure 2.12. The aligned dipole moment produces a dipole magnetic field axisymmetric to the spin axis which does not generate a time-varying magnetic field at the moon's orbits. The dipole moment perpendicular to the spin axis (red arrow in Jupiter in Figure 2.12) generates a time-variable magnetic field within one synodic rotation period of Jupiter at the locations of the moons (red arrow at the moon). If the moon possesses a subsurface conductive layer, Jupiter's time periodic magnetic field (inducing field) at the moon's location will induce electric currents in the conductive layer after Faraday's law of induction, generating a secondary magnetic field (induced field). The associated magnetic moment of the secondary field is represented by the blue arrow in Figure 2.12. The orientation of the rotating dipole moment is modified by the angle Ωt. At $\Omega t = 0°, 180°$ the inclination angle $alpha$ is minimal and the induction effect is maximal. The secondary magnetic field mainly determines the magnetic field (inducing field) in the vicinity of the moon. In the far-field, the induced magnetic field which is proportional to $1/r^3$ vanishes but the induction in the subsurface ocean results in a weak shrinkage and a displacement of the Alfvén wings (Neubauer, 1999).

2.3.1. Induced Signals from a Subsurface Magma Ocean at Io

The existence of a global subsurface partially molten layer has been discussed since the Voyager encounters (Peale et al., 1979). Tidal dissipation in the interior might result in a partially molten layer at the base of the lithosphere (e.g., Peale et al., 1979, Keszthelyi et al., 2004). Such a global conductive layer could induce secondary magnetic fields which could be measurable in Io's vicinity (Seufert et al., 2011). Khurana et al. (2011) used Galileo MAG data obtained during the I24 and I27 flybys and inferred from MHD modeling and multiple-shell models the existence of a near-surface partially molten region in Io's interior with a melt fraction $\geq$20 %, a thickness $\geq$50 km and a conductivity of 0.43 S/m below a 30 km thick rigid non-conductive lithosphere. Their results reproduce the observed magnetic field data during the Galileo flybys, but the authors do not discuss other possible explanations for the magnetic field measurements, e.g., an asymmetric atmosphere. We discuss this issue in detail in Chapter 5.2. Recently, Roth et al. (2017) provided another technique to study Io's interior by analyzing the oscillation of Io's FUV auroral spots and investigating the influence of magnetic field perturbations on it. This technique has already been applied to constrain Ganymede's subsurface ocean through HST observations by Saur et al. (2015). Therefore, Roth et al. (2017) compare the derived locations of the auroral spots from HST FUV observations and their oscillation with the effects of induced magnetic fields from Io's interior. They find that a global subsurface magma ocean as claimed by Khurana et al. (2011) is generally not consistent with the observed aurora oscillation. The contradiction between the conclusions of Khurana

et al. (2011) and Roth et al. (2017) leaves the question about the existence of a global subsurface magma ocean still unanswered.

2.3.2. Induced Signals from a Subsurface Water Ocean at Europa

The surface morphology of Europa provides indications of the existence of liquid water under its icy crust (Carr et al., 1998, Pappalardo et al., 1999). The thickness of the water ice-liquid shell is estimated in a range of a few km to 200 km (e.g. Zimmer et al., 2000, Schenk, 2002, Schilling et al., 2007). The properties of the subsurface water ice-liquid shell like the composition, the conductivity or the thickness, are not well constrained. A permanent internal magnetic field is not detectable at Europa (Schilling et al., 2004). Observations of Europa's surface by Galileo's Near Infrared Mapping Spectrometer indicate the presence of hydrated minerals (McCord et al., 1998). These minerals are expected to originate from the underlying ice crust indicating a considerable salt concentration and hence a high conductivity for a subsurface ocean (e.g., Hand and Chyba, 2007). Galileo magnetic field measurements provide a suitable diagnostic tool to investigate a potential subsurface ocean at Europa (e.g., Khurana et al., 1998, Kivelson et al., 2000, Zimmer et al., 2000, Schilling et al., 2007, 2008). Due to Jupiter's time varying magnetic field at Europa's location, electromagnetic induction will take place in a saline, electrically conductive subsurface water ocean (e.g., Neubauer, 1999). By using a shell model for Europa's interior Zimmer et al. (2000) investigated the electrical subsurface structure based on the observed induced magnetic fields. The authors found that Europa must possess regions with conductivities of at least 0.06 S/m and thicknesses between 100 km and 200 km at a depth of less than 200 and 300 km below the surface. Schilling et al. (2007) analyzed Galileo magnetic field data during several Europa flybys taking into account the plasma interaction at Europa and the induced magnetic field and derived ocean conductivities of 0.5 S/m or larger with ocean thicknesses of 100 km and smaller to explain the data. The amplitudes A of the induction signals ($0.7 \leq A \leq 1.0$ (Zimmer et al., 2000), $A = 0.97$ (Schilling et al., 2004)) detected during several Galileo flybys indicate that a freshwater ocean is possible on Europa (Hand and Chyba, 2007).

3. Magnetohydrodynamic Model for Io's and Europa's Plasma Interaction

In this Chapter we present the 3D MHD model which we apply to describe Io's and Europa's interaction with the ambient magnetospheric torus plasma. The model results are used to study the influence of an atmospheric inhomogeneity on the overall structure of Io's and Europa's plasma environment. Additionally, we compare our model results with measured magnetic field data obtained during Galileo flybys at Io and Europa in order to verify the validity of our model and to reproduce the key features of the measured data. We focus on the satellite's near plasma environment and Alfvénic far-field (which ranges within a few satellite radii). The one-fluid MHD equations, which we apply, have been derived from a set of two-fluid equations for ions and electrons where the sources according to mass loading, plasma loss and collisions have been included (e.g., Schunk, 1975, Schunk and Nagy, 2009). We present an overview of the derivation of the MHD equations in the following Section. Afterwards, we apply a scale analysis of each term in the one-fluid MHD equations similar to Chané et al. (2013) with typical values for Io's and Europa's environment to determine which of these terms can be neglected without changing the important physical processes of the model. Furthermore, we describe the plasma sources and sinks in our model. The models for Io and Europa are similar but there are differences in the calculation of the plasma production, loss and the molecular rates which we specify in this Chapter. Subsequently, we explain our neutral atmosphere models for Io's and Europa's atmosphere, which are crucial for the modeling of the plasma interaction. Finally, we discuss the numerics, boundary conditions and initial values of our MHD model. Parts of this chapter have already been published in Blöcker et al. (2016).

The MHD approach is a suitable method to describe the interaction of the cold bulk plasma with Europa's and Io's atmosphere. Now, we go into further detail why the MHD approach is suitable for the description of our problem. The charged particles in the orbit of Europa can be subdivided into cold plasma and energetic particles. The energetic ions which can have gyroradii $>$500 km at Europa (Sittler et al., 2013) are not included in the MHD approach. At keV energies individual particle motions become important and the particles cannot be treated as a fluid anymore (Paranicas et al., 2009). The energetic particles affect mainly the thermal plasma pressure but have little effects on the momentum and force balance of the plasma flow. This balance shapes the flow and magnetic field environment around Europa and Io. The undisturbed plasma betas

in our simulations are $\sim$ 0.05 (Europa) and $\sim$ 0.06 (Io) implying that the thermal plasma pressure has a minor effect on the plasma interaction. However, we have to note here that the plasma betas may change essentially in the near vicinities of the satellites. The pressures of energetic ions (20 keV–100 MeV) are 12 nPa for Europa and 10 nPa for Io (Kivelson et al., 2004). Including the energetic ions, the plasma beta rises to $\sim$0.1 at Europa, which indicates that the thermal pressure does not play a key role in shaping the interaction. Figure 6 in the work of Bagenal and Delamere (2011) shows that the energetic ion pressure at Io's position is by an order of magnitude smaller compared to the thermal plasma pressure, which implies that the plasma beta at Io's position does not rise due to energetic ions (see also figure 5 in the work of Mauk et al. (2004)).

The gyroradii of the thermal ions are approximately 8 km at Europa and 1.8 km at Io and the ion cyclotron frequencies are 0.5 Hz at Europa and 1.5 Hz at Io (Kivelson et al., 2004). These gyroradii are much smaller than typical scales of the interaction, i.e., the radii of the satellites, the scales of the atmospheres or the scales of the plumes under consideration here. Similarly, the period of ion cyclotron motion (Europa $\sim$2 s, Io $\sim$0.7 s) is much smaller than typical convection time scales for the plasma to pass the object of 30 s for Europa and 64 s for Io. The dominant sources which drive Europa's and Io's interaction are ionization and charge exchange, which are commonly referred to as pickup processes, and the elastic collision between ions and neutrals. These processes modify the mass, momentum and energy density of the fluid and are the root cause of the magnetic field perturbations. The effects of these processes are well resolved in MHD or fluid models as long as the gyroradius is smaller than the typical length scales of the interaction, and the period of cyclotron motion is smaller than the typical time scales of the interaction (see, for example, discussion in chapter 7 of Baumjohann and Treumann (1996) on the applicability of the MHD approach). The inclusion of pickup and elastic collisions in fluid models has been described, e.g., in Neubauer (1998) and Schunk and Nagy (2009) and their principal effects in previous MHD models have been demonstrated in, e.g., Kabin et al. (1999), Liu et al. (2000), Schilling et al. (2007, 2008), Linker et al. (1998), Combi et al. (1998) or Khurana et al. (2011). Its physical effects are rigorously discussed, e.g., in Vasyliūnas (2016). In summary, the MHD approach is well suited to describe the global plasma interaction of Jupiter's magnetosphere with Io's and Europa's atmospheres and their ionospheres.

We use a Cartesian and a spherical coordinate system, both centered at the satellite. The Cartesian system is the EPhiO system for Europa and IPhiO system for Io with its x axis along the flow direction of the corotational plasma, the z axis is parallel to Jupiter's spin axis, and the Jupiter-facing y axis completes the right-handed system. The spherical coordinate system is described by the radius r, the colatitude θ measured from the positive z axis, and the longitude ϕ measured from the positive y axis in direction to the negative x axis.

3.1. Derivation of the One-Fluid Equations

We derive the one-fluid MHD equations from the two-fluid equations for one ion and one electron species where we include source terms describing electron impact ionization, dissociative recombination, and collisions between charged particles and neutrals. The two-fluid equations have been derived by taking velocity moments of the terms of Boltzmann's equation (e.g., Schunk, 1975, Szegö et al., 2000). The set of equations for the electrons and ions consists of the continuity, momentum, and energy equation as follows:

$$\partial_t n_s + \nabla \cdot (n_s \underline{v}_s) = \frac{\delta n_s}{\delta t} \tag{3.1}$$

$$\rho_s(\partial_t \underline{v}_s + \underline{v}_s \cdot \nabla \underline{v}_s) + \nabla p_s - n_s q_s(\underline{E} + \underline{v}_s \times \underline{B}) = \frac{\delta \underline{M}_s}{\delta t} - m_s \underline{v}_s \frac{\delta n_s}{\delta t} \tag{3.2}$$

$$\partial_t \epsilon_s + \nabla \cdot (\epsilon_s \underline{v}_s) + p_s \nabla \cdot \underline{v}_s = \frac{\delta E_s}{\delta t} \tag{3.3}$$

with

$$\frac{\delta n_s}{\delta t} = P_s - L_s \tag{3.4}$$

$$\frac{\delta \underline{M}_s}{\delta t} = -\nu_{s,n} \rho_s \underline{v}_s - L_s m_s \underline{v}_s \tag{3.5}$$

$$\frac{\delta E_s}{\delta t} = \frac{m_s}{m_s + m_n} \nu_{s,n} n_s \left[3k_B(T_n - T_s) + m_n \underline{v}_s^2\right] + \frac{1}{2} m_s \underline{v}_s^2 P_s - \frac{3}{2} k_B T_s L_s \,. \tag{3.6}$$

The index s describes the corresponding species, i.e., ions or electrons. The parameter n_s represents the number density, $\underline{v}_s$ is the plasma bulk velocity, and $\rho_s = m_s n_s$ is the mass density with the mass m_s. The parameter $p_s = n_s k_B T_s$ is the thermal pressure with the temperature T_s and the Boltzmann constant k_B. The internal energy density of the species s is given by $\epsilon_s = \frac{3}{2} p_s$. The parameter $\nu_{s,n}$ is the momentum transfer collision frequency between species s and the neutrals, and P_s and L_s are the production and loss rates, respectively. The remaining parameters are the charge q_s, the electric field $\underline{E}$, and the mass and the temperature of the neutrals m_n and T_n, respectively. In addition, $\frac{\delta n_s}{\delta t}$, $\frac{\delta \underline{M}_s}{\delta t}$, and $\frac{\delta E_s}{\delta t}$ are the net source, the change in momentum, and the local change in internal energy density, respectively, per unit volume of the fluid species s due to collisions, plasma production, and loss. Here it is assumed that the neutrals are at rest and that the distribution functions of the plasma species are isotropic in the plasma frame.

To derive the MHD equations, we consider one electron and one singly charged ion species. After combining Equations (3.1)-(3.6) with Faraday's and Ampère's law, we

find a set of complex one-fluid equations as follows:

$$\partial_t \rho + \nabla \cdot (\rho \underline{v}) = m_i (P - L) \tag{3.7}$$

$$\begin{aligned}\rho(\partial_t \underline{v} + \underline{v} \cdot \nabla \underline{v}) &= -\nabla p + \underline{j} \times \underline{B} - (\rho_e \nu_{\mathsf{en}} + \rho_i \tilde{\nu}_{\mathsf{in}})\underline{v} - m_i P \underline{v} + \frac{m_e}{e}(\nu_{\mathsf{en}} - \tilde{\nu}_{\mathsf{in}})\underline{j} \\ &\quad - \frac{m_e}{e^2}\underline{j} \cdot \nabla \left(\frac{\underline{j}}{n}\right)\end{aligned} \tag{3.8}$$

$$\begin{aligned}\partial_t \underline{B} &= \nabla \times \left(-\frac{m_e}{ne^2}\partial_t \underline{j} - \frac{m_e}{ne^2}\nabla \cdot \left(\underline{v}\,\underline{j} + \underline{j}\,\underline{v} - \frac{1}{\mathsf{en}}\,\underline{j}\,\underline{j}\right) + \frac{1}{ne}\nabla\left(p_e - \frac{m_e}{m_i}p_i\right)\right) \\ &\quad + \nabla \times \left(\underline{v} \times \underline{B} - \frac{1}{ne}(\underline{j} \times \underline{B}) + \frac{m_e}{e}(\nu_{en} - \tilde{\nu}_{\mathsf{in}})\underline{v}\right) \\ &\quad + \nabla \times \left(-\frac{m_e}{ne^2}\left(\frac{m_e}{m_i}\tilde{\nu}_{\mathsf{in}} + \nu_{\mathsf{en}}\right)\underline{j} - \frac{m_e}{n^2 e^2}L\underline{j}\right)\end{aligned} \tag{3.9}$$

$$\begin{aligned}\partial_t \epsilon + \nabla \cdot (\epsilon \underline{v}) &= -p\nabla \cdot \underline{v} - \frac{3k_B}{2e}\nabla \cdot \left(\left(\frac{m_e}{m_i}T_i - T_e\right)\underline{j}\right) - \frac{1}{e}\left(\frac{m_e}{m_i}p_i - p_e\right)\nabla \cdot \left(\frac{\underline{j}}{n}\right) \\ &\quad + \frac{\tilde{\nu}_{\mathsf{in}}\rho}{m_i + m_n}\left(3k_B(T_n - T_i) + m_n\frac{m_e^2}{\rho^2 e^2}j^2 + 2\frac{m_n m_e}{\rho e}\underline{j} \cdot \underline{v} + m_n v^2\right) \\ &\quad + \frac{n m_e \nu_{\mathsf{en}}}{m_e + m_n}\left(3k_B(T_n - T_e) + \frac{m_n}{n^2 e^2}j^2 + m_n v^2 - \frac{2m_n}{ne}\underline{v} \cdot \underline{j}\right) \\ &\quad + \frac{m_e}{n^2 e^2}P\underline{j}^2 - \frac{3}{2}k_B L(T_e + T_i) + \frac{1}{2}m_i P v^2\,,\end{aligned} \tag{3.10}$$

with the plasma mass density ρ, the plasma bulk velocity $\underline{v}$, the magnetic field $\underline{B}$, and the internal energy density ϵ, which is related to the plasma thermal pressure p through $\epsilon = 3/2\,p$. m_i is the ion mass and n is the plasma particle density. For the calculation of $p = nk_B(T_e + T_i)$ we consider the electron temperature T_e and the ion temperature T_i. The current density $\underline{j}$ is determined via Ampère's law $\underline{j} = \frac{1}{\mu_0}\nabla \times \underline{B}$ with the vacuum permeability μ_0. The model takes into account the produced and lost number of charged particles per time in the plasma production rate P and loss rate L.

For the calculation of Equations (3.7)–(3.10), we apply the simplification: $m_e \ll m_i$ and quasi-neutrality $n = n_e \approx n_i$. For a one-fluid plasma consisting of one ion and an electron species the plasma bulk variables: plasma velocity $\underline{v}$, total plasma mass density ρ, and total plasma pressure p are given by

$$\underline{v} = \frac{\rho_e \underline{v}_e + \rho_i \underline{v}_i}{\rho} \tag{3.11}$$

$$\rho = \rho_i + \rho_e \approx \rho_i \tag{3.12}$$

$$p = p_i + p_e\,. \tag{3.13}$$

The current density is given by $\underline{j} = ne(\underline{v}_i - \underline{v}_e)$ and the total momentum transfer collision frequency between ions and neutrals $\tilde{\nu}_{\mathsf{in}} = \nu_{\mathsf{in}} + \nu_{\mathsf{ex}}$ takes into account elastic collisions and charge exchange. The temperature of the neutrals ($T_n \approx$130 K on the dayside region of Europa (Shematovich et al., 2005) and $T_n \approx$120 K on the dayside region of Io (Rathbun et al., 2004)) can be neglected for the plasma interaction compared with the plasma

temperature of about 1160 $\times$ 10^3 K for Europa and of about 70 $\times$ 10^3 K for Io (Kivelson et al., 2004). Quantitative expressions for the source and loss terms are provided and explained in detail in Section 3.2.1. The ratio of specific heats is assumed to be 5/3.

3.2. MHD Model Equations

In Appendix A.1, we applied a scale analysis of each term in the one-fluid MHD equations presented in the previous Section to determine which of these terms can be neglected without changing the important physical processes of the model. The resultant set of MHD equations are then given by

$$\partial_t \rho + \nabla \cdot (\rho \underline{v}) = (P - L) m_i \tag{3.14}$$

$$\rho \partial_t \underline{v} + \rho \underline{v} \cdot \nabla \underline{v} = -\nabla p + \underline{j} \times \underline{B} - \rho \tilde{\nu}_{\text{in}} \underline{v} - P m_i \underline{v} \tag{3.15}$$

$$\partial_t \underline{B} = \nabla \times (\underline{v} \times \underline{B}) - \frac{m_i}{e} \nabla \times \left[\left(\tilde{\nu}_{\text{in}} + \frac{P m_i}{\rho} \right) \underline{v} \right] \tag{3.16}$$

$$\partial_t \epsilon + \nabla \cdot (\epsilon \underline{v}) = -p \nabla \cdot \underline{v} + \frac{1}{2} \rho \underline{v}^2 \left(\frac{P}{n} + \tilde{\nu}_{in} \right) - \epsilon \left(\frac{L}{n} + \tilde{\nu}_{in} \right) . \tag{3.17}$$

In the momentum Equation (3.15), we consider the change of the plasma bulk velocity via collisional momentum exchange between the atmosphere and the magnetospheric plasma ($\rho \tilde{\nu}_{\text{in}} \underline{v}$) and ionization ($P m_i \underline{v}$). The last two terms on the right-hand side of Equation (3.17) represent the change of internal energy density due to elastic collisions, charge exchange, ionization, and recombination. The blue-colored term on the right-hand side of the induction Equation (3.16) represents the ionospheric Hall effect. The traditional form of the Hall term ($\nabla \times \left(-\frac{1}{ne} (\underline{j} \times \underline{B}) \right)$) introduces whistler waves to the system which would significantly extend the simulation time (Huba, 2003, Blöcker, 2013). Saur et al. (1999) showed that the ionospheric Hall effect has a strong influence on the fields inside Io's ionosphere and Alfvén wings (see Section 2.1.3.1). By considering the terms in Table A.3 for Io, it stands out that three terms are orders of magnitude more important than the other terms. Therefore, to account for the ionospheric Hall effect in Io's plasma interaction we apply the approximation which is valid in Io's ionosphere (see also, e.g., Chané et al., 2013, Blöcker, 2013):

$$\underline{j} \times \underline{B} \approx (\rho \tilde{\nu}_{\text{in}} + P m_i) \underline{v} \, . \tag{3.18}$$

This approximation reflects the force balance in the ionosphere: the ion-neutral collisions and mass loading are balanced by the Lorentz forces. The advantage of this approximation is that it introduces the ionospheric Hall effect into the system without developing whistler waves and strongly enhancing the simulation time step. The model without the ionospheric Hall effect calculates the plasma interaction with a linearized Pedersen conductivity which is only applicable for $\nu_{\text{in}} < 0.5 \; \omega_{ci}$ (see figure 5.1 in Blöcker, 2013). The ionospheric Hall effect approximation gives us a better description of the ionospheric currents without solving Hall MHD equations and was already applied in the model of

Chané et al. (2013) for modeling of Jupiter's magnetosphere.

At Europa, the contribution due to the ionospheric Hall effect is small and only slightly disturbs the symmetry of the plasma flow with respect to the y axis (Saur et al., 1998). Since we are interested in the main effects of the atmospheric inhomogeneities on Europa's plasma interaction, the ionospheric Hall effect will be neglected in the model of Europa's plasma interaction. However, we note that due to localized enhanced neutral density in Europa's atmosphere the influence of the ionospheric Hall effect could locally become important. This case will be discussed with the support of the analytic model which includes the ionospheric Hall effect in Chapter 6.

3.2.1. Plasma Sources and Sinks

3.2.1.1. Electron Impact Ionization

The main ionization process in Io's and Europa's atmosphere is electron impact ionization, which is more than one order of magnitude larger than photoionization at Europa (Saur et al., 1998). At Io, photoionization accounts for less than $\sim$15 % compared to electron impact ionization to the plasma mass balance (Saur et al., 2003). We only include electron impact ionization in our MHD model. The production rate for the electron impact ionization of the population j ($j =$$O_2$ at Europa and $j =$$SO_2$ at Io) is calculated by

$$P = f_j(T_e) n_{\mathsf{ms}} n_n \,, \tag{3.19}$$

where $f_j(T_e)$ is the electron impact ionization rate of the population j for a specific electron temperature T_e, and n_{ms} is the number density of the magnetospheric electrons. Electron impact ionization strongly depends on the temperature T_e of the electrons. Magnetospheric electrons which collide with the neutral particles in the atmosphere are locally cooled down. The electrons, which loose energy due to the electron impact process with the atmospheric neutrals, are reheated by the energy reservoir provided by the plasma torus. Energy is transported via heat conduction along the magnetic field lines from the plasma torus to the cooler regions of the flux tubes. Saur et al. (1998, 1999) show that heat conduction is very effective at Europa and Io which results in weak temperature gradients along the field lines. In our MHD model, T_e is not calculated self-consistently. To approximately account for the effect of heat conduction and to ensure conservation of energy, we apply the following description: First, we consider the electron energy flux F_{Torus} from the plasma torus, which is available for the reheating of the cooled magnetospheric electrons:

$$F_{\mathsf{Torus}} = \frac{3}{2} n_0 k_B T_e v_0 D_{\mathsf{tube}} L_{\mathsf{Torus}} \tag{3.20}$$

$$= \frac{3}{2} n_0 k_B T_e v_0 2 (R_{\mathsf{sat}} + H_0) \alpha_{\mathsf{Plasma}} L_{\mathsf{Torus}} \,. \tag{3.21}$$

This flux is based on the total flux tube energy, which is convected across the satellite with the radius R_{sat}. We additionally assume that electron heat conduction parallel to the magnetic field effectively transports electron energy within the flux tube above and below the satellite into the ionosphere. The electron temperature in our model is assumed to be constant along the magnetic field lines. The parameter $L_{\text{Torus}} = 1.7\ R_J$ for Europa and $L_{\text{Torus}} = 1.2\ R_J$ for Io is the vertical extent of the plasma torus with Jupiter's radius R_J (Bagenal and Delamere, 2011). The parameter D_{tube} is the width of the flux tubes approaching the interaction region. The upstream width of the flux tube $2(R_{\text{sat}} + H_0)$ changes when the flux tube is convected across the satellite depending on the strength of the plasma interaction. The width decreases by the factor α_{plasma}, which is given by

$$\alpha_{\text{plasma}} = v_{\text{wing}}/v_0\,. \tag{3.22}$$

The parameter α_{plasma} is the ratio between the x component of the perturbed plasma velocity v_{wing} inside the Alfvén wing and the unperturbed upstream plasma velocity v_0. This factor is a measure of the fraction of the upstream plasma flow that can enter the satelite's ionosphere and can also be expressed by conductances (e.g., Southwood and Dunlop, 1984):

$$\alpha_{\text{plasma}} = \frac{2\Sigma_A}{\Sigma_P + 2\Sigma_A}\,. \tag{3.23}$$

We determine the perturbed plasma velocity inside the Alfvén wing at a distance of three satellite radii following the northern or southern characteristic. The maximum energy flux which is lost due to electron impact ionization within the satelite's atmosphere is calculated by

$$F_{\text{lost}} = f_{\text{imp,max}} n_0 E_{\text{ion,eff}} \int_{R_{\text{sat}}}^{\infty} \int_0^{2\pi} \int_0^{\pi} n_n(r,\phi,\theta)\mathrm{d}V\,. \tag{3.24}$$

For the effective ionization energy of O_2 and SO_2, we use $E_{\text{ion,eff}} = 32$ eV (Banks and Kockarts, 1973) and $E_{\text{ion,eff}} = 13.1$ eV (Saur et al., 1999), respectively. The ionization rate by the background magnetospheric plasma $f_{\text{imp,0}}$ represents in our calculation an upper limit for the applicable ionization rate. $f_{\text{imp,0}}$ for a specific electron temperature is calculated by (Banks and Kockarts, 1973)

$$f_{\text{imp,0}}(T_e) = \int_{E_{\text{ion}}}^{\infty} \mathrm{d}E\, f_E(E)\sigma_{\text{imp}}(E)v_{\text{el}}(E) \tag{3.25}$$

with the normalized Maxwellian distribution function in energy space

$$f_E(E) = \frac{2\sqrt{E}}{\pi}(k_B T_e)^{-\frac{3}{2}} \exp\left(-\frac{E}{k_B T_e}\right)\,, \tag{3.26}$$

the kinetic electron velocity at a given energy

$$v_{\mathrm{el}}(E) = \sqrt{\frac{2E}{m_e}}\,, \tag{3.27}$$

and the ionization cross sections $\sigma_{\mathrm{imp}}(E)$ for O_2 adopted from Hwang et al. (1996) and for SO_2 adopted from Kim et al. (1997). E_{ion} is the threshold for ionization of the population j. In order to obey energy conservation, we take into account that the energy flux that is available from the plasma torus for the reheating of the cooled magnetospheric electrons needs to be larger than the energy flux which is used up by electron impact ionization ($F_{\mathrm{lost}} \leq F_{\mathrm{Torus}}$). To ensure that this condition is fulfilled at every time step in our MHD simulations, we compute the maximum possible ionization rate $f_{\mathrm{imp,max}}$. This is done by equating $F_{\mathrm{Torus}} = F_{\mathrm{lost}}$:

$$f_{\mathrm{imp,max}} = \frac{3k_B T_e v_0 (R_{\mathrm{sat}} + H_0)\alpha_{\mathrm{Plasma}} L_{\mathrm{Torus}}}{E_{\mathrm{ion,eff}} \int_V n_n \,\mathrm{d}V}\,. \tag{3.28}$$

The electron impact ionization rate in Equation (3.19) is then calculated by:

$$f_j = \begin{cases} f_{\mathrm{imp,max}} & \text{for } f_{\mathrm{imp,max}} \leq f_{\mathrm{imp,0}} \\ f_{\mathrm{imp,0}} & \text{for } f_{\mathrm{imp,max}} > f_{\mathrm{imp,0}}\,, \end{cases} \tag{3.29}$$

where f_j is controlled by the strength of the plasma interaction to avoid overestimation of the plasma production.

We discriminate between the hot magnetospheric and the newly created ionospheric electrons, which are produced by electron impact ionization. They generate two populations of electrons that are energetically different and hence their treatment in the model has to be different (Schilling et al., 2007). The separation of the magnetospheric and ionospheric electrons is implemented by the method presented in Schilling et al. (2007, 2008). The cooler ionospheric electrons with temperatures of about 0.5 eV at Europa and (Johnson et al., 2009) 0.2 eV (Saur et al., 1999) at Io do not contribute to the ionization process. The evolution of the number density of the ionospheric electrons is calculated by Equation (3.14). We solve a separate continuity equation for the number density of the magnetospheric electrons n_{ms}

$$\partial_t n_{\mathrm{ms}} + \nabla \cdot (n_{\mathrm{ms}} \underline{v}) = 0\,. \tag{3.30}$$

The number density of the magnetospheric electrons does, therefore, not increase due to electron impact ionization.

3.2.1.2. Dissociative Recombination

Dissociative recombination is the sink of plasma particles in our model. Molecular ions recombine with electrons. The loss process involving magnetospheric electrons is negligible because of their high temperatures. For the loss rate, we apply the expression adopted from Saur et al. (2003):

$$L_{rec} = \begin{cases} \alpha_{\text{rec}} n_e (n - n_0) & \text{for} \quad n > n_0 \\ 0 & \text{for} \quad n < n_0 \end{cases} \tag{3.31}$$

with a rate coefficient α_{rec} given in Equation (3.35) for Io and Equation (3.41) for Europa. When the plasma number density $n = \rho/m_i$ decreases below the background ion density $n_0 = \rho_0/\tilde{m}_i$ with the unperturbed plasma mass density ρ_0, then the dissociative recombination is set to zero. The reason for this definition is that the plasma outside of the satellite's ionosphere mostly consists of atomic ions with very small recombination rates which can be neglected on the scales of the satellite's interaction, while the plasma in the ionosphere consists of molecular ions with large dissociative recombination rates.

3.2.2. Specific Features of Io's Plasma Interaction Model

The average mass of the upstreaming magnetospheric plasma at Io is $\tilde{m}_i$=19 amu (Kivelson et al., 2004). Based on charge neutrality, the total magnetospheric electron number density n_e relates to the total ion number density n_i through an effective ion charge of z_c =1.25–1.55 (Delamere and Bagenal, 2003) and the upstream plasma density is calculated by $\rho_0 = \tilde{m}_i n_i = \tilde{m}_i n_e / z_c$. In our model singly charged ions are produced in the ionosphere with m_i=$m_{SO_2^+}$=64 amu. We neglect the contribution of a subsurface magma ocean (Khurana et al., 2011) since we are interested in the influence of different asymmetries in the atmosphere on Io's plasma interaction.

3.2.2.1. Elastic Collisions and Charge Exchange

The plasma exchanges momentum with Io's atmosphere through elastic collisions, charge exchange, and mass loading. Elastic collisions and charge exchange are both included in the ion-neutral collision frequency $\tilde{\nu}_{in}$. We calculate the ion-neutral collision frequency with equation (34) from Saur et al. (1999) (in esu-cgs-units):

$$\tilde{\nu}_{in} = \frac{m_n}{m_i + m_n} \sigma_{in}(v_{\text{rel}}) v_{\text{rel}} n_n \,. \tag{3.32}$$

The effective cross section is given by

$$\sigma_{in} = 2.21\pi \sqrt{\frac{\alpha e^2}{32 m_p v_{\text{rel}}^2}} + 2 \left(7.0 \times 10^{-8} - 0.65 \times 10^{-8} \log \left(\frac{32 m_p v_{\text{rel}}^2}{1.6 \times 10^{-12}} \right) \right)^2 \tag{3.33}$$

with the polarizability $\alpha = 4,28 \times 10^{-24}$ cm^3 (McDaniel, 1989) and the electron charge $e = 4,8 \times 10^{-10}$ esu. The cross section σ_{in} accounts for both effects, induced dipole polarization and charge exchange. While induced dipole polarization is important for low relative velocities between neutrals and ions, charge exchange dominates for higher relative velocities. The effective relative velocity between neutrals and ions is given by

$$v_{\mathrm{rel}} = \sqrt{\frac{8k_B T_i}{\pi m_i} + \underline{v}^2} \quad . \tag{3.34}$$

3.2.2.2. Dissociative Recombination

The plasma loss rate L is determined by dissociative recombination with the recombination rate coefficient α_{rec} for SO_2^+ given by

$$\alpha_{\mathsf{rec}}(T_e) = 3 \times 10^{-13} \left(\frac{300}{T_e}\right)^{0.5} \quad \mathsf{m^3 s^{-1}} \tag{3.35}$$

according to Torr (1985). For this process, we use an ionospheric electron temperature T_e of 0.2 eV.

3.2.3. Specific Features of Europa's Plasma Interaction Model

The magnetospheric electrons at Europa's location mainly consist of two populations, the thermal and the suprathermal populations with temperatures of $k_B T_{\mathsf{th}} = 20$ eV and $k_B T_{\mathsf{sth}} = 250$ eV (Sittler and Strobel, 1987, Johnson et al., 2009), respectively. The temperature of the magnetospheric electrons T_e is not calculated self-consistently. However, to avoid overestimation of the plasma production the ionization process in our model is restricted by the amount of electron energy which possibly can enter Europa's atmosphere. The total electron energy flux transferred into the atmosphere is controlled by the strength of the plasma interaction (see Equation (3.22)). We assume an electron fluid with an averaged temperature from the thermal and suprathermal populations given by

$$T_e = \frac{n_{\mathsf{th}} T_{\mathsf{th}} + n_{\mathsf{sth}} T_{\mathsf{sth}}}{n_{\mathsf{th}} + n_{\mathsf{sth}}} \, . \tag{3.36}$$

The number density of the thermal electrons n_{th} varies with Europa's position in the plasma sheet. For the number density of the suprathermal electrons n_{sth}, we use the ratio $n_{sth}/n_{th} \approx 5\%$ (Bagenal et al., 2015). Based on charge neutrality, the total magnetospheric electron number density relates to the total ion number density through an effective ion charge of $z_c = 1.5$ (Kivelson et al., 2004). The upstream plasma mass density thus can be written as

$$\rho_0 = \tilde{m}_i n_i = \frac{\tilde{m}_i (n_{\mathsf{th}} + n_{\mathsf{sth}})}{z_c} \, . \tag{3.37}$$

The average mass of the upstreaming magnetospheric plasma is $\tilde{m}_i$=18.5 amu (Kivelson et al., 2004). In our model singly charged ions are produced in the ionosphere with m_i=$m_{O_2^+}$=32 amu. For the modeling of Europa's plasma interaction, we consider the ideal MHD form of the induction Equation:

$$\partial_t \underline{B} = \nabla \times (\underline{v} \times \underline{B}) \ . \tag{3.38}$$

3.2.3.1. Elastic Collisions and Charge Exchange

We implement the elastic collisions between ions and neutrals by introducing the average ion-neutral collision frequency

$$\nu_{\text{in}} = 2.6 \times 10^{-15} n_n \sqrt{\frac{\alpha_0}{\mu_a}} \quad \text{s}^{-1} \tag{3.39}$$

from Banks and Kockarts (1973). α_0 is the polarizability of the neutral gas in units of 10^{-24} cm^{-3} and $\mu_a = m_{O_2^+} m_{O_2}/(m_{O_2^+} + m_{O_2}) = \frac{1}{2} m_{O_2^+}$ is the reduced mass in amu. The polarizability of O_2 is given by $\alpha_0 = 1.59$ (Banks and Kockarts, 1973).

Charge exchange plays an important role in the calculation of the energy balance and the momentum, but it does not affect the plasma density. In our model, we use the ion-neutral charge exchange collision frequency

$$\nu_{\text{ex}} = 1.7 \times 10^{-19} n_n \sqrt{T_i + T_n} \ (10.6 - 0.76 \ \log_{10}(T_i + T_n))^2 \quad s^{-1} \,, \tag{3.40}$$

for the reaction $O_2^+ + O_2 \rightarrow O_2 + O_2^+$ derived by Banks (1966). Charge exchange reactions between O_2^+ ions and their parent O_2 molecules depend explicitly on the energy of the impacting ion. The ion temperature in Equation (3.40) is calculated through the internal energy density via the relation $\epsilon = \frac{3}{2} n k_B (T_i + T_e)$.

3.2.3.2. Dissociative Recombination

We use the dissociative recombination rate coefficient for O_2^+ given in Schunk and Nagy (2009):

$$\alpha_{\text{rec}}(T_e) = 2 \times 10^{-13} \left(\frac{300}{T_e} \right)^{0.7} \quad \text{m}^3\text{s}^{-1} \,. \tag{3.41}$$

For the dissociative recombination, the temperature T_e of the ionospheric electrons of 0.2 eV was used.

3.2.3.3. Induction in a Subsurface Water Ocean

Due to the tilt of Jupiter's magnetic moment with respect to its spin axis of $\sim 10^\circ$, the x and y components of the Jovian background magnetic field periodically vary at Europa's location. This results in an inducing field with Jupiter's synodic period of $\sim$11.1 h. The

variability of the Jovian background magnetic field including the effects of the magnetospheric current sheet is expressed in our model by

$$B_{x,0}(\lambda_{\text{III}}) = -84\text{nT}\sin(\lambda_{III} - 200^\circ)\,, \tag{3.42}$$

$$B_{y,0}(\lambda_{\text{III}}) = -210\text{nT}\cos(\lambda_{III} - 200^\circ) \tag{3.43}$$

with system-III-longitude λ_{III} (Schilling et al., 2007). The time-varying inducing field drives currents in Europa's subsurface ocean and, thus, generates a time-varying induced magnetic dipole field. Assuming a radially symmetric ocean and a spatially homogeneous induced field, the resultant induced field is dependent on the ocean's conductivity, the ocean's thickness, and the thickness of the crust between Europa's surface and the ocean. The effect of induction in the subsurface conducting water layer on the magnetic field is included in the inner boundary conditions at the surface of Europa (see Section 3.4.1). The derivation of the induced dipole field is described in the work of, e.g., Zimmer et al. (2000) and Saur et al. (2010). We assume an ocean that is 100 km thick and lies 25 km beneath the surface with a conductivity of 0.5 S/m according to the findings of Schilling et al. (2007).

3.3. Atmosphere Model

3.3.1. Neutral Atmosphere and Local Atmospheric Inhomogeneities at Io

As already mentioned in Chapter 2.1.2, Io possesses a very complex atmosphere with a partly unknown density distribution. Compared to Europa's atmosphere, Io's atmosphere is denser and drives, therefore, a stronger plasma interaction. The dominant molecular species in Io's atmosphere is SO_2. We construct a simplified analytic expression of Io's atmosphere and assume that it solely consists of SO_2. We investigate longitudinal and latitudinal asymmetries of the global atmosphere based on several observations and theoretical predictions as we explain in the following. The number density of the atmosphere is given by

$$n_A(r,\theta,\phi) = (n_{\text{pol}} + n_s(\theta,\phi))\,\exp\left[-\left(\frac{h}{H_0}\right)\right] \tag{3.44}$$

with the low surface number density at the poles $n_{\text{pol}} = 0.02\,n_0$, the constant scale height H_0, and altitude $h = r - R_{Io}$ above the surface. The surface number density is described as

$$n_s = (n_0 - n_{\text{pol}})\beta_1(\theta)\beta_2(\phi)\beta_3(\phi)\beta_4(\theta,\phi) \tag{3.45}$$

with the surface number density at equatorial latitude n_0 and a latitudinal and longitudinal dependence considered in the functions β_1, β_2, β_3, and β_4. For the description of the latitudinal variation of the SO_2 surface number density, we adopt the column density profile derived by Strobel and Wolven (2001) from Lyman-α observations (their equation

9):

$$\beta_1(\theta) = \exp\left(-\left(\frac{\theta}{0.625\text{rad}}\right)^2\right). \tag{3.46}$$

We applied a less steep decrease of the surface number density poleward of 35° compared to Strobel and Wolven (2001) due to numerical reasons. Besides the latitudinal asymmetry, there exist also several observations of global longitudinal asymmetries in Io's atmosphere: The average dayside atmosphere is reported to be densest on the anti-Jovian hemisphere in the equatorial region probably due to the correlation with volcanic hot spots (Spencer et al., 2005, Feaga et al., 2009, Moullet et al., 2010). Saur et al. (2002) inferred that Io's downstream atmosphere is denser and stretched compared to the upstream atmosphere which is compressed because of the drag force on the neutral atmosphere produced by the impinging torus plasma. Tsang et al. (2016) concluded from the data which was taken by the Gemini North telescope during Io's eclipse ingress, that the atmospheric column number density collapses by a factor of 5±2 on the nightside. Following the conclusions of the mentioned authors, we include these geometrical effects in a very simplified way in our atmosphere model by modifying the β_2, β_3, and β_4 functions in the surface density as follows:

$$\beta_2(\phi) = \left(1 + \frac{1}{3}\sin(\phi - \pi)\right) \tag{3.47}$$

$$\beta_3(\phi) = \left(1 + \frac{3}{5}\sin\left(\phi - \frac{1}{2}\pi\right)\right) \tag{3.48}$$

$$\beta_4(\theta, \phi) = \left(1 + \frac{2}{3}\cos(\psi(\theta, \phi))\right), \tag{3.49}$$

where ψ is the solar zenith angle. The described neutral number density possesses an upstream-downstream asymmetry with a decrease from the downstream to the upstream hemisphere by a factor of two according to Saur et al. (2002) described in the β_2 function. Additionally, the atmosphere features an anti-/sub-Jovian asymmetry with a decrease from the anti- to the sub-Jovian hemisphere by a factor of four which is described by the β_3 function, and a day/night asymmetry with a decrease from the day to the night side hemisphere by a factor of five described in the β_4 function. The density peak lags the subsolar point by about 30° behind the local noon due to high thermal inertia of the frost (Moore et al., 2009, Walker et al., 2010).

For our study of the influence of volcanic plumes on the plasma interaction, we chose the Pele and Tvashtar volcanoes because of their different planetographic locations on Io and their large eruption plumes. In our model, we treat the Tvashtar and Pele volcanoes as localized enhancements of the atmospheric neutral number density. We superimpose the plume onto the global atmosphere by adding the volcanic plume number density to the global atmosphere number density. The neutral density distribution within the Pele-type plume is assumed to be a function of the altitude h and the angular

distance from its center $\tilde{\theta}(\theta, \phi)$ of the form:

$$n_V(h, \tilde{\theta}) = n_{V,0} \left(\exp\left[-\left(\frac{h}{H_s}\right)^2 - \left(\frac{\tilde{\theta}}{H_a}\right)^2 \right]^3 + 30 \exp\left[-\left(\frac{h}{0.1H_s}\right)^2 - \left(\frac{\tilde{\theta}}{0.05H_a}\right)^2 \right]^3 \right) . \tag{3.50}$$

The factor $n_{V,0}$ is the surface number density of the neutral gas in the center of the plume, H_s is the scale height, and H_a is the angular scale of the latitudinal extent. The angular distance from the plume center $\tilde{\theta}(\theta, \phi)$ is given by

$$\tilde{\theta}(\theta, \phi) = \arccos\left(\sin(\theta)\sin(\theta_{\mathsf{ap}})\cos(\phi - \phi_{\mathsf{ap}}) + \cos(\theta)\cos(\theta_{\mathsf{ap}})\right) \tag{3.51}$$

with the spherical coordinates of the plume center θ_{ap} and ϕ_{ap}. The description of the plume density is based on the models of Zhang et al. (2003) and Roth et al. (2011). The plume possesses a high density region near the surface in the center considered by the second term in Equation (3.50). We do not account for the low density region within the plume and the formation of a canopy shock as shown by (Zhang et al., 2003). The scale height H_s and width of the latitudinal extent H_a for both plumes are chosen to be 360 km and 17.3° (∼550 km), respectively, based on the plume observations in sunlight according to Roth et al. (2011). For the surface density $n_{V,0}$, we apply $n_{V,0} = 0.4 \times 10^{15}$ m^{-3} and $n_{V,0} = 0.3 \times 10^{15}$ m^{-3} (Jessup and Spencer, 2011) for the Tvashtar plume located at $\theta_{\mathsf{ap}} = 28°$ and $\phi_{\mathsf{ap}} = 238°$ and the Pele plume located at $\theta_{\mathsf{ap}} = 108°$ and $\phi_{\mathsf{ap}} = 104°$, respectively.

To get an idea how the plumes in the atmosphere effect Io's plasma environment, we consider two scenarios for Io's global atmosphere: First, we choose a latitudinally asymmetric atmosphere with the dayside hemisphere on the upstream side, so that Tvashtar is located on the nightside and Pele on the dayside. The surface neutral number density of the global atmosphere is then characterized by

$$n_s = (n_0 - n_{\mathsf{pol}})\beta_1(\theta)\beta_4(\theta, \phi) \tag{3.52}$$

with the subsolar point on the upstream side (ϕ=90°, θ=90°). Second, we choose the subsolar point on the downstream side (ϕ=270°, θ=90°), so that Tvashtar is located on the dayside and Pele on the nightside. In Figures 3.1a and 3.1b, we present the neutral number density distribution of the downstream-dayside atmosphere with the Tvashtar plume on the dayside and the Pele plume on the nightside, respectively. The results of the plasma interaction with these atmospheric scenarios are presented in Section 5.1.

Khurana et al. (2002) suggested that some magnetic field perturbations observed in the Alfvén wing during I31 are influenced by volcanic signals. We include a plume at two different planetographic locations inside Io's global atmosphere and compare our model results with the measured MAG data along the I31 trajectory. We use a latitudi-

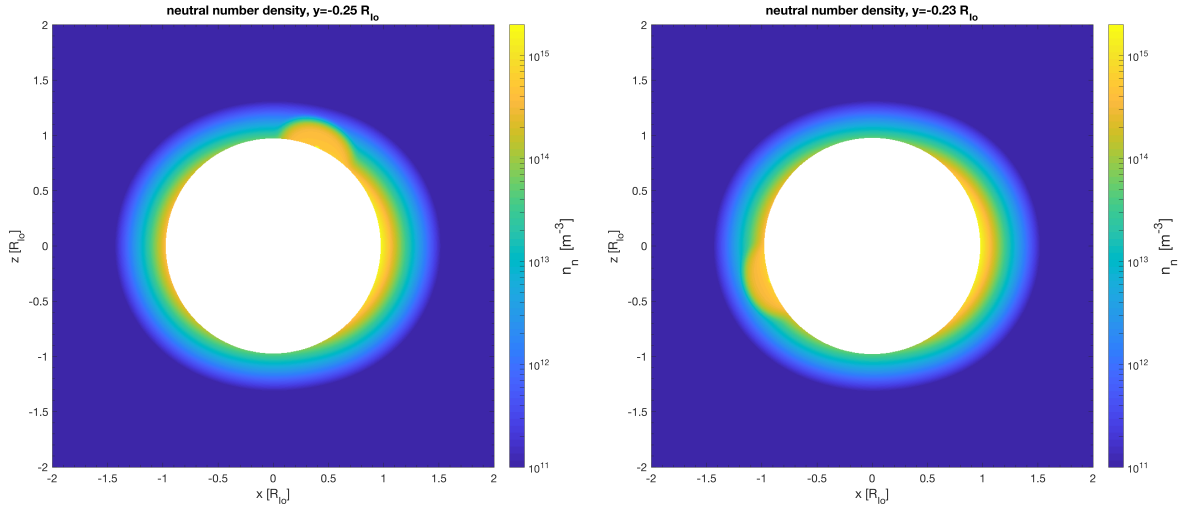

(a) day-downstream atmosphere + Tvashtar **(b)** day-downstream atmosphere + Pele

Figure 3.1. – Neutral number density of an atmosphere which is concentrated on the downstream side at the equatorial latitudes and includes (a) the Tvashtar plume and (b) the Pele plume. The plots are displayed in a vertical plane through the center (y=−0.25 R_{Io} for Tvashtar and y=−0.23 R_{Io} for Pele).

nally asymmetric atmosphere with the atmosphere concentrated at the subsolar point at ϕ=290°, θ=90° and a plume located at the location of the Thor volcano (see Table 3.1, "I31 atm.+Thor") and a plume located near the Tvashtar volcano, i.e., near the northern pole (see Table 3.1, "I31 atm.+plume"). We investigate the effect of these plumes on the magnetic field along the I31 trajectory. The results of the plasma interaction during the flyby I31 are presented in Section 5.1.6.

To study the influence of global asymmetries on Io's plasma environment during the I24 and I27 flybys presented in Section 5.2 we apply three different atmospheric scenarios: A latitudinally asymmetric atmosphere where the surface number density is described by $n_s = (n_0 - n_{\text{pol}})\beta_1(\theta)$, a latitudinally and longitudinally asymmetric atmosphere where the surface number density is described by $n_s = (n_0 - n_{\text{pol}})\beta_1(\theta)\beta_2(\phi)\beta_3(\phi)\beta_4(\theta,\phi)$ and in the third atmospheric scenario we include a thin corona in addition to the latitudinally and longitudinally asymmetric atmosphere ($n_A(r,\theta,\phi) + n_{\text{cor}}(r)$). The corona is calculated by the power law fall off

$$n_{\text{cor}} = n_{\text{cor,0}} \left(\frac{R_{Io}}{r} \right)^{3.5} \tag{3.53}$$

according, e.g, to Schneider et al. (1991), Combi et al. (1998) and Khurana et al. (2011). The parameter $n_{\text{cor,0}} = 0.8 \times 10^{13}$ m^{-3} represents the surface number density of the thin corona. These three model scenarios are referred to as *atm. model 1*, *atm. model 2*, and *atm. model 3*. In the model scenario *atm. model 4* the same case as in atm. model 2 is considered for Io's atmosphere but the surface number densities n_0 and the scale heights H_0 are different (see Table 3.1). We made different tests in order to constrain the plasma density and scale height to fit the data during the Galileo I24 and I27 flyby. The

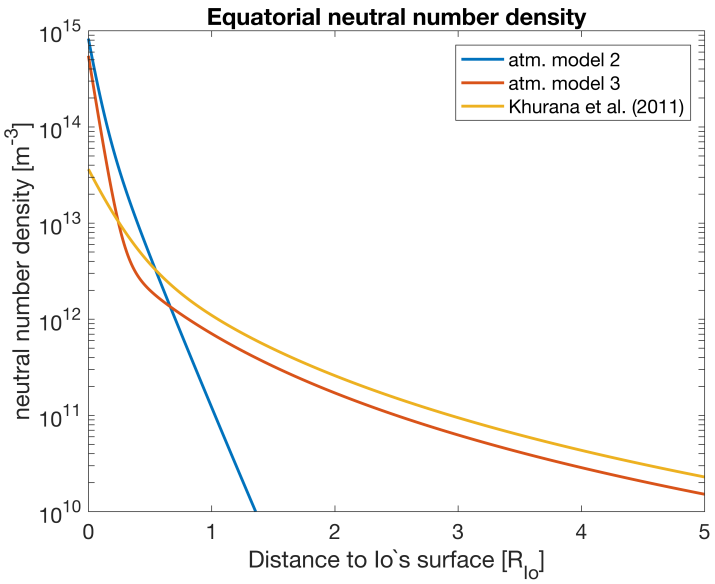

Figure 3.2. – Radial profile of the equatorial number density on the anti-Jovian side for the atmospheric scenarios atm. model 2, atm. model 3, and the neutral number density used in Khurana et al. (2011).

values used for the atmospheric parameters are summarized in Table 3.1. The subsolar point used for modeling of the flybys I24 and I27 is ϕ=230°, θ=90°. In Figure 3.2 we show a comparison between the radial profiles of the different atmospheric configurations and the atmosphere applied by Khurana et al. (2011). The different configurations of the atmosphere affect the plasma interaction during the flybys I24 and I27 as it will be shown in Section 5.2. We aim to compare our results with the results from the work of Khurana et al. (2011) where an atmospheric configuration with a small surface number density and a wide extent was used as shown in the yellow line in Figure 3.2.

3.3.2. Neutral Atmosphere and Local Atmospheric Inhomogeneities at Europa

We prescribe Europa's molecular oxygen atmosphere with an analytic expression. We apply a radially symmetric description of Europa's global atmosphere. The global distribution of the neutral atmosphere is observationally not very well constrained, but there are several predictions about global asymmetries in the sputtering atmosphere. Atmospheric modeling suggests that sputtering decreases from the trailing to the leading hemisphere and depends both on solar illumination and plasma impact direction (e.g., Pospieszalska and Johnson, 1989, Plainaki et al., 2013). We do not consider in our model a global asymmetry of the atmosphere compared to, e.g., Schilling et al. (2007) or Rubin et al. (2015), since our focus is on the influence of local atmospheric inhomogeneities. Therefore, we keep the global atmosphere as simple as possible to better demonstrate the effects of the localized inhomogeneity. The number density of the radially symmetric sputtering

Table 3.1. – Atmospheric Properties of Io's Simulation Runs

Model Scenario/ Flyby	n_0 (m^{-3})	$n_{V,0}$ (m^{-3})	H_0 (km)	H_s (km)	H_a (deg)	θ_{ap} (deg)	ϕ_{ap} (deg)	Asym.[a]
Day/night atm.[b]	2×10^{15}	–	100	–	–	–	–	$\beta_1\beta_4$
Atm.[b]+Pele	2×10^{15}	0.3×10^{15}	100	360	17.3	108	104	$\beta_1\beta_4$
Atm.[b]+Tvashtar	2×10^{15}	0.4×10^{15}	100	360	17.3	28	238	$\beta_1\beta_4$
I31 atm.	2×10^{15}	–	100	–	–	–	–	$\beta_1\beta_4$
I31 atm.+Thor	2×10^{15}	0.4×10^{15}	100	500	17.3	49.3	226	$\beta_1\beta_4$
I31 atm.+plume	2×10^{15}	0.4×10^{15}	100	500	17.3	25.3	226	$\beta_1\beta_4$
atm. model 1	2.5×10^{14}	–	100	–	–	–	–	β_1
atm. model 2	2.4×10^{14}	–	100	–	–	–	–	$\beta_1\beta_2\beta_3\beta_4$
atm. model 3	2.1×10^{14}	–	100	–	–	–	–	$\beta_1\beta_2\beta_3\beta_4$
atm. model 4	9.3×10^{14}	–	140	–	–	–	–	$\beta_1\beta_2\beta_3\beta_4$

[a]Applied asymmetry in the atmospheric configuration (see Equations (3.46)–(3.49)).

[b]The atmospheric configurations include two cases of a day/night asymmetry: upstream-dayside and downstream-dayside atmoshere.

atmosphere is given by

$$n_A(r) = n_{A,0} \exp\left[-\left(\frac{h}{H_0}\right)\right] \tag{3.54}$$

with the surface density $n_{A,0}$, atmospheric scale height H_0, and altitude $h = r - R_E$ above the surface.

Following Roth et al. (2014b), the density profile of the atmospheric inhomogeneity is assumed to be a function of the altitude h and the angular distance from its center, $\tilde{\theta}(\theta, \phi)$, of the form

$$n_{ap}(h, \tilde{\theta}) = n_{ap,0} \exp\left[-\left(\frac{h}{H_h}\right)^{\alpha} - \left(\frac{\tilde{\theta}}{H_\theta}\right)^{2}\right] . \tag{3.55}$$

$n_{ap,0}$ is the surface number density of the neutral gas in the center of the inhomogeneity, H_h is the scale height, and H_θ is the angular scale of the latitudinal extent of the inhomogeneity. The angular distance from the plume center is given by Equation (3.51). The factor α varies in our model from one to two, with $\alpha = 1$ representing the hydrostatic case with a constant scale and $\alpha = 2$ representing a Gaussian structure varying with altitude. The parameters $n_{A,0}$, $n_{ap,0}$, H_h and H_Θ are treated as free parameters and are varied among different simulation runs. The neutral number density is given by $n_n(r, \theta, \phi) = n_A(r) + n_{ap}(r, \theta, \phi)$. The scale height of the atmosphere H_0 is assumed to be 100 km for all simulations. The surface number density $n_{A,0}$ varies between 2×10^{13} m^{-3} and 14×10^{13} m^{-3} resulting in an O_2 column density of (2–14) $\times 10^{18}$ m^{-2}.

For our studies, we will consider an atmosphere model with one plume with similar parameters as derived by Roth et al. (2014b) (see their supplementary material). In

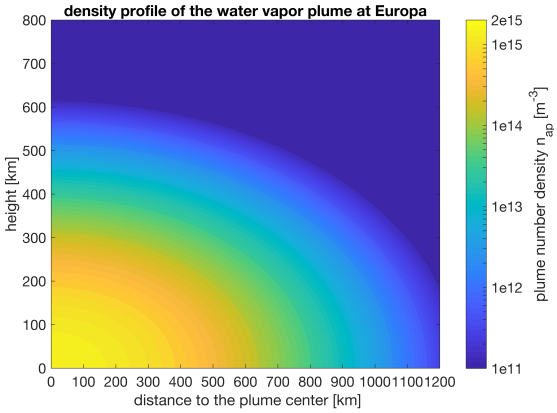

Figure 3.3. – The density distribution model for the water vapor plume at Europa displayed in a vertical plane through the center for $n_{\mathrm{ap},0}$=1.64 $\times$ 10^{15} m^{-3}, H_h=200 km, H_Θ=15°.

Table 3.2. – Atmospheric Properties of Europa's Simulation Runs[a]

Model Scenario/ Flyby	$n_{A,0}$ (m^{-3})	$n_{\mathrm{ap},0}$ (m^{-3})	H_0 (km)	H_h (km)	H_Θ (deg)	α	θ_{ap} (deg)	ϕ_{ap} (deg)	γ^{b} (%)
General model I	5×10^{13}	1.9×10^{14}	100	200	15	2	180	180	10
General model I	5×10^{13}	1.64×10^{15}	100	200	15	2	180	180	50
General model I	5×10^{13}	4.92×10^{15}	100	200	15	2	180	180	75
General model II	5×10^{13}	1.64×10^{15}	100	200	15	2	180	180	50
E17	2.0×10^{13}	5.3×10^{14}	100	200	15	2	140	290	50
E25A	1.0×10^{13}	2.6×10^{14}	100	200	15	2	0	0	50
E26	5.0×10^{13}	1.3×10^{15}	100	200	15	1	135	55	50
E26	5.0×10^{13}	1.3×10^{15}	100	200	15	1	125	35	50

[a] Additionally, simulation runs with a radially symmetric atmosphere but without the atmospheric inhomogeneity ($\gamma = 0\%$) were made with the surface number density $n_{A,0}$ presented in this table.
[b] The ratio between the gas content of the atmospheric inhomogeneity and the gas content of the total atmosphere.

Figure 3.3, we show the vertical and horizontal extension of the plume density distribution according to Equation (3.55) for one set of parameters which was used for the plume study presented in Chapter 6 (see also Table 3.2).

3.4. Numerics, Boundary Conditions and Initial Conditions

To solve the set of the differential Equations (3.14)-(3.17), we apply a modified version of the publicly available ZEUS-MP MHD code. ZEUS-MP is a multiphysics, massively parallel, message-passing code for astrophysical fluid dynamics (Norman, 2000), which solves the one-fluid, ideal MHD equations in three dimensions. The code utilizes a staggered-grid finite-difference scheme and the second-order accurate, monotonic advection scheme. In addition, the code applies a combination of the Constraint Transport algorithm and the Method of Characteristics treatment for Alfvén waves. The solution of the differential equations is computed time forward. The time step of the physical

Table 3.3. – Initial and Boundary Condition Values and Calculated Parameters in the IPhiO System for Io's Simulations

Model Scenario/ Flyby	$\underline{B}_0$ (nT)	$\underline{v}_0$ (km/s)	ρ_0[a] (amu/m^{-3})	ϵ_0[b] (nPa)	M_A	Σ_A (S)
Day/night atm.+pl.[c]	(0, 0, −1960)	(57, 0, 0)	2.95×10^{10}	19.9	0.23	3.10
I31	(250, −675, −1930)	(57, 0, 0)	2.95×10^{10}	19.9	0.22	2.96
I24	(307, 517, −1908)	(57, 0, 0)	3.06×10^{10}	14.2	0.23	3.10
I27	(300, 510, −1890)	(57, 0, 0)	2.05×10^{10}	16.4	0.19	2.58

[a]The used charge state z_c for the incident plasma is 1.55 for I24, and 1.3 otherwise.

[b]$\epsilon_0 = 3/2 n_0 k_B (T_e + T_{i,0})$ with $k_B T_{i,0} = 50$ eV for I24, $k_B T_{i,0} = 90$ eV for I27, and $k_B T_{i,0} = 75$ eV otherwise.

[c]Concerning the models "Day/night atm.", " Atm.+Pele", and "Atm.+Tvashtar" in Table 3.1.

processes is controlled by the Courant-Friedrichs-Lewy criterion. A detailed description of the algorithms used in ZEUS-MP can be found in Stone et al. (1992), Hayes et al. (2006).

For our numerical simulations, we use a spherical grid in order to facilitate the use of the inner boundary condition explained below. The model domain extends to 20 R_E in the case of Europa and 25 R_{Io} in the case of Io from the satellite's center in radial direction. The spherical grid consists of 160 × 120 × 120 (r, θ, ϕ) cells in the case of Europa and 240 × 120 × 120 cells in the case of Io. The angular resolution of the grid in θ and ϕ is equidistant with $\triangle\theta = 1.5°$ and $\triangle\phi = 3°$. The radial resolution is not equidistant and increases by a factor of 1.022 in the case of Europa and 1.016 in the case of Io from cell to cell from the inner boundary, i.e., r=1 R_{sat} to the outer boundary, i.e., r=20 R_E for Europa and r=25 R_{Io} for Io. The resolution at the surface is chosen to be 21 km at Europa and 16 km at Io. The simulation is performed until the Alfvén wings reach the outer boundary and approximately steady state solution in the vicinity of Europa is reached. In this way, reflections of the Alfvén waves from the outer boundary are avoided. The typical time required for the corotation flow at 104 km/s to cross Europa's diameter is 30 s and for the corotation flow at 57 km/s to cross Io's diameter is 64 s. With an Alfvén velocity of 350 km/s, the Alfvén wave needs about 90 s to reach the outer boundary in the case of Europa and with an Alfvén velocity of 250 km/s the Alfvén wave needs about 175 s in the case of Io. Flow and magnetic perturbations do not evolve noticeably after 90 s or 175 s in our simulation runs. Europa's and Io's ionospheres are not in chemical equilibrium but in a strongly advection-dominated equilibrium. From Equation (3.14), we can estimate (with Table A.1) an ionization time scale in the model by $\sim \frac{1}{f_{imp,0} n_A(h=100 \text{ km})} \approx 0.7$ s for Europa and ≈ 1.5 s for Io. Therefore, the equilibrium of the neutral atmosphere is assured in our model.

3.4.1. Inner and Outer Boundary Values

Our simulation domain has two boundary areas, namely the outer sphere at r=20 R_E in the case of Europa and r=25 R_{Io} in the case of Io, and the inner sphere at r=1 R_{sat}. In

Table 3.4. – Initial and Boundary Condition Values and Calculated Parameters in the EPhiO System for Europa's Simulations

Model Scenario/ Flyby	$\underline{B}_0$ (nT)	$\underline{v}_0$ (km/s)	ρ_0 (amu/m^{-3})	ϵ_0[a] (nPa)	M_A	Σ_A (S)
General model I	(0, 0, −450)	(104, 0, 0)	4.93×10^8	0.56	0.24	1.75
General model II	(0, −210, −450)	(104, 0, 0)	4.93×10^8	0.56	0.21	1.60
E17	(73, −100, −425)	(104, 0, 0)	1.73×10^9	1.97	0.45	3.11
E25A	(−7, −209, −382)	(104, 0, 0)	8.60×10^8	1.47	0.32	2.33
E26	(−22, 203, −380)	(104, 0, 0)	4.93×10^8	0.56	0.25	1.82

[a] $\epsilon_0 = 3/2 n_0 k_B (T_e + T_{i,0})$ with $k_B T_{i,0} = 100$ eV (Kivelson et al., 2004)

our numerical simulations, the outer boundary is not a real boundary in the sense that physical properties abruptly change or jump. We apply open boundary conditions for the four MHD variables ρ, e, $\underline{v}$, and $\underline{B}$ at the outer boundary. At the downstream region of the outer boundary ($\phi > 180°$), the outflow method is used; i.e., the plasma quantities are extrapolated from the grid cells near the boundary to the boundary cells. At the upstream region ($\phi \leq 180°$), the inflow method is applied, i.e., all plasma quantities are held constant. At the inner boundary, i.e., the surface of the satelite, plasma is assumed to be absorbed, which we implement by open boundary conditions for ρ, e, and $\underline{v}$ by an outflow method. The radial component of the plasma bulk velocity v_r is constrained in the way that $v_r \leq 0$ so that plasma does not flow out of the surface (see also discussion in Duling et al., 2014). The satellite's surface is not only absorbing but also possesses a negligible electrical conductivity. The insulating nature of the surface does not allow electric currents to penetrate the surface. Although hot spot regions near the volcanic vents could be sufficiently conductive, Io's surface consisting of silicates, frozen sulfur dioxide, and elementary sulfur can be regarded as highly resistive at surface temperatures of $\leq$130 K (Neubauer, 1998). Boundary conditions for the magnetic field have been derived by Duling et al. (2014) ensuring that there is no radial electric current. The boundary condition is constructed in a way that it also can consistently include any time-dependent internal potential fields from below the surface, e.g., caused by induction in an ocean below the nonconducting ice crust. The inner and outer boundary values for our simulations at Io and Europa are presented in Tables 3.3 and 3.4, respectively.

4. Analytic Model

In Section 2.1.3.1 we gave an overview of the models of Saur et al. (1999, 2007). Both models are the basis of our analytic approach to study the influence of plumes on Europa's plasma interaction. For the derivation of our analytic model, we use a coordinate system with the x axis pointing along the unperturbed plasma flow, the z axis is antiparallel to the background magnetic field, and the y axis completes the right handed coordinate system and is pointing toward Jupiter. We call it the EPhiB coordinate system. The model of Saur et al. (2007) developed for Enceladus but here used for Europa needs to be extended to take a global atmosphere into account. With our modifications of the model we are able to study the Alfvén winglets inside of the Alfvén wings.

4.1. Analytic Model for Europa's Electrodynamic Interaction

Europa's conductive ionosphere acts as an obstacle to the unperturbed plasma flow. The electrodynamic interaction creates a current system composed of ionospheric currents, Alfvén wing currents, and additional hemisphere coupling currents when an asymmetric atmosphere is present. In this Section we present an analytic solution of the electric potential for asymmetric ionospheric quantities and for a constant magnetic field. Note, that this solution is only applicable for the Alfvénic far field. Sketches of the constant ionospheric conductances and the geometry of the electric current system are displayed in Figures 4.1 and 4.2. We aim to elucidate with this solution the implications of an atmospheric inhomogeneity in a global atmosphere on Europa's plasma interaction in the Alfvénic far field. Although the electric potential is reduced to two dimensions, the ionospheric conductivities and the ionospheric current system are three dimensional.

We aim to derive a solution of the electric potential for Europa's electrodynamic interaction. The electric potential depends on the ionospheric conductances. Therefore, we develop a model of the conductance profile of the moon's ionosphere. $\Sigma_{P,H}$ are the ionospheric Pedersen and Hall conductances, which are obtained by the integration of the Pedersen and Hall conductivities $\sigma_{P,H}$ (see Equations (2.2) and (2.3)) along the direction of the background magnetic field, i.e.,

$$\Sigma_{P,H}(x,y) = \int_{z_0}^{z_i} \sigma_{P,H}(x,y,z)\mathrm{d}z\,. \tag{4.1}$$

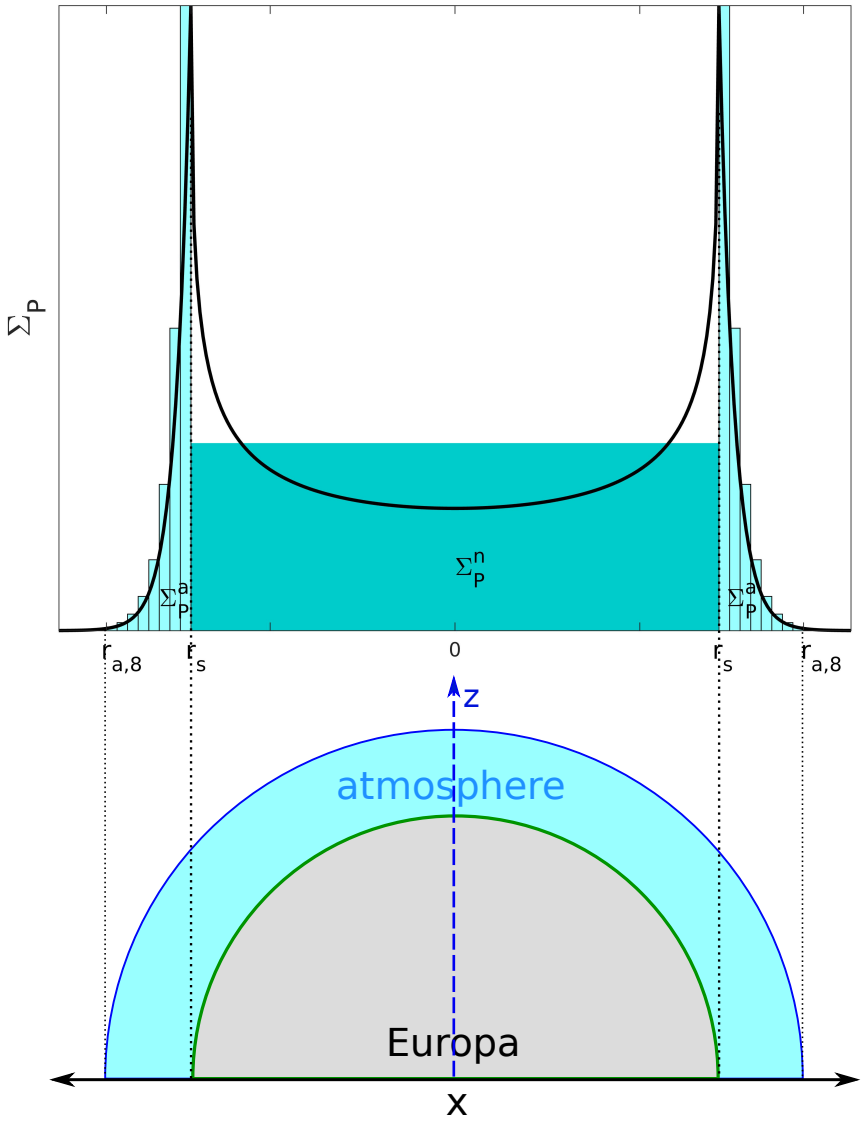

Figure 4.1. – Top sketch: Pedersen conductance profile $\Sigma_P(x) = \int_{z_0}^{z_i} \sigma_{P,H}(x,z)\mathrm{d}z$ (black line), see, e.g., Neubauer (1998), Simon (2015). The integration is performed from the surface (green line, bottom sketch) or the equatorial plane ($z_0 = 0$) along z up to the region where the conductivities vanish (z_i), shown by the dark blue line, over one half-space for a symmetric atmosphere. An exponential conductivity profile was assumed ($\sigma_P \sim \exp\left(\frac{h}{H_e} + \frac{h}{H_a}\right)$. The conductance achieves its maximum where the field lines are tangent to Europa, i.e., $r = r_s$. It has a local minimum at the poles because of the shortest integration path in this region. Σ_H (not shown here) looks qualitatively similar but decreases faster than Σ_P due to $\sigma_H \propto n_n^2$ and $\sigma_P \propto n_n$ (in the limit of $\nu_{in}/\omega_{ci} << 1$ with the ion gyro frequency ω_{ci}). The blue areas in the upper panel represent the approximated Pedersen conductances within each domain in the northern hemisphere in our analytic model and refer to Figure 4.2. The light blue areas, where the conductance decreases with distance from the moon, are subdivided in eight regions with the radial extent $r_{a,0\ldots8}$ in the equatorial plane. The expression $r_{a,0} = r_s$ indicates Europa's surface and the region with the extent $r_{a,8}$ represents the area, where the conductance nearly vanishes. The ratio between the conductances Σ_P^n and Σ_P^a shown here is 1:2.

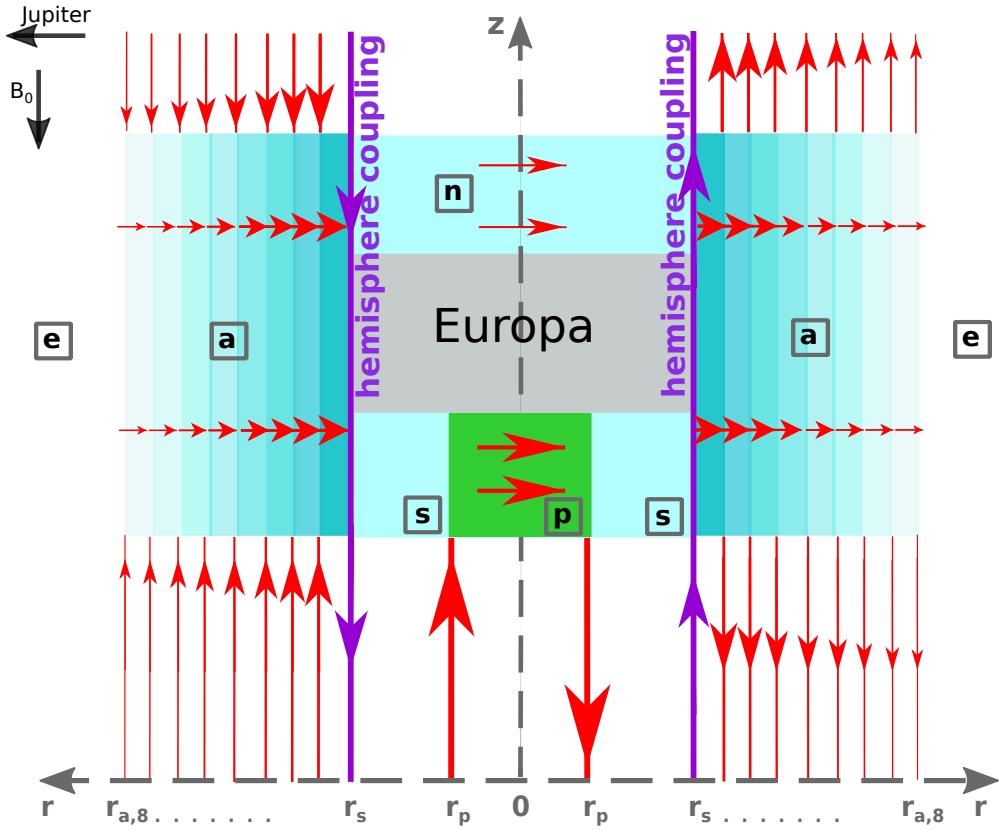

Figure 4.2. – Sketch of the geometry of the electric current system (red and purple arrows) for the analytic model with a south polar plume with the radial extent r_p. Europa's solid body is displayed as grey area. The extent of Europa's solid body is r_s. The currents driven in the interaction region are partially volume currents and partially surface currents. The ionospheric currents are volume currents shown in the horizontal red arrows. The Alfvénic currents are volume currents for a smoothly varying ionosphere but in our analytic model represented to a number of surface currents shown as vertical red arrows. The thickness of the red arrows represents the different strengths of the currents in each domain. Due to the north-south asymmetry additional surface currents, which couple the northern and southern hemisphere are shown as purple arrows. The interaction region is separated in different domains (n, a, e, s, and p) with constant conductances in each domain. Domain p represents the south polar plume, domain n and s represent the global atmosphere in the northern and southern hemisphere, respectively, domain a represents the region where the wing aligned currents are concentrated, and domain e the region outside Europa's atmosphere where ionospheric conductivities vanish. The different brightnesses in domain a represent the gradual decrease of the conductances away from Europa in order to consider the decrease of the ionospheric density with distance from Europa (see Figure 4.1). For a detailed description see text in Section 4.1.

Note, that in the analytic model the background magnetic field lines coincide with the isolines of the electric potential. So the integration is performed along the field lines (over z) from the equatorial plane or the moon's surface z_0 out to a distance z_i where the conductivities vanish (similar to previous calculations of the conductances in sub-Alfvénic interactions, e.g., Neubauer, 1998, Saur et al., 1999, Kivelson et al., 2004).

The black line in Figure 4.1 sketches Europa's Pedersen conductance profile for a radially symmetric atmosphere similar to Figure 6 in the work of Neubauer (1998). As the neutral density decreases exponentially, we assume an exponential profile for the ionospheric conductivities $\sigma_{P,H} \sim \exp(h/\tilde{H})$ with the altitude h and the effective scale height $\tilde{H}$ (see Equation (4.7)). It shows minimum conductances above the pole and maximum conductances at the moon's diameter ($r = r_s$). The variation of Σ_P (and Σ_H) arises due to the change of the length of the integration path along the magnetic field lines through the atmosphere (see Equation (4.1)), which is shortest at the poles. At the field lines tangent to Europa given by r_s two peaks occur due to the sudden change of the integration path through the atmosphere (Neubauer, 1998). The magnetic field lines are not connected to the solid surface of the moon anymore (i.e., for $r_\perp > r_s$ with $r_\perp = \sqrt{x^2 + y^2}$). The ionospheric currents couple to the Alfvénic currents at the field lines that are tangent to the moon's solid body. Moving away from the moon, the neutral density of the atmosphere decreases and hence the ionospheric conductances. In the area of the two peaks (see Figure 4.1) the field-aligned currents are maximum. Therefore, steep gradients in the magnetic field and velocity are expected along field lines crossing this region. An asymmetric atmosphere, e.g., due to an atmospheric inhomogeneity such as a plume, would generate additional rotational discontinuities in the magnetic field at the Alfvénic flux tubes. This means that there is a magnetic jump across the flux tubes but the density is the same on both sides of it. Our analytic model includes both steep gradients due to the global atmosphere and hemisphere coupling currents due to an atmospheric inhomogeneity.

Figure 4.2 shows a sketch of the geometry and the electric current system for the interaction region of the analytic model. A similar modification of the analytic model was also performed by Simon et al. (2011) and Simon (2015) for Enceladus. The extended version of the model presented here considers, in addition to a cylindrical plume (domain p), a less dense atmosphere region (domain s and n) and a second region (domain a) where the wing-aligned currents are concentrated. The region a is subdivided into eight subdomains as shown in Figure 4.1 and 4.2. This description represents a simplified approximation of the peak of the conductances at the location of field lines tangent to the solid body and a continuously decreasing neutral density and therefore decreasing conductances when moving outward of region a (see light blue area between $r_s < r_\perp < r_{a,8}$ in Figure 4.1). Within each domain the ionospheric conductances are spatially constant. The increased conductance within the plume (domain p) compared to

the ambient atmosphere (domain s) results in the formation of the Alfvén winglet within the Alfvén wing in the far field. Besides the hemisphere coupling effect, the analytic model is also suitable to study the effects of the Alfvén winglet. We calculate the solution for the electric potential and thus for the electric field in each domain for the scenarios when the plume is located at the south or the north pole. We proceed as follows: In analogy to the calculations of Saur et al. (2007) we apply the following approach in polar coordinates ($x = r\cos\phi$ and $y = r\sin\phi$):

$$\hat{\Phi}(\hat{r},\phi) = \sum_{l=1}^{\infty}[\hat{r}^{l}(a_l\sin(l\phi) + b_l\cos(l\phi)) + \hat{r}^{-l}(g_l\sin(l\phi) + h_l\cos(l\phi))] \tag{4.2}$$

for the solution of the Laplace equation $\Delta\Phi(x,y) = 0$, where we use $\hat{r} = r/R$ for the radial component and $\hat{\Phi} = \Phi/\Phi_0$ for the electric potential with the radius of the moon R, the unperturbed electric potential $\Phi_0 = E_0 R$, and the unperturbed corotational electric field E_0. The constants a_l, b_l, g_l, and h_l are to be determined from the boundary conditions. Note, within each area of constant conductances where the Laplace equation needs to be solved, a separate set of a_l, b_l, g_l, and h_l have to be calculated. The solution for the electric potential should fulfill the boundary and the jump conditions. Additionally, it has to be continuous without singularities. Only coefficients with $l = 1$ are nonzero because the perturbed electric field vanishes at infinity and the potential is given by

$$\Phi_0 = E_0 y \quad \text{for} \quad r \to \infty\,. \tag{4.3}$$

We subdivide our interaction region in five domains (see Figure 4.2): In the external domain, where the field lines do not intersect the solid body and the ionospheric conductances vanish, the electric potential with superscript e is given by

$$\hat{\Phi}^{e}(\hat{r},\phi) = \hat{r}\sin(\phi) + \hat{r}^{-1}(g_1^e\sin(\phi) + h_1^e\cos(\phi)) \quad \text{for} \quad \hat{r}_{a,8} \le \hat{r}\,. \tag{4.4}$$

The domain with superscript a represents the area where the conductances peak and decrease approximately in an exponential form, when moving outward and where the currents feed into the global ionosphere are located. The potential in this area is given by

$$\hat{\Phi}^{a,k}(\hat{r},\phi) = \hat{r}(a_1^{a,k}\sin(\phi)+b_1^{a,k}\cos(\phi))+\hat{r}^{-1}(g_1^{a,k}\sin(\phi)+h_1^{a,k}\cos(\phi)) \quad \text{for} \quad \hat{r}_{a,k-1} < \hat{r} \le \hat{r}_{a,k}\,. \tag{4.5}$$

This exponential-ionospheric domain is subdivided into eight regions in order to construct the decrease of the conductances as visible in Figure 4.1. The index k runs from 1 to 8 and $r_{a,0} = r_s$ correspond to the radius of the moon. In each region the conductances $\Sigma_{P,H}^{a,k}$ are constant and each region is spatially limited by $r_{a,k}$. The conductances are constructed in the way that

$$\Sigma_{P,H}^{a,k} = \Sigma_{P,H}^{a,1}\exp\left(-(k-1)\,\Delta/\tilde{H}\right)\,. \tag{4.6}$$

For the step size Δ we chose a value of $0.04\,r_s$. Here we introduced the effective scale height $\tilde{H}$. Our purpose with the approximation to an exponentially decreasing ionospheric domain is to investigate if the steep gradient seen in the measured magnetic field when Galileo crossed the Alfvén wing during the E17 flyby can be explained by Europa's global atmosphere. Therefore, we consider the average electron density which has its maximum near the surface. The average profile of the electron density is best described by an exponential decrease with altitude with a model having a plasma scale height of H_e=240$\pm$40 km below 300 km according to the results of Kliore et al. (1997). We describe Europa's global atmosphere radially symmetric (Equation (3.54)). The atmospheric neutral density is described by an exponential decrease in altitude. The Pedersen conductivity depends approximately on the product of the electron and the neutral density which is particularly correct farther away from the surface. Thus, we assume for the linear Pedersen conductivity $\sigma_P \sim \exp\left(\frac{h}{H_e} + \frac{h}{H_a}\right)$. The effective scale height is then given by

$$\tilde{H} = \frac{H_a H_e}{H_a + H_e}\,. \tag{4.7}$$

For the atmospheric scale height we choose H_a=145 km (Saur et al., 1998, Roth et al., 2016) and for the plasma scale height H_e=240 km (Kliore et al., 1997) (see discussion in Section 6.2.1). The spatial extent of domain a strongly depends on the effective scale height. In the northern hemisphere we assume a global atmosphere with constant conductances $\Sigma^n_{P,H}$. Thus, the electric potential within the northern tube is given by

$$\hat{\Phi}^n(\hat{r},\phi) = \hat{r}(a^n_1 \sin(\phi) + b^n_1 \cos(\phi)) \quad \text{for} \quad \hat{r} \leq \hat{r}_s\,. \tag{4.8}$$

In this calculation the inhomogeneity with conductances $\Sigma^p_{P,H}$ is assumed to lie at the south pole of the moon and the electric potential in domain p is calculated by

$$\hat{\Phi}^p(\hat{r},\phi) = \hat{r}(a^p_1 \sin(\phi) + b^p_1 \cos(\phi)) \quad \text{for} \quad \hat{r} \leq \hat{r}_p\,. \tag{4.9}$$

The region outside of the dense inhomogeneity is characterized by the electric potential with superscript s:

$$\hat{\Phi}^s(\hat{r},\phi) = \hat{r}(a^s_1 \sin(\phi) + b^s_1 \cos(\phi)) + \hat{r}^{-1}(g^s_1 \sin(\phi) + h^s_1 \cos(\phi)) \quad \text{for} \quad \hat{r}_p \leq \hat{r} \leq \hat{r}_s\,. \tag{4.10}$$

The free parameters a^j_1, b^j_1, g^j_1 and h^j_1 with the superscript j=e, a, n, s, and p depend on the conductances within each domain and the spatial boundaries of each domain. To compute these constants, we have to consider the boundary conditions between individual domains. The electric potential has to be continuous at the boundaries of the domains, so $\hat{\Phi}^e(\hat{r} = \hat{r}_{a,8}) = \hat{\Phi}^{a,8}(\hat{r} = \hat{r}_{a,8})$, $\hat{\Phi}^{a,8}(\hat{r} = \hat{r}_{a,7}) = \hat{\Phi}^{a,7}(\hat{r} = \hat{r}_{a,7})$, ..., $\hat{\Phi}^{a,2}(\hat{r} = \hat{r}_{a,1}) = \hat{\Phi}^{a,1}(\hat{r} = \hat{r}_{a,1})$, $\hat{\Phi}^{a,1}(\hat{r} = \hat{r}_s) = \hat{\Phi}^n(\hat{r} = \hat{r}_s) = \hat{\Phi}^s(\hat{r} = \hat{r}_s)$, and $\hat{\Phi}^s(\hat{r} = \hat{r}_p) = \hat{\Phi}^p(\hat{r} = \hat{r}_p)$. The condition of continuity does not hold for the normal component of the electric potential. For the boundaries at the domain at r_p and r_a we use

the jump condition (Equation(A2) in Saur et al., 1999)

$$\lim_{\epsilon\to 0}\left| r\left(\Sigma_P+\Sigma_A\right)\frac{\partial\Phi}{\partial r}+\Sigma_H\frac{\partial\Phi}{\partial\phi}\right|_{r_j-\epsilon}^{r_j+\epsilon}=0 \tag{4.11}$$

with $r_j = r_{p,a}$. At $r = r_s$ the hemisphere coupling occurs and the potentials $\Phi^{a,1}$, Φ^s and Φ^n are linked through Equation (9) in the work of Saur et al. (2007). We apply a computer algebra program to calculate the 42 free parameters from the boundary and jump conditions. The Equations for the electric potential (4.4)–(4.10) are uniquely solved. The calculation of the electric potential for a north polar inhomogeneity is analogous.

In the Alfvén wings the frozen-in-field theorem holds, so the electric field is given by $\underline{E} = -\underline{v}\times\underline{B}$. The analytic model is based on pure Alfvénic interaction in the far field so the perturbed magnetic field $\delta\underline{B}$ and velocity $\delta\underline{v}$ are related by $\delta\underline{B} = \pm\sqrt{\mu_0\rho_0}\,\delta\underline{v}$. Combining these relationships it is possible to calculate the perturbed magnetic field from the electric field (Neubauer, 1980). Neubauer (1980) uses a coordinate system with the z axis aligned with either the northern or the southern Alfvén characteristic. The northern ($\underline{c}_A^-$) and southern ($\underline{c}_A^+$) Alfvén characteristics are given by

$$\underline{c}_A^{\pm} = \underline{v}_0 \pm \underline{B}_0/(\sqrt{\mu_0\rho_0})\,. \tag{4.12}$$

The y axis in the system of Neubauer (1980) is the same as in the EPhiB system and the x axis completes the right-handed coordinate system. Transforming Equations (14) and (15) of his work into the EPhiB system leads to the expression of the magnetic field for the Alfvénic far field:

$$\underline{B} = \frac{1}{\sqrt{1+M_A^2}}\begin{pmatrix} \mp\mu_0\Sigma_A E_y \mp M_A\sqrt{B_0^2-\mu_0^2\Sigma_A^2\left(E_y^2+\frac{1}{1+M_A^2}E_x^2\right)} \\ \pm\mu_0\Sigma_A E_x \\ \mu_0\Sigma_A M_A E_y - \sqrt{B_0^2-\mu_0^2\Sigma_A^2\left(E_y^2+\frac{1}{1+M_A^2}E_x^2\right)} \end{pmatrix}, \tag{4.13}$$

where $\underline{B}$ and $\underline{E}$ are given in the EPhiB system. The upper and lower signs refer to the northern and southern Alfvén wings, respectively. The Alfvén conductance is given by

$$\Sigma_A = \frac{1}{\mu_0 v_{A_0}\sqrt{1+M_A^2}} \tag{4.14}$$

for low Alfvénic Mach numbers M_A (Neubauer, 1980). The parameter v_{A_0} is the Alfvén velocity of the upstream plasma. Incorporating our solutions for the electric potential given in Equations (4.4)–(4.10) in the calculations of the magnetic field allows us to calculate the magnetic field in the Alfvénic far field for our specific problem. It is not applicable to calculate the magnetic field perturbation in the near field since local ionospheric effects become important in this region.

The calculations made here are based on the fact that the chosen geometry of the conductances possesses rotational symmetry around the z axis. A breakup of this symmetry, for example by choosing a position for the inhomogeneity away from the north or south pole, would make the calculations exceedingly complex. The real plasma interaction is not purely Alfvénic and the interaction region is much more complex. However, the here presented approach is useful for a first analysis to search for potential local atmospheric inhomogeneities in the magnetic field and, if available, plasma velocity data.

5. Results: Modeling of Io's Plasma Interaction

In this chapter we will focus on the model results of Io's plasma interaction. We begin with global considerations of the plasma interaction for different model atmospheres. We describe in particular how the volcanic plumes, Tvashtar and Pele, affect Io's plasma environment. Furthermore we investigate if signatures of plumes are present in the MAG data of the Galileo I31 flyby. Afterwards, we discuss the influence of a volcanic plume on the supply rate of the plasma torus according to our model results. In the last part of this Chapter, we compare our model results with the data measured during the Galileo flybys I24 and I27 and deal with the question if induction signals from a magma ocean are necessary to explain this data. We will give a detailed discussion of our results and of the discrepancies of our MHD model and the model of Khurana et al. (2011). Properties of the Io Flybys are given in Table 5.1. All results are presented in the IPHIO coordinate system.

5.1. Influence of Global Asymmetries and Plumes in Io's Atmosphere on the Global Plasma Interaction

Here we apply a simplified geometry so that the background magnetic field is pointing in the negative z direction perpendicular to the plasma flow velocity (in direction of the positive x axis). For the simulation results of the plasma interaction presented in this Section, we use the atmospheric properties and initial values given in Tables 3.1 denoted by "Day/night atm." and "Atm.+Tvashtar (or Pele)", and 3.3 .

Table 5.1. – Properties of the Io Flybys I31, I24, and I27.

Flyby	Date time[a] (UT)	Altitude (km)	Local time[a] (deg)	λ_{III}[b] (deg)	Lat.[a,c] (deg)	E long.[a,c] (deg)
I31	2001-08-06 04:59:21	194	4.33	159.6	77.5	187.7
I24	1999-10-11 04:33:03	611	10.7	80.3	4.5	135.9
I27	2000-02-22 13:46:41	200	8.91	81.1	18.5	157.4

[a]At the closest approach CA.

[b]West longitude.

[c]Satellite planetocentric coordinates at CA.

5.1.1. Magnetic Field and Velocity Field

Io acts as an obstacle to the flowing plasma. Collisions with the atmospheric neutrals, charge exchange and electron impact ionization generate perturbations in the plasma flow and the magnetic field. The plasma flow is slowed near Io and partially redirected around it. Perturbations propagate along the magnetic field lines and form standing Alfvén waves in the rest frame of Io. The Alfvén waves perturb simultaneously the magnetic field and the plasma velocity in the Alfvénic far field. Figures 5.1a and 5.1b display the magnitude of the plasma flow velocity in the xz plane for the plasma interaction with Io's global atmosphere without a plume and with Io's global atmosphere in which the Tvashtar plume is included, respectively. The Alfvén characteristics are plotted as dashed lines. The Alfvén wings are clearly recognizable in the decreased plasma velocity compared to the upstream flow velocity of 57 km s^{-1}. In the rest frame of Io, the Alfvén wings are bend back at an angle of $\theta_A = \arctan M_A \approx 13^\circ$ to the background magnetic field for the upstream conditions we used here. The radius of the wings is larger than one R_{Io} because of the extended atmosphere which forms the main obstacle to the magnetospheric plasma flow. Io's sub-Alfvénic plasma interaction is comparable with Europa's interaction discussed in Chapter 6.1 when induction is not considered. The main difference is that Io's global atmosphere is denser than Europa's global atmosphere hence we expect Io's plasma interaction to be in general more strongly developed than Europa's plasma interaction.

We introduce the factor $\overline{\alpha} = 1 - \alpha_{plasma}$ (see Equations (3.22) and (3.23)) which is a measure for the relative strength of the sub-Alfvénic interaction (see also Saur et al. (2013)). When the plasma interaction is saturated, the maximum value of $\overline{\alpha} = 1$ is reached and $\overline{\alpha} = 0$ when no interaction takes place. We calculate the measure for the relative strength of the sub-Alfvénic interaction in the Alfvén wings of $\overline{\alpha} \geq 0.8$ (see Figure 5.1a) which is much higher than for Europa ($\overline{\alpha} \approx 0.4$ see Section 6.1.1). Figures 5.1a and 5.1c show that the plasma flow velocity inside the Alfvén wings is not homogeneous. The reason is the asymmetric distribution of the neutral gas in the atmosphere. At the poles, the neutral density is very thin and therefore collisional interaction between the neutrals and ions, and electron impact ionization is weaker than at equatorial latitudes. At equatorial latitudes, the ionospheric conductances are large and the shielding and deflection of the plasma around the moon is very effective. On the upstream side of Io at the equatorial latitudes the perturbation of the incident plasma achieves its maximum and the plasma velocity is decreased to ~ 4 km s^{-1} as a result of ion-neutral collisions and pickup. The strength of the plasma interaction upstream of the moon with $\overline{\alpha} \approx 0.93$ indicates that the interaction is almost saturated. The plasma then slowly convects through Io's atmosphere. Downstream of Io at the equatorial latitudes the plasma velocity increases from ~ 20 km s^{-1} to its upstream velocity of 57 km s^{-1}. This inhomogeneous flow pattern maps out into the Alfvén wings where the magnetic field lines are frozen into the plasma fluid. It is visible that the slowing of the flow is strongest

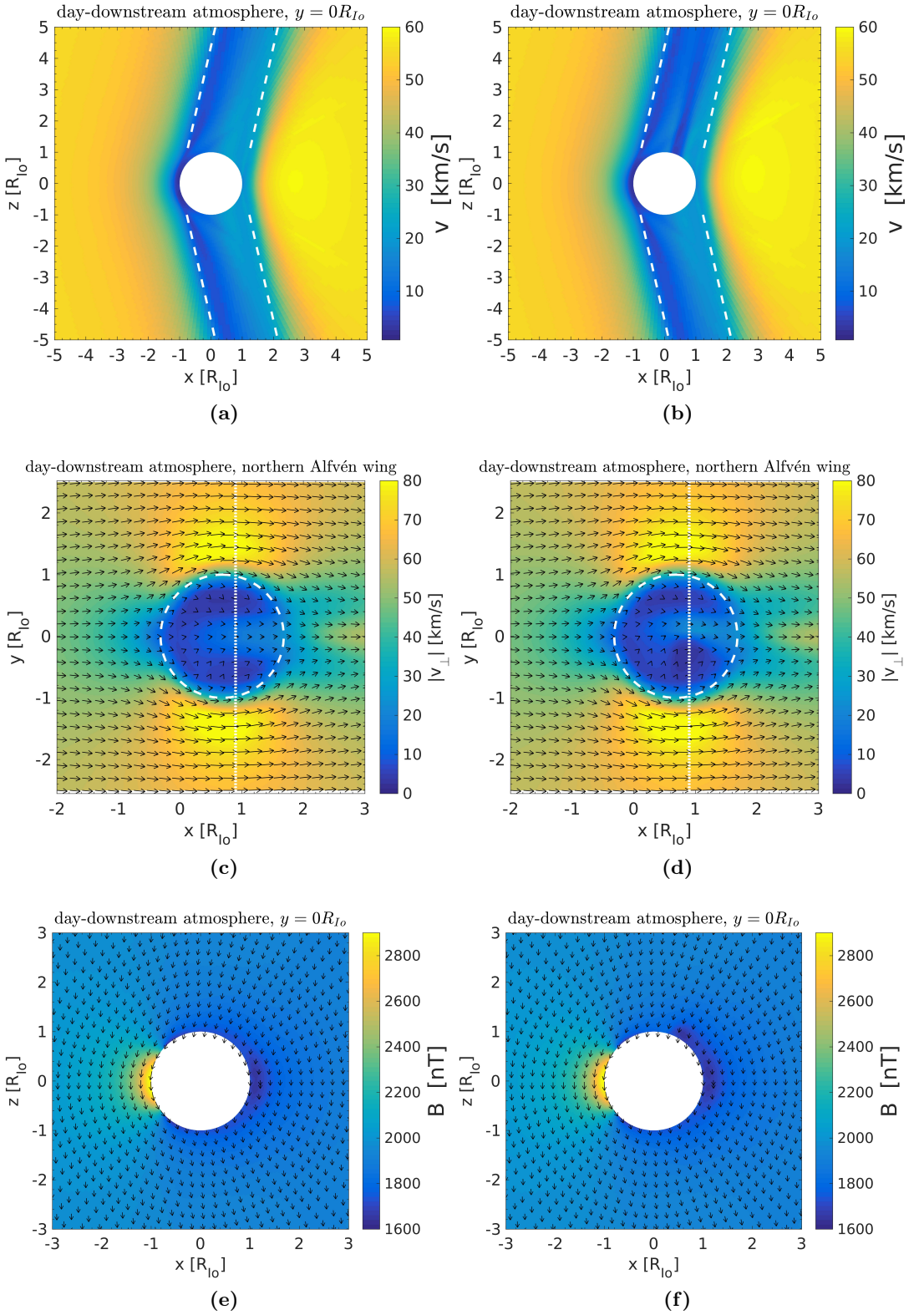

Figure 5.1. – (a) and (b): Magnitude of the plasma bulk velocity in the xz plane. (c) and (d): Plasma flow velocity field in a cut at $z = 3\ R_{Io}$ through the northern Alfvén wing. The color scale represents the magnitude of the plasma velocity perpendicular to the magnetic field. (e) and (f): Magnitude of the magnetic field in the xz plane. The results are shown for an atmosphere which is concentrated on the downstream side at the equatorial latitudes with and without Tvashtar near the north pole. The white circle indicates the projection of Io's surface. The white vertical dotted line shows the trajectory along which the magnetic field is displayed in Figure 5.2. The arrows show the orientation of the plasma flow ((c) and (d)) and the magnetic field ((e) and (f)), and their lengths linearly scale with highest magnitude of this plane: 83.1 km/s (c), 83.6 km/s (d), 2892 nT (e), 2921 nT (f).

on the upstream side and the edges and weaker in the center to the downstream side of the wings (see Figure 5.1a).

The Tvashtar plume introduces a north-south asymmetry in the Alfvén wings (see Figure 5.1b). Note that Tvashtar is not directly located at the northern pole but shifted to the downstream and anti-Jupiter side, hence the xz plane shown in Figure 5.1b do not cross the plume center. However, the formation of an Alfvén winglet inside the northern Alfvén wing due to the plume is visible in the local decrease of the velocity inside the northern Alfvén wing from $\sim$15 km s^{-1} to $\sim$4 km s^{-1} and the increase of the velocity at the sub-Jovian flank of the winglet to $\sim$18 km s^{-1} inside the northern Alfvén wing (see Figure 5.1d). The northern and southern hemisphere are not directly linked together due to the blockage of the solid body and no local perturbations due to the plume are visible in the southern Alfvén wing (see Figure 5.1b). The interaction with the plume results in locally enhanced elastic collisions between the neutrals and ions and pickup leading to stronger perturbations within the interaction region. The local enhancement of the neutral density in the plume with an average column density over the plume region of $\sim$1.2 $\times$ 10^{20} m^{-2} compared to the thin ambient atmosphere at the poles with an average column density of $\sim$4 $\times$ 10^{18} m^{-2} does not have such a strong effect as it has at Europa when a plume in the global atmosphere is included (see Section 6.1.1). The reason is that most of the interaction processes in our model happen upstream of the moon in the equatorial latitudes since the global atmosphere is concentrated around Io's equator. The plasma then slowly convects through Io's atmosphere downstream where electron impact ionization becomes weaker (see Section 5.1.3). The maximum vertical column density of the global atmosphere at the equator of $N_{A,\mathrm{max}} \approx 2 \times 10^{20}$ m^{-2} is larger than the average column density over the plume region of $\sim$1.2 $\times$ 10^{20} m^{-2}. Although the density of the Tvashtar plume forms a contrast to the small density in the ambient atmosphere at the northern pole, it does not provide such a great contrast to the global atmosphere as it is the case at Europa (see Section 6.1) resulting in a less developed Alfvén winglet.

Figures 5.1c and 5.1d show the magnitude of the velocity perpendicular to the background magnetic field in a cross section though the northern Alfvén wing. The wings act as an obstacle to the flow so that most of the plasma is deflected around the wings which is visible in the slowdown upstream of the wing and the enhanced velocity ($\sim$84 km s^{-1}) at the flanks of the wing. On the downstream side of the Alfvén wing the plasma is reaccelerated to the corotation velocity by the $\underline{j} \times \underline{B}$ force.

During the plasma interaction, Io's plasma environment is exposed to three different MHD wave modes, the Alfvén mode as already discussed above, and the compressional fast and slow magnetosonic modes, which propagate in different directions with different velocities. These wave modes are generated by the collisions of the plasma with the

neutrals and by the pickup processes. The fast mode travels in all directions and its amplitude can be neglected sufficiently far away from Io (a few R_{Io}). In Io's vicinity the fast mode is connected to the compressional perturbations. The slow down of the plasma upstream of Io leads to a compression and bending of the field lines which are frozen into the plasma fluid so that the magnitude of the magnetic field increases to $\sim$2900 nT in this region (see Figure 5.1e). A second pileup region due to the plume is hardly observable by comparing Figures 5.1e and 5.1f. A very weak pileup of the magnetic field due to the plume can be seen at x=0.5 R_{Io} and z=0.9 R_{Io}. On the downstream side the plasma flow is reaccelerated and the magnitude of the magnetic field decreases to $\sim$1670 nT. In the Alfvénic far field the magnitude of the magnetic field is constant but the magnetic field components are perturbed similar to the velocity field components following the Alfvénic relationship $\delta\underline{B} = \pm\sqrt{\mu_0\rho_0}\,\delta\underline{v}$.

We have not shown the plasma flow velocity and magnetic field results for the plasma interaction with Io's global atmosphere in which the Pele plume is included, because the results are very similar to the one without a plume shown here in Figures 5.1a, 5.1c, and 5.1e. The Pele plume is located on the upstream side near the equator in the dense global atmosphere where the interaction is almost saturated. The plume locally rises above and blankets the global atmosphere but the vertical column density does not provide a strong contrast to the vertical column density of the atmosphere. Therefore, differences in the velocity field and the magnetic field perturbations between the plasma interaction with the global atmosphere and the plume are barely identifiable.

5.1.2. Influence of the Tvashtar Plume on the Magnetic Field in the Alfvénic Far Field

The magnetic field in the Alfvén wings is modified by the neutral atmosphere. Here we present how the Tvashtar plume affects the magnetic field in the northern and southern Alfvén wings. The effect of Pele is hardly seen in the magnetic and velocity field perturbations due to the dense ambient upstream atmosphere as already mentioned in Section 5.1.1. Hence, we do not show the results for Pele in this Section. Figure 5.2 shows the components of the magnetic field along trajectories parallel to the y axis shifted $\sim$0.2 R_{Io} downstream from the center of the wing in the southern and northern Alfvén wings. The hypothetical trajectories go through the main interaction region and are displayed as white vertical lines in Figures 5.1c and 5.1d. The perturbations for models with day-downstream and -upstream atmospheres without a plume (light green and dark green lines) show very similar structures which are symmetric in the northern (Figure 5.2a) and southern wing (Figure 5.2b). Due to the bending of the magnetic field lines in the Alfvén wings the magnetic field is strongly perturbed in the negative (positive) x direction in the northern (southern) wing. Inside the Alfvén wings the magnitude of the B_x component decreases by about 70 nT in the center of the wing (see Figures 5.2a (top) and 5.2b (top)). This is

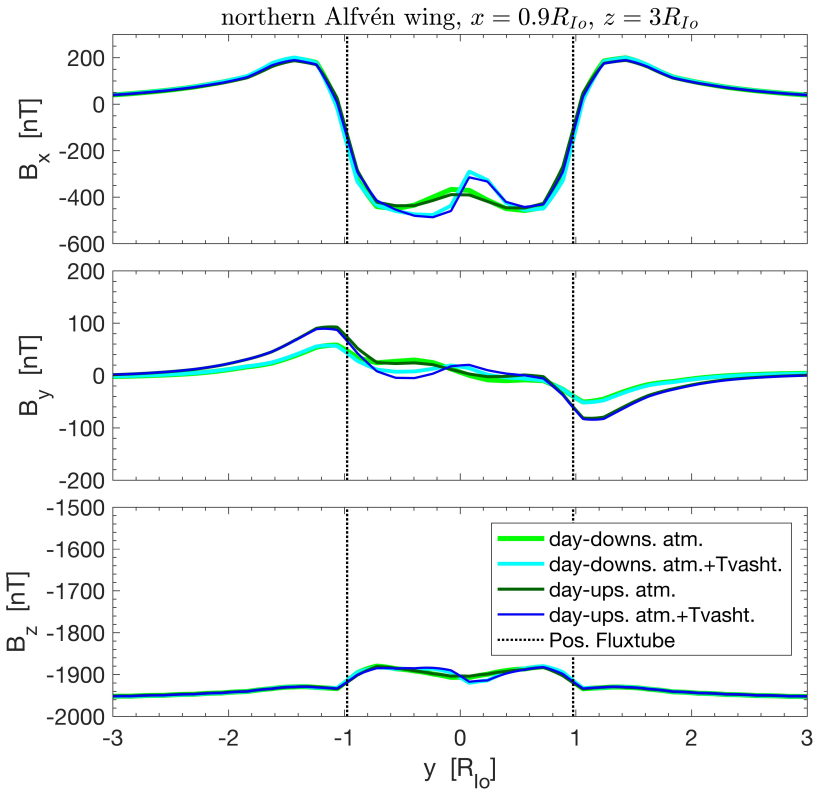

(a)

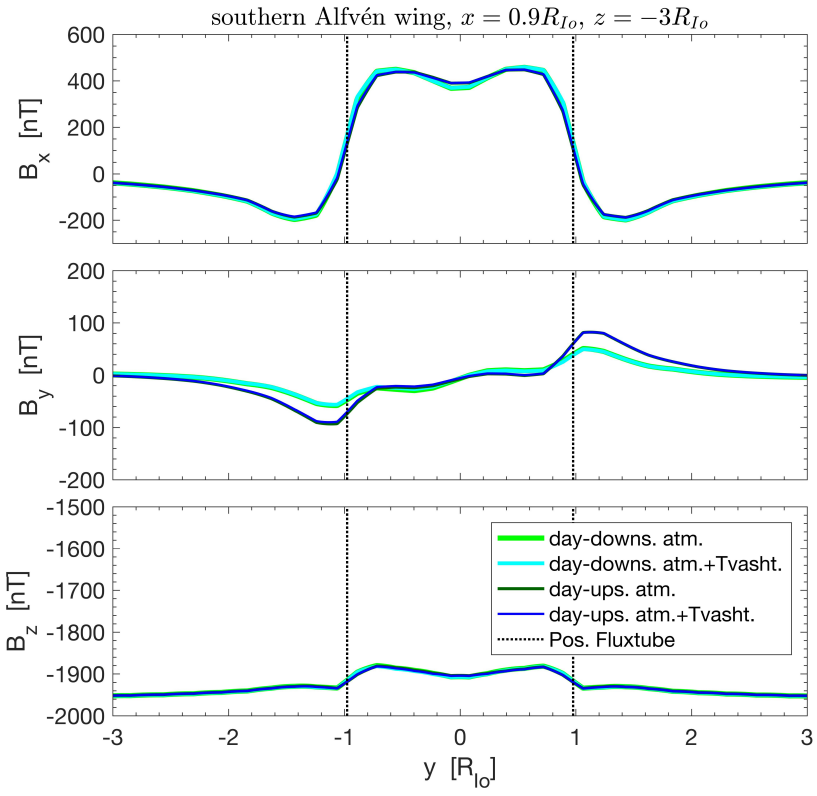

(b)

Figure 5.2. – Magnetic field components in the (a) northern and (b) southern Alfvén wing along a trajectory parallel to the y axis and shifted $\sim$0.2 R_{Io} downstream from the wing center. Results are calculated with the MHD model for four different atmosphere models with and without the Tvashtar plume. The Tvashtar plume is located near the northern pole. The initial values and atmospheric properties can be found in Tables 3.3 and 3.1. The vertical lines represent the position of the flux tube (dotted black line).

a result of the mapping of the plasma interaction with the thin atmosphere at the poles into the Alfvénic far field. A similar behavior as a consequence of the Alfvénic relationship is also observed in the plasma velocity field in Figure 5.1c. The interaction with the Tvashtar plume (light blue and dark blue lines in Figure 5.2a) causes perturbations on smaller scales most visible in the B_x component. The decrease of the magnitude of the B_x component from about 500 nT to 300 nT inside the northern Alfvén wing is the result of the acceleration of the plasma at the sub-Jovian flank of the Alfvén winglet (see Figure 5.1d). Inside the Alfvén winglet (at $y \approx -0.25$ R_{Io}) the magnitude of the B_x component increases to about 500 nT. The B_y and B_z component in the northern wing are only weakly perturbed by about 20 nT compared to the perturbations without the plume. The global day/ night asymmetries in the atmosphere have only a minor effect for the results shown here. In contrast to the northern wing, the magnetic field perturbations for all four atmospheric configurations in the southern Alfvén wing are very similar as displayed in Figure 5.2b. The plume is located near the north pole. Io's solid body blocks the effect of the plume to the southern hemisphere resulting in an interaction which is comparable to the interaction with an atmosphere without the plume. We see that the plume does not have such a great effect on the Alfvénic far field compared to the case at Europa discussed in Section 6.1.4.

5.1.3. Plasma Density

The magnetospheric plasma convects through Io's atmosphere and ionizes the SO_2 molecules of the atmosphere by electron impact. Io's ionosphere is strongly influenced by convection and, hence, it is mainly affected by the plasma flow velocity. Figures 5.4a and 5.4b present the plasma number density in the equatorial plane for two different atmospheric configurations with the atmosphere concentrated on the downstream side and on the upstream side, respectively. The results of the plasma number density for both configurations are very similar. While upstream of the moon and at its flanks the density achieves its maximum of $\sim$3.2 $\times$ 10^4 cm^{-3} produced mainly by electron impact ionization, the plasma density downstream of the moon decreases to $\sim$3.2 $\times$ 10^2 cm^{-3} ($\sim$4.2 $\times$ 10^2 cm^{-3} in Figure 5.4b).

The comparison between the two day/night side atmosphere models shows that the region upstream of the moon where the plasma density is enhanced, is more extended ($\sim$ 400 km above the surface, see Figure 5.4b) for an atmosphere which is denser on the upstream side than on the downstream side ($\sim$ 240 km above the surface, see Figure 5.4a). The day-upstream atmosphere is exposed to a stronger electron impact ionization process and shielding. As visible in the equatorial plane, most of the magnetospheric plasma is deflected around Io. The amount of plasma which reach Io's surface will be absorbed. The area of deflection along the flanks further downstream is wider for an atmosphere which is concentrated on the downstream side (see Figure 5.4a).

The maximum of the plasma number density is achieved at about 180 km above the surface on the upstream hemisphere whereas for the thinner atmosphere on the upstream side the maximum is shifted more to the surface. The maximum of the plasma number density occurs in the location of the peak of the number density of the magnetospheric electrons. Below this region the ionospheric electrons with a temperature of 0.2 eV dominate over the magnetospheric electrons (5 eV). The ionospheric electrons do not contribute to the ionization and stay cold around the moon as they are slowly convected downstream. In this region dissociative recombination becomes effective.

In our model plasma is produced by electron impact ionization from magnetospheric electrons and lost by dissociative recombination. In Figure 5.3 we show the electron production rates per unit volume plotted along the x axis and z axis for an atmosphere which is concentrated on the downstream side (day-downstream atmosphere) and for an atmosphere which is concentrated on the upstream side (day-upstream atmosphere). A plume is not included in both atmosphere models shown in this Figure. Additionally, we show the total elastic collision rates (induced dipole and charge exchange collisions), the recombination rates, the plasma number density and the number density of the magnetospheric electrons. Figures 5.3a and 5.3b display the profiles along the flow direction for two cases of day/night asymmetry. We see that the total elastic collision rate P_{coll} exceeds the electron impact ionization rate P_{imp} downstream and upstream of the moon. The high momentum transfer from the ions to the neutrals peaks at the surface. The collision frequency depends linearly on the neutral density and since charge exchange is the dominant collision process, the collision frequency only weakly depends on the relative velocity (see Equation (3.32)). However, for both atmosphere models the collisional rate is strongest near the surface on the upstream side because P_{coll} is a product of ν_{in} and the plasma number density n_{plasma}. The plasma number density achieves its maximum on the upstream side for both models and is lower on the downstream side. The electron impact ionization rate peaks at $\sim$2.5$\times$10^8 m^{-3} s^{-1} on the upstream side for both atmosphere models but its maximum is shifted away from the surface similar to the plasma number density n_{plasma} as already seen in Figure 5.4. The plasma interaction is already saturated on the upstream side (see Section 5.1.1). Our model discriminates between magnetospheric and ionospheric electrons by solving two different continuity equations. Therefore, it shows that the thicker the atmosphere is the lower is the penetration depth of the magnetospheric electrons into the atmosphere as also seen in the decrease of the number density of the magnetospheric electrons n_{mag}. The magnetospheric electrons are shielded from the surface by the atmosphere and consequently the peak of P_{imp} is shifted from the surface. In this area the cooler ionospheric electrons, which do not contribute to the ionization process, become important. High energetic electrons, which are not included in our model, could also be important in this region. For these electrons the atmosphere is collisionally thin (Saur et al., 2003). Very energetic electrons would enter deep into the atmosphere down

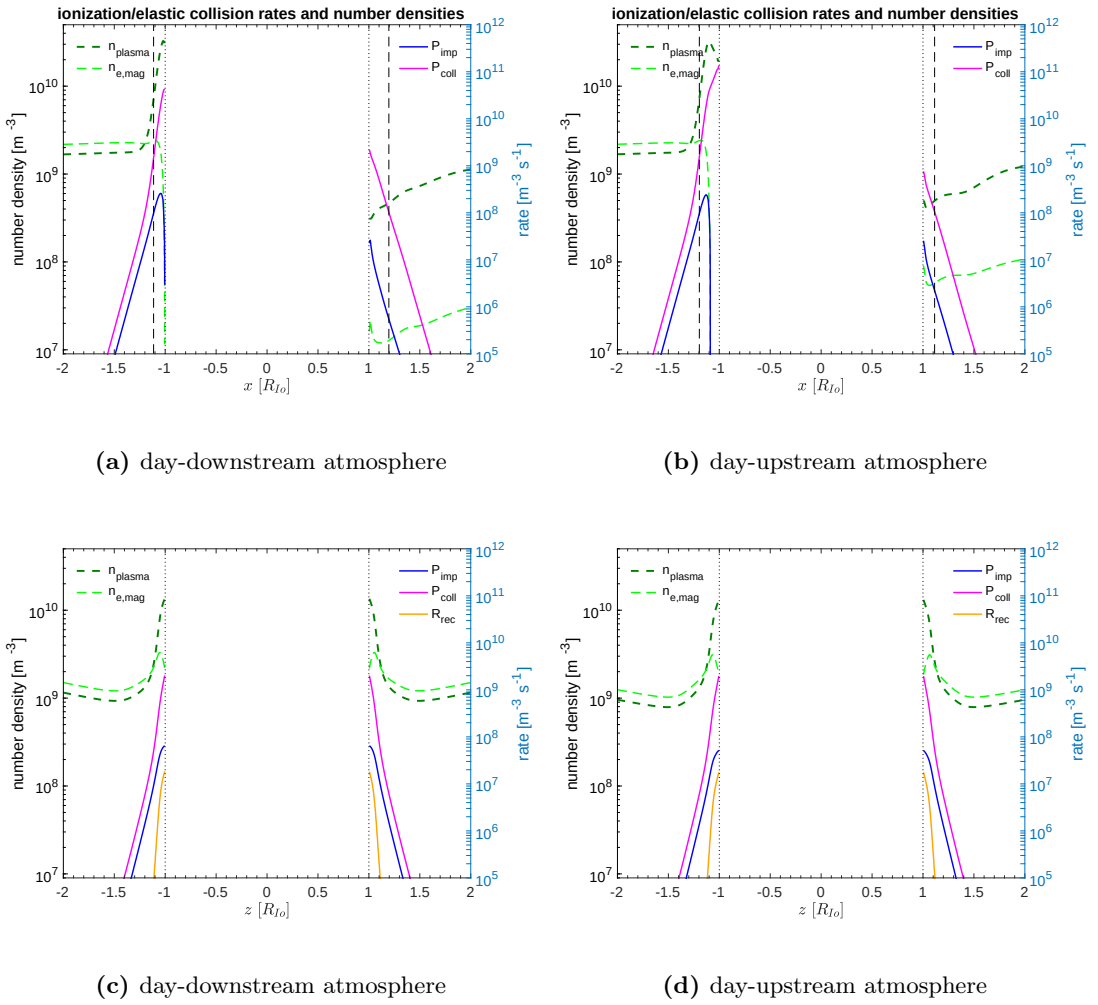

(a) day-downstream atmosphere

(b) day-upstream atmosphere

(c) day-downstream atmosphere

(d) day-upstream atmosphere

Figure 5.3. – Electron impact ionization rates per unit volume $P_{\text{imp}} = P$, elastic collision rates per unit volume $P_{\text{coll}} = \nu_{\text{in}} n_{\text{plasma}}$, plasma number density $n_{\text{plasma}} = \rho/m_i$, and number density of the magnetospheric electrons $n_{\text{e,mag}}$ profiles (a) and (b) along the x axis (flow direction), (c) and (d) along the z axis (poles). $R_{\text{rec}} = L_{\text{rec}}$ is the dissociative recombination rate per unit volume. The vertical dotted and dashed lines represent the positions of Io's surface and the exobase, respectively. At the poles the exobase is close to the surface.

to Io's surface.

The rates and densities along the z axis, i.e. through the polar regions are presented in Figures 5.3c and 5.3d. The rates and densities are lower than on the upstream side and nearly symmetric between the south pole (negative z axis) and north pole (positive z axis). The results show that dissociative recombination (R_{rec}) takes only a small fraction of the rates for the atmospheres discussed in our model.

The analysis of radioscience occultation measurements of Pioneer 10 and the Galileo spacecraft showed larger plasma densities on the downstream side than on the upstream side (Kliore et al., 1975, Hinson et al., 1998) which is not in accordance with our results

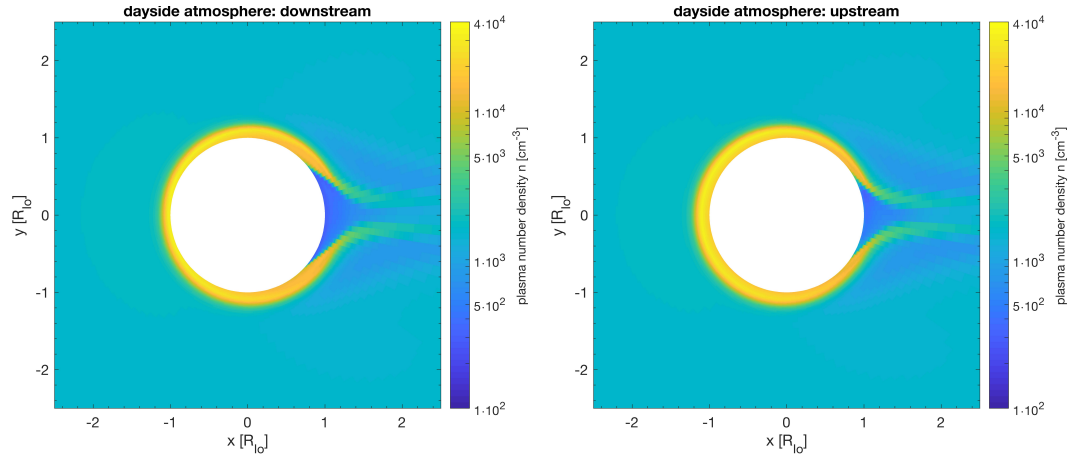

(a) day-downstream atmosphere **(b)** day-upstream atmosphere

Figure 5.4. – Plasma number density in the equatorial plane z=0 R_{Io} for two different cases of an atmospheric day/night asymmetry: (a) The subsolar point is located on the downstream side, (b) the subsolar point is located on the upstream side.

for both atmospheric configurations in our model. Downstream of the moon energetic particles like bidirectional high-energy electrons which were observed in the wake of Io (Williams et al., 1996) and are not included in our model could play an important role. They provide an ionization source in the wake of Io (Saur et al., 2002, Dols et al., 2008, 2012), likely on the flanks and above the poles (Williams et al., 1996, Williams and Thorne, 2003, Frank and Paterson, 1999). Also photoionization could affect the plasma density in this region.

The radio occultation measurements show that the dayside ionosphere achieves its maximum electron density of about 6×10^4 cm^{-3} at an altitude of about 100 km and has a scale height of 220 km (Kliore et al., 1974). These values are similar to the findings in Figure 5.3b (negative x axis). On the nightside the ionosphere is confined much closer to Io and achieves its maximum electron density of about 9×10^3 cm^{-3} at an altitude of about 50 km with a scale height of about 60 km (Kliore et al., 1975). Considering Figure 5.3b (positive x axis) the plasma number density is smaller on the nightside (4.2×10^2 cm^{-3}) in our model.

The influences of the Pele and Tvashtar plumes on the plasma number density are shown in vertical planes through the main interaction region in Figure 5.5. The plumes are located in a day-downstream atmosphere, so that Tvashtar is situated on the dayside and Pele on the nightside of Io. Figures 5.5b and 5.5c show that the plumes locally enhance the plasma number density. The plasma number density do not peak at the plume center but is located farther above the plume center. The enhancement of the atmosphere due to the plume locally shields the magnetospheric electrons to enter the atmosphere as discussed above.

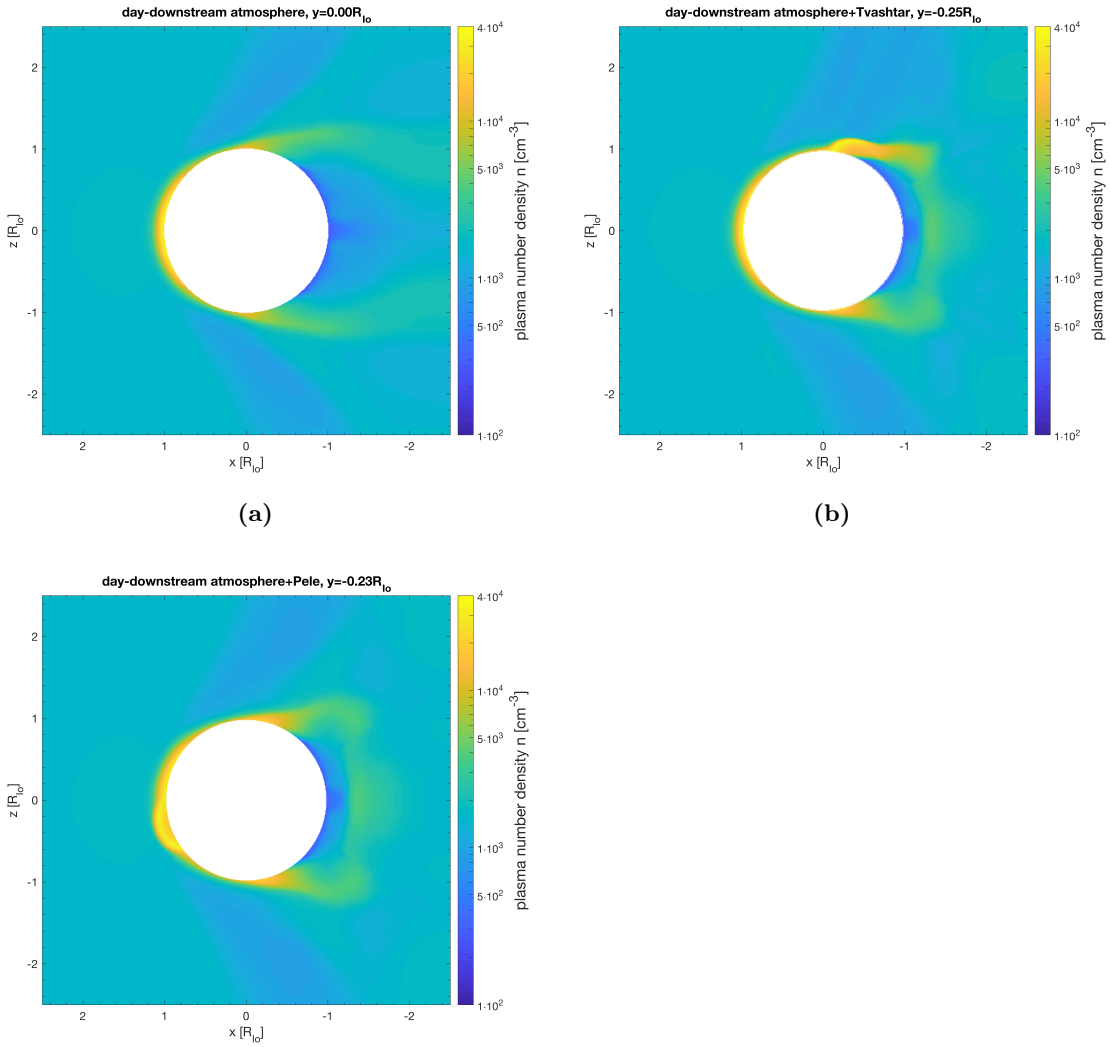

Figure 5.5. – Plasma number density in cm^{-3} (a) in the xz plane (y=0 R$_{Io}$) for an atmosphere which is concentrated on the downstream side at the equatorial latitudes; (b) in the xz plane (y=$-$0.25 R$_{Io}$) for an atmosphere which is concentrated on the downstream side at the equatorial latitudes with the Tvashtar plume near the northern pole; (c) in the xz plane (y=$-$0.23 R$_{Io}$) for an atmosphere which is concentrated on the downstream side at the equatorial latitudes with the Pele plume at the upstream side.

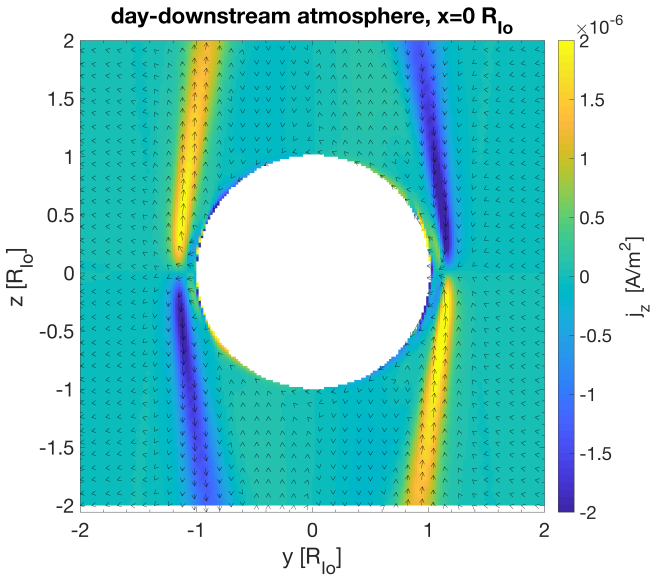

Figure 5.6. – Current density parallel to the background magnetic field j_z in the yz plane ($x = 0R_{Io}$). The arrows show the orientation of the current density and their lengths linearly scale with highest magnitude of this plane: 2.5 $\times$ 10^{-6} A/m^2.

5.1.4. Electric Current Density in the Alfvén Wings

The bending of the field lines generates a curl of the magnetic field, which establishes associated currents. The magnetic and velocity field perturbations associated with the bending of the field lines propagate along the magnetic field lines north and south of the moon via Alfvén waves which carry field-aligned currents. In Figure 5.6 we show the current density $\underline{j}_z$ parallel to the background magnetic field in the yz plane. The main electric current system is orientated along the Alfvén characteristics, which are besides the small Alfvén angle Θ_A directed along the z axis. The currents are directed downward (upward) on the Jupiter-facing side and upward (downward) on the anti-Jupiter side of the northern (southern) Alfvén tube. Current closure perpendicular to the magnetic field occurs in Io's ionosphere, where the neutral density is sufficiently high. Note that the boundary condition in our model does not allow currents to flow through Io's surface. Since the current density is divergence-free, the perpendicular currents are continued along the field lines. Above Io's poles the neutral density is very thin so that the perpendicular currents are very small and can not be maintained. They are then continued along the field lines before reaching the poles. These weak parallel currents can be recognized inside the northern wing in Figure 5.7a.

The currents in the Alfvén wing can be divided into the Alfvén wing currents parallel to the northern and southern Alfvén characteristic and into Alfvén wing currents perpendicular to the characteristics. Figure 5.7 displays the parallel Alfvénic currents $\underline{j}_{c_A^-}$ for the plasma interaction with and without the Tvashtar plume in a cross section through the northern Alfvén wing in the plane perpendicular to $\underline{c}_A^-$ (Equation 4.12) at $z = 3\ R_{Io}$

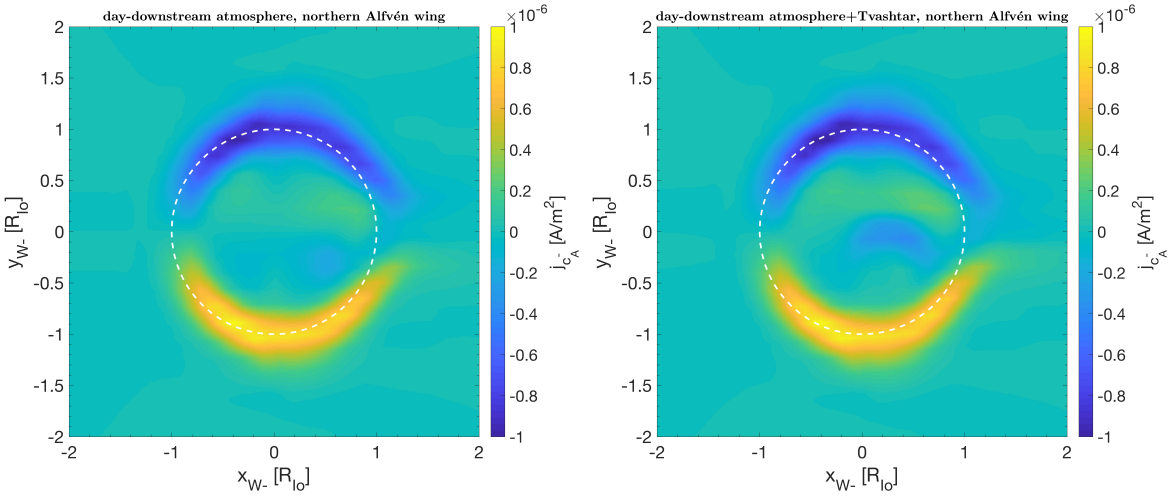

Figure 5.7. – Alfvénic current $j_{c_A^-}$ in A/m^2 in a cut through the northern Alfvén wing in a plane perpendicular to the northern Alfvén characteristic at $z = 3\ R_{Io}$. (a) Results for the global day-downstream atmosphere. (b) Results for the global day-downstream atmosphere in which a plume is included. In the wing coordinate system, the z_{W+} (z_{W-}) axis is parallel to the southern (northern) Alfvén characteristic, the $y_W\pm$ axis is the same as in the IPhiO-system and the $x_{W\pm}$ axis completes the right-handed coordinate system.

in the wing coordinate system. Most of the current $j_{c_A^-}$ is concentrated at the flanks of the northern Alfvén wing. We determine a total electric current in the northern Alfvén wing for the plasma interaction with Io's global atmosphere of $\sim 2.8 \times 10^6$ A ($\sim 3 \times 10^6$ A with Tvashtar and 2.8×10^6 A with Pele). This value is comparable to the electric current of 2.8×10^6 A deduced from Voyager magnetometer data by Acuna et al. (1981), but it is lower than the value derived by Saur et al. (1999) of 5×10^6 A. The values of the electric current are different because Saur et al. (1999) applied a higher electron number density ($n_e = 3.6 \times 10^3$ cm^{-3}) compared to the plasma density we use in our simulation and the plasma density measured during the Voyager encounter ($n_e = 2 \times 10^3$ cm^{-3}).

The plume introduces a second current system (see Section 5.1.1) which is visible in the parallel electric current at the flanks of the Alfvén winglet inside the northern Alfvén wing in Figure 5.7b. Unlike at Europa, the currents corresponding to the plume are much weaker than the currents corresponding to the global atmosphere (see Section 6.1.3).

5.1.5. Mass Loss at Io

The interaction between Io's atmosphere and the magnetospheric plasma leads to mass loss of about one ton per second which maintains the torus (Broadfoot et al., 1979). Most of this material is lost from Io in form of neutrals. These neutrals then orbit Jupiter forming large neutral clouds. Ejected neutrals are eventually ionized, mainly by electron impact. The newly created ions are picked up and accelerated to the corotational velocity supplying the Io plasma torus. One of the challenging problems is the understanding of

the effect of the magnetospheric torus plasma on Io's atmosphere and its feedback onto the torus.

We can distinguish between at least three different atmospheric escape processes: First, electron impact ionization which releases ions into the torus and the subsequent pickup of this particles by the corotating magnetic field. Second, atmospheric sputtering of neutrals at the exobase by corotating magnetospheric ions. And third, Jeans escape. While Jeans escape is thought to contribute to a small amount of atmospheric loss ($\sim$ 10%) (e.g., Pospieszalska and Johnson, 1996) the mass loading is assumed to account for about 20% of the material which escapes as ions (Saur et al., 2003). Here, mass loading or pickup refers to the ionization process of the neutrals. The dominant escape mechanism at Io seems to be atmospheric sputtering (e.g., Haff and Watson, 1979, Haff et al., 1981). The canonical value of one ton per second is therefore a value of the neutral loss rate. Observations of the Io plasma torus from the Voyager era and Cassini era suggest that the mass and energy flow through the torus can be highly variable (Delamere and Bagenal, 2003). Kumar (1984) concluded that direct escape from volcanoes is negligible in order to maintain the torus because he assumed the volcanic gas to come out of the ground with a maximum velocity of about 1.1 km s^{-1} (e.g., Johnson et al., 1979), which is much less than the escape velocity of $\sim$ 2.56 km s^{-1}. However, Tsuchiya et al. (2015) concluded from observations of the HISAKI extreme ultraviolet (EUV) spectroscope that volcanic activity on Io should cause a change of the supply rate. Furthermore, Brown and Bouchez (1997) inferred from 6-month-long observations of S^+ in the Io torus and Na in the extended neutral cloud that a large outburst of material from Io, which was most likely caused by the eruption of a volcanic plume, produced a transient increase in the neutral cloud and plasma torus masses. However, the response of the magnetosphere to the volcanic activity is still not fully understood. Variations in the supply rate are often connected to volcanic activity but the lack of continuous and long term observations of Io's volcanism, the plasma torus, and the activity of the magnetosphere makes a definite analysis of the observations complicated.

We calculate the overall production and loss rates by integrating the rates per unit volume over the whole simulation domain. These rates are given in units kg s^{-1} and are presented in Table 5.2 for different atmospheres. The ion mass loading rate and dissociative recombination rate per unit volume describe the rate of addition and loss of plasma mass per unit volume $Pm_{SO_2^+}$ and $Lm_{SO_2^+}$ (see Equation (3.14)), respectively. The rate of momentum transfer per unit volume $\rho\tilde{\nu}_{\mathsf{in}}$ (see Equation (3.15)), where induced dipole attraction and charge exchange are included, describes the neutral loss rate. We estimate the total amount of mass per second which is produced by impact ionization F_{imp} and lost due to recombination F_{rec} as well as the total elastic collision rate (or also called the total momentum transfer rate) $F_{\nu_{\mathsf{in}}}$. Note that the total elastic collision rate includes induced

Table 5.2. – Total Production and Loss Rates

	atmosphere		atmosphere+Tvashtar		atmosphere+Pele		Lit.[a]
	up	down	up/night	down/day	up/day	down/night	
F_{imp} $[kg/s]$	92	87	92	87	91	89	60
$F_{\nu_{\text{in}}}$ $[kg/s]$	5354	3308	5514	3421	5457	3518	5963
$F_{\text{atm. sput.}}$ $[kg/s]$	122	126	122	125	114	120	–
F_{rec} $[kg/s]$	33	25	34	26	33	27	20

[a]Values were adopted from Saur et al. (2003). For further information see text.

dipole attraction and charge exchange. Concerning the collisions, we estimate from our model that charge exchange is the dominant process and that induced dipole attraction contributes only by ∼10% to the total ion-neutral collision rate. The comparison of the rates for different atmospheres in Table 5.2 shows that the total rates of elastic collisions exceed the other rates by a factor >26. The rates are higher for an atmosphere which is concentrated on the upstream side (see also Figure 5.3). The day/night asymmetry in particular affects the collision rate $F_{\nu_{\text{in}}}$. $F_{\nu_{\text{in}}}$ is by a factor of 1.6 higher for an atmosphere which is concentrated on the upstream side than on the downstream side. This is a consequence of the plasma density which is mostly concentrated on the upstream side in our model (see Section 5.1.3) whereas the collision frequency linearly depends on the neutral number density and is therefore concentrated on the downstream side for a day-downstream atmosphere diminishing the momentum transfer on the upstream side.

We compare our calculated rates with the rates derived by Saur et al. (2003) in their figure 3. Note that they do not consider asymmetries in the atmosphere, so we take average values of the rates for a surface number density between 4×10^{14} m^{-3} and 2×10^{15} m^{-3}. In order to compare both models, we multiplied the rates of Saur et al. (2003) by $m_{SO_2^+} = 64$ amu since their rates are given in particles per second. They used an average torus electron density of 3.6×10^9 m^{-3} which is higher than our applied density of n_{th}=2.02×10^9 m^{-3} so we multiplied their rates with the factor $n_{\text{th}}/3.6 \times 10^9$ m^{-3} ≈ 0.56 according to Saur et al. (2003). The comparison between the values of Saur et al. (2003) and our calculated values in Table 5.2 shows that the total rates for dissociative recombination and electron impact ionization are by a factor of ∼1.5 higher calculated with our model than the values derived by Saur et al. (2003).

We estimated that a large volcanic plume such as the Tvashtar or Pele plume does not significantly change the mass loading rate compared to the atmosphere without plume. Therefore, we suggest that an eruption of a plume would unlikely modify the supply rate to the torus. Magnetospheric ions and locally produced pick-up ions impinge onto Io's atmosphere and transfer energy to the atmospheric molecules in energetic collisions. When plasma particles impinge onto the atmosphere, the charged particles introduce a series of energy transfer events resulting in heating and expansion of the atmospheric

corona and atmospheric loss. The expanded corona is then a larger target for the incident charged particles enhancing the pick-up and collisional processes. The complex feedback mechanism of the plasma-atmosphere interaction is explained in (Johnson, 1994). Furthermore, induced currents associated with Io's plasma interaction deflect the plasma flow and neutrals, which escape from the atmosphere and are ionized, can be accelerated back into the atmosphere (e.g. Zhang et al., 1993). Therefore, Io's plasma interaction determines the flux and energy of the ions penetrating Io's atmosphere (e.g. Johnson and McGrath, 1993). The atmospheric bombardment leads to loss of material from Io (McGrath and Johnson, 1987), which supplies the neutral Na cloud (Matson et al., 1974, Summers et al., 1983, Smyth and Combi, 1988a,b) and the plasma torus (e.g., Huang and Siscoe, 1987, Schneider et al., 1989, Thomas, 1992, Johnson and McGrath, 1993). The loss process has been called *atmospheric sputtering* (e.g. Haff and Watson, 1979, Johnson, 1990) and has been extensively studied at Io by, e.g., McGrath and Johnson (1987), Johnson (1994), Pospieszalska and Johnson (1996) with analytic and Monte Carlo approaches.

The collisional ejection of matter happens in a region of the atmosphere from which unhindered escape is possible, the exosphere, and its lower boundary, the exobase. In this region collisions are unlikely and neutral particles travel in ballistic trajectories. At the exobase, the Knudsen number K_n, which is the ratio between the mean free path l_c and the density length scale, is approximately one. The mean free path for collisions in a gas of randomly moving molecules is $l_c \approx 1/(\sqrt{2}\sigma_d n_n)$ where n_n is the molecular number density and σ_d the hard sphere cross section which is independent of energy and assumes isotropic scattering (Johnson et al., 2008). Atoms and molecules can be sputtered from the exobase if they possess sufficient energy through recoil collisions to overcome the gravitational attraction of the satellite (McGrath and Johnson, 1987).

Several processes for the ejection of sulfur and oxygen from Io to the torus have been studied, including direct volcanic outgasing, sputtering of surface material by the incident plasma, and atmospheric sputtering. Sputtering directly from the surface is expected to be insufficient to maintain the torus since only a small fraction of the sputtered material can escape Io's gravitational field (Haff et al., 1981, Cheng, 1984, Chrisey et al., 1987).

We apply our MHD model results to estimate the contribution of volcanic plumes on the injection of neutral material from atmospheric sputtering into the Jovian magnetosphere. We calculate the rates of neutrals which are produced near Io by charge exchange and direct collisional ejection. The atmosphere, which we use, is assumed to consist only of SO_2 molecules. Wong and Johnson (1995) have demonstrated that the SO_2 transport from the surface is rapid, so the region at the exobase is likely to be dominated by molecular species. In order to determine the rate from atmospheric

sputtering we proceed as follows: First we have to determine the height of the exobase of the atmosphere which we use in the simulation runs. Since our atmosphere is asymmetric, the height of the exobase varies with longitude and latitude. The exobase is defined as the height $h_{\text{exo}} = r_{\text{exo}} - R_{Io}$ where the probability for a molecule traveling upward with speed larger than the escape velocity is e^{-1} for escape without colliding with another particle (Strobel, 2002) and is given by

$$\text{Probability} = \exp\left(-\int_{r_{\text{exo}}}^{\infty} \mathrm{d}r\ \sigma_d\ n_n(r,\theta,\phi)\right) = e^{-1}\,. \tag{5.1}$$

We calculate the isosurface of the exobase by

$$\int_{r_{\text{exo}}}^{\infty} \mathrm{d}r\ n_n(r,\theta,\phi) = \frac{1}{\sigma_d} = N_{\text{exo}}\,. \tag{5.2}$$

Here we assumed that the molecules interact with each other by the constant momentum transfer cross section $\sigma_d = 1.67 \times 10^{-19}$ m^2 which is the inverse of the exospheric column density for SO_2, $N_{\text{exo}} = 6 \times 10^{18}$ m^{-2}, adopted from Pospieszalska and Johnson (1996). While the exobase in our simulation is located near the surface in the vicinity of the poles due to the thin atmosphere in these regions, the height of the exobase achieves its maximum value of $h_{\text{exo}} = 360$ km at the densest part at the equator where most of the atmospheric gas is concentrated ($h_{\text{exo}} = 190$ km at the thinnest part of the atmosphere at the equator). The position of the exobase is marked in the vertical dashed line in Figure 5.3. If a plume is included in the atmosphere, the exobase is located in a distance of about 230 km above the Tvashtar plume center at the surface ($\sim$300 km above Pele on the night side) and then falls off due to the decrease of the atmospheric density with horizontal distance from the plume center. The calculated maximum heights of the exobase are comparable to the values calculated in the work of Pospieszalska and Johnson (1996) ($r_{\text{exo}} = 1.13\ R_{Io}$) or used in Moore et al. (2011) (200–400 km). Afterwards we check at every position (r, θ, ϕ) in the volume between the exobase ($r = r_{\text{exo}}$) and $r = 6\ R_{Io}$ the direction of the velocity (v_r, v_θ, v_ϕ) in order to eliminate the collisions with trajectories that intersect the exobase. Similar to Saur et al. (1998) we assume purely head-on collisions, so that the molecules have the same velocities after the collisions as the ions before their collisions with the neutrals. With the assumed constraints for the collisions discussed above, the atmospheric sputtering rate is then calculated by

$$F_{\text{atm. sput.}} = \int_V \mathrm{d}V \tilde{\nu}_{\text{in}}\ \rho \tag{5.3}$$

and the values are presented in Table 5.2. Note that we use a very simplified method to calculate the atmospheric sputtering rate. We apply a static atmosphere consisting of SO_2 molecules. Io's atmospheric composition does not only consist of SO_2 molecules. Dols et al. (2008, 2012) discussed the consequences of the composition of the atmosphere on the plasma supply to the torus. They report that if the atmosphere

is purely atomic, the ions provided by the interaction close to Io contribute directly to the plasma and energy supply to the torus leading to different conclusions as for an SO_2 atmosphere. However, a totally realistic and self-consistent calculation of the total atmospheric sputtering rate is beyond the scope of this work.

The estimated rate from atmospheric sputtering correspond to about 120 kg/s. Taking into consideration both the total mass loading rate of about 90 kg/s and the total rate of ejected neutrals from the atmosphere, we get a contribution of about 20% of the canonical mass loading rate of 1 ton/s of mass in form of neutrals and ions. Most of the plasma production does not occur near Io, but could occur in the extended neutral clouds, as proposed, e.g., by Dols et al. (2008, 2012) and which are not described by our model here. The height of the exobase depends on the value of σ_d in our calculations. Note, that if we apply a smaller momentum transfer cross section of 0.25 σ_d the height of the exobase shifts to $\sim$210 km above the surface on the densest side of the atmosphere and the atmospheric sputtering rate enhances to about 1000 kg s^{-1} implying how sensitive the atmospheric sputtering rate is to h_{exo} in our calculation. However, the comparison between the rates with and without plume shows that the plumes contribute to a very small amount of about less than 7% ($\pm$8 kg s^{-1}) to total atmospheric sputtering rate as well as the day/night asymmetry of the atmosphere. Taking into account both, the negligible contribution of a plume to the total mass loading rate (F_{imp}, see Table 5.2) and the total atmospheric sputtering rate, we conclude that volcanic plume eruptions of, e.g., Tvashtar would not significantly change the supply rate to the plasma torus. Note that the ejected neutrals do not directly contribute to the mass of the torus since they only determine the momentum of the plasma. After their ejection out off the atmosphere they have to be ionized by electron impact ionization or photoionization in order to supply the plasma torus. So, the estimated 7% represent only an upper limit when assuming that all neutrals will be ionized after their ejection.

The comparison between the total collision rates F_{imp} and atmospheric sputtering rates $F_{\text{atm. sput.}}$ suggests that most of the ion-neutral collisions (about $>$96 %) occur in the close vicinity of Io below the exobase (see therefore also Figure 5.3).

5.1.6. Galileo Flyby I31

The Galileo flyby I31 provided the first close pass of the north polar region. The closest approach to Io was at a distance of 194 km above the surface near latitude 78° N and east longitude 188° (in the satellite planetocentric coordinates) at 04:59 UT on 6 August 2001. Io's sunlit side was principally directed along the wake and slightly turned toward Jupiter. Further properties of the flyby are presented in Table 5.1. The spacecraft trajectory passed directly over Tvashtar. Images and spectra showed that Tvashtar was probably not active at the time of the flyby (Perry et al., 2007). Nevertheless, regional observations of the Near-Infrared Mapping Spectrometer (NIMS) revealed a major new

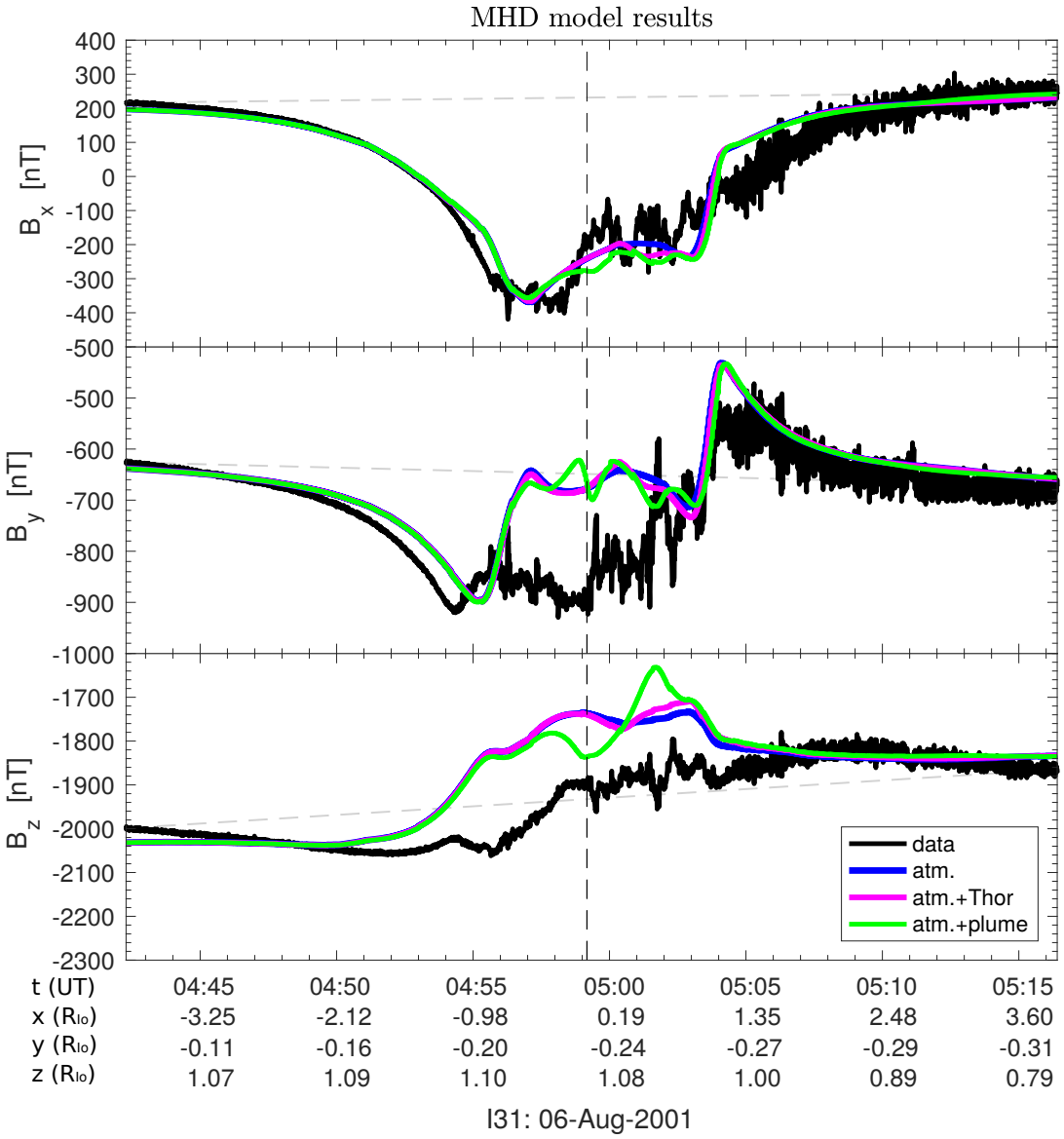

Figure 5.8. – Magnetic field components along the I31 flyby trajectory in the IPHIO coordinate system. Comparison between the Galileo MAG data (black lines) and the results obtained from the MHD model where different atmospheric configurations are considered: Latitudinally asymmetric atmosphere which is concentrated on the dayside (LT at 4.33 h) (blue line), and additional plumes at θ_{ap} =49° and ϕ_{ap} =226° (magenta line), and θ_{ap} =25° and ϕ_{ap} =226° (green line). The dashed vertical line displays the closest approach at 04:59 UT, x=0.0 R_{Io}, y=−0.24 R_{Io}, and z=1.08 R_{Io}. The dashed nearly horizontal line shows the background magnetic field.

eruption at a volcano named Thor (Lopes et al., 2004) and the Solid-State Imaging system (SSI) observations showed a 500 km tall plume over Thor (Turtle et al., 2004).

Khurana et al. (2002) concluded that some magnetic field perturbations observed in the Alfvén wing during I31 occur near locations of some well-known volcanoes.

We investigate the influence of the Thor plume on the magnetic field data which was

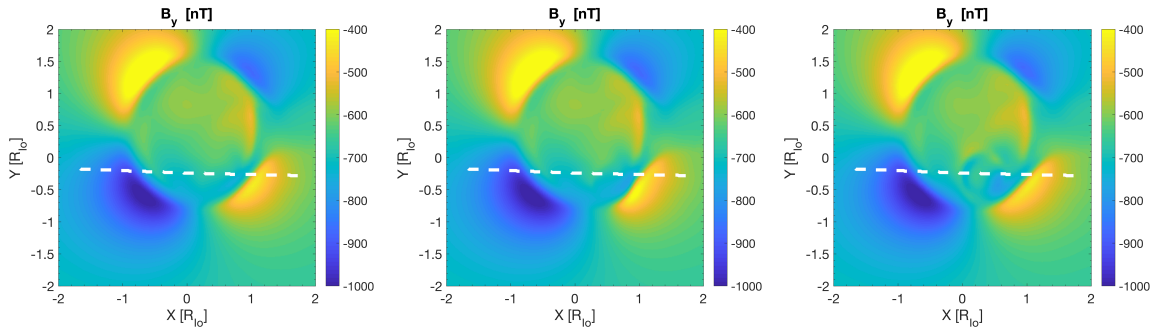

(a) Latitudinally and longitudinally asymmetric atmosphere (atm.)

(b) Latitudinally and longitudinally asymmetric atmosphere with the Thor plume (atm.+Thor)

(c) Latitudinally and longitudinally asymmetric atmosphere with a plume near Tvashtar (atm.+plume)

Figure 5.9. – Magnetic field components in the xy plane at $z = 1.08\ R_{Io}$ for three different MHD model runs with different atmospheric configurations (see Figure 5.8) during the I31 flyby. The dashed white line shows the trajectory of I31.

obtained along the trajectory of the I31 flyby. The MAG measurements are presented in the black line in Figure 5.8. The trajectory crossed the northern Alfvén wing which is visible in the large magnetic field perturbation in particular in the B_x component due to the bending of the wing. Since the spacecraft passed very close to Io, perturbations due to the ionospheric current system can also be present in the magnetic field data. The crossing occurred from about 04:54 UT to 05:04 UT. Inside this region a burst of intense wave emissions is clearly recognizable in the small-scale fluctuations on top of the main perturbations (Chust et al., 2005). Downstream from Io (at about 05:04 UT) strong ion cyclotron waves were seen (Russell et al., 2003). The blue, magenta, and green lines in Figure 5.8 show the MHD model results of the plasma interaction with Io's global atmosphere and additional plumes at two different locations. We did not investigate the effect of different global asymmetries in the atmosphere on the plasma interaction during I31. The MHD model results reproduce the general structure of the perturbation. The B_x component fits well the entry of the Alfvén wing at about 04:54 UT. The B_z component is overestimated by our models and the perturbation is shifted more to the upstream side of the trajectory. The B_y component shown in the blue line exhibits only weak perturbations ($\sim$30 nT) inside the Alfvén wing. The plume at the position of the Thor volcano (magenta line) only weakly affects the magnetic field components. The plume shifted nearer the northern pole (green line) shows small-scale fluctuations in particular in the B_y component (see also the cross section in Figure 5.9c). Due to the plume a weak Alfvén winglet inside the northern Alfvén wing forms which is visible in Figure 5.9c. A plume which is located near the northern pole generates stronger perturbations since it is embedded in a thinner ambient atmosphere as a plume which is located near the equatorial latitudes (see Section 5.1.1). The small-scale perturbations have similar amplitudes as the small-scale fluctuations generated by the intense wave

emissions, therefore, it is difficult to distinguish between the two kinds of fluctuations in the observed data.

5.2. MHD Modeling of the Galileo Flyby Scenarios

In this section, we present a study of the influence of an asymmetric atmosphere on Io's plasma environment during the Galileo spacecraft flybys: I24 and I27. The properties of the flybys are summarized in Table 5.1. The I24 and I27 flybys occurred near Io's equator when Io was in the low plasma density region in the Jovian plasma sheet, where induction signals are expected to be maximum and the plasma interaction to be minimum. Therefore these flyby are especially useful to recognize potential induced signals from a subsurface magma ocean as it was done by Khurana et al. (2011). Our goal is to investigate whether significant parts of the magnetic field perturbations, associated with the induction signals by Khurana et al. (2011) can alternatively be explained by considering global asymmetries of the atmosphere without induced fields from a subsurface magma ocean. We compare our simulation results with the high time resolution data of the magnetic field measured along the flyby trajectories. Through additional comparisons with the plasma density, ion average temperature, and flow velocity obtained by the Plasma Spectrometer (PLS) and Plasma Wave Science (PWS) instruments on board of the Galileo spacecraft, we test whether the simulations provide reliable and consistent results which agree with several independent in situ measurements. The magnetic field measurements were taken from the Planetary Data System archive (http://pds.nasa.gov/). The PWS electron density, PLS ion density, the average ion temperature and the velocity were visually taken from Gurnett et al. (2001) and Frank and Paterson (2000, 2001).

The most common method which is used to derive the electron density is based on the frequency of a thermally excited electrostatic emission at the upper hybrid resonance frequency measured by PWS (Gurnett et al., 2001). The PLS measures particle flux as functions of energy per charge and angle. The derivation of the ion density and the average ion temperature from PLS measurements is achieved by the computation of moments of the measured velocity distribution function (Frank et al., 1996). This calculation is a rough approximation because assumptions about the composition of the plasma, undersampling of the distribution function, and the charge of the spacecraft have to be made (Dols et al., 2012, Bagenal et al., 2016).

The flyby trajectories are displayed in Figure 5.10. The initial values and atmospheric properties of the flybys used in the MHD model are summarized in Tables 3.3 and 3.1 (denoted by "atm. model 1"–"atm. model 4"), respectively. Note, that induction in a subsurface magma ocean and plumes are not included in the following presented results of our MHD model. Finally, we will illuminate the differences of our MHD model

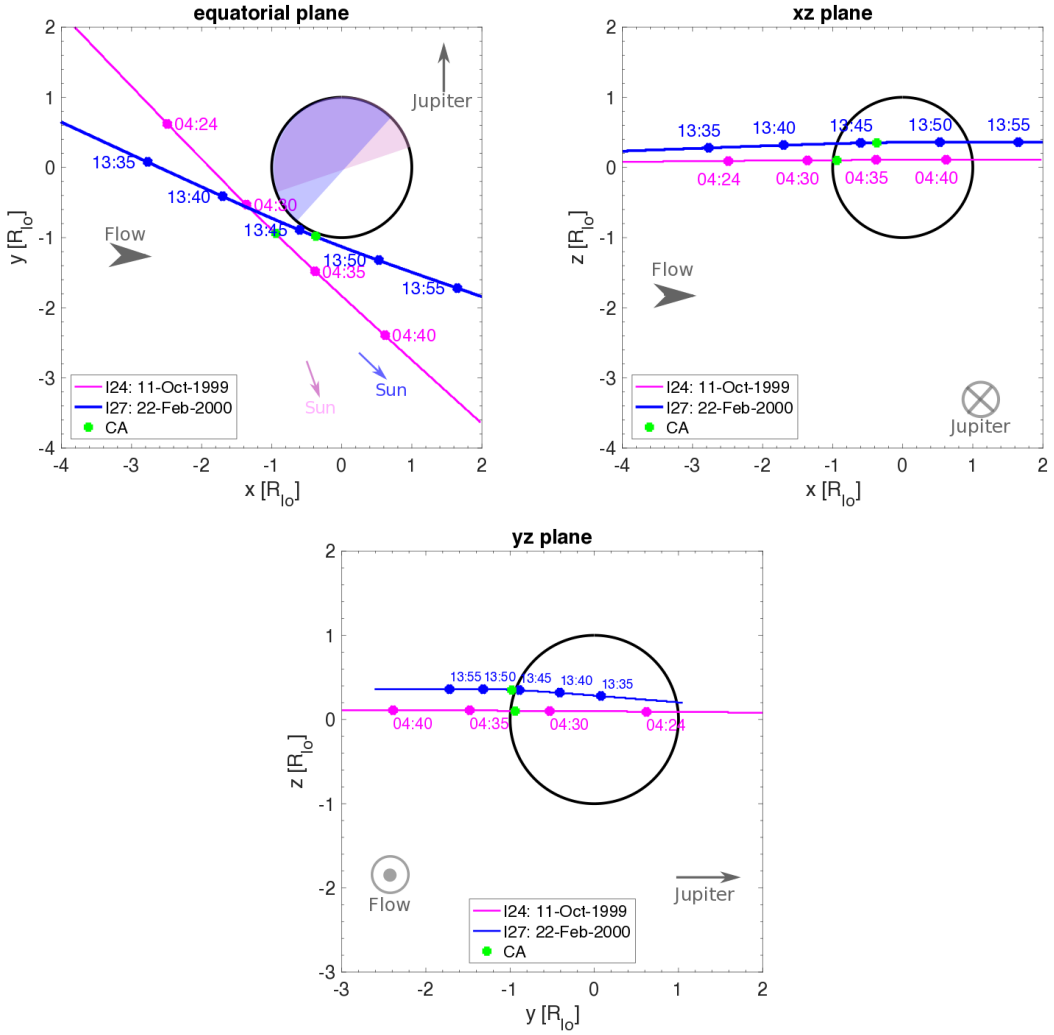

Figure 5.10. – Trajectories of the Galileo flybys I24 (magenta line) and I27 (blue line) in the IPhiO coordinate system in the xy (top left), xz (top right), and yz plane (bottom). The times (in UT) associated with the spacecraft's positions are labeled on the trajectories. The green point marks the position of the closest approach. In the equatorial plane the nightside during I24 is magenta shaded and the nightside during I27 is blue shaded.

and the model by Khurana et al. (2011) and discuss the possible consequences of these discrepancies on the model results of Io's plasma environment.

5.2.1. Io Flyby I24

During the flyby I24, Galileo passed Io on the upstream side close to the equatorial plane near the dawn terminator and then continued to the anti-Jovian side on Io's dayside (see Figure 5.10). The closest approach (CA) occurred at an altitude of 611 km at 04:33 UT. The measured PWS data suggest that Galileo did not pass Io's ionosphere since no density enhancements were detected during the flyby implying that the pass did not link directly to Io's ionosphere (Gurnett et al., 2001) .

5.2.1.1. Magnetic Field

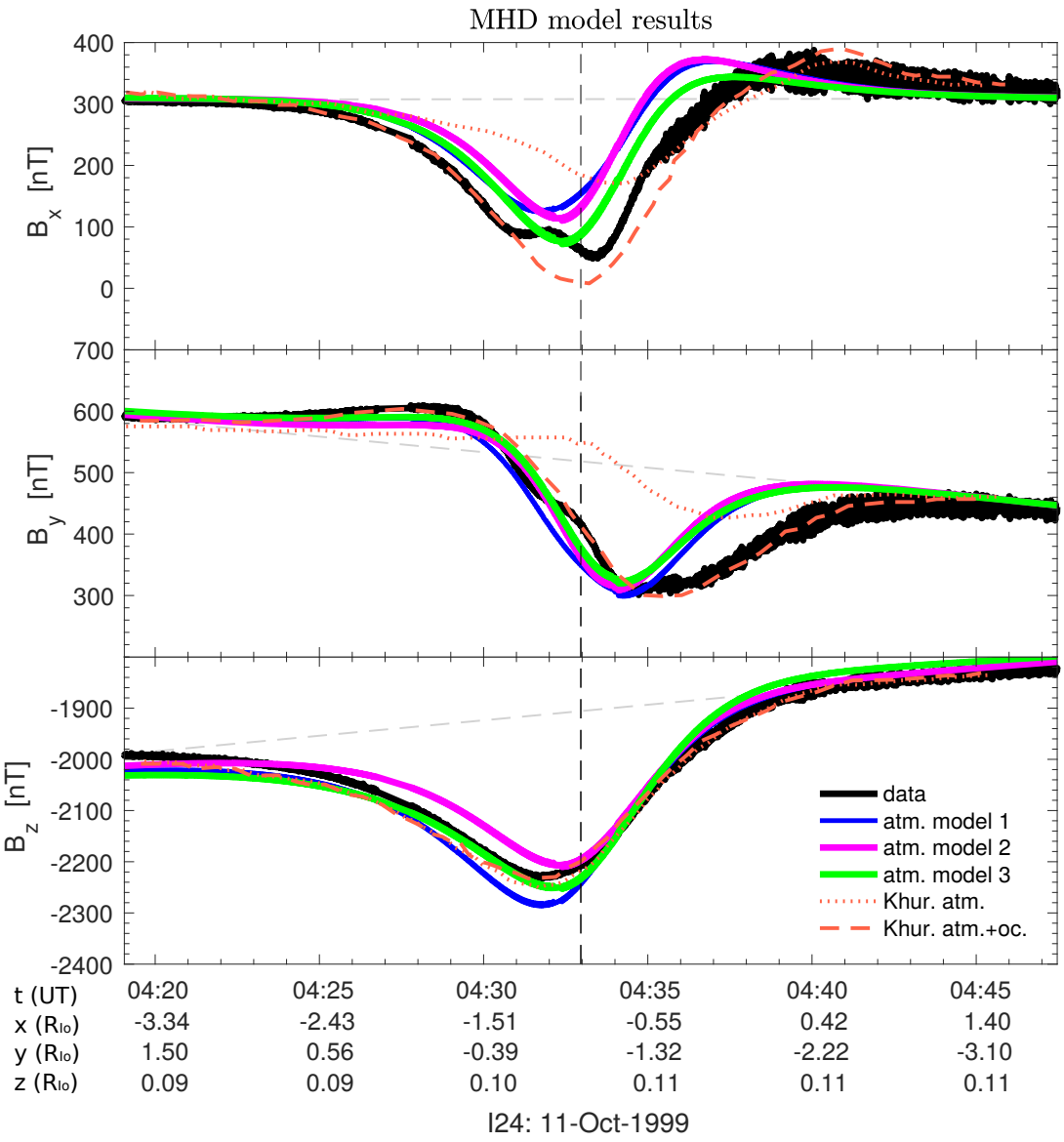

Figure 5.11. – Magnetic field components along the I24 flyby trajectory in the IPHIO coordinate system. Comparison between the Galileo MAG data (black lines) and the results obtained from the MHD model where different atmospheric configurations are considered: a latitudinally asymmetric atmosphere (atm. model 1, blue line), a latitudinally and longitudinally asymmetric atmosphere (atm. model 2, magenta line), and a latitudinally and longitudinally asymmetric atmosphere with an extended corona (atm. model 3, green line). The dashed vertical line displays the closest approach at 04:33 UT, $x = -0.94\ R_{Io}$, $y = -0.94\ R_{Io}$, and $z = 0.1\ R_{Io}$. The dashed nearly horizontal line shows the background magnetic field. The dashed and dotted orange lines represent the model results of Khurana et al. (2011) with and without a subsurface magma ocean, respectively. The data was visually taken from Khurana et al. (2011).

The magnetometer measurements for B_x, B_y, and B_z are shown in the black line

in Figure 5.11. Perturbations are present in all magnetic field components as the magnetic field is influenced by the ionospheric current system and its non-local response to Io's interaction. The strongest perturbations were measured near CA when the spacecraft passed the moon above the equatorial plane (at latitude 4.5° N, see Table 5.1). The main interaction region is confined to the upstream region in direction of the anti-Jovian flank for $y \leq 0\ R_{Io}$ and $x \leq 0\ R_{Io}$ (see equatorial plane in Figure 5.10). On the upstream side the ionospheric currents are mainly directed from the Jupiter facing side to the anti-Jupiter facing side, producing a perturbation in the negative z direction and in the negative x direction above the equator. This can be illustrated by applying the right-hand rule following the Ampère's law (see also Figure 2.4). Just outside the ionosphere, the magnetic field lines are frozen into the fluid and the plasma is diverted around Io in the region from the upstream side to the anti-Jovian flank of the pass producing a perturbation in the direction away from Jupiter in the B_y component.

With regard to the plasma flow the measured magnetic field perturbations can be interpreted as follows: The primary reason for the perturbation of the plasma and magnetic field is the slowdown of the plasma upstream of the moon by elastic collisions (in which charge exchange is included) and mass loading. Compressional perturbations propagate upstream away from Io in form of fast magnetosonic waves. The amplitudes of this perturbation fall off with the distance from Io. These perturbations decelerate and divert the incoming plasma flow around the ionosphere affecting the magnetic field lines which are frozen into the fluid. The draping and the bending of the northern Alfvén wing create the measured perturbations in the negative x and in the negative y direction, see Figure 2.5.

Small-scale fluctuations on top of the main perturbations are measured mainly in the region passing from 04:35 UT and could be due to kinetic effects such as SO^+ and SO_2^+ ion-cyclotron waves generated by pickup (Russell and Kivelson, 2000). Russell et al. (2003) showed that as Galileo moved to the downstream side of Io strong ion cyclotron waves arose. The position of the measured waves is consistent with the region of the small-scale fluctuations seen from 04:35 UT in the magnetic field components. We will not go further into detail concerning the kinetic effects because they are not subject of this thesis. Further information about the plasma interaction measured during the I24 and I27 passes can be found in Russell and Kivelson (2000), Kivelson et al. (2001a) and Saur et al. (2004).

In interpreting the data from the I24 flyby, we ran several cases by representing different configurations of Io's atmosphere. We varied the parameters such as the atmospheric surface number density and the atmospheric scale height. In order to adjust the maximum column density of our model atmosphere, we focused on the fit of our model results with the measured B_z profile and the measured PWS electron density

profile (discussed in the following Section). In Figure 5.11 we illustrate the modeled magnetic field components for three different atmospheric configurations displayed in the blue, magenta and green lines. The results of the plasma interaction with different atmospheres reproduce well the overall magnetic field data structure.

Considering the B_x component, our model results of the three atmospheric scenarios underestimate the width of the perturbation region. We tested different neutral densities in our simulations. According to our model results, the atmosphere is dilute, i.e. the vertical column density is about 2×10^{19} m^{-2} (atm. model 3), on the upstream side during this flyby. Although we can fit better the B_x component with a denser atmosphere, the amplitude of the perturbation in B_z then becomes too large. The results of the interaction with an atmospheric model with a corona (atm. model 3, green line) provide a wider extent and a larger amplitude of the perturbation region in B_x than the atmospheres without corona (atm. model 1 and 2, blue and magenta lines). The comparison between the results of the models with a latitudinally asymmetric atmosphere (atm. model 1, blue line) and with additional longitudinal atmospheric asymmetries (atm. model 2, magenta line) shows that the different longitudinal atmospheric asymmetries shift the dip of the B_x component closer to the closest approach, i.e., in direction of the anti-Jovian flank. This is a consequence of the shifted maximum of the neutral density to the subsolar point in our model.

The modeled B_y components in all three models reproduce well the entry into the interaction region but return faster (from about 04:36 UT) to its unperturbed state than the measured B_y component (see also Figure B.2 middle) . The B_z component is fitted by all three models though the model with a latitudinally asymmetric atmosphere slightly overestimates the measured B_z component by $\sim$60 nT.

According to our model results, we suggest an atmosphere with a maximum column density of 6.6×10^{19} m^{-2}. This value is smaller than the expected values for the mean vertical column density of (1-5)$\times10^{20}$ m^{-2} on Io's dayside (Lellouch et al., 2007) obtained from observations. The reason might be that the spacecraft has probably probed only Io's nightside atmosphere where the atmosphere has collapsed (see subsequent Section). By testing different scenarios for the upstream conditions of the plasma such as the electron density, the ion charge state, the velocity, the mass of the newly created plasma, and the temperature, we found that the magnetic field during I24 is sensitive to the properties of the incident plasma because it influences the plasma interaction strength (see Section 5.2.4). For example a smaller electron temperature results in a smaller production rate and hence in a decrease of the interaction strength. Then a higher atmospheric density would be required to fit the data.

Considering the results from the model of Khurana et al. (2011) displayed in the

dashed and dotted orange lines, almost all the B_y and B_x perturbations during I24 can be explained by the induced dipole from a subsurface magma ocean (see also the pure induction signal from the magma ocean shown in Figure B.1). The induction signal does not perturb the B_z component since the dipole is almost in the equatorial plane. In comparing the different simulation cases with the model results from Khurana et al. (2011) for the plasma interaction without a magma ocean shown in the dotted orange line, the most important discrepancy is that the amplitudes of the transverse components (B_x and B_y) are smaller than in our model and shifted more to the right, i.e., in direction of the anti-Jupiter flank. The transverse perturbations in our model are confined more to the upstream region of Io as it is also visible in the cross section in Figure B.2. The discrepancies can be attributed to the differences in the models which will be discussed in Section 5.2.3. Khurana et al. (2011) concluded from their model results that a subsurface magma ocean is necessary to explain the observed data. However, the interpretation of the observations is ambiguous. Considering our model results with the expected induction signal from a conductive subsurface magma ocean (see Figure B.1), the induced signals would overestimate the perturbations of the transverse components in our model and therefore we suggest that a subsurface magma ocean is not absolutely essential to explain the data.

5.2.1.2. Plasma Density, Ion Temperature, and Velocity Field

The Figures 5.12 (top) and 5.13 (top) show the ion density profile derived from PLS measurements (dashed blue line) and the electron density profile derived from PWS measurements (dashed red line) along the trajectory of I24. The observed PWS data show a flat electron density profile reported by Gurnett et al. (2001) implying that the Galileo spacecraft did not pass through Io's ionosphere. Because Galileo missed Io's atmosphere at an altitude of about 600 km, it can be concluded that the upstream atmosphere is compressed to the surface as it was suggested by Saur et al. (2002) probably due to the drag force of the torus plasma on the neutral atmosphere. This conclusion is also supported by the interpretation of the magnetic field observations from the previous Section. The PLS profile shows small perturbations of the ion density at the closest approach with a maximum of about 1200 cm^{-3}. In order to compare the PLS ion densities and the PWS electron densities we have to multiply the PLS ion densities with the charge state of the torus plasma. This charge state may vary between the different Galileo flybys (Delamere and Bagenal, 2003). It is not clear why the ion density shows an enhancement at the closest approach while the electron density does not show any signatures. The differences in the PLS and PWS profiles may be caused by inferences of ion charge states and plasma velocities associated with the data analysis (Saur et al., 2002).

In the solid blue line in Figures 5.12 (top) and 5.13 (top), we present the electron densities calculated with the MHD model with two different atmospheric models: a

latitudinally and longitudinally asymmetric atmosphere (atm. model 2) and additional corona (atm. model 3), respectively. While the plasma interaction with the asymmetric atmosphere shows no variations of the electron density, the results calculated with an atmosphere model in which a corona is included show a modest enhancement along the I24 trajectory by a factor of $\sim$1.8 at the closest approach. The model results with a corona indicate that the trajectory slightly crosses Io's ionosphere in this model scenario.

As seen in the equatorial plane in Figure 5.10 the spacecraft approaches Io on the nightside and is on the dayside when approaching the closest approach. Due to thermal inertia the peak of the atmospheric density might be lagging (Moore et al., 2009). With a possible collapse of the atmosphere on the nightside (Tsang et al., 2016) and the lag of the atmospheric density, the spacecraft has probably probed only Io's nightside atmosphere implying that the atmosphere had a smaller atmospheric density than on the dayside (factor $\sim$ 5 difference (Tsang et al., 2016)) during the measurements. Although the atmospheric model with a corona provides better results for the magnetic field perturbations (see Figure 5.11) it has an effect on the plasma density resulting in an enhancement of the density which is not seen in the PWS measurements (but in the PLS measurements).

The observed ion temperature presented in the blue dashed line in Figures 5.12 (middle) and 5.13 (middle) shows variations between 50 eV and 100 eV. The temperature deduced from PLS observations shows a decrease at the closest approach where an increase is observable in the PLS inferred ion density. Contradictory to the PWS electron density observations, the decrease of the ion temperature probably indicates the presence of mass loading processes. The results from the model with a latitudinally and longitudinally asymmetric atmosphere show nearly a flat temperature profile (see Figure 5.12) while the results from the model with a dilute corona in Figure 5.13 show an enhancement of the temperature when approaching Io's anti-Jovian side due to plasma interaction processes with the extended corona.

The ion velocity field shown in Figures 5.12 (bottom) and 5.13 (bottom) is perturbed due to the diversion of the plasma flow around Io. The non-local response of the ionospheric current system perturbs the velocity far upstream of Io with a slowdown of the flow upstream of the moon and an acceleration of the flow at the anti-Jovian flank (from about 04:35 UT) by $\sim$30% relative to the flow speed for rigid corotation. Both models can reproduce the general perturbation structure. However, the model scenario without the dilute and extended corona provides a better fit to the decrease in v_y and with the profile of v_z (see Figure 5.12 (bottom)).

In summary, by comparing both, the MAG and plasma measurements, with our model results, the atmosphere during this flyby can be interpreted as dilute (maximum

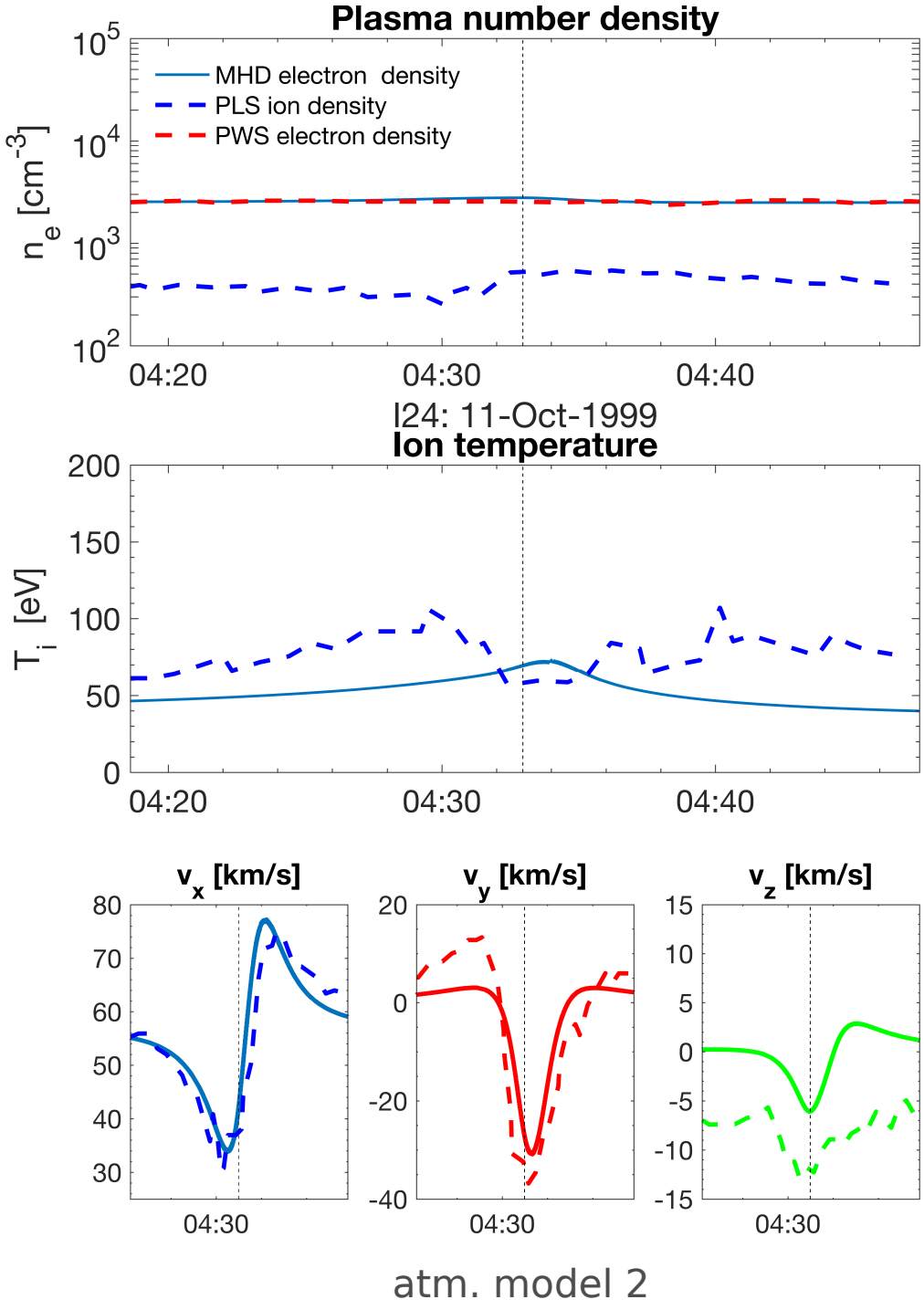

Figure 5.12. – (Top) PWS electron density (red dashed line) and PLS ion density (blue dashed line) measurements compared to the MHD model results of the plasma interaction with a latitudinally and longitudinally asymmetric atmosphere (atm. model 2, blue solid line) along the I24 trajectory. (Middle) The PLS inferred ion temperature (blue dashed line) compared to the model results (blue solid line). (Bottom) PLS inferred ion velocity components (dashed lines) compared to the model results (solid lines). The dashed vertical line marks the position of the closest approach.

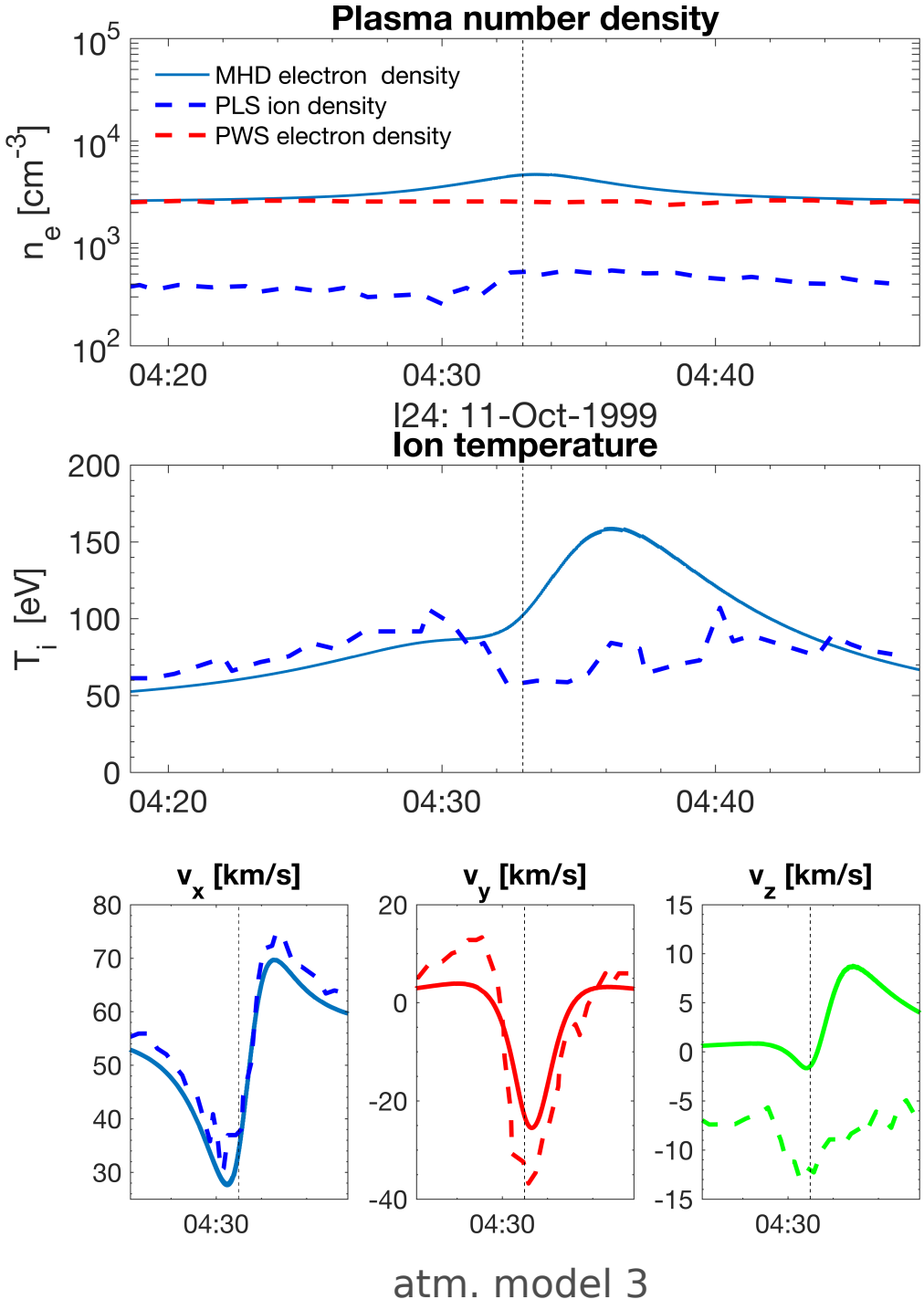

Figure 5.13. – Same as Figure 5.12 modeled with a latitudinally and longitudinally asymmetric atmosphere (atm. model 3).

column density of 6.6×10^{19} m^{-2}) with a scale height less than 100 km on the upstream side. On the downstream side the atmosphere might be denser and might have a large extent so that the wide range of the perturbed B_x component can be explained. We suggest that the longitudinal atmospheric asymmetry is much stronger with a variable

scale height than the one assumed here with a constant scale height. Variations of the conditions of the upstream magnetospheric plasma during the flyby could also lead to the modification of the plasma variables. The lack of consistency between PLS and PWS data makes a conclusive interpretation of the plasma data difficult.

5.2.2. Io Flyby I27

The trajectory of the flyby is similar to I24 (see Figure 5.10). The spacecraft approaches Io on the upstream side above the equatorial plane and then goes in direction toward the anti-Jupiter flank where it reaches its closest approach at an altitude of about 200 km at 13:46 UT.

5.2.2.1. Magnetic Field

The magnetometer measurements for B_x, B_y, and B_z along the I27 trajectory are shown in the black line in Figure 5.14. During the I27 pass, Io was exposed to similar background magnetic field variations as during the I24 pass (see Figure 5.10). Thus analogues arguments for the interpretation of the magnetic field and velocity field can be used. The main differences between the two flybys are the stronger perturbation in the negative x direction (-670 nT compared to 50 nT during I24), the smaller perturbation in B_y, the change of the orientation of the perturbations of the B_z component, and the stronger influence of small-scale fluctuations on top of the main perturbations in the interaction region. Additionally, the PWS and PLS data show a strong increase in the plasma density during I27 inferring that the pass crossed Io's ionosphere (see below). Therefore the frozen-in field description cannot be used here.

Between 13:45 UT and 13:48 UT transverse MHD waves are identifiable in the small scale perturbations mainly in the B_x and B_y component (Kivelson et al., 2001a). The location of these waves is correlated with the region of high plasma density (see next Section) and can be explained by the crossing of the boundary of the Io flux tube by the spacecraft. The B_x component is determined by the ionospheric current flowing from the sub-Jovian to the anti-Jovian hemisphere on the upstream side and the Alfvén wing current which couples to the ionospheric current and flows parallel to the magnetic field away from Io on the anti-Jovian side. Before entering the Io flux tube, B_x decreases from $\sim$280 nT to ~ -340 nT due to the diversion of the plasma flow upstream of the moon controlled by the ionospheric conductivity. Inside the flux tube the B_x component experiences a further decrease to about -670 nT directly at the anti Jovian flank, where the ionospheric currents couple to the Alfvén wing currents and are expected to be at maximum. Kivelson et al. (2001a) suggest that the stronger decrease of B_x inside the flux tube could be attributed to pickup. Such a decrease in B_x requires unreasonably large Mach numbers and can not be attributed only to the bending of the Alfvén wing.

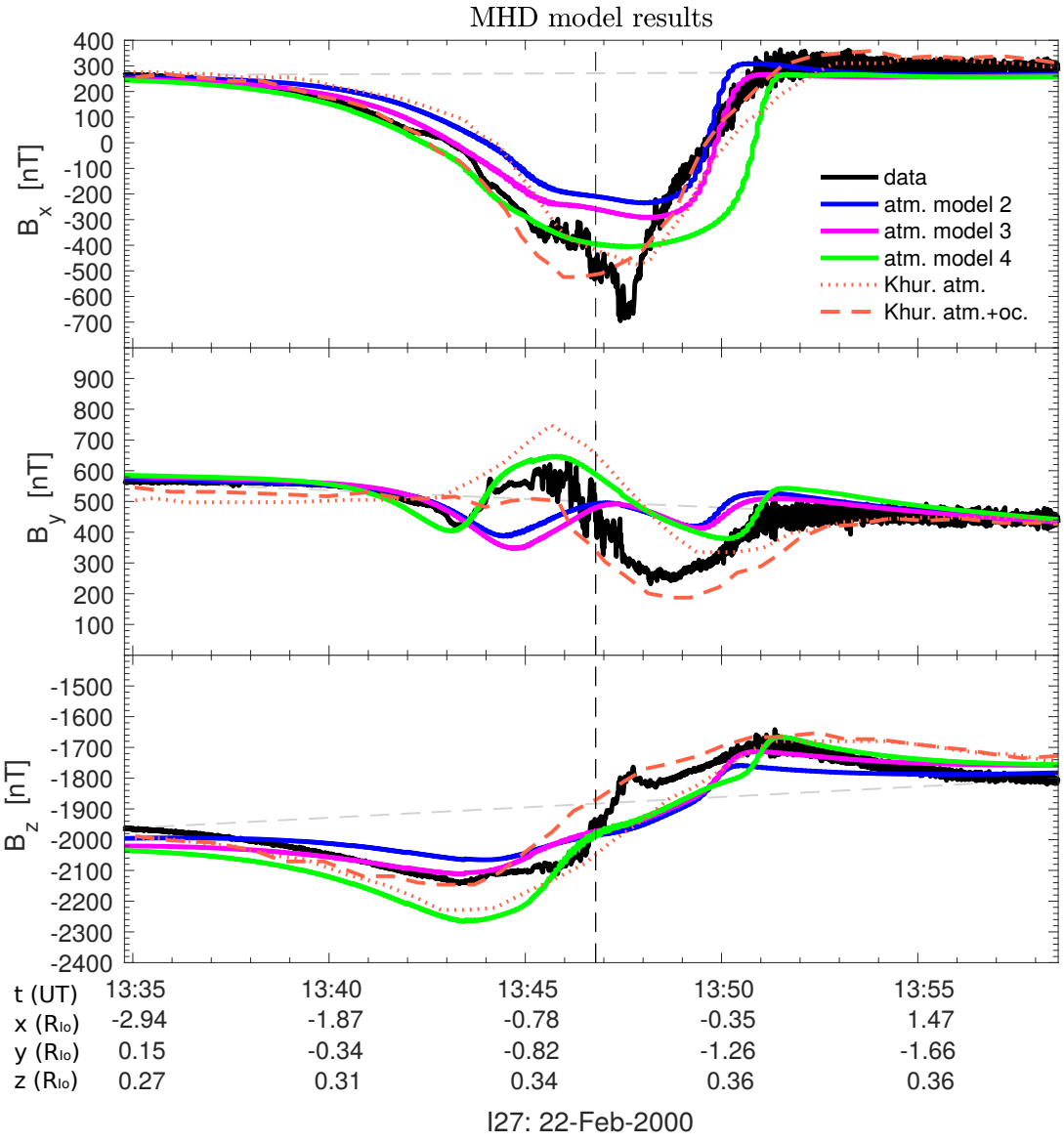

Figure 5.14. – Magnetic field components along the I27 flyby trajectory in the IPHIO coordinate system. Comparison between the Galileo MAG data (black lines) and the results obtained from the MHD model where different atmospheric configurations are considered: Latitudinally and longitudinally asymmetric atmospheres (blue and green lines) and additional corona (magenta line), see Table 3.1. The dashed vertical line displays the closest approach at 13:47 UT, $x = -0.37\ R_{Io}$, $y = -0.98\ R_{Io}$, and $z = 0.35\ R_{Io}$. The dashed nearly horizontal line shows the background magnetic field. The dashed and dotted orange lines represent the model results of Khurana et al. (2011) with and without a subsurface magma ocean, respectively. The data was visually taken from Khurana et al. (2011).

The perturbation in the B_y component is a consequence of the diversion of the flow around the moon in direction downstream to the flanks. At the closest approach the B_y component shows almost no disturbances as expected within the ionosphere. The perturbation of the B_z component changes its sign along the trajectory of the flyby ap-

proximately at the closest approach and is attributed to the ionospheric currents flowing from the sub-Jovian to the anti-Jovian hemisphere on the upstream and downstream sides.

Model results of the magnetic field components are shown in the blue, magenta, and green lines in Figure 5.14 for thee different atmospheric scenarios. Different atmospheric configurations lead to different variations in the magnetic field components implying that the magnetic field is sensitive to the atmospheric configuration along the I27 trajectory (see also Figure B.4). However, all three models fit the general structure of the observed magnetic field. Our model results do not match the dip of the B_x component between 13:47 UT and 13:48 UT. The model results show that the denser the atmosphere is the stronger is the perturbation in the B_x component with the strongest perturbation in atm. model 4 (green line). However, applying large atmospheric densities it was not possible to reproduce the deep dip at the closest approach with our model. Probably the model lacks some effects, such as the influence of high energetic electrons, to describe this perturbation. Mauk et al. (2001) report that a hint of a weak field-aligned intensity enhancement was observed during the I27 flank encounter. Electron beams provide a source of ionization which might determine the ionospheric currents and the magnetic field. The influence of the beams cannot be modeled with our model.

The model results shown in the green line can reproduce the B_x and B_y perturbations until the entry into the Io flux tube (13:47 UT) but the B_x component of atm. model 4 shows a too wide range of the perturbation region and is not in agreement at the exit of the flux tube (13:48 UT). Considering the results with atm. model 2 and 3, the B_x components show an agreement with the data in the region of the exit of the flux tube. The results indicate a further asymmetry in the atmosphere which was not considered in our model. The main difference between model 2 and 4 is the scale height and the neutral density. The model results point to a varying scale height along the trajectory of I27 with a smaller scale height on the anti-Jupiter side. We note that the atmosphere models with small surface densities (less than 2.5×10^{14} m^{-3}) which were used to match the data during I24 (atm. model 2 and atm. model 3) produce weak perturbations in all three magnetic field components during I27. The thin corona (atm. model 3, magenta line) has only a weak influence on the magnetic field compared to the model without the corona (atm. model 2, blue line) and does not improve the fit. The spacecraft might have probed Io's dayside atmosphere during its flyby and therefore a denser atmosphere compared to the one during I24 is required to generate the observed magnetic field perturbations.

The main difference between the three models in the B_y component is the position of the change of slope which occurred at 13:43:30 UT in the measured magnetic field. The change of slope indicates the position when the trajectory moves into a region

in which the interaction directly with Io dominates the signature (Kivelson et al., 2001a). This position is shifted to later times (around 13:45 UT), i.e., closer to the moon, for atm. model 2 and 3 in which the atmosphere is confined closer to the surface than in atm. model 4. The better fit in B_y near the entry into the Io flux tube for atm. model 4 indicates an atmosphere with a higher scale height at the entry than at the exit of the flux tube which is surprising because Io was probably on the nightside at that time. The dip in the B_y component at the exit of the flux tube (at $\sim$13:48 UT) occurred when the spacecraft was at Io's anti-Jovian flank and almost coincide with the dip in the B_x component. Similar to the dip in B_x, none of our models is able to reproduce the dip.

Induction signals from a subsurface magma ocean would in particular affect the B_y component along the trajectory of I27 (see Figure B.3). Considering the results with and without an ocean from Khurana et al. (2011) displayed in the dashed and dotted orange lines in Figure 5.14 suggest that both models are in good agreement with the measured perturbations. The measured perturbations of the B_y component lie between the model results without an ocean (dotted orange line) and with an ocean (dashed orange line). Thus we think that a definite conclusion about the existence of a magma ocean from the results of Khurana et al. (2011) can not be made during the I27 flyby. Considering our model results, additional induction signals from a magma ocean would overestimate the amplitudes of the calculated, perturbed magnetic field components.

5.2.2.2. Plasma Density, Ion Temperature, and Velocity Field

Gurnett et al. (2001) report a large density enhancement by more than a factor ten on the anti-Jovian flank and abrupt step-like changes at the outer boundaries of the region of enhanced electron density which occur as the spacecraft penetrated the boundary of the flux tube. The enhanced electron density inside the flux tube is associated with magnetic field lines that are directly linked to Io by the high conductivity of its atmosphere thereby enhancing the escape of plasma along the magnetic field lines that pass through Io's ionosphere (Gurnett et al., 2001). The electron density is shown in the dashed red line in Figures 5.15 (top) and 5.16 (top). The peak electron density of 6.8 $\times$ 10^4 cm^{-3} is much larger than during I24 (0.27 $\times$ 10^4 cm^{-3}) but is comparable with the downstream peak density during flyby I0 which occurred farther away from Io (CA at an altitude of about 900 km) than I24. The abrupt step-like density discontinuities are not consistent with an exponential radial density distribution (Gurnett et al., 2001). The comparison of the observed electron densities (PWS) during different Io flybys shows that there is no logical dependence between the densities and the radial distance as well as solar zenith angle, implying a mobile complex ionosphere (see Gurnett et al., 2001). Furthermore, Mauk et al. (2001) report a strong decrease in electron intensities measured by the Energetic Particle Detector (EPD) instrument that coincides with the region of high density measured by the PWS instrument. The reasons for the region depleted of energetic electrons could be collisions with the increasingly dense plasma when getting

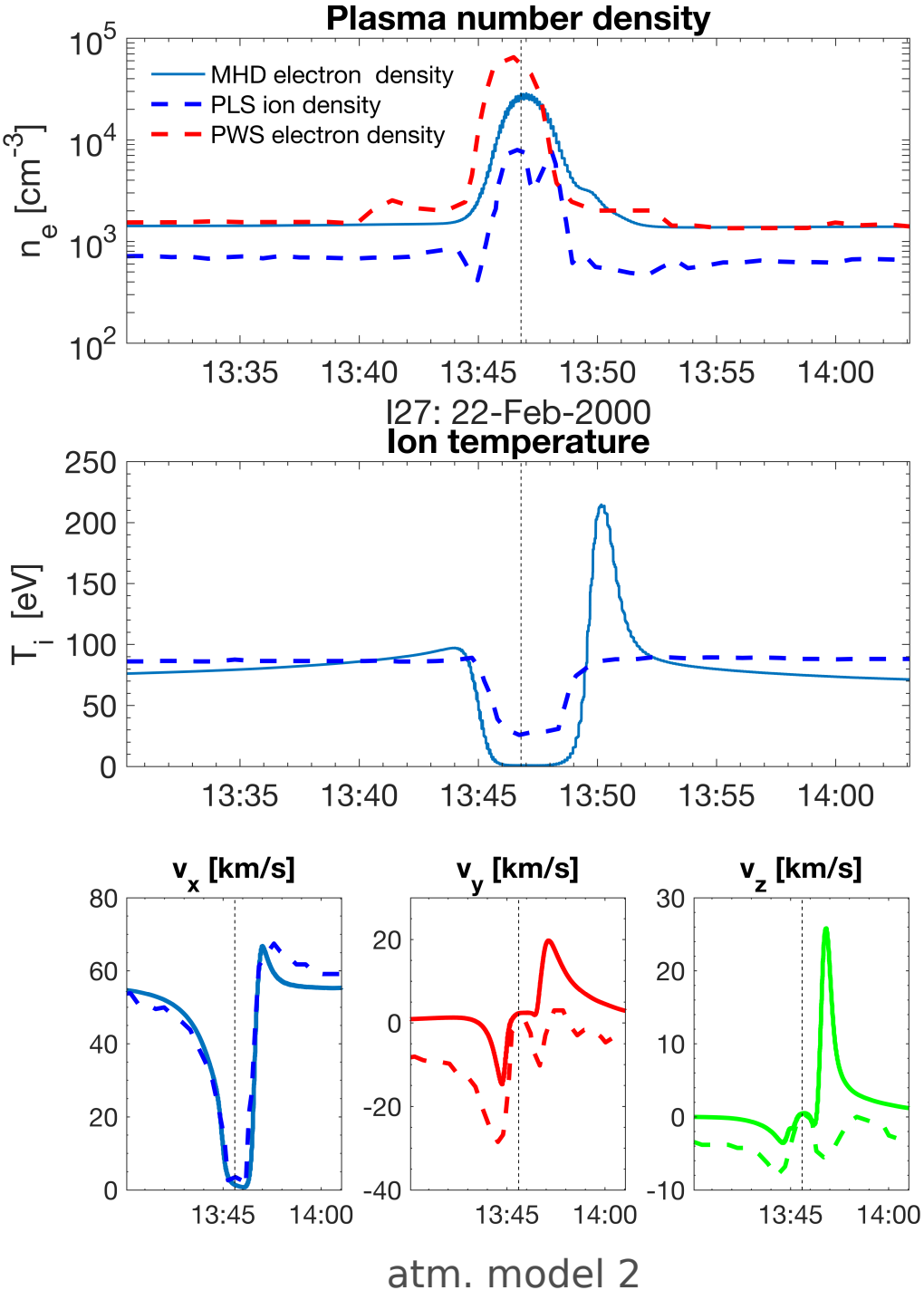

Figure 5.15. – (Top) PWS electron density (red dashed line) and PLS ion density (blue dashed line) measurements compared to the MHD model results of the plasma interaction with a latitudinally and longitudinally asymmetric atmosphere (atm. model 2, blue solid line) along the I27 trajectory. (Middle) The PLS inferred ion temperature (blue dashed line) compared to the model results (blue solid line). (Bottom) PLS inferred ion velocity components (dashed lines) compared to the model results (solid lines). The dashed vertical line marks the position of the closest approach.

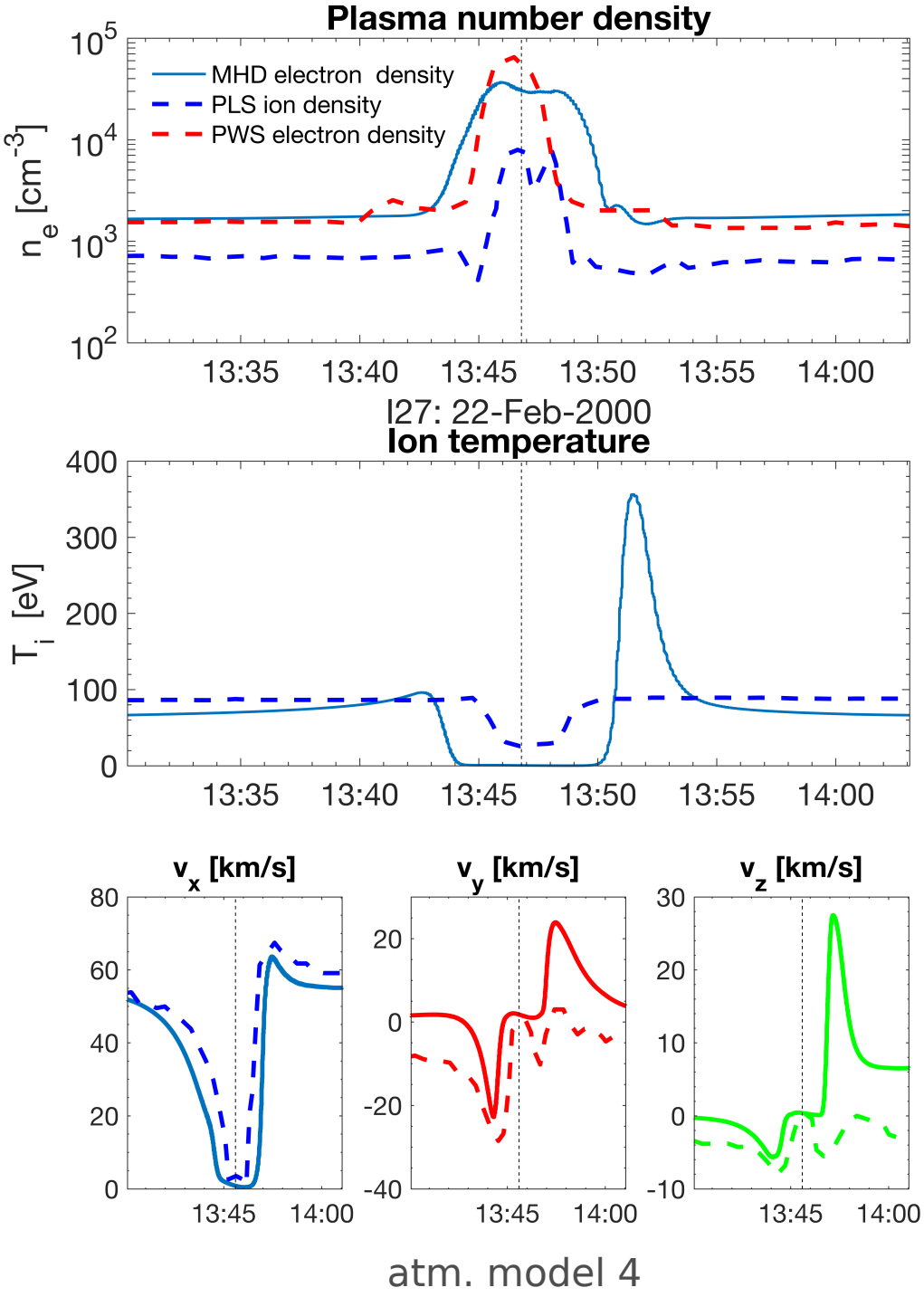

Figure 5.16. – Same as Figure 5.15 modeled with a latitudinally and longitudinally asymmetric atmosphere (atm. model 4).

closer to the moon or due to shadowing effects because Galileo probably moved onto magnetic field lines that were connected directly to either Io or Io's atmosphere (Mauk et al., 2001).

The pickup density depends on the time that a flux tube, which is directly connected to Io's ionosphere, passes in the atmosphere. Between 13:45 UT and 13:48 UT the PLS instrument observed a plasma velocity nearly at rest with respect to Io ($\sim$2 km/s) and a low ion temperature of $\sim$30 eV as shown in Figures 5.15 and 5.16. The plasma inside the flux tube is isolated from the plasma outside the flux tube which is frozen into the corotating magnetic field lines. Due to the low plasma velocity, the plasma density increases via pickup (Hill and Pontius, 1998) inside the flux tube because more time is provided for the plasma diffusion upward out of the ionosphere (Gurnett et al., 2001). Impact ionization of the energetic electrons could also be a reason for the enhancement of the density. The PLS data presented by Frank and Paterson (2001) show a similar density enhancement at the anti-Jovian flank displayed in the blue dashed line in Figures 5.15 (top) and 5.16 (top).

In the solid lines in Figures 5.15 and 5.16 we display the model results for the electron number density, the average ion temperature and the velocity field for the plasma interaction with two different latitudinally and longitudinally asymmetric atmospheres (atm. model 2 and atm. model 4). An obvious discrepancy between the two models is the width of the perturbation region which is bigger in atm. model 4 due to the more extended atmosphere and does not match the observed width of the interaction region. The electron density reaches a lower maximum of about 3×10^4 cm^{-3} than observed.

Another striking feature of our model results is the abrupt strong enhancement of the ion temperature at the exit of the flux tube. The enhancement is stronger for the denser atmosphere (atm. model 4). Inside Io's ionosphere the plasma is strongly cooled down (about 0.3 eV) and remains cold as it is convected downstream (see solid blue lines in Figures 5.15 (middle) and 5.16 (middle)). While the deep dip in the ion temperature at the closest approach indicates pickup at a very slow flow velocity close to Io, the abrupt enhancement at the outbound edge is probably due to concentration of newly created ions which are picked up along the stream line intersecting the trajectory in our model. These considerations are not consistent with the measured ion temperature which shows a flat profile at the outbound edge indicating little ionization or charge exchange. Dols et al. (2012) extensively discussed the surprising profile of the ion temperature during I27 and propose for the possible causes for this discrepancy the time variability of Io's volcanic activity with an almost disappearing atmosphere on the anti-Jovian flank or the inaccuracy of the data analysis. The interpretation of a dilute atmosphere at the outbound leg is also supported by our magnetic field model results (see Section 5.2.2.1). Similar to the peak of the ion temperature, the v_z component also provides a strong enhancement at the outbound leg.

The picture that can be drawn for Io's atmosphere during I27 from the comparison

of the measurements (MAG, PLS, and PWS) with our model results is that the atmospheric density was higher during this pass than during I24. The atmosphere was denser on the upstream side than on the anti-Jovian flank which is not consistent with the dependence of the atmospheric density on the dayside and nightside hemisphere. Moreover, a dilute atmospheric corona as assumed in our model is not in agreement with the measured width of the interaction region.

5.2.3. Comparison between the MHD Model of Khurana et al. (2011) and our MHD Model

We demonstrated that the perturbations modeled by Khurana et al. (2011) have generally smaller amplitudes in B_x and B_y during I24 than our modeled magnetic field perturbations (see Figure 5.11). The discrepancies in the magnetic field components between the results of the MHD model by Khurana et al. (2011) and ours are crucial for the conclusion about the existence of a subsurface magma ocean and may have different reasons. Here we outline several differences between both models and the consequences of these differences on the plasma interaction.

An important difference of the models is the description of the atmosphere. Khurana et al. (2011) apply a latitudinally asymmetric, binary scale-height atmosphere which is confined largely to within 40° of the equator and follows a power law fall off at large distances (see supplementary materials of Khurana et al., 2011). A striking feature of their atmosphere model is the very low surface number density of $\sim$3.6$\times10^{13}$ m^{-3} at the equator resulting in a low equatorial column density of $\sim$1.6$\times10^{19}$ m^{-2}. The small column density of $\sim$1.6$\times10^{19}$ m^{-2} is only a lower limit for the column density which is expected for Io's atmosphere on the nightside and was rarely concluded from the observations. For example from the recent observations from the Gemini North telescope, Tsang et al. (2016) concluded an atmospheric column density of $\sim$5$\times10^{19}$ m^{-2} on the nightside. Our studies suggest a similar thin atmosphere but with the neutral gas more confined to Io's surface. The atmospheric model in Khurana et al. (2011) has a very large extent with a scale height of 270 km and an additional corona. This scale height is not in agreement with simple considerations of the hydrodynamic theory. According to our model results, the plasma data do not favor an extended atmosphere in the region of the Galileo passes.

The Khurana et al. model is composed of 3-D resistive MHD equations in spherical coordinates. In order to solve these equations they apply a modified version of the simulation code already used by Linker et al. (1998) and Jia et al. (2008, 2009) for Io's and Ganymede's plasma interaction. The MHD equations include charge exchange and electron impact ionization but they neglect induced dipole attraction and dissociative recombination. Both processes are included in our model. Although we calculated that induced dipole attraction contributes only by $\sim$10% to the total ion-neutral collision rate

(see Section 5.1.5), at low ion temperatures and flow velocities ion-neutral interaction arises from an induced dipole attraction (Banks, 1966) and might be important in the low altitudes of the ionosphere. Dissociative recombination is also a process which contributes less to the evolution of the density (see Table A.2) but might modify the density especially in regions where the ionospheric electrons become dominant, i.e., close to Io.

The resulting mass loading from the model of Khurana et al. probably largely overestimates the total amount of mass per second lost from Io's atmosphere. We have estimated the mass loading based on the information available on the Khurana et al. model and find that their total impact ionization rate of 7×10^{27} ions/s for the I24 flyby is much higher than the total electron impact rate of 1.5×10^{27} ions/s derived by Saur et al. (2003) (see their figure 3). The electron number density during I24 was smaller (about 2500 cm^{-3}) than the density applied in the studies of Saur et al. (2003) (3600 cm^{-3}), so the mass loading rate could be further reduced by a factor of 0.7 resulting in a mass loading rate of 0.5×10^{27} ions/s. The computation of the ion mass-loading rate is based on a spherical symmetric neutral density profile for a constant ionization lifetime in Khurana et al.'s model. It was not clearly stated how the ionization rate was computed. Since the model is based on the model of Linker et al. (1998) we expect that the calculation of the interaction processes resembles the one of Linker et al. (1998). Khurana et al. (2011) assume that the neutrals and ions have the same mass of 20 amu (the average mass of O and S atoms in the torus). The neutral density profile and the mass of the neutrals are therefore not consistent with their latitudinally asymmetric atmospheric model and the mass of the SO_2 molecules ($\sim$64 amu) which dominate the atmosphere. Due to the spherical prescription of the neutral density their calculation overestimates the plasma production volume and the mass-loading process. Khurana et al.'s model does not account for the effect of heat conduction and hence do not ensure conservation of energy. Our model ensures conservation of energy and the total mass-loading rate in our model varies between 4.9×10^{26} (atm. model 2) and 9.7×10^{26} (atm. model 3) for the I24 flyby conditions.

Moreover, the diffusivity is included in the model of Khurana et al. (2011) which can be characterized by the ionospheric conductances (see, e.g., Linker et al., 1998). However, the ionospheric Hall effect in our model is also influenced by the conductances and can also be considered as a resistivity term. We have performed simulations with and without the Hall effect and came to the conclusion that the ionospheric Hall effect has a small influence on the magnetic field components along the I24 and I27 trajectories.

Additionally, there are differences in the formulation of the inner boundary between the models. The inner boundary condition used in Khurana et al. (2011) is based on the boundary condition derived by Jia et al. (2009). They move the inner simulation boundary

to the core boundary of the moon and solve the induction equation outside of the moon and within its mantle with a strongly varying electric conductivity. Afterwards they smooth the magnetic resistivity profile across the moon's surface that can result in electric currents inside this region. The inner boundary condition affects not only the convection pattern but also the magnetic field and could also provide a difference between the model of Khurana et al. (2011) and our model which uses the boundary condition derived by Duling et al. (2014). Further uncertainties persist about the assumed initial values of the upstream plasma.

5.2.4. Discussion

Simulation results are sensitive to assumptions of the atmospheric configurations, since the properties of the atmosphere determine the ionospheric conductivities which can be important by considering the plasma environment near the ionosphere as it is the case at I24 and I27. According to our model results and considering the observed plasma data of the two flybys, Io's ionosphere seems to be strongly asymmetric and complex. Although the observed magnetic field during I24 components can better be explained with an extended atmosphere, the explanation of the measured plasma data favors the scenario of plasma interaction with an atmosphere that is more confined to the surface on the upstream side. However, a stronger longitudinal asymmetry, than the one assumed here, with varying scale height and an extended atmosphere on the downstream side could be a possible explanation for the measurements.

The interpretation of the data during I27 suggest a complex atmosphere with a dense atmosphere near the surface and an abrupt fall off of the atmospheric density when moving away from Io's surface on the anti-Jovian flank. Whereas the decrease of the atmospheric density with distance from the surface seems to be much smoother on the upstream side than on the anti-Jovian flank during I27. Khurana et al. (2011) do not provide results of the plasma density, temperature and velocity from their simulations which they used to fit the magnetic field data. The atmospheric scenario with an extended atmosphere which they apply can not be in agreement with the observed plasma density for several reasons. Additionally to the extended atmosphere with a scale height of 270 km and a corona, the high mass loading rate applied by Khurana et al. (2011) would lead to an enhancement of the electron density at the closest approach during I24. According to our model results, we have shown that already a dilute (with a neutral number density of $n_{\text{cor},0}$ =0.8 $\times$ 10^{13} m^{-3} compared to 1.1 $\times$ 10^{13} m^{-3} in Khurana et al. (2011)) and extended corona determines the electron density by producing an enhancement at the closest approach. Furthermore we doubt that such a dilute and extended atmosphere could generate the peak in the observed plasma density and the abrupt fall off near the closest approach during I27.

The results of Khurana et al. (2011) have shown that the ocean in combination

with their atmospheric model produces a good fit to the measured magnetic field data. Unlike the results of Khurana et al. (2011), our simulation results do not require induction signals from a subsurface ocean. We suggest that the measured perturbations during the flybys can be explained with strong atmospheric asymmetries. Note that the differences in the magnetic field components between the model results of different model atmospheres are similar in magnitude to the differences between our best-fit results and the measurements. Hence, a possible interpretation could be that a more complex configuration of Io's atmosphere than the one applied in our model could provide the remaining discrepancies between the model results and the data.

When considering only the magnetic field results, we suggest that the interpretation is ambiguous. The existence of a magma ocean is only one possible solution to explain the magnetic field data but not a unique one as we have shown by our model results. Note that also other configurations are possible to explain the data, for example the existence of induction signals from a conductive layer which lies deeper below the surface and which is less conductive than the proposed magma ocean with another atmospheric configuration than the one assumed by Khurana et al. (2011) as it would generate induction signals with smaller amplitudes and weakly determine the magnetic field components. Another technique to derive constraints on the interior provided by the HST observations indicate that a magma ocean is inconsistent with the observed oscillation of the aurora spot locations around Io's equator. However, conclusions on the possible existence of the magma ocean in the interior require further studies of the plasma interaction and a better understanding of Io's atmosphere.

Furthermore the discrepancy between the plasma variables calculated with different atmospheric scenarios in our MHD model and the published one may have further causes: The incident plasma composition is time variable as suggested by Delamere and Bagenal (2003) and might have been different from the one we assume here. While the electron density of the upstream plasma has been measured, uncertainties exist, e.g., about the mass of the plasma particles and the plasma temperature as well as the properties of the newly created ions by electron impact ionization. Small variations of these parameters can modify Io's plasma interaction and the plasma environment close to Io. Kinetic effects which can not be modeled with our MHD model might also influence the perturbed plasma environment.

The model of Khurana et al. (2011) and our model lack a self-consistent calculation of the evolution of the electron temperature for a given distribution of the neutral atmosphere around Io. The effectiveness of electron heat conduction along the magnetic field lines crucially determines the plasma ionization source. In the region of Io's ionosphere heating, the electron temperature can reach 40 eV (Shaposhnikov et al., 2013). In our model we approximately account for the effect of heat conduction and

ensure conservation of energy. As the incident plasma composition is time variable, the electron temperature of the plasma could be different from the one assumed here. This would change the plasma production and hence the interaction strength in our model.

6. Results: Modeling of Europa's Plasma Interaction

We now quantitatively investigate the effects of an atmospheric inhomogeneity on Europa's plasma interaction with the MHD model and the analytic model introduced in Chapter 4. With the knowledge about the influence of an atmospheric inhomogeneity on the magnetic field, we will afterward compare the results of the analytic and MHD models with the Galileo magnetic field measurements in order to investigate if signatures of atmospheric inhomogeneities are present in the observations. All results are presented in the EPhiO coordinate system.

6.1. Influence of a Local Atmospheric Inhomogeneity on Europa's Global Plasma Interaction

For a first basic study with the MHD approach the atmospheric inhomogeneity is implemented at the south pole of Europa and contains 50% of the total gas content of Europa's atmosphere. A simplified geometry is chosen here with the background magnetic field pointing in the negative z direction. The initial values and atmospheric properties for the MHD simulation runs used here are given in Tables 3.4 and 3.2 denoted by "general model I". The induction in a subsurface water ocean is not included in the first step because it would generate additional asymmetries in the plasma interaction and we are interested in understanding the basic influence of the atmospheric inhomogeneity on the plasma interaction.

6.1.1. Magnetic Field and Plasma Velocity

Europa's atmosphere and plume generate plasma flow and magnetic field perturbations, which propagate as Alfvén waves away from Europa. The root cause of these perturbations are elastic collisions between the ions and the neutrals, plus charge exchange and ionization, where the latter two are often referred to as pickup (see Equation (3.15)). We take into account both the velocity and the magnetic field for the consideration of the development of the Alfvén wings and winglets (see Figure 6.1). The formation of the Alfvén wings is clearly visible in the regions with decreasing plasma bulk velocity v and perturbed B_x north and south of Europa in the xz plane in Figures 6.1a and 6.1e, respectively. The Alfvén wings are bent back by a constant angle of $\Theta_A \approx 13^\circ$ with

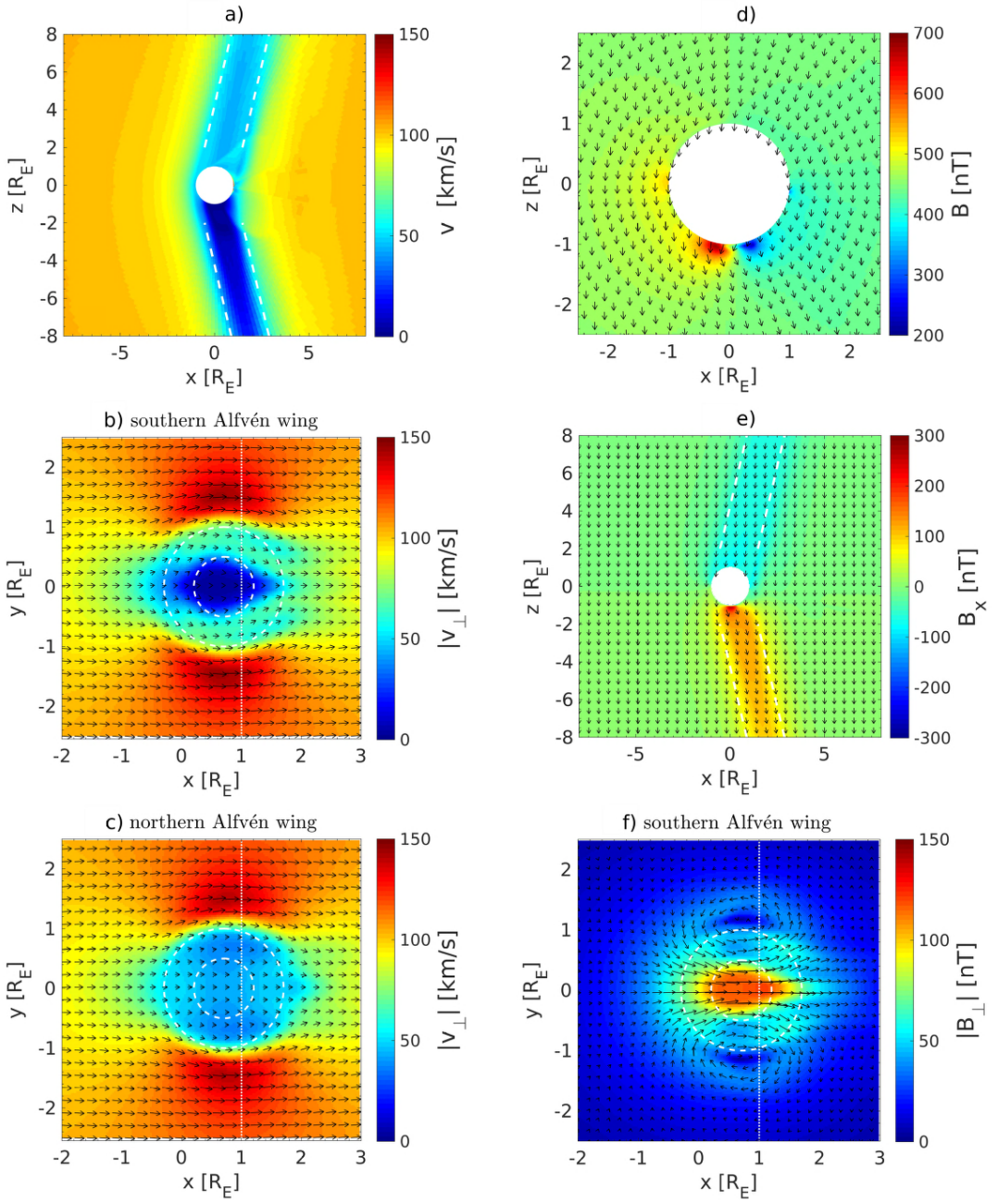

Figure 6.1. – (a) Plasma bulk velocity in the xz plane (y=0 R_E) calculated with the MHD model. (b) and c) Plasma flow velocity field in a cut at z=±3 R_E through the southern and northern Alfvén wings, respectively, in the xy plane. The color scale represents the magnitude of the plasma velocity perpendicular to the magnetic field. (d) Magnitude of the magnetic field in nT in the xz plane (y=0 R_E) calculated with the MHD model. (e) B_x in nT in the xz plane (y=0 R_E). (f) Magnetic field in a cut through the southern Alfvén wing (z=−3 R_E) in the xy plane. The color scale represents the magnitude of the magnetic field perpendicular to the background magnetic field. The Alfvén characteristics are shown as white dashed lines in (a) and (e). The white outer circle indicates the projection of Europa's surface and the white inner circle the projection of the south polar atmospheric inhomogeneity into the southern Alfvén wing in (b), (c) and (f). The white vertical dotted line shows the trajectory along which the magnetic field is displayed in Figure 6.4. The arrows show the orientation of the plasma flow ((a), (b), and (c)) and magnetic field ((d), (e), and (f)) and their lengths linearly scale with highest magnitude of this plane: (b) 145 km/s, (c) 141 km/s, (d) 679 nT, (e) 262 nT, (f) 121 nT.

respect to the unperturbed background magnetic field displayed in the white dashed lines (see Figures 6.1a and 6.1e). The perturbation of the magnetic field is correlated with the perturbation of the velocity field and can be related through $\delta\underline{B} = \pm\sqrt{\mu_0\rho_0}\,\delta\underline{v}$ in the northern ($+$ sign) and southern ($-$ sign) Alfvén wing (Neubauer, 1980). The magnetic field components are primarily perturbed in the negative (positive) x direction in the northern (southern) wing (see Figure 6.1e) and the velocity components in the negative x direction in both wings. Evident in Figures 6.1a and 6.1e is the pronounced north-south asymmetry due to the formation of the Alfvén winglet in the southern Alfvén wing. A dense atmospheric inhomogeneity leads to locally enhanced collisional and ionization processes and stronger perturbations within the interaction region. The local atmospheric inhomogeneity at the surface is much denser by a factor of ~ 30 compared to the ambient atmosphere for the results shown here. The enhanced local perturbations are the main cause for the development of an additional, smaller Alfvén wing within the main southern Alfvén wing. Succinctly speaking, the Alfvén winglet is the result of the plasma interaction with an atmospheric inhomogeneity within a global atmosphere, located within the main Alfvén wing. It possesses the same basic properties as the Alfvén wing, i.e., the same bend back and the $\delta\underline{B} = \pm\sqrt{\mu_0\rho_0}\,\delta\underline{v}$ correlations. The atmospheric inhomogeneity at the south pole modifies the southern Alfvén wing but only weakly changes the main overall structure. The Alfvén angle is independent of the atmospheric asymmetry.

Figures 6.1b and 6.1c show that the plasma flow is diverted around and accelerated up to $|v_\perp| = \sqrt{v_x^2 + v_y^2}$ ≈140 km/s at the flanks of the Alfvén wings (outside the white dashed outer circle). The $\underline{j} \times \underline{B}$ force slows the plasma velocity upstream and reaccelerates it downstream of the wings. In the ionosphere the $\underline{j} \times \underline{B}$ force is predominantly in equilibrium with the forces related to the ion-neutral collisions, electron impact ionization and charge exchange, while in the Alfvén wings the $\underline{j} \times \underline{B}$ force is in equilibrium with the plasma inertia ($\rho\underline{v} \cdot \nabla\underline{v}$). A result of the interaction is that most of the plasma flow into the ionosphere is reduced and is swept around the moon and the wings.

In the center of the southern Alfvén wing the plasma flow experiences a second shielding as clearly visible in Figure 6.1b. The interaction strength in the winglet is much higher ($\overline{\alpha}$ ≈0.95) than in the surrounding Alfvén wing ($\overline{\alpha}$ ≈ 0.4). The radius of the winglet depends on the horizontal extent of the surface neutral number density of the inhomogeneity. In the results shown here the extent of the inhomogeneity is $\sim$ 0.5 R_E. Within the winglet the magnitude of the perpendicular velocity is reduced to $\sim$ 5 km/s (see Figure 6.1b) and the magnitude of the perpendicular magnetic field $|B_\perp| = \sqrt{B_x^2 + B_y^2}$ is perturbed by $\sim$ 120 nT (see Figure 6.1f). At the flanks of the Alfvén winglet the plasma flow is slightly accelerated by $\sim$ 9% (outside the white dashed inner circle in Figure 6.1b). Alfvén waves associated with the inhomogeneity at the south pole can not propagate into the northern hemisphere along field lines intersecting the

moon. No local perturbations within the northern wing are recognizable as a direct consequence of the inhomogeneity (see Figure 6.1c).

A basic property of the wings is that the magnitude of the magnetic field is constant inside the Alfvén wings (Neubauer, 1980), also visible in the far field in our results in Figure 6.1d. The fast mode generated by the interaction upstream of the moon propagates in all directions. The amplitude of the fast magnetosonic mode perturbations decreases as a function of distance from Europa and can be neglected a few R_E away from Europa. The propagation of the fast mode is associated with a compression and bending of the magnetic field lines. The compression of the field lines upstream of Europa leads to a pileup and thus to an enhancement of the magnitude of the magnetic field. This increase of the magnitude of $\sim$ 100 nT is visible in Figure 6.1d. It is also visible that a second pileup region develops at the south pole associated with the inhomogeneity. This region is more distinctive than the large-scale upstream region and the perturbed magnitude of the magnetic field increases up to $\sim$ 700 nT.

Figure 6.1a shows structures especially in the northern but also southern hemisphere in the plasma velocity going from the poles downstream of the moon by an angle of about 50° to the axis (on the northern hemisphere). These perturbations require a more detailed study but might develop in our simulations due to density and pressure gradients within the Alfvén wing related to the compressional slow mode also observable in the plasma number density in Figure 6.2.

In summary, our simulation shows that due to a local atmospheric inhomogeneity an Alfvén winglet within the large-scale southern Alfvén wing forms. In the winglet the magnetic field and the velocity experience a stronger perturbation compared to the perturbations in the main wing due to the dense atmospheric inhomogeneity.

6.1.2. Plasma Density

In Figure 6.2 we display the plasma number density in the xz plane. As magnetospheric electrons flow past the atmosphere and convect through it, the neutral particles in the atmosphere are ionized and the plasma density upstream of the moon increases. The ionized plasma gets picked up and moves downstream. Europa's ionosphere is therefore not an ionosphere in chemical equilibrium, i.e., where production and recombination differ strongly. At Europa, production and convection determine the ionospheric mass balance. Most of the plasma is concentrated at the region of the local inhomogeneity with densities up to $\sim 1 \times 10^5$ cm^{-3}. Farther away from the moon the density decreases to its ambient value. No significant perturbation of the plasma density is expected in the Alfvénic far field. Downstream of the moon, recombination but no ionization takes place. Since the ionospheric particles which impinge Europa's surface are absorbed, a wake downstream of the moon forms where the plasma density is strongly decreased. Compressional slow

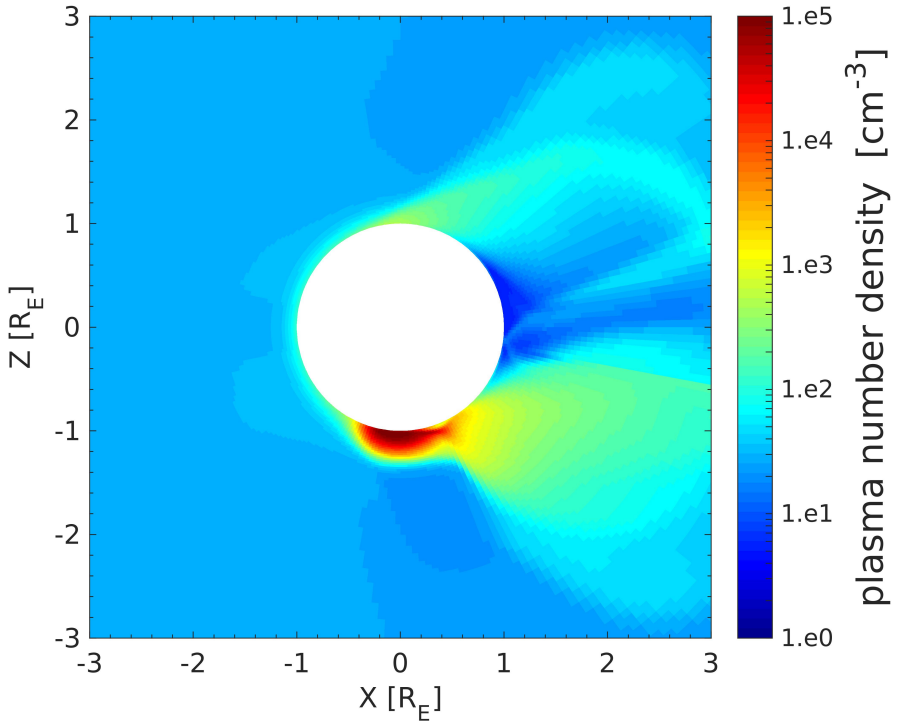

Figure 6.2. – Plasma number density in cm^{-3} in the xz plane (y=0 R_E) calculated with the MHD model.

mode perturbations act downstream of the moon to reestablish pressure equilibrium. The increased density structure at the northern hemisphere in Figure 6.2 might be attributed to a combination of convection of plasma and of slow mode perturbations which propagate with a local sound speed velocity of $\sim$ 30 km/s.

6.1.3. Electric Currents in the Alfvén Wings

Collisions, charge exchange, and electron impact ionization modify the plasma flow and thus generate magnetic field perturbations and associated electric currents. The ionospheric electric currents are determined by the local ionospheric conductivities and electric field. Farther away from Europa, the ionospheric conductivities vanish and the ionospheric currents are fed into the Alfvén wing currents. The Alfvénic currents $\underline{j}_{\underline{c}_A^{\pm}}$ parallel to the wing, i.e., the Alfvén characteristics are displayed in a cross section through the southern and northern Alfvén wings in the plane perpendicular to $\underline{c}_A^{\pm}$ (Equation (4.12)) at z=$\pm$3 R_E in Figures 6.3a and 6.3b, respectively. When we only consider a radially symmetric atmosphere, we expect $\underline{j}_{\underline{c}_A^{\pm}}$ to be concentrated at the flanks of the Alfvén wings as it is shown for $\underline{j}_{\underline{c}_A^{-}}$ in Figure 6.3b. Due to the local atmospheric inhomogeneity, a pronounced second current system in the southern Alfvén wing arises (see Figure 6.3a). The inhomogeneity drives a surplus of the ionospheric electric current at the south pole that is closed in the southern far field. The current density is concentrated at the flanks of this Alfvén winglet and the direction of the currents is the same as in the southern

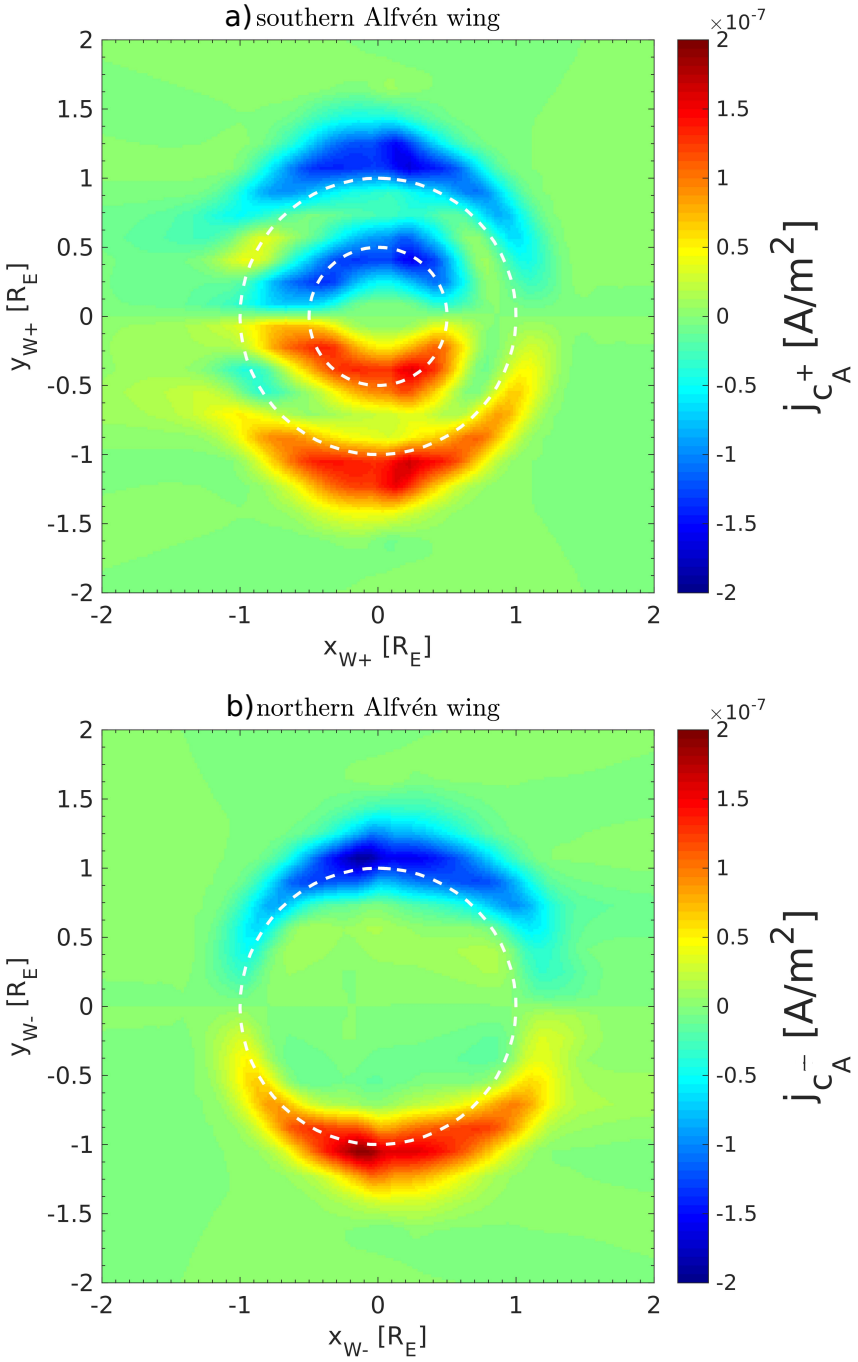

Figure 6.3. – (a) Alfvénic current $\underline{j}_{\underline{c}_A^+}$ in A/m^2 in a cut through the southern Alfvén wing in a plane perpendicular to the southern Alfvén characteristic at z=−3 R$_E$. (b) Alfvénic current $\underline{j}_{\underline{c}_A^-}$ in A/m^2 in a cut through the northern Alfvén wing in a plane perpendicular to the northern Alfvén characteristic at z=3 R$_E$. In the wing coordinate system, the z_{W+} (z_{W-}) axis is parallel to the southern (northern) Alfvén characteristic, the $y_W\pm$ axis is the same as in the EPhiO system and the $x_W\pm$ axis completes the right-handed coordinate system. The white outer circle indicates the projection of Europa's surface and the white inner circle the projection of the south polar atmospheric inhomogeneity into the southern Alfvén wing.

Alfvén wing. A fraction of the current associated with the local inhomogeneity is closed in the northern far field through surface currents. For the model scenario shown here we

have calculated a total Alfvén wing current through the whole southern Alfvén wing of 4.9 $\times$ 10^5 A and an Alfvénic current through the winglet of 1.8 $\times$ 10^5 A.

6.1.4. Influence of Varying Neutral Density Distribution on the Magnetic Field in the Alfvénic Far Field

As demonstrated in the previous Section, the perturbations of the magnetic field in the Alfvén wings are controlled by the neutral atmosphere. Here we show how different atmospheric inhomogeneities affect the perturbations of the magnetic field in the northern and southern Alfvén wings. Figures 6.4a and 6.4b show the components of the magnetic field along trajectories parallel to the y axis shifted 0.3 R_E downstream from the center of the wing in the southern and northern Alfvén wings, respectively. The hypothetical trajectories are displayed as white vertical lines in Figures 6.1b, 6.1c, and 6.1f. We display the magnetic field on a shifted trajectory away from the center of the wings because on a trajectory through the center some properties of the magnetic field are less significant due to symmetry reasons. The different lines show the magnetic field from the MHD models with a radially symmetric atmosphere (grey line) and different densities of the atmospheric inhomogeneity in the ambient radially symmetric atmosphere. The

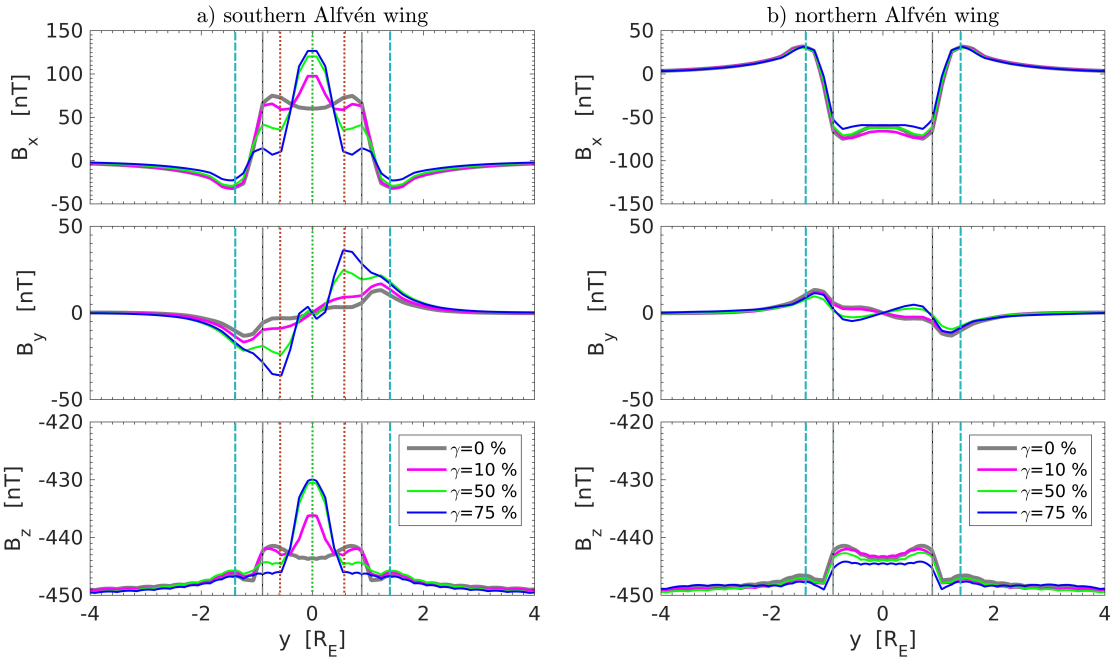

Figure 6.4. – Magnetic field components in the (a) southern and (b) northern Alfvén wings along a trajectory parallel to the y axis and shifted 0.3 R_E downstream from the wing center. Results are calculated with the MHD model. The inhomogeneity is located at the south pole in a radially symmetric atmosphere. The initial values and atmospheric properties can be found in Tables 3.4 and 3.2 denoted by "general model I". γ denotes the ratio between the mass content of the atmospheric inhomogeneity to the mass content of the total atmosphere. The vertical lines represent the projection of the position of the center of the inhomogeneity into the southern Alfvén wing (dotted green line), the position of the flanks of the Alfvén winglet (dotted red lines), the Alfvén wing crossing (dashed grey line), and the position of the flanks of the Alfvén wings (dashed blue line).

factor γ indicates the ratio between the total mass of the atmospheric inhomogeneity and the total mass of the global atmosphere. This ratio γ is varied between 0% and 75%.

As expected the perturbations of the magnetic field are symmetric in the northern and southern Alfvén wings for a radially symmetric atmosphere and dominant in the x component due to the bending of the magnetic field lines, as visible in the grey line in Figures 6.4a and 6.4b. Within the wings the magnetic field is more perturbed at the inner face of the wings (at $y \approx \pm 0.8$ R_E) with 75 nT than in the center (at y=0 R_E) with a perturbation of 60 nT in the x component. This is a result of the increased conductances on field lines more tangential to Europa, i.e., for regions characterized by $x^2 + y^2 \approx R_E^2$ (see also maximum of conductance near r_s in Figure 4.1). The magnetic field perturbations are structured similar to the plasma velocity perturbations in the wings. Therefore, the acceleration of the plasma at the flanks of the Alfvén wings results in a local decrease (increase) of B_x in the southern (northern) wing as visible in the grey line at the position of the vertical dashed blue line in Figures 6.4a (top) and 6.4b (top). Due to the diversion of the plasma flow around the Alfvén wing the magnetic field is perturbed in the y direction at the flanks of the wings. B_z is more perturbed at the inner face of the wings with a perturbation of 9 nT than in the center of the wings with a perturbation of 6 nT shown in the grey line in Figures 6.4a (bottom) and 6.4b (bottom). This follows from $|\underline{B}| =$const in the Alfvén wings and the described B_x dependence.

A south polar inhomogeneity in a radially symmetric atmosphere leads to the formation of an Alfvén winglet within the southern wing. At the dense inhomogeneity more perturbations are generated which map out into the southern Alfvén wing as visible in the global maximum in the center of the wing (at the position of the dotted green line) in the B_x component in the magenta, green, and blue lines in Figure 6.4a (top). The perturbations in all three components become stronger with increasing density of the inhomogeneity. The perturbation in the wing center reaches a value up to $\sim$125 nT for γ=75%. The plasma flow within the southern Alfvén wing is directed around the winglet and is accelerated at its flanks (at the position of the vertical dotted red lines) resulting in a decrease of the perturbation of the B_x component. We see that the denser the inhomogeneity, the slower the plasma flow within it and the faster the flow around the flanks of the winglets. Faster flows leads to smaller perturbation in B_x in the surrounded Alfvén wing. Farther away from the projection of the center of the inhomogeneity (at the position of the vertical dashed grey lines), the influence of the Alfvén winglet decreases and the effect of the Alfvén wing becomes visible in the increase of B_x (see Figure 6.4a, top). The diversion of the plasma flow becomes also more effective with increasing density of the inhomogeneity. Therefore, the perturbation of B_y around the winglet becomes stronger as evident in the minimum and maximum at the position of the vertical dotted red line in Figure 6.4a (middle). For example, a plume at Europa that contains 50% of the total mass content of the atmosphere can exhibit a perturbation

in the y direction of ∼25 nT. The behavior of the magnetic field in the northern Alfvén wing is very similar in all four cases (see Figure 6.4b). Here B_y and B_z are weakly disturbed. In the northern hemisphere the atmosphere is homogeneous and therefore no local perturbations within the northern wing develop on smaller scales in contrast to the southern wing.

6.1.5. Comparison Between Analytic Model and MHD Model Results

In Figures 6.5a and 6.5b we display the calculated magnetic field in the northern and southern Alfvén wings on a trajectory along the y direction shifted by 0.3 R_E downstream from the center of the wings. The red lines show the analytic model results calculated with a south polar atmospheric inhomogeneity. Additionally, we compare these results with MHD model results calculated with an inhomogeneity which contains 50% of the total gas content of Europa's atmosphere displayed in the green lines. For the analytic model, we chose values for the conductances which fit the MHD model data.

Within the plume indicated by p in Figure 6.5a the magnetic field experiences the maximum perturbation in B_x direction. At the boundaries of the plume to the global atmosphere indicated with s, a magnetic field discontinuity arises in the analytic model

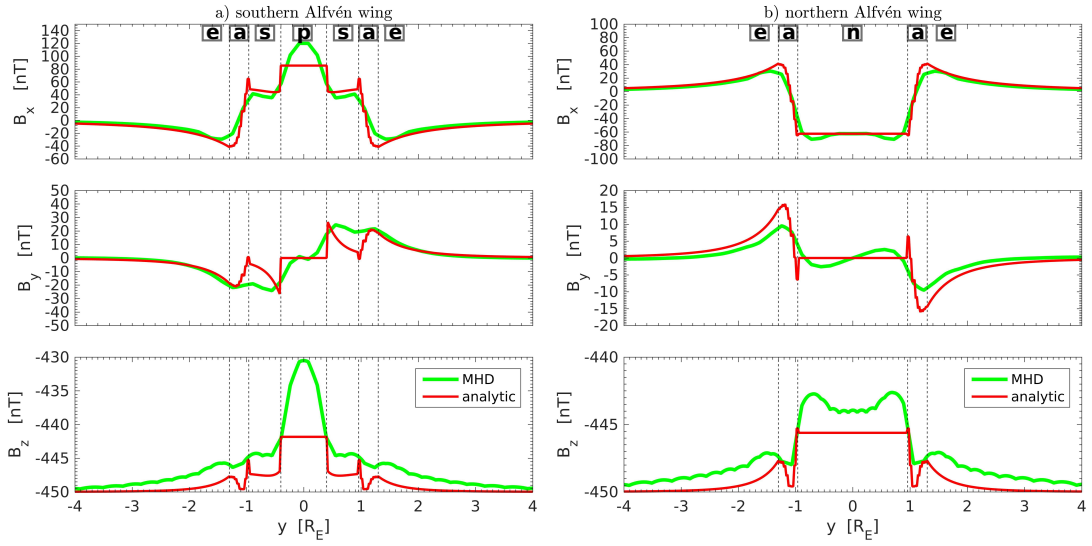

Figure 6.5. – Magnetic field components in the (a) southern and (b) northern Alfvén wings along a trajectory parallel to the y axis and shifted 0.3 R_E downstream from the wing center. The green lines show the solution with a south polar atmospheric inhomogeneity (γ=50%) calculated with the MHD model. The red lines indicate the Alfvénic perturbation for a nonsymmetric interaction with an atmospheric inhomogeneity at the south pole with r_s=1 R_E, r_p=0.5 R_E, $\Sigma_P^s = \Sigma_P^n$ =1 S, Σ_P^p=15 S, Σ_P^a=6 S calculated with the analytic model. The ionospheric Hall effect was neglected with $\Sigma_H^s = \Sigma_H^n = \Sigma_H^p = \Sigma_H^a$ =0 S. The values were chosen to fit the MHD model results (green lines). The other quantities for the calculation of the magnetic field perturbation can be found in Table 3.4 denoted by "general model I". The red lines show a stepwise behavior due to the sharp boundaries between each domain. The vertical dashed lines represent the boundaries between the domains a, n, s, and p referring to Figure 4.2. The wavelike structure of the green lines in B_z is a pure numerical effect.

results (red lines). This discontinuity is a model discontinuity because the real plume density does not abruptly jump but its transitions are smoothly to the global atmospheric density. Inside the southern Alfvén wing (domain s) the B_x component is still perturbed in the positive x direction due to the bending of the wing. At the boundary between outside ($r >$R$_E$) and inside the Alfvén wing ($r <$R$_E$) indicated with a and s, respectively, a jump of the magnetic field components can be observed. The jump is a result of the peak of the Pedersen conductance in Europa's atmosphere and the effect of the hemisphere coupling currents. The part of the discontinuity due to the hemisphere coupling is a real physical discontinuity. This transition region is located between the volume currents which are fed into the southern atmosphere and the surface currents which connect both hemispheres. The volume and surface currents have opposite directions (see also Figure 4.2) and therefore produce the magnetic field signatures in the transition region a to s shown as red lines in Figure 6.5a. Outside the Alfvén wing (domain a) the ionospheric conductance gradually decreases and so do the magnetic field perturbations. In the region where the ionospheric conductance vanishes (domain e) the magnetic field components return to their upstream conditions. On the northern hemisphere there is no inhomogeneity in the atmosphere, therefore the magnetic field in the northern Alfvén wing (Figure 6.5b) only experiences perturbations which occur from the interaction with a global atmosphere except in the transition region between n and a. The hemisphere coupling effect also generates discontinuities in the northern Alfvén wing as visible in the magnetic field components in the red lines in Figure 6.5b between n and a.

Europa's global atmosphere weakens the effect of the hemisphere coupling currents. This effect is very small compared with the effect generated by the global atmosphere which occurs due to the peak of the ionospheric conductances. We calculated a jump of about 5% of the global perturbation in the magnetic field components associated with the hemispheric coupling currents for the approach used here. Consequently, an observed large jump of the magnetic field over a short but still sufficiently finite length scale during an Alfvén wing crossing at Europa is most likely a steep gradient due to the atmospheric effect and a discontinuity due to an asymmetric atmosphere would be hardly detectable in the data set (see further discussion in Section 6.2.1).

The analytic model results provide information on the influence of the hemisphere coupling due to the inhomogeneity and the atmospheric effect due to the peak of the ionospheric conductances at the flux tube boundary. The comparison between the analytic and MHD model shows that the results are in general agreement with each other except for the discontinuities. The transition regions calculated with the MHD model (green lines) are much smoother in comparison with the analytic model results for two reasons:

1. A more realistic smoother neutral atmosphere.

2. Remaining small discontinuities from the hemispheric coupling currents are smeared out due to the finite resistivity and viscosity of the MHD codes.

The maximum perturbation in B_x direction in the Alfvén winglet (domain p in Figure 6.5a, top) is larger in the MHD model results than in the analytic model results, because the conductance calculated with the MHD model in domain p reaches its maximum in the center of the inhomogeneity while the conductance given in the analytic model is constant in this domain. The B_z component also experiences stronger perturbations with a decrease in magnitude to ensure the required constancy of the magnetic field magnitude in the northern and southern Alfvén wings and winglet (see Figures 6.5a (bottom) and 6.5b (bottom)). Due to the diversion of the plasma flow around the Alfvén winglet, the B_y component is perturbed in the negative and positive y direction around the winglet in the ambient Alfvén wing (see red and green lines in Figure 6.5a, middle). In the northern Alfvén wing (domain n in Figure 6.5b) the B_y component calculated with the MHD model is slightly perturbed ($\sim$3 nT) while the B_y component calculated with the analytic model does not experience any perturbation due to the constancy of the conductance inside domain n.

6.1.6. Influence of Induced Fields on the Alfvén winglet

A spatially homogeneous inducing field in a radially symmetric ocean induces a dipole field. Deviations from these idealized conditions of the inducing field and the conductive regions will result in higher-order multipole fields (see, e.g, Schilling et al., 2004, 2007). The induced magnetic field directly modifies the magnetic field in the surrounding of the moon. However, it also affects the far field through a shrinkage and a displacement of the Alfvén wings (Neubauer, 1999). The inducing field is strongest when Jupiter's dipole moment points toward or away from Europa. In this Section we study the case when Europa is located north of the magnetic equator (λ_{III}=200°). In this case the induced dipole moment points mainly toward the Jupiter-facing side at the position of Europa. The setup of the plasma conditions for the MHD simulation used here are given in Tables 3.4 and 3.2 denoted by "general model II". In Figure 6.6b we display the perpendicular plasma velocity in a cross section through the southern wing when induction is included and compare it to the case without induction in Figure 6.6a. The background magnetic field has a strong y component and therefore the Alfvén wings are additionally tilted in the y direction (see also figure 7A in Neubauer (1999)). The consequence of the y tilt of the large Alfvén wing is that the Alfvén winglet sitting exactly at the south pole is not in the center of the large wing anymore. The winglet is shifted to the Jupiter-facing side as visible within the white dashed circle representing the projection of Europa's surface into the wing in Figure 6.6a. To quantify the relative importance of the induced fields compared with the background magnetic field Neubauer (1999) introduced the inclination angle of the Jovian magnetic field with respect to the Jovian equator at the location of the moon (see equation (5) in Neubauer, 1999). For the scenario shown here the inclination

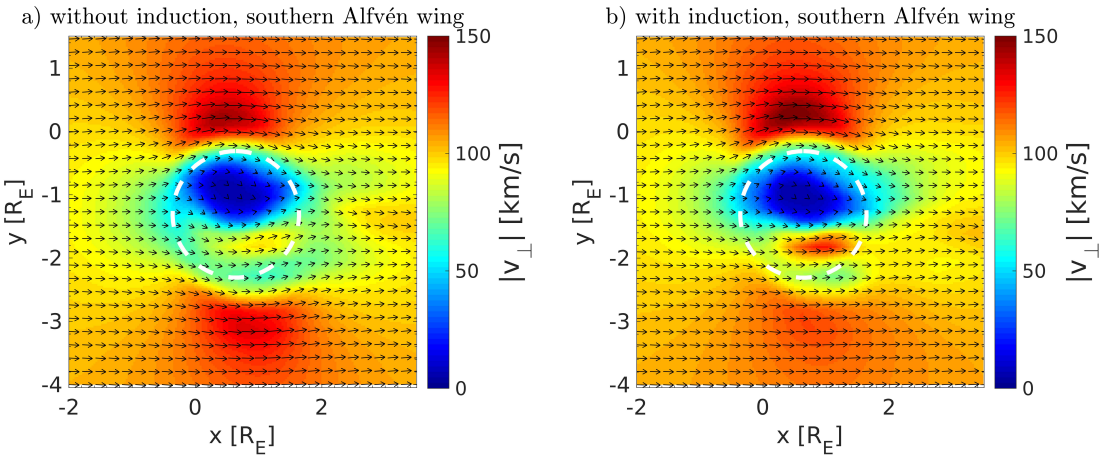

Figure 6.6. – Plasma flow velocity field in a cut through the southern Alfvén wing ($z = -3\ R_E$) in the xy plane for plasma interaction (a) without and (b) with induction in a subsurface water ocean. The magnitude of the plasma velocity perpendicular to $\underline{B}_0$ is color coded. The white outer circle indicates the projection of Europa's surface into the southern Alfvén wing. The lengths of the arrows linearly scale with highest magnitude of this plane: (a) 144 km/s, (b) 151 km/s.

angle is 65°. Therefore, we expect a small distortion of the cross section of the Alfvén wings by less than 10% according to Figure 5 in Neubauer (1999). Comparing the results with and without induction (see Figure 6.6), a small displacement to the anti-Jupiter facing side and a distortion along the x direction of the winglet can be observed. Moreover, the results of the plasma interaction plus induced fields in a subsurface ocean show that the acceleration of the plasma at the flanks of the Alfvén wings and the winglet is more distinctive than it is the case without induction. This is a result of the small displacement of the winglet and its flanks to the negative y direction and the nonconstant behavior of the velocity within the Alfvén wing.

6.2. Modeling of the Galileo Flyby Scenarios

Now we study the influence of an inhomogeneity by comparing our simulation and analytic results with the Galileo MAG data along trajectories of three different flybys: E17, E25A, and E26. The flyby trajectories are displayed in Figure 6.7 with associated properties of the flybys summarized in Table 6.1. Since the Alfvénic far field is diagnostic of

Table 6.1. – Properties of the Europa Flybys E17, E25A, and E26

Flyby	Date time[a] (UT)	Altitude (km)	TA[b] (deg)	Mag. lat. (deg)	λ_{III} (deg)
E17	1998-09-26 03:53:52	3581	293.9	4.6	140
E25A	1999-11-25 16:29:00	8648	187.2	9.5	200
E26	2000-01-03 17:59:37	340	216.4	-7.8	346

[a] At the closest approach CA.
[b] True anomaly.

Europa's atmospheric properties, a strong local atmospheric inhomogeneity should be

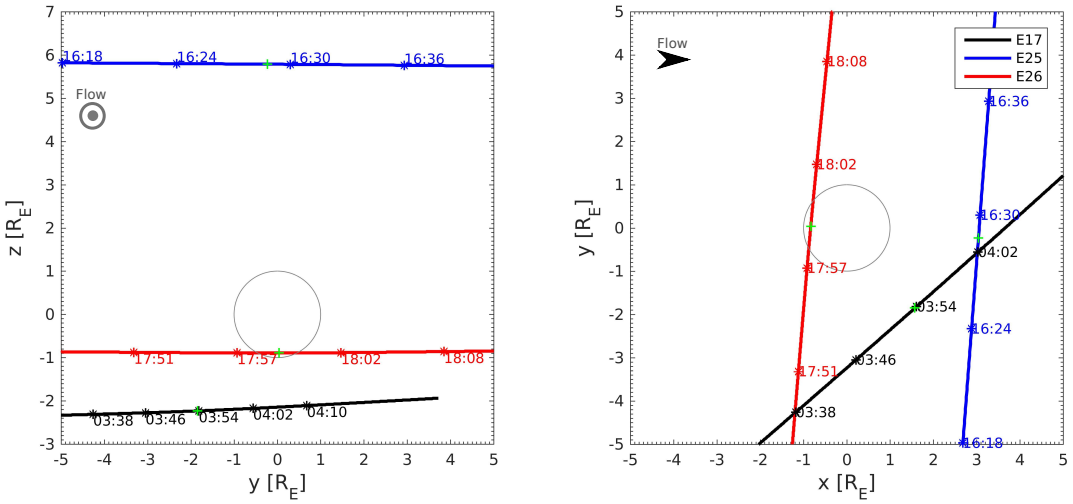

Figure 6.7. – Trajectories of the Galileo flybys E17 (black line), E25A (blue line), and E26 (red line) in the EPhiO coordinate system. The times associated with the spacecraft's positions are labeled on the trajectories. The green crosses mark the position of the closest approach.

detectable in the magnetic field perturbations in the Alfvén wing. Among the twelve Europa flybys, only the three flybys studied here crossed the Alfvén wings. Our aim is to investigate whether signatures of atmospheric inhomogeneities are present in the measured data and whether we can draw conclusions on the existence of an inhomogeneity in the atmosphere only from magnetic field data. The initial values and atmospheric properties of the flybys used in the MHD model are presented in Tables 3.4 and 3.2. Induction in a subsurface water ocean is included in the associated MHD simulations.

6.2.1. Europa Flyby E17

The flyby E17 occurred in the high plasma density region near the center of the Jovian plasma sheet at an altitude of $\sim$ 3600 km. Galileo passed downstream through the southern Alfvén wing. The data (black line) in Figure 6.8 shows a strong perturbation of the magnetic field in the positive x direction due to the bending of the magnetic field lines and weak perturbations in the B_y and B_z component. Furthermore, small-scale fluctuations on top of the main perturbations are measured and could be due to kinetic effects but are not subject of this thesis.

The analytic model results with a symmetric atmosphere (see blue line in Figure 6.8a) are in good agreement with the overall data structure. A local atmospheric inhomogeneity in the southern hemisphere (see red line in Figure 6.8a) would generate perturbations that are not seen in the data during this flyby. For the radius r_s of the region where the field lines are tangent to Europa we chose a value of 0.9 R_E because it better fits the extent of the crossing of the Alfvén wing, but it does not qualitatively change the form and the amplitude of the perturbation. The smaller extent of the interaction region could be an

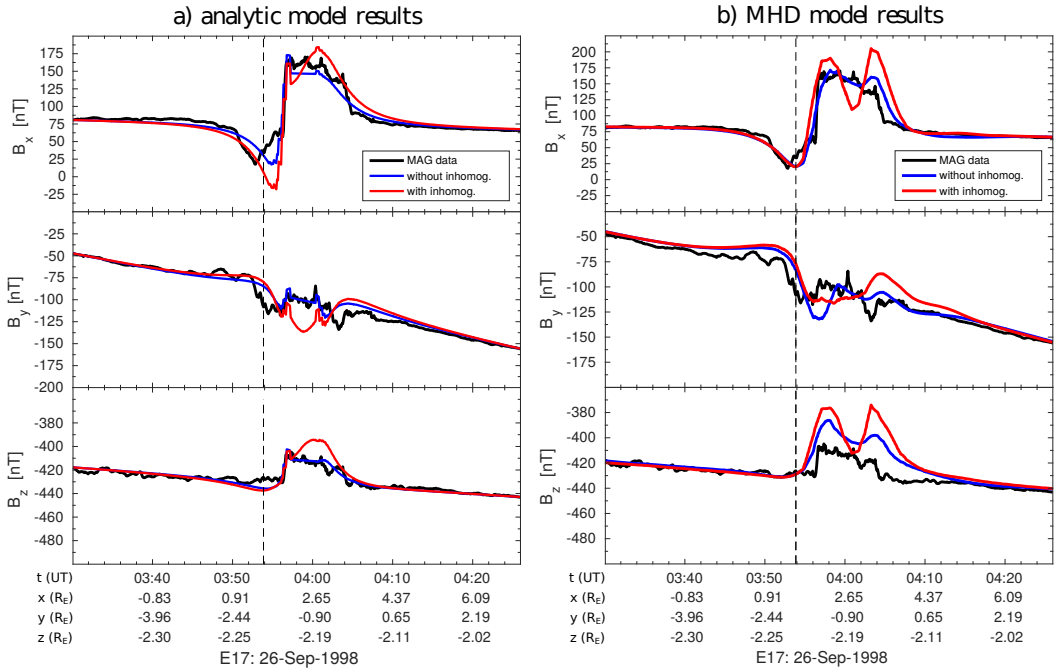

Figure 6.8. – Magnetic field components along the E17 flyby trajectory in the EPHIO coordinate system. (a) Comparison between the Galileo MAG data (black lines) and the results obtained from the analytic model where a south polar inhomogeneity in a global atmosphere (red lines) with r_s=0.9 R_E, r_p=0.7 R_E, $\Sigma_P^s = \Sigma_P^n$=3 S, Σ_P^p=15 S, Σ_P^a=6 S, $\Sigma_H^p = \Sigma_H^s = \Sigma_H^n = \Sigma_H^a$=0 S is considered. The values were chosen to fit the measured data (black lines). The other quantities for the calculation of the magnetic field perturbation can be found in Table 3.4. The blue lines show the analytic results for a homogeneous atmosphere. b) Comparison between the MAG data (black lines) and the results obtained from the MHD model where a radially symmetric atmosphere (blue lines) is considered. The red lines show the model results with an inhomogeneity at ϕ=290° and θ=140° in a radially symmetric atmosphere. The dashed vertical line displays the closest approach at 03:54 UT, x=1.57 R_E, y=−1.85 R_E, and z=−2.23 R_E.

effect of the induced magnetic field. Volwerk et al. (2007) estimated a shrinkage of 0.96 and an offset of 0.1 R_E of the Alfvén wing during E17.

The MHD model results confirm the picture that we have from the analytic model (see Figure 6.8b). The results from the model with the radially symmetric atmosphere (blue line) fit the overall structure very well. The model results with a local inhomogeneity in the atmosphere (red line) show that the magnetic field would experience a local perturbation in the negative x and y directions that we do not see in the measured data. The B_z component is slightly overestimated by our MHD model compared to the measured data. The magnitude of the B_z component in the MHD model results without inhomogeneity is reduced up to 45 nT in order to maintain the constancy of the magnitude of the magnetic field in the Alfvén wing. The perturbations in the analytic and MHD model due to the atmospheric inhomogeneity (see red lines in Figures 6.8a and 6.8b) are slightly different because the location of the inhomogeneity differ between both models. In the analytic model used here, we only have the opportunity to place the

center of the inhomogeneity exactly at the north or south pole and vary the extent.

In the time interval before the Galileo spacecraft enters the Alfvén wing at 03:56 UT, the measured B_x component shows a decrease which is associated with the Alfvén wing currents. This decrease is followed by a steep gradient in the positive x direction at the entry of the Alfvén wing. This may be explained by the fact that Galileo entered the Alfvén wing at the location of maximum current (Volwerk et al., 2007). The steep gradient is measured over four data points with a resolution of 6 s per data point implying a distance of 176 km.

Our model can explain this steep gradient. The ionospheric conductances given by Equation (4.1) peak at the location with field lines tangent to Europa because of the change of the integration path length. Moving outward from Europa the conductances decrease since the neutral gas density falls off and therefore collisions between magnetospheric particles and neutrals decrease. The region of the decrease is strongly dependent on the atmospheric and ionospheric scale heights. Assuming an effective scale height for the ionospheric Pedersen conductivity of $\tilde{H}$=90 km in the analytic model (with an atmospheric scale height H_a=145 km and plasma scale height H_e=240 km, see Equation (4.7)) leads to a steep gradient in the conductances and thus also to a steep gradient in the magnetic field. The gradients are consistent with the measured magnetic field data. An effective scale height larger than 90 km results in a decrease of the steepness of the gradient and does not fit the measured data very well anymore. The atmospheric and plasma scale heights are variable with the distance from Europa because they are influenced by heating and cooling of the atmosphere and ionization, recombination and transport processes in the ionosphere. The variability of the scale height could be an explanation for the perturbation structure in B_x seen in the observed data between 03:50 UT and 03:56 UT. We can not rule out that the steep gradient still contains a contribution due to a strongly asymmetric atmosphere, e.g., due to a plume in the northern hemisphere or on the upstream side of the southern hemisphere, since the jumps in the magnetic field data coincide with the location of the hemisphere coupling currents. As we already discussed in Section 6.1.5, it is difficult to separate between the atmospheric effect (i.e., the jump in the vertical column density through a radially symmetric atmosphere at the limb of the moon) and the hemisphere coupling effect in the jump of the magnetic field. High time resolution data would therefore help to further disentangle these effects.

Another possible explanation for steep gradients in the magnetic field could in principle be surface current balance. Teolis et al. (2014) explain the sharp magnetic perturbations seen at the edge of the Rhea fluxtube with a current system that results from the difference of ion and electron gyroradii and the balance of currents on Rhea's surface. We estimated this effect for Europa by approximating this surface current with

$I_{\text{surface}} = ne\alpha_{\text{plasma}}v_0 2R_E r_g$. The parameter $n \approx 95$ cm^{-3} is the plasma number density, $\alpha_{\text{plasma}}v_0 \approx 0.4 \times 100$ km/s the perturbed plasma bulk velocity near the surface and $2R_E r_g$ the effective cross sectional area of the pickup ions. Due to the higher upstream plasma mass density during this flyby than in the general model scenario the plasma interaction is stronger and the interaction factor is lower ($\alpha_{\text{plasma}} \approx 0.4$). The gyroradii of the O_2^+ ions can be approximated by $r_g = m_{O_2^+}/(eB)\alpha_{\text{plasma}}v_0 \approx 30$ km. The estimated value for the surface currents is then 5.6×10^4 A. The maximum total current closing through Europa's atmosphere can be estimated by a value of $2 \times 5 \times 10^5$ A (see Section 6.1.3) if we assume that the spatial structure of the surface current is similarly wide structured as the ionospheric currents. With this estimate, the surface currents could generate an effect of ∼6% of the perturbation that is generated by the Alfvén currents. However plasma variables are more variable around Europa compared to our estimate and therefore more detailed studies are required for a refined quantitative calculation of surface charging effects (similar to Teolis et al. (2014)). A detailed study has to be done as it was made for Rhea in the work of Teolis et al. (2014).

6.2.2. Europa Flyby E25A

The flyby E25A occurred at a large distance of $\sim$ 5.5 R_E when Europa was located outside the plasma sheet. Galileo passed downstream through the northern Alfvén wing nearly radially towards Jupiter. The resolution is low compared to the other flybys with ∼140 km between two data points and therefore insufficient to resolve the high-frequency perturbations or steep gradients due to hemisphere coupling currents if a strongly asymmetric atmosphere existed at that time. Since the flyby occurred in the Alfvénic far field of the moon it is not influenced by the effects of the ionospheric currents and therefore particularly well suited for the application of the analytic model. The measured data (black line) presented in Figure 6.9 shows a perturbation of the magnetic field in the negative x direction due to the bending of the magnetic field lines in the northern Alfvén wing. The magnetic field signatures are better reproduced by our analytic model (see Figure 6.9a) when a local inhomogeneity is included in the northern hemisphere in a global radially symmetric atmosphere (red line). The atmospheric inhomogeneity is located at the north pole and has a radial extent of about 0.8 R_E. The conductance of the inhomogeneity (Σ_P^p=4 S) at this location is more than twice as large as the conductance of the global atmosphere (Σ_P^n=1.5 S). The values of the magnetic field along the trajectory indicate that the enhancement of the atmospheric density in the area of the inhomogeneity is not that significant as it is, e.g., for an inhomogeneity with γ=50% and Σ_P^p=15 S as presented in Figure 6.5a. The contribution of the denser north polar inhomogeneity and especially the ionospheric Hall effect generate the local perturbation of ∼20 nT in B_y at 16:38 UT in our analytic model. Also the direction of the perturbation of the B_z component is consistent with the observed data.

Figure 6.9b shows the results from our MHD model with a radially symmetric at-

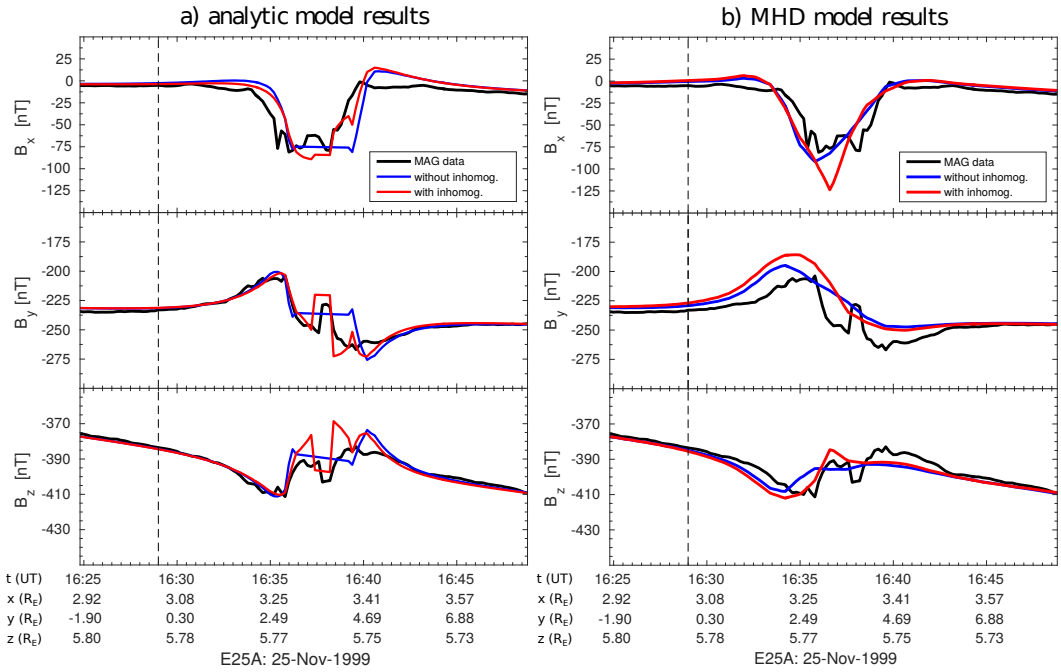

Figure 6.9. – Magnetic field components along the E25A flyby trajectory in the EPHIO coordinate system. (a) Comparison between the Galileo MAG data (black lines) and the results obtained from the analytic model where a north polar inhomogeneity in a global atmosphere (red lines) with r_s=1 R_E, r_p=0.8 R_E, $\Sigma_P^s = \Sigma_P^n$ =1.5 S, Σ_P^p=4 S, Σ_P^a=2 S, $\Sigma_H^p = 3.5$ S, $\Sigma_H^s = \Sigma_H^n = \Sigma_H^a$=0 S is considered. For further information see Figure 6.8. b) Comparison between the Galileo MAG data (black lines) and the results obtained from the MHD model where a radially symmetric atmosphere (blue lines) is considered. The red lines show the model results with an inhomogeneity at the north pole (θ=0°) in the radially symmetric atmosphere. The dashed vertical line displays the closest approach at 16:29 UT, x=3.04 R_E, y=−0.23 R_E, and z=5.79 R_E.

mosphere (blue line) and results with a local inhomogeneity at the north pole in a radially symmetric atmosphere (red line). We do not have the ionospheric Hall effect included in the MHD model for Europa so that we can not confirm the significant influence of the Hall effect in the atmospheric inhomogeneity that we see in the results of the analytic model. Both results fit the global structure of the data and an atmospheric inhomogeneity is not indicated.

Although the analytic model results indicate the possibility of a local inhomogeneity in the northern hemisphere, it is not possible to draw clear conclusions on the existence of an inhomogeneity during this flyby. Other reasons causing the observed magnetic field signature could be perturbations of Jupiter's magnetosphere or small-scale dynamic plasma processes. Additionally, there are other magnetic field substructures along the flyby which are not explained by our analytic model.

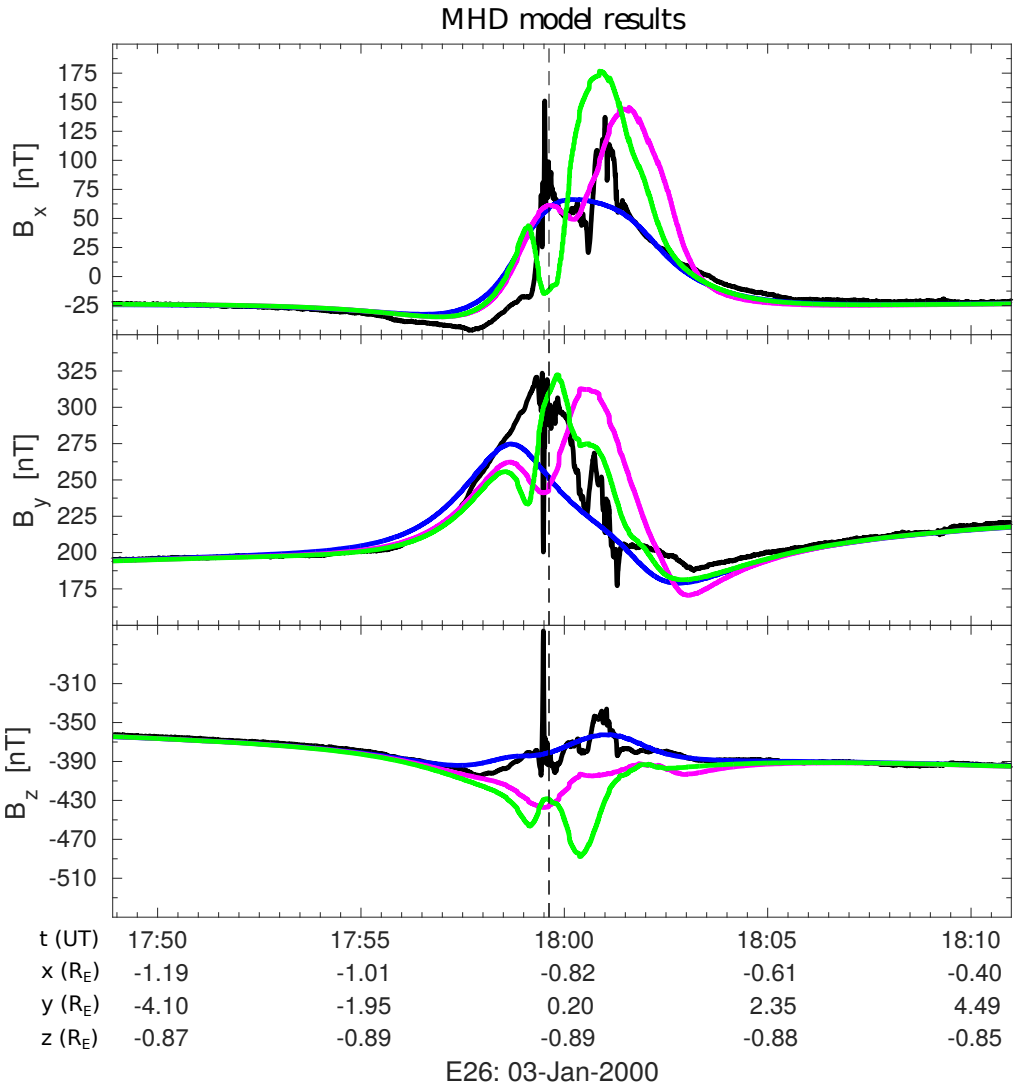

Figure 6.10. – Magnetic field components along the E26 flyby trajectory in the EPHIO coordinate system. Comparison between the Galileo MAG data (black lines) with the results from the MHD model where a radially symmetric atmosphere (blue lines) and different locations of the atmospheric inhomogeneities are considered. The magenta lines show the results with an inhomogeneity at ϕ=35° and θ=125° and the green lines with one at ϕ=55° and θ=135°. The dashed vertical line displays the closest approach at 17:59 UT, x=−0.83 R_E, y=0.04 R_E, and z=−0.89 R_E.

6.2.3. Europa Flyby E26

The E26 flyby was a south polar pass, upstream of the moon, and almost radially towards Jupiter. Europa was located south of Jupiter's magnetic equator in a low plasma density environment. The signals from induced magnetic fields are particularly strong during this flyby. This pass occurred very close to the moon with a closest approach altitude of ∼340 km. The analytic model is not applicable here because at this altitude the interaction is not purely Alfvénic, and additionally to the Alfvénic currents, ionospheric currents also modify the magnetic field environment. The black line in Figure 6.10 shows the measured data during E26. The perturbations in the

B_x component in the interaction region are similar to the perturbations during the E17 flyby. The B_x component is affected by the bendback of the southern Alfvén wing resulting in a slight decrease shortly before the Alfvén wing entry at 17:59 UT and a global enhancement of B_x during the Alfvén wing crossing. The rotation of B_y and B_z is the result of the influence of the induced magnetic field and the ionospheric currents. The B_x component shows a strong gradient with an increase from -14 nT to 150 nT during the Alfvén wing entry similar to the E17 data. The strong increase of the B_x component takes place over 19 s (57 data points), which corresponds to a length scale of 152 km of the moving spacecraft. Inside the interaction region all three magnetic field components show a very disturbed structure. Outside of the interaction region the data shows a smooth trend indicating a fairly quiet magnetic field environment during this flyby.

The MHD model results from a simulation with a radially symmetric atmosphere (blue line in Figure 6.10) fit the overall signature very well similar to the results of Schilling et al. (2007) and Rubin et al. (2015). A prominent double-peak structure is evident in the measured B_x component. Neither Schilling et al. (2007) nor Rubin et al. (2015) could fit this double-peak signature with a global atmosphere. When we include a dense inhomogeneity on the southern hemisphere (longitude ϕ=35° and colatitude θ=125°) within the atmosphere, our model is able to produce a double-peak structure in B_x but width and amplitude differ compared to the observations (see magenta line in Figure 6.10). The first peak in our model is a result of the maximum of B_x that occurs in the southern main wing and the second peak is a result of the maximum in the southern Alfvén winglet. The ionospheric closure currents increase the effect of the atmospheric inhomogeneity. The B_y component of the model with an atmospheric inhomogeneity is also perturbed on smaller scales compared to the model with a radially symmetric atmosphere. By shifting the location of the inhomogeneity more to the upstream side at the longitude ϕ=55° and colatitude θ=135° (green line) the double-peak structure changes. The B_y component provides a better fit to the data but the perturbation of the B_z component in the MHD model is not in agreement with the measured perturbation. Hence, the exact magnetic field signature is very sensitive to the location of the prescribed atmospheric inhomogeneity. The modifications of the magnetic field due to the variation of the location of the atmospheric inhomogeneity is shown in Figure 6.11. It displays the magnetic field components in the xy plane at the altitude $z = -0.89\ R_E$ for the three different cases discussed in Figure 6.10. The inhomogeneity generates an area of enhanced B_x and B_z in this plane (see Figures 6.11b, top, bottom, 6.11c, top, bottom). B_y is influenced by the induced field at this altitude (see Figure 6.11a, middle). The inhomogeneity modifies the plasma flow and thus also the resultant magnetic perturbations and associated electric currents. Both the induced fields and the magnetic field perturbation contribute to the structure in B_y seen in Figures 6.11b (middle) and 6.11c (middle).

Although the model is not able to reproduce the exact structure of the magnetic

field perturbations during this flyby, it suggests that a dense and localized inhomogeneity in the atmosphere could perturb the magnetic field on smaller scales with a similar orientation like the observed perturbations. The large number of possibilities to describe

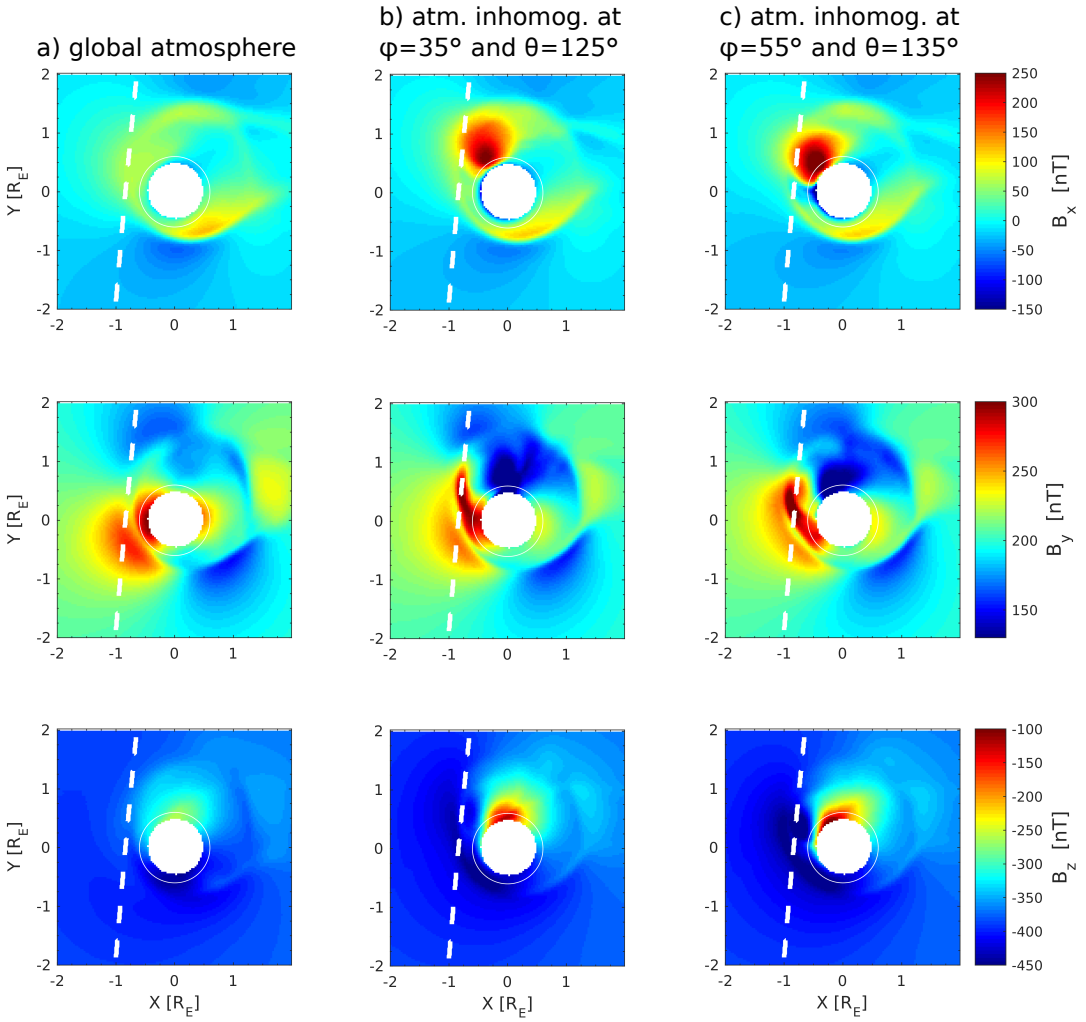

Figure 6.11. – Magnetic field components in the xy plane at z=−0.89 R_E for three different MHD model runs (see Figure 6.10) with a radially symmetric atmosphere (a) and additional atmospheric inhomogeneity at different locations ((b) and (c)) during the E26 flyby. The dashed white line shows the trajectory of E26.

such an inhomogeneity with the free parameters like the latitudinal extent, density, scale height and position and also the number of inhomogeneities makes it difficult to find the best fit parameters for the data. During the flyby, Europa was at an orbital true anomaly of 216° similar to the true anomaly during the December 2012 HST observations when the plume was identified. Tensile stresses on polar fractures and fractures around the leading and trailing meridians are expected to be highest when Europa is located in the apocenter of its orbit (Roth et al., 2014a). The plumes that are included in our model are located in the southern hemisphere between the equator and the south pole and between the sub-Jovian and the leading side. Therefore, a clear correlation between

the stresses for a certain true anomaly and the possible occurrence of atmospheric inhomogeneities is not given here.

It is also possible that other effects play a role in the modification of the magnetic field that we have not included in our MHD model such as the ionospheric Hall effect, solar illumination, or day-night asymmetry. Plainaki et al. (2013) demonstrate that the spatial distribution of Europa's atmosphere depends on the time-varying relative orientations of solar illumination and the incident plasma direction. Their study suggests an increase in the atmospheric density by a factor of $\sim$4 depending on the configuration between the Sun and Europa. But their model does not produce sharp gradients in the neutral density. Solar illumination, according to their model, would produce a more global asymmetry which would appear not to be the reason for the generation of such an inhomogeneous localized structure in the magnetic field components. But further modeling of Europa's atmosphere is required to better understand the real spatial structure of its atmosphere. Besides the atmospheric and ionospheric effects, sudden magnetospheric effects (e.g., flux tube interchange, pressure balanced structures) during the time of the flyby could also affect the observed magnetic field. Therefore, the magnetic field data needs to be interpreted with caution and it is not possible to derive a rigorous conclusion about an atmospheric inhomogeneity during this flyby. Velocity and plasma pressure data, if available, would be very helpful for the interpretation of the plasma interaction. The analysis of plasma data would serve to separate between Alfvénic and magnetospheric effects, e.g., pressure balanced structures during the flyby. An asymmetric atmosphere, e.g., due to the plumes, is expected to produce Alfvénic perturbations, which are visible in the velocity and magnetic field data in the far field in a distinctly correlated way. Magnetospheric perturbations would be present in the magnetic field, density, and plasma pressure data in a different way.

The MAG data from the E26 flyby indicates puzzling features in the plasma interaction close to the moon such as the strong peaks in the magnetic field components at the closest approach. These peaks coincide with the location of very intense whistler mode emissions (see therefore Kurth et al., 2001). Both features are probably linked to each other and deserve further investigations.

7. Summary

In this thesis we deal with the modeling of Io's and Europa's plasma interaction with an inhomogeneous atmosphere. We present a study of the influence of inhomogeneities in Io's and Europa's atmospheres, such as plumes, on the interaction between the corotating magnetospheric plasma and the satellites' atmospheres. To model the satellite's interaction, we apply two different approaches, a 3-D MHD approach applied to Io and Europa, and an analytic approach used for further discussions on the influence of plumes on Europa. The MHD model considers self-consistently physical processes of the plasma interaction and includes plasma production, and loss, due to electron impact ionization and dissociative recombination, respectively. Moreover, it considers induction in a subsurface water ocean at Europa. The analytic approach to describe the effects of a local inhomogeneity is based on the model for sub-Alfvénic nonsymmetric interaction by Saur et al. (2007) which we expand and solve for conditions adopted to Europa. The analytic calculations support the MHD model results and provide additional insight into the influence of local inhomogeneities when embedded in Europa's global atmosphere, e.g., the ionospheric Hall effect and discontinuities associated with the hemisphere coupling due to a strong asymmetric atmosphere.

By applying these models, we demonstrate that atmospheric inhomogeneities do not only have an effect on the plasma and magnetic field environment near the satellites but also affect the Alfvén wings in the far field. This effect is strongly developed at Europa and less developed at Io due to the different densities of the atmospheres and plumes. Our study shows that an inhomogeneity in the atmosphere located near the poles causes a pronounced north-south asymmetry in the Alfvén wings and the development of an Alfvén winglet within the Alfvén wing which is connected to the hemisphere with the inhomogeneity. The global form of the Alfvén wings does not change since the Alfvén velocity in the far field is unaffected by the distribution of the neutral density in the atmosphere.

Io's atmospheric density has been investigated by various observations and methods revealing a dense atmospheric ring around the equator with pronounced longitudinal asymmetries. Local density enhancements at volcanically active regions might be present in addition. For Io we consider different atmosphere models with latitudinal and longitudinal asymmetries. Including local volcanic plumes, we show that such local density enhancements influence the plasma interaction locally but do not significantly

change the mass supply rate to the plasma torus. We estimate that the injected neutrals, associated with a volcanic plume, contribute by less than 7 % to the total atmospheric sputtering rate. For our studies we consider the locations and magnitudes of three of the largest observed volcanic plumes on Io: Pele, Tvashtar, and Thor. While volcanic plumes near the poles, such as the Tvashtar plume, produce visible effects in the magnetic and velocity field in the Alfvénic far field, plumes located near the equatorial latitudes barely produce any signals in the magnetic and velocity fields because of the dense ambient atmosphere around Io's equator. However the global dense equatorial atmosphere dominates the interaction and weakens the effect of plume signals in the Alfvénic far field.

We investigate if signatures of volcanic plumes are locally detectable and visible in magnetic field measurements of the Galileo Magnetometer during the I31 flyby. Our modeling shows inconclusive results since the weak amplitudes of the plume signals in the magnetic field data are of similar magnitudes as the small-scale fluctuations produced by intense wave emissions on top of the main magnetic field perturbations.

We demonstrate that significant parts of the magnetic field perturbations measured during the Galileo flybys I24 and I27, associated with the induction signals from a subsurface magma ocean by Khurana et al. (2011) can alternatively be explained by considering global asymmetries of the atmosphere. Therefore we analyze the effects of an asymmetric atmosphere on Io's plasma environment during the flybys I24 and I27 by using different atmosphere models with longitudinal and latitudinal dependencies in our MHD model. Additionally to the magnetic field data, we use plasma data measured with the PLS and PWS instrument during the flybys in order to verify whether the simulations provide reliable and consistent results which agree with several independent in situ measurements.

We also apply our MHD model to Europa. At Europa the effect of atmospheric inhomogeneities is more important than at Io due to its thinner atmosphere and the very dense plume relative to its global atmosphere. Our MHD model results show that in the presence of a global atmosphere with a surface density of $\sim$5 $\times$ 10^{13} m^{-3} and a plume with a surface density of $\sim$1.6 $\times$ 10^{15} m^{-3}, a height of 200 km, and a latitudinal extent of $15°$, the plasma velocity experiences a decrease up to 95% of the upstream velocity in the Alfvén winglet and a decrease up to 60% of the upstream velocity in the ambient Alfvén wing. The magnetic field perturbations are stronger in the Alfvén winglet with up to 120 nT than in the ambient southern Alfvén wing with 40 nT in the positive x direction.

According to our analytic model results, Europa's global atmosphere weakens the effect of the hemisphere coupling and generates steep gradients in the magnetic field. Unlike Enceladus, which lacks a global atmosphere and where the plasma interaction is driven by the plumes, Europa's global atmosphere has a huge effect on the plasma

interaction. Our analytic model results show that the resultant discontinuities for a plume that contains 50% of the mass content of Europa's atmosphere would only contribute with $\sim$5% to magnetic field amplitudes generated by the global atmosphere. Within the temporal resolution of the available data, such a discontinuity is difficult to detect given the additional steep gradients due to the global atmosphere.

Additionally, we investigate if signatures of atmospheric inhomogeneities are locally detectable and visible in magnetic field measurements of the Galileo Magnetometer. Therefore, we compare the MHD and analytic model results with the observed magnetic field data from three flybys of Europa which include Alfvén wing crossings: E17, E25A, and E26.

Our results demonstrate that the perturbations during the E17 flyby do not show signals from local inhomogeneities in the atmosphere and can be explained by a plasma interaction with a radially symmetric atmosphere. The steep gradient in the magnetic field at the location of the Alfvén wing entry seen in the data provides information about the scale height of the atmosphere and the ionosphere. According to the analytic model results an effective scale height of about 90 km fits the measured steep gradient in the data very well.

The measurements during the E25A flyby in the Alfvénic far field, in particular the B_y, component could be weakly influenced by an inhomogeneous atmosphere in the northern hemisphere especially by the ionospheric Hall effect according to the analytic model results. However, the modeling is inconclusive as discussed earlier. The MHD model results can not reproduce the B_y perturbations since the ionospheric Hall effect is not included in the MHD model for Europa.

Our analysis demonstrates that the magnetic field perturbations during the E26 flyby could be consistent with an atmospheric inhomogeneity on the southern hemisphere between the upstream and the Jupiter-facing side according to our results. The extent of the inhomogeneity in our model is similar to the plume derived by Roth et al. (2014b). The inhomogeneity contains 50% of the gas content of the total atmosphere. The results also show that the magnetic field perturbation is very sensitive to the shape and the location of the inhomogeneity. However, we cannot exclude other effects which might cause comparable magnetic field perturbations, e.g., atmospheric day-night asymmetries, magnetospheric pressure balanced structures being convected over Europa or, flux tube interchange. With the previous searches (Roth et al., 2014b,a) the occurrence patterns of plumes could not be unveiled. The plumes could be sporadic events on unknown time scales and with uncertain locations. These temporal and spatial variabilities make the development of observational strategies difficult. The present study provides ideas how a future spacecraft mission to Europa could be able to de-

tect and distinguish signals from plumes in the measured magnetic field and plasma data.

A more comprehensive data set recorded with sufficient time resolution is required such as the data set which will be taken by the planned Europa Mission. The results will therefore be helpful for the search of plumes at Europa during the JUICE mission of ESA and the Europa mission of NASA. Our findings suggest that signals from the plume can be detected in the magnetic field, the velocity field, and the density. Due to the locally increased neutral density in the atmosphere when a plume is present, collisional and mass loading processes increase at the location of the plume causing a local perturbation of the plasma parameters. The requirement for the detection of local plumes in the measured plasma density is that the spacecraft passes the center of the plume in the near field as close as possible. Plumes can also be detected on distant flybys in the Alfvénic far field. The local perturbation in the velocity and magnetic field due to the plume in the satellite's near field maps out into the Alfvén wing along the Alfvén characteristics. To achieve a pronounced signal from the plume in the Alfvén wing, it is important that the spacecraft trajectory crosses the center of the characteristics which are connected to the center of the plume, i.e., crosses the center of the Alfvén winglet that maps to the center of the plume. The farther away the spacecraft passes the center of the winglet, the more complicated is the detection of plume signals in the data especially when an additional global asymmetry of the atmosphere is present as predicted by, e.g., Pospieszalska and Johnson (1989) or Plainaki et al. (2013) for Europa. Both velocity and magnetic field measurements are required to distinguish between a pure Alfvénic structure such as generated by a plume and magnetospheric structures that are convected across Europa and its Alfvén wings. Alfvénic structures generated at the satellite will obey the relationship $\delta\underline{B} = \pm\sqrt{\mu_0\rho_0}\,\delta\underline{v}$, while convecting magnetospheric signatures might simply be pressure-balanced structures. A perturbation in the density in the far field due to the plume will not or only barely be visible.

A. Appendix

A.1. Scale Analysis of the MHD Equations

We perform a scale analysis to estimate the importance of each term in the set of Equations (3.7)–(3.10). Therefore, we apply typical values of each plasma variable to evaluate the typical scale of each term in equations (3.7)–(3.10). Typical values in Europa's and Io's plasma environments used for our estimations are summarized in Table A.1. Typical

Table A.1. – Typical values for each plasma variable

Plasma Variable	Europa	Io
v_0, Plasma bulk velocity	104 km s^{-1}	57 km s^{-1}
R_{sat}, Europa's radius	1569 km (R_E)	1821 km (R_{Io})
B_0, Background magnetic field	4.5×10^{-7} T	2×10^{-6} T
ρ_0, Plasma mass density	4.93×10^8 amu m^{-3}	3.1×10^{10} amu m^{-3}
$k_B T_e$, Electron temperature[b]	100 eV	5 eV
$k_B T_i$, Ion temperature[b]	100 eV	70 eV
m_i, Ion mass[c]	32 amu (O_2^+)	64 amu (SO_2^+)
m_n, Mass of the neutrals	32 amu (O_2)	64 amu (SO_2)
$p_e = n_e k_B T_e$, Pressure of electrons (thermal)[a]	0.6 nPa	1.3 nPa
$p_i = n_i k_B T_i$, Pressure of ions (cold plasma)[a]	0.4 nPa	26.1 nPa
T_n, Temperature of the neutral gas	130 K	120 K
$\tilde{\nu}_{\rm in}$, Momentum transfer collision frequency[d,e]	0.1 Hz	5 Hz
$\nu_{\rm en}$, Electron-neutral collision frequency[e,f]	0.02 Hz	220 Hz
L, Recombination rate, eq. (3.31) [g]	40.2 m^{-3} s^{-1}	6.4×10^5 m^{-3} s^{-1}
P, Production rate, eq. (3.19) [e,h]	2.4×10^7 m^{-3} s^{-1}	1.6×10^9 m^{-3} s^{-1}

[a] $\rho = \tilde{m}_i\, n_e/1.5$

[b] Kivelson et al. (2004), Sittler and Strobel (1987)

[c] Here, the ion species we take to be O_2^+ and SO_2^+ in the close vicinity of the moon which is different from the impinging torus plasma.

[d] For Europa calculated with Equations (3.39), (3.40) and for Io taken from our simulations.

[e] In the calculations, a neutral number density $n_A(h = 100\text{ km}) = 1.8 \times 10^{13}$ m^{-3} for Europa and $n_A(h = 100\text{ km}) = 3.7 \times 10^{14}$ m^{-3} was used.

[f] $\nu_{\rm en} = 1 \times 10^{-15} n_A$ after Schilling et al. (2007) for Europa.
$\nu_{\rm en} = 4/3 n_A \sigma_{en} \sqrt{8 k_B T_e/(\pi m_e)}$ in cgs-units (Banks and Kockarts, 1973) with the elastic electron-SO_2 cross section $\sigma_{en} = 3 \times 10^{-19}$ m^2 (Moore et al., 2010) for Io.

[g] For the calculation of $\alpha_{\rm rec}$ (Equation (3.41), (3.35)) the temperature of the ionospheric electrons (0.5 eV for Europa and 0.2 eV for Io) was used.

[h] $f_{\rm imp,0}(T_e = 100\text{ eV}) = 0.83 \times 10^{-13}$ $m^3 s^{-1}$ (O_2) for Europa and $f_{\rm imp,0}(T_e = 5\text{ eV}) = 1.8 \times 10^{-15}$ $m^3 s^{-1}$ (SO_2) for Io was applied.

scales for each term of the continuity (3.7), momentum (3.8), induction (3.9), and energy

density equation (3.10) are presented in Tables A.2–A.5, respectively. In these Tables the terms which are considered to be negligible are separated from the ideal MHD terms and other important terms by a blue horizontal line. In the next step, we remove the terms pertaining to small scales, because they do not alter the important physics of our model. Although, the loss terms in the continuity (3.7) and energy density Equations (3.10) are of insignificant scales, we included them in our MHD equations, because they have been traditionally included in modeling of Europa's and Io's interaction (e.g., Saur et al., 1998, Schilling et al., 2007, Rubin et al., 2015, Linker et al., 1998, Saur et al., 1999). Finally, we end up with the simplified set of Equations (3.14)–(3.17) of our MHD model which we present in Section 3.2. Note that we neglect electrons in our model although electron-neutral collisions could be important in particular in regions of volcanic eruptions near Io's surface (Neubauer, 1998).

Table A.2. – Typical scales for each term of the continuity equation[a]

Term	Europa	Io
$\partial_t \rho$[b]	1.0×10^0	1.0×10^0
$\nabla \cdot (\rho \underline{v})$	1.0×10^0	1.0×10^0
$m_i P$	2.3×10^1	1.1×10^2
$m_i L$	3.9×10^{-5}	4.3×10^{-2}

[a]The terms below the blue horizontal line can be neglected because their typical scales are very small.
[b]The values were normed so that $\partial_t \rho$ is 1.

Table A.3. – Typical scales for each term of the velocity equation[a]

Term	Europa	Io
$\rho \partial_t \underline{v}$[b]	1.0×10^0	1.0×10^0
$\rho \underline{v} \cdot \nabla \underline{v}$	1.0×10^0	1.0×10^0
∇p	1.2×10^{-1}	1.7×10^{-1}
$\underline{j} \times \underline{B}$	1.8×10^1	1.7×10^1
$m_i P \underline{v}$	2.3×10^1	1.1×10^2
$\rho_i \tilde{\nu}_{in} \underline{v}$	2.1×10^0	1.6×10^2
$\rho_e \nu_{en} \underline{v}$	1.2×10^{-5}	3.1×10^{-1}
$\frac{m_e}{e} \tilde{\nu}_{in} \underline{j}$	3.1×10^{-5}	2.6×10^{-4}
$\frac{m_e}{e} \nu_{en} \underline{j}$	4.2×10^{-6}	1.1×10^{-2}
$\frac{m_e}{e^2} \underline{j} \cdot \nabla \left(\frac{\underline{j}}{n} \right)$	5.2×10^{-6}	6.0×10^{-8}

[a]The terms below the blue horizontal line can be neglected because their typical scales are very small.
[b]The values were normed so that $\rho \partial_t \underline{v}$ is 1.

Table A.4. – Typical scales for each term of the induction equation[a]

Term	Europa	Io
$\partial_t \underline{B}$[b]	1.0×10^{0}	1.0×10^{0}
$\nabla \times (\underline{v} \times \underline{B})$	1.0×10^{0}	1.0×10^{0}
$\nabla \times \left(\frac{1}{ne}\nabla p_e\right)$	1.4×10^{-3}	2.5×10^{-5}
$\nabla \times \left(\frac{1}{ne}\underline{j} \times \underline{B}\right)$	3.4×10^{-1}	3.7×10^{-2}
$\nabla \times \left(\frac{m_e}{e}\tilde{\nu}_{in}\underline{v}\right)$	1.7×10^{-6}	1.5×10^{-5}
$\nabla \times \left(\frac{m_e}{e}\nu_{en}\underline{v}\right)$	2.3×10^{-7}	6.6×10^{-4}
$\nabla \times \left(\frac{1}{ne}\nabla\frac{m_e}{m_i}p_i\right)$	1.6×10^{-8}	2.9×10^{-9}
$\nabla \times \frac{m_e}{ne^2}\partial_t \underline{j}$	2.9×10^{-7}	3.5×10^{-9}
$\nabla \times \frac{m_e}{ne^2}\nabla \cdot (\underline{v}\,\underline{j})$	2.9×10^{-7}	3.5×10^{-9}
$\nabla \times \frac{m_e}{ne^2}\nabla \cdot (\underline{j}\,\underline{v})$	2.9×10^{-7}	3.5×10^{-9}
$\nabla \times \left(\frac{m_e}{ne^2}\nu_{en}\underline{j}\right)$	8.0×10^{-8}	2.5×10^{-5}
$\nabla \times \frac{m_e}{ne^2}\nabla \cdot \left(\frac{1}{en}\,\underline{j}\,\underline{j}\right)$	9.8×10^{-8}	1.3×10^{-10}
$\nabla \times \left(\frac{m_e}{ne^2}\left(\frac{m_e}{m_i}\tilde{\nu}_{in}\right)\underline{j}\right)$	1.0×10^{-11}	4.8×10^{-12}
$\nabla \times \left(\frac{m_e}{n^2e^2}L\underline{j}\right)$	4.4×10^{-12}	2.9×10^{-11}

[a]The terms below the blue horizontal line can be neglected because their typical scales are very small.
[b]The values were normed so that $\partial_t \underline{B}$ is 1.

Table A.5. – Typical scales for each term of the energy equation[a]

Term	Europa	Io
$\partial_t \epsilon$[b]	1.0×10^{0}	1.0×10^{0}
$\nabla \cdot (\epsilon \underline{v})$	1.0×10^{0}	1.0×10^{0}
$p\nabla \cdot \underline{v}$	6.7×10^{-1}	6.7×10^{-1}
$\frac{1}{2}m_i P v^2$	6.4×10^{1}	2.1×10^{2}
$\frac{\tilde{\nu}_{in}\rho}{m_i+m_n}m_n v^2$	5.7×10^{0}	3.2×10^{2}
$\frac{\tilde{\nu}_{in}\rho}{m_i+m_n}3k_B T_i$	4.7×10^{-1}	4.4×10^{1}
$\frac{\tilde{\nu}_{in}\rho}{m_i+m_n}3k_B T_n$	4.9×10^{-5}	4.6×10^{-3}
$\frac{nm_e\nu_{en}}{m_e+m_n}m_n v^2$	2.6×10^{-5}	8.1×10^{-1}
$\frac{3k_B}{2e}\nabla \cdot \left(T_e\,\underline{j}\right)$	2.1×10^{-1}	2.6×10^{-3}
$\frac{1}{e}p_e\nabla \cdot \left(\frac{\underline{j}}{n}\right)$	2.1×10^{-1}	2.6×10^{-3}
$\frac{nm_e\nu_{en}}{m_e+m_n}3k_B T_e$	3.8×10^{-6}	5.6×10^{-3}
$\frac{3}{2}k_B L T_i$	9.1×10^{-6}	7.8×10^{-3}
$\frac{3}{2}k_B L T_e$	9.1×10^{-6}	3.9×10^{-4}
$\frac{\tilde{\nu}_{in}\rho}{m_i+m_n}2\frac{m_n m_e}{\rho e}\underline{j} \cdot \underline{v}$	1.7×10^{-4}	1.0×10^{-3}
$\frac{nm_e\nu_{en}}{m_e+m_n}\frac{2m_n}{ne}\underline{v} \cdot \underline{j}$	2.3×10^{-5}	4.5×10^{-2}
$\frac{3k_B}{2e}\nabla \cdot \left(\frac{m_e}{m_i}T_i\,\underline{j}\right)$	3.5×10^{-6}	4.4×10^{-7}
$\frac{nm_e\nu_{en}}{m_e+m_n}3k_B T_n$	4.3×10^{-10}	1.2×10^{-5}
$\frac{1}{e}\frac{m_e}{m_i}p_i\nabla \cdot \left(\frac{\underline{j}}{n}\right)$	2.3×10^{-6}	1.0×10^{-6}
$\frac{m_e}{n^2e^2}P\underline{j}^2$	5.8×10^{-4}	1.1×10^{-5}
$\frac{nm_e\nu_{en}}{m_e+m_n}\frac{m_n}{n^2e^2}j^2$	1.2×10^{-5}	2.5×10^{-3}
$\frac{\tilde{\nu}_{in}\rho}{m_i+m_n}m_n\frac{m_e^2}{\rho^2e^2}j^2$	1.3×10^{-9}	8.2×10^{-10}

[a]The terms below the blue horizontal line can be neglected because their typical scales are very small.
[b]The values were normed so that $\partial_t \underline{\epsilon}$ is 1.

B. Io Flybys I24 and I27

Here, we present additional material for the discussion of the magnetic field model results along the trajectory of I24 and I27 in Chapter 5.2.

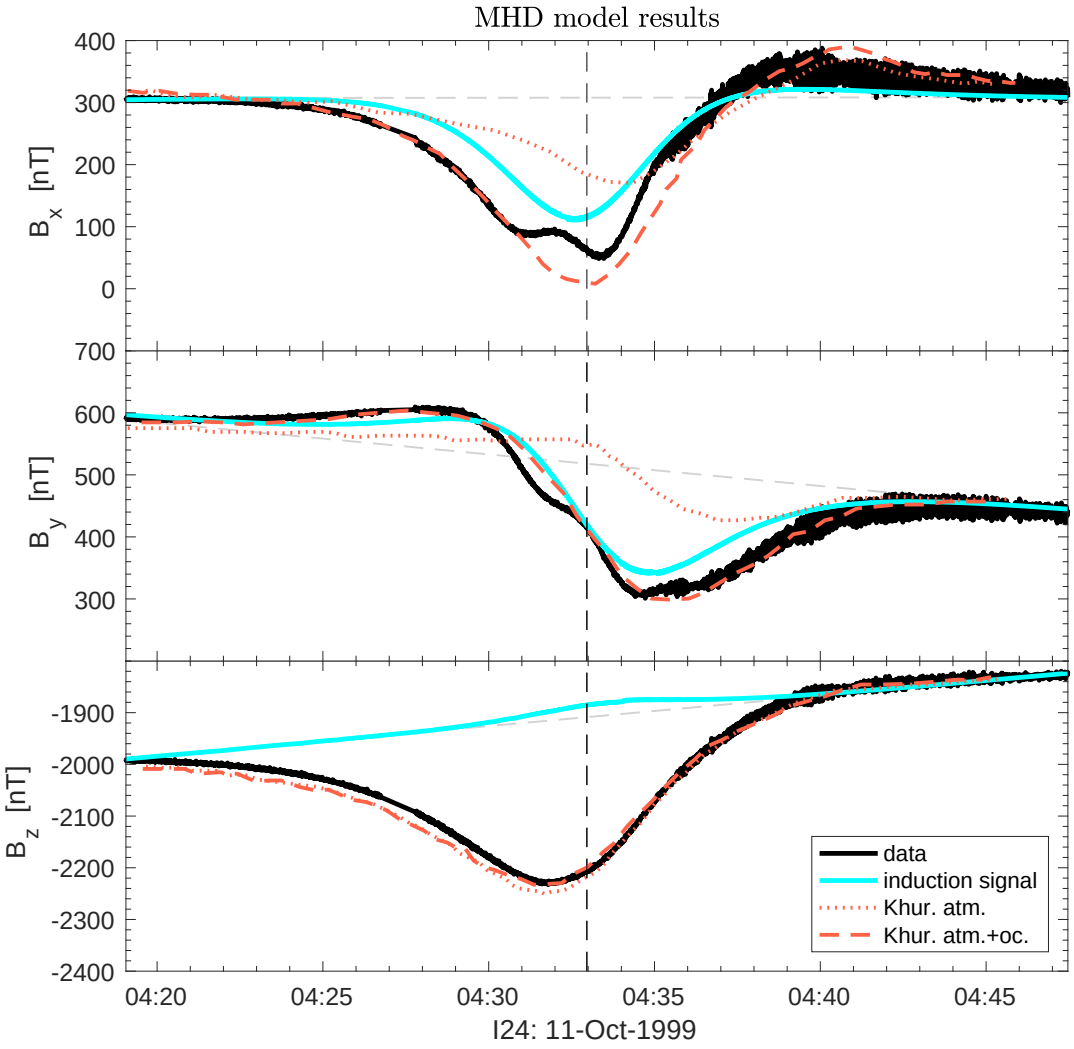

Figure B.1. – Magnetic field components along the I24 flyby trajectory in the IPHIO coordinate system. Comparison between the Galileo MAG data (black lines) and induction signal from a subsurface magma ocean derived by Khurana et al. (2011) (without plasma interaction). The dashed vertical line displays the closest approach at 04:33 UT, $x = -0.94\ R_{Io}$, $y = -0.94\ R_{Io}$, and $z = 0.1\ R_{Io}$. The dashed nearly horizontal line shows the background magnetic field. The dashed and dotted orange lines represent the model results of Khurana et al. (2011) with and without a subsurface magma ocean, respectively. The data was visually taken from Khurana et al. (2011).

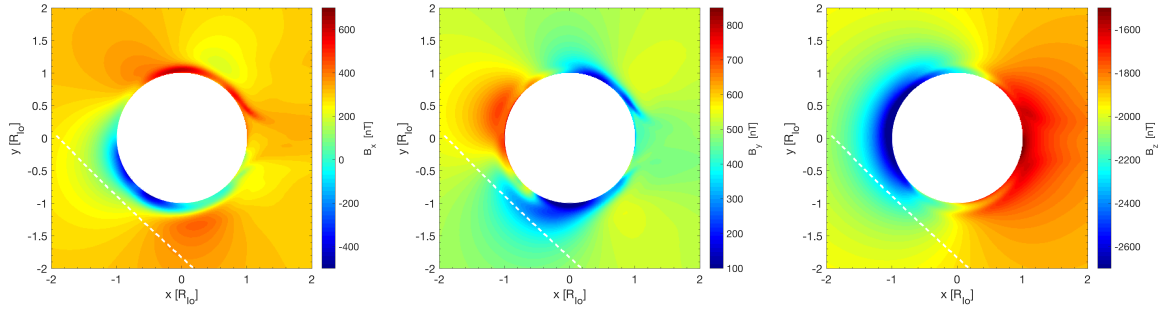

(a) Latitudinally asymmetric atmosphere (atm. model 1)

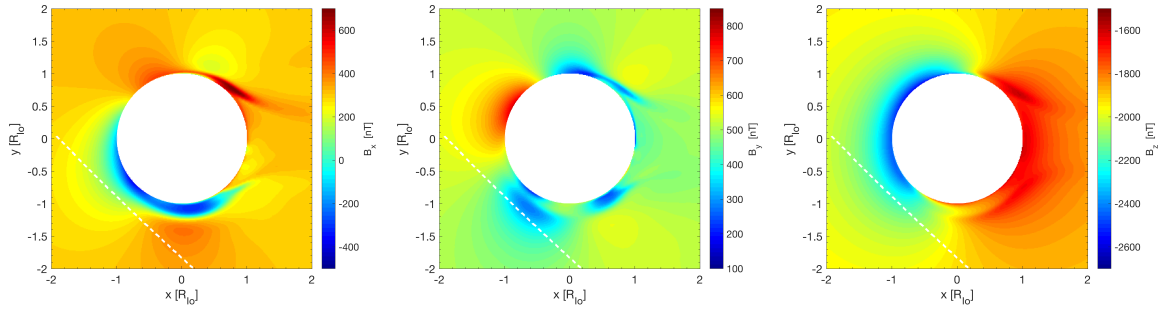

(b) Latitudinally and longitudinally asymmetric atmosphere (atm. model 2)

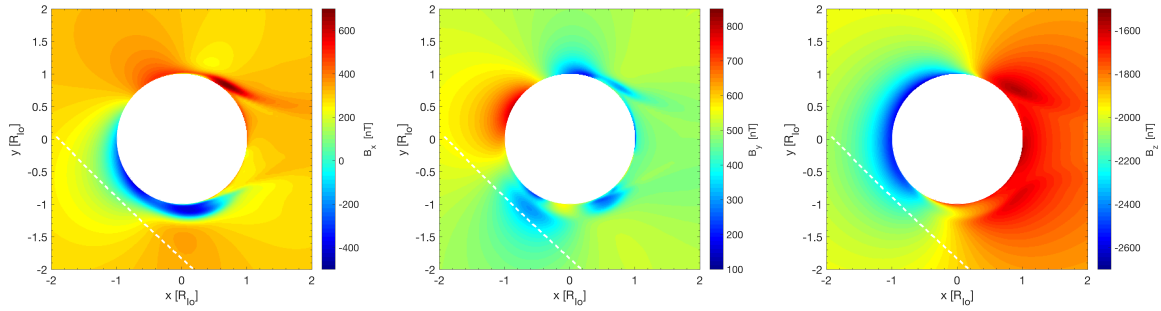

(c) Latitudinally and longitudinally asymmetric atmosphere and corona (atm. model 3)

Figure B.2. – Magnetic field components in the xy plane at $z = 0.1\ R_{Io}$ for three different MHD model runs with different atmospheric configurations (see Figure 5.11) during the I24 flyby. The dashed white line shows the trajectory of I24.

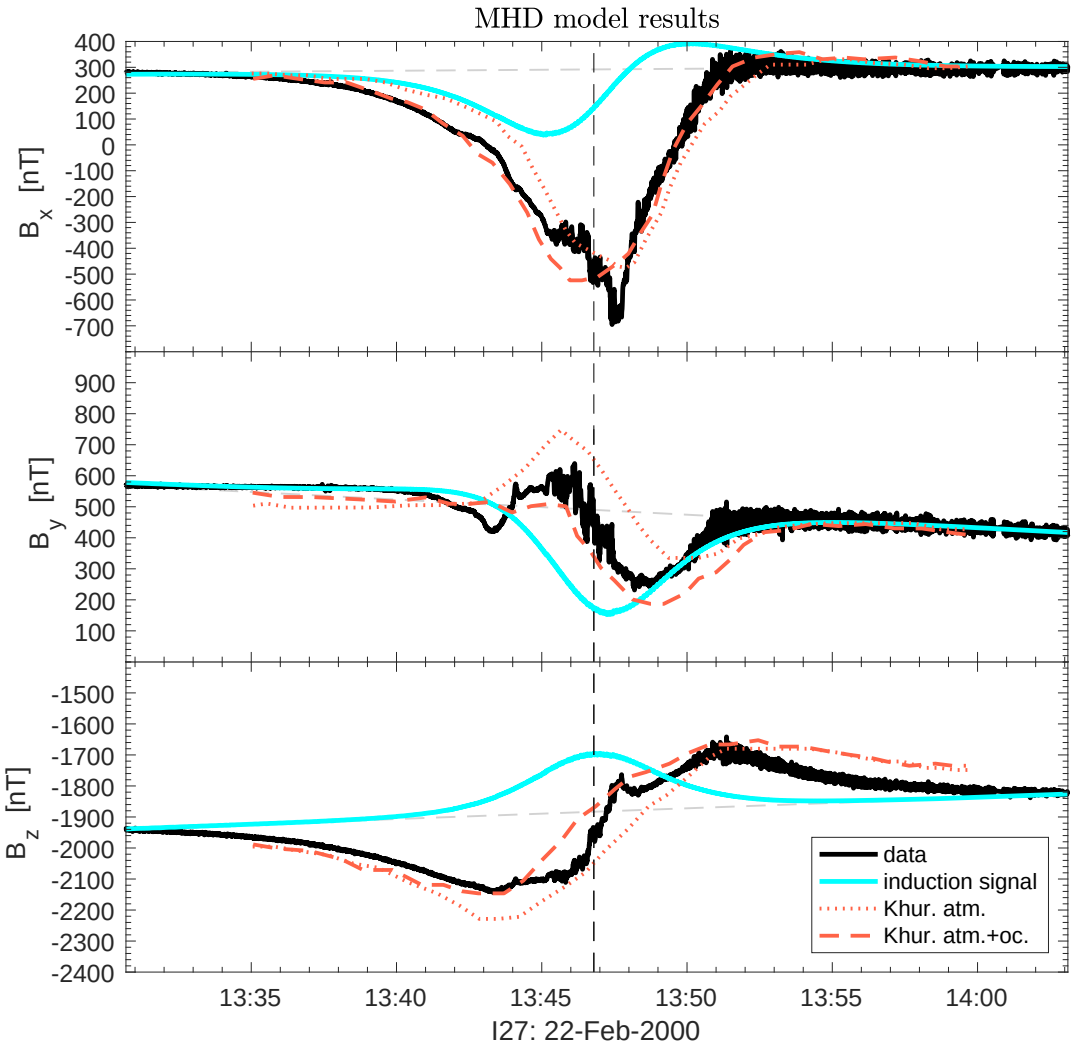

Figure B.3. – Magnetic field components along the I27 flyby trajectory in the IPHIO coordinate system. Comparison between the Galileo MAG data (black lines) and induction signal from a subsurface magma ocean derived by Khurana et al. (2011) (without plasma interaction). The dashed vertical line displays the closest approach at 13:47 UT, $x = -0.37\ R_{Io}$, $y = -0.98\ R_{Io}$, and $z = 0.35\ R_{Io}$. The dashed nearly horizontal line shows the background magnetic field. The dashed and dotted orange lines represent the model results of Khurana et al. (2011) with and without a subsurface magma ocean, respectively. The da was visually taken from Khurana et al. (2011).

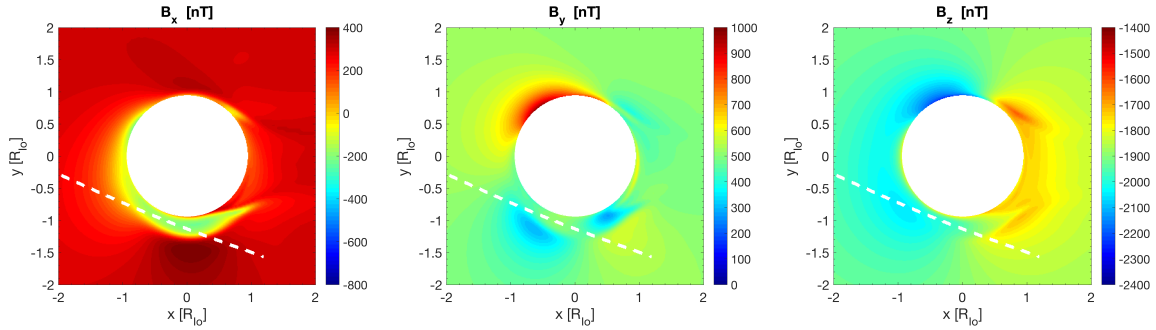

(a) Latitudinally and longitudinally asymmetric atmosphere (atm. model 2)

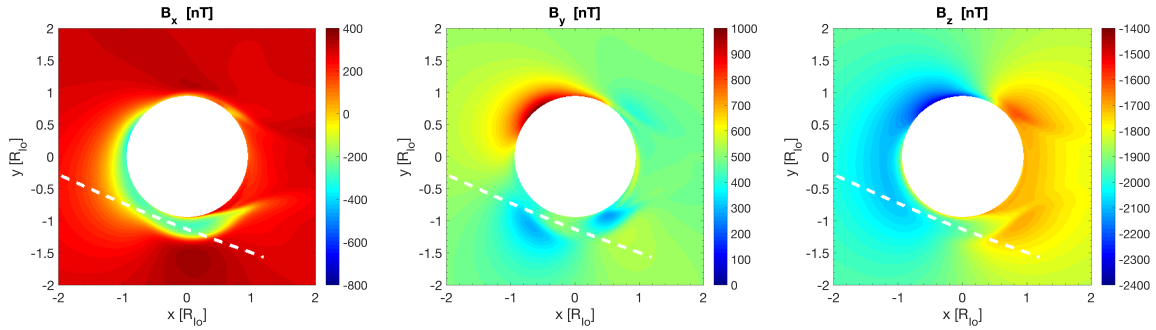

(b) Latitudinally and longitudinally asymmetric atmosphere and corona (atm. model 3)

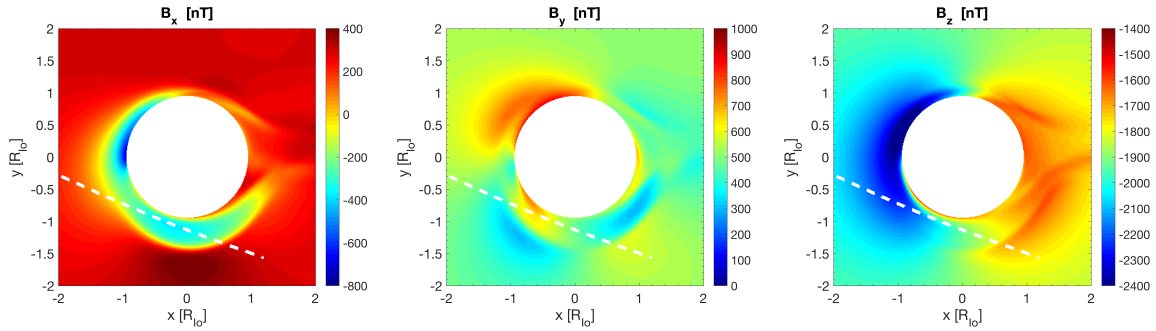

(c) Latitudinally and longitudinally asymmetric atmosphere (atm. model 4)

Figure B.4. – Magnetic field components in the xy plane at $z = 0.35\ R_{Io}$ for three different MHD model runs with different atmospheric configurations (see Figure 5.14) during the I27 flyby. The dashed white line shows the trajectory of I27.

List of Figures

List of Tables

References

M. H. Acuna, F. M. Neubauer, and N. F. Ness. Standing Alfven wave current system at Io - Voyager 1 observations. *Journal of Geophysical Research*, 86:8513–8521, September 1981. doi: 10.1029/JA086iA10p08513.

J. D. Anderson, E. L. Lau, W. L. Sjogren, G. Schubert, and W. B. Moore. Europa's differentiated internal structure: Inferences from two Galileo encounters. *Science*, 276: 1236–1239, May 1997. doi: 10.1126/science.276.5316.1236.

J. D. Anderson, G. Schubert, R. A. Jacobson, E. L. Lau, W. B. Moore, and W. L. Sjogren. Europa's Differentiated Internal Structure: Inferences from Four Galileo Encounters. *Science*, 281:2019, September 1998. doi: 10.1126/science.281.5385.2019.

F. Bagenal and P. A. Delamere. Flow of mass and energy in the magnetospheres of Jupiter and Saturn. *Journal of Geophysical Research (Space Physics)*, 116:A05209, May 2011. doi: 10.1029/2010JA016294.

F. Bagenal, E. Sidrow, R. J. Wilson, T. A. Cassidy, V. Dols, F. J. Crary, A. J. Steffl, P. A. Delamere, W. S. Kurth, and W. R. Paterson. Plasma conditions at Europa's orbit. *Icarus*, 261:1–13, November 2015. doi: 10.1016/j.icarus.2015.07.036.

F. Bagenal, R. J. Wilson, S. Siler, W. R. Paterson, and W. S. Kurth. Survey of Galileo plasma observations in Jupiter's plasma sheet. *Journal of Geophysical Research (Planets)*, 121:871–894, May 2016. doi: 10.1002/2016JE005009.

G. E. Ballester, D. F. Strobel, H. W. Moos, and P. D. Feldman. The atmospheric abundance of SO2 on Io. *Icarus*, 88:1–23, November 1990. doi: 10.1016/0019-1035(90)90174-8.

G. E. Ballester, M. A. McGrath, D. F. Stobel, X. Zhu, P. D. Feldman, and H. W. Moos. Detection of the SO2 atmosphere on Io with the Hubble Space Telescope. *Icarus*, 111: 2–17, September 1994. doi: 10.1006/icar.1994.1129.

P. Banks. Collision frequencies and energy transfer. Ions. *Planetary Space Science*, 14: 1105–1122, November 1966. doi: 10.1016/0032-0633(66)90025-0.

P. M. Banks and G. Kockarts. Aeronomy. *Aerospace UK*, 1973.

W. Baumjohann and R. A. Treumann. Basic space plasma physics. *London: Imperial College Press, |c1996*, 1996. doi: 10.1142/p015.

E. B. Bierhaus, K. Zahnle, and C. R. Chapman. Europa's Crater Distributions and Surface Ages. *Europa, Edited by Robert T. Pappalardo, William B. McKinnon, Krishan K. Khurana ; with the assistance of René Dotson with 85 collaborating authors.*, page 161, 2009.

E. K. Bigg. Influence of the Satellite Io on Jupiter's Decametric Emission. *Nature*, 203: 1008–1010, September 1964. doi: 10.1038/2031008a0.

A. Blöcker. *MHD-Modellierung der Plasmawechselwirkung bei Io und Enceladus*. Master thesis, Institut für Geophysik und Meteorologie, Universität zu Köln, 2013.

A. Blöcker, J. Saur, and L. Roth. Europa's plasma interaction with an inhomogeneous atmosphere: Development of Alfvén winglets within the Alfvén wings. *Journal of Geophysical Research (Space Physics)*, 121:9794–9828, October 2016. doi: 10.1002/2016JA022479.

H. S. Bridge, J. W. Belcher, A. J. Lazarus, J. D. Sullivan, R. L. McNutt, F. Bagenal, J. D. Scudder, E. C. Sittler, G. L. Siscoe, U. M. Vasyliunas, C. K. Goertz, and C. M. Yeates. Plasma observations near Jupiter - Initial results from Voyager 1. *Science*, 204:987–991, June 1979. doi: 10.1126/science.204.4396.987.

A. L. Broadfoot, M. J. Belton, P. Z. Takacs, B. R. Sandel, D. E. Shemansky, J. B. Holberg, J. M. Ajello, H. W. Moos, S. K. Atreya, T. M. Donahue, J. L. Bertaux, J. E. Blamont, D. F. Strobel, J. C. McConnell, R. Goody, A. Dalgarno, and M. B. McElroy. Extreme ultraviolet observations from Voyager 1 encounter with Jupiter. *Science*, 204:979–982, June 1979. doi: 10.1126/science.204.4396.979.

M. E. Brown. Potassium in Europa's Atmosphere. *Icarus*, 151:190–195, June 2001. doi: 10.1006/icar.2001.6612.

M. E. Brown and A. H. Bouchez. The response of Jupiter's magnetosphere to an outburst on Io. *Science*, 278:268–271, October 1997. doi: 10.1126/science.278.5336.268.

M. E. Brown and R. E. Hill. Discovery of an extended sodium atmosphere around Europa. *Nature*, 380:229–231, March 1996. doi: 10.1038/380229a0.

R. A. Brown and F. H. Chaffee, Jr. High-Resolution Spectra of Sodium Emission from IO. *Astrophysical Journal, Letters*, 187:L125, February 1974a. doi: 10.1086/181413.

R. A. Brown and F. H. Chaffee, Jr. High-Resolution Spectra of Sodium Emission from IO. *Astrophysical Journal, Letters*, 187:L125, February 1974b. doi: 10.1086/181413.

R. A. Brown and W.-H. Ip. Atomic clouds as distributed sources for the Io plasma torus. *Science*, 213:1493–1495, September 1981. doi: 10.1126/science.213.4515.1493.

M. H. Carr, A. S. McEwen, K. A. Howard, F. C. Chuang, P. Thomas, P. Schuster, J. Oberst, G. Neukum, G. Schubert, and Galileo Imaging Team. Mountains and Calderas on Io:

Possible Implications for Lithosphere Structure and Magma Generation. *Icarus*, 135: 146–165, September 1998. doi: 10.1006/icar.1998.5979.

P. Cassen, R. T. Reynolds, and S. J. Peale. Is there liquid water on Europa. *Geophysical Research Letters*, 6:731–734, September 1979. doi: 10.1029/GL006i009p00731.

P. Cassen, S. J. Peale, and R. T. Reynolds. Tidal dissipiation in Europa - A correction. *Geophysical Research Letters*, 7:987, November 1980. doi: 10.1029/GL007i011p00987.

T. A. Cassidy, R. E. Johnson, M. A. McGrath, M. C. Wong, and J. F. Cooper. The spatial morphology of Europa's near-surface O $_2$ atmosphere. *Icarus*, 191:755–764, November 2007. doi: 10.1016/j.icarus.2007.04.033.

T. A. Cassidy, R. E. Johnson, and O. J. Tucker. Trace constituents of Europa's atmosphere. *Icarus*, 201:182–190, May 2009. doi: 10.1016/j.icarus.2008.12.033.

E. Chané, J. Saur, and S. Poedts. Modeling Jupiter's magnetosphere: Influence of the internal sources. *Journal of Geophysical Research (Space Physics)*, 118:2157–2172, May 2013. doi: 10.1002/jgra.50258.

A. F. Cheng. Escape of sulfur and oxygen from Io. *Journal of Geophysical Research*, 89: 3939–3944, June 1984. doi: 10.1029/JA089iA06p03939.

D. B. Chrisey, R. E. Johnson, J. A. Phipps, M. A. McGrath, and J. W. Boring. Sputtering of sulfur by kiloelectronvolt ions - Application to the magnetospheric plasma interaction with Io. *Icarus*, 70:111–123, April 1987. doi: 10.1016/0019-1035(87)90078-9.

T. Chust, A. Roux, W. S. Kurth, D. A. Gurnett, M. G. Kivelson, and K. K. Khurana. Are Io's Alfvén wings filamented? Galileo observations. *Planetary Physics*, 53:395–412, April 2005. doi: 10.1016/j.pss.2004.09.021.

J. T. Clarke, J. Ajello, J. Luhmann, N. Schneider, and I. Kanik. Hubble Space Telescope UV spectral observations of Io passing into eclipse. *Journal of Geophysical Research*, 99:8387–8402, April 1994. doi: 10.1029/93JE02547.

J. T. Clarke, G. E. Ballester, J. Trauger, R. Evans, J. E. P. Connerney, K. Stapelfeldt, D. Crisp, P. D. Feldman, C. J. Burrows, S. Casertano, J. S. Gallagher, III, R. E. Griffiths, J. J. Hester, J. G. Hoessel, J. A. Holtzman, J. E. Krist, V. Meadows, J. R. Mould, P. A. Scowen, A. M. Watson, and J. A. Westphal. Far-Ultraviolet Imaging of Jupiter's Aurora and the Io "Footprint". *Science*, 274:404–409, October 1996. doi: 10.1126/science.274.5286.404.

J. T. Clarke, J. Ajello, G. Ballester, L. Ben Jaffel, J. Connerney, J.-C. Gérard, G. R. Gladstone, D. Grodent, W. Pryor, J. Trauger, and J. H. Waite. Ultraviolet emissions from the magnetic footprints of Io, Ganymede and Europa on Jupiter. *Nature*, 415:997–1000, February 2002.

M. R. Combi, K. Kabin, T. I. Gombosi, D. L. DeZeeuw, and K. G. Powell. Io's plasma environment during the Galileo flyby: Global three-dimensional MHD modeling with adaptive mesh refinement. *J. Geophys. Res.*, 103:9071–9082, May 1998. doi: 10.1029/98JA00073.

J. E. P. Connerney, R. Baron, T. Satoh, and T. Owen. Images of Excited H_3ˆ+ at the Foot of the Io Flux Tube in Jupiter's Atmosphere. *Science*, 262:1035–1038, November 1993. doi: 10.1126/science.262.5136.1035.

J. E. P. Connerney, M. H. Acuña, N. F. Ness, and T. Satoh. New models of Jupiter's magnetic field constrained by the Io flux tube footprint. *J. Geophys. Res.*, 103:11929–11940, June 1998. doi: 10.1029/97JA03726.

P. A. Delamere and F. Bagenal. Modeling variability of plasma conditions in the Io torus. *Journal of Geophysical Research (Space Physics)*, 108:1276, July 2003. doi: 10.1029/2002JA009706.

V. Dols, P. A. Delamere, and F. Bagenal. A multispecies chemistry model of Io's local interaction with the Plasma Torus. *Journal of Geophysical Research (Space Physics)*, 113:A09208, September 2008. doi: 10.1029/2007JA012805.

V. Dols, P. A. Delamere, F. Bagenal, W. S. Kurth, and W. R. Paterson. Asymmetry of Io's outer atmosphere: Constraints from five Galileo flybys. *Journal of Geophysical Research (Planets)*, 117:E10010, October 2012. doi: 10.1029/2012JE004076.

V. J. Dols, F. Bagenal, T. A. Cassidy, F. J. Crary, and P. A. Delamere. Europa's atmospheric neutral escape: Importance of symmetrical O_2 charge exchange. *Icarus*, 264:387–397, January 2016. doi: 10.1016/j.icarus.2015.09.026.

S. Douté, B. Schmitt, R. Lopes-Gautier, R. Carlson, L. Soderblom, J. Shirley, and Galileo NIMS Team. Mapping SO_2 Frost on Io by the Modeling of NIMS Hyperspectral Images. *Icarus*, 149:107–132, January 2001. doi: 10.1006/icar.2000.6513.

S. D. Drell, H. M. Foley, and M. A. Ruderman. Drag and Propulsion of Large Satellites in the Ionosphere: An Alfvén Propulsion Engine in Space. *J. Geophys. Res.*, 70:3131–3145, July 1965. doi: 10.1029/JZ070i013p03131.

S. Duling, J. Saur, and J. Wicht. Consistent boundary conditions at nonconducting surfaces of planetary bodies: Applications in a new Ganymede MHD model. *Journal of Geophysical Research (Space Physics)*, 119:4412–4440, June 2014. doi: 10.1002/2013JA019554.

S. T. Durrance, P. D. Feldman, and H. A. Weaver. Rocket detection of ultraviolet emission from neutral oxygen and sulfur in the IO Torus. *Astrophysical Journal, Letters*, 267:L125–L129, April 1983. doi: 10.1086/184016.

A. Eviatar and C. Paranicas. The plasma plumes of Europa and Callisto. *Icarus*, 178: 360–366, November 2005. doi: 10.1016/j.icarus.2005.06.007.

S. A. Fagents. Considerations for effusive cryovolcanism on Europa: The post-Galileo perspective. *Journal of Geophysical Research (Planets)*, 108:5139, December 2003. doi: 10.1029/2003JE002128.

L. M. Feaga, M. McGrath, and P. D. Feldman. Io's dayside SO $_2$ atmosphere. *Icarus*, 201: 570–584, June 2009. doi: 10.1016/j.icarus.2009.01.029.

P. D. Feldman, D. F. Strobel, H. W. Moos, K. D. Retherford, B. C. Wolven, M. A. McGrath, F. L. Roesler, R. C. Woodward, R. J. Oliversen, and G. E. Ballester. Lyman-α imaging of the SO_2 distribution on Io. *Geophys. Res. Lett.*, 27:1787–1790, 2000. doi: 10.1029/1999GL011067.

L. A. Frank and W. R. Paterson. Intense electron beams observed at Io with the Galileo spacecraft. *Journal of Geophysical Research*, 104:28657–28670, 1999. doi: 10.1029/1999JA900402.

L. A. Frank and W. R. Paterson. Return to Io by the Galileo spacecraft: Plasma observations. *Journal of Geophysical Research*, 105:25363–25378, November 2000. doi: 10.1029/1999JA000460.

L. A. Frank and W. R. Paterson. Passage through Io's ionospheric plasmas by the Galileo spacecraft. *Journal of Geophysical Research*, 106:26209–26224, November 2001. doi: 10.1029/2000JA002503.

L. A. Frank, E. L. Ackerson, J. H. Wolfe, and J. D. Mihalov. Observations of plasmas in the Jovian magnetosphere. January 1975.

L. A. Frank, W. R. Paterson, K. L. Ackerson, V. M. Vasyliunas, F. V. Coroniti, and S. J. Bolton. Plasma Observations at Io with the Galileo Spacecraft. *Science*, 274:394–395, October 1996. doi: 10.1126/science.274.5286.394.

P. E. Geissler and D. B. Goldstein. Plumes and their deposits. *Io After Galileo: A New View of Jupiter's Volcanic Moon*, page 163, 2007. doi: 10.1007/978-3-540-48841-5-8.

P. E. Geissler, R. Greenberg, G. Hoppa, P. Helfenstein, A. McEwen, R. Pappalardo, R. Tufts, M. Ockert-Bell, R. Sullivan, R. Greeley, M. J. S. Belton, T. Denk, B. E. Clark, J. Burns, and J. Veverka. Evidence for non-synchronous rotation of Europa. *Nature*, 391:368, January 1998. doi: 10.1038/34869.

P. E. Geissler, A. S. McEwen, W. Ip, M. J. S. Belton, T. V. Johnson, W. H. Smyth, and A. P. Ingersoll. Galileo Imaging of Atmospheric Emissions from Io. *Science*, 285, August 1999. doi: 10.1126/science.285.5429.870.

C. K. Goertz. Io's interaction with the plasma torus. *Journal of Geophysical Research*, 85:2949–2956, June 1980. doi: 10.1029/JA085iA06p02949.

J. D. Goguen, D. L. Matson, W. M. Sinton, R. R. Howell, and H. M. Dyck. Io hot spots - Infrared photometry of satellite occultations. *Icarus*, 76:465–484, December 1988. doi: 10.1016/0019-1035(88)90015-2.

P. Goldreich and D. Lynden-Bell. Io, a jovian unipolar inductor. *Astrophys. J.*, 156:59–78, April 1969. doi: 10.1086/149947.

R. Greeley, R. Sullivan, J. Klemaszewski, K. Homan, J. W. Head, R. T. Pappalardo, J. Veverka, B. E. Clark, T. V. Johnson, K. P. Klaasen, M. Belton, J. Moore, E. Asphaug, M. H. Carr, G. Neukum, T. Denk, C. R. Chapman, C. B. Pilcher, P. E. Geissler, R. Greenberg, and R. Tufts. Europa: Initial Galileo Geological Observations. *Icarus*, 135:4–24, September 1998. doi: 10.1006/icar.1998.5969.

D. A. Gurnett, A. M. Persoon, W. S. Kurth, A. Roux, and S. J. Bolton. Electron densities near Io from Galileo plasma wave observations. *J. Geophys. Res.*, 106:26225–26232, November 2001. doi: 10.1029/2000JA002509.

P. K. Haff and C. C. Watson. The erosion of planetary and satellite atmospheres by energetic atomic particles. *Journal of Geophysical Research*, 84:8436–8442, December 1979. doi: 10.1029/JB084iB14p08436.

P. K. Haff, C. C. Watson, and Y. L. Yung. Sputter ejection of matter from Io. *Journal of Geophysical Research*, 86:6933–6938, August 1981. doi: 10.1029/JA086iA08p06933.

D. T. Hall, D. F. Strobel, P. D. Feldman, M. A. McGrath, and H. A. Weaver. Detection of an oxygen atmosphere on Jupiter's moon Europa. *Nature*, 373:677–679, February 1995. doi: 10.1038/373677a0.

D. T. Hall, P. D. Feldman, M. A. McGrath, and D. F. Strobel. The Far-Ultraviolet Oxygen Airglow of Europa and Ganymede. *Astrophysical Journal*, 499:475–481, May 1998. doi: 10.1086/305604.

K. P. Hand and C. F. Chyba. Empirical constraints on the salinity of the europan ocean and implications for a thin ice shell. *Icarus*, 189:424–438, August 2007. doi: 10.1016/j.icarus.2007.02.002.

J. C. Hayes, M. L. Norman, R. A. Fiedler, J. O. Bordner, P. S. Li, S. E. Clark, A. ud-Doula, and M.-M. Mac Low. Simulating Radiating and Magnetized Flows in Multiple Dimensions with ZEUS-MP. *Astrophys. J. Suppl.*, 165:188–228, July 2006. doi: 10.1086/504594.

M. M. Hedman, C. M. Gosmeyer, P. D. Nicholson, C. Sotin, R. H. Brown, R. N. Clark, K. H. Baines, B. J. Buratti, and M. R. Showalter. An observed correlation between

plume activity and tidal stresses on Enceladus. *Nature*, 500:182–184, August 2013. doi: 10.1038/nature12371.

A. R. Hendrix, C. A. Barth, and C. W. Hord. Io's patchy SO_2 atmosphere as measured by the Galileo ultraviolet spectrometer. *Journal of Geophysical Research*, 104:11817–11826, May 1999. doi: 10.1029/1999JE900009.

T. W. Hill. Inertial limit on corotation. *Journal of Geophysical Research*, 84:6554–6558, November 1979. doi: 10.1029/JA084iA11p06554.

T. W. Hill and D. H. Pontius. Plasma injection near Io. *Journal of Geophysical Research*, 103:19879–19886, September 1998. doi: 10.1029/98JE00945.

D. P. Hinson, A. J. Kliore, F. M. Flasar, J. D. Twicken, P. J. Schinder, and R. G. Herrera. Galileo radio occultation measurements of Io's ionosphere and plasma wake. *J. Geophys. Res.*, 103:29343–29358, December 1998. doi: 10.1029/98JA02659.

T. S. Huang and G. L. Siscoe. Corotation lag limit on mass-loss rate from Io. *Astrophysical Journal*, 319:1003–1009, August 1987. doi: 10.1086/165517.

J. D. Huba. Hall Magnetohydrodynamics - A Tutorial. In J. Büchner, C. Dum, and M. Scholer, editors, *Space Plasma Simulation*, volume 615 of *Lecture Notes in Physics, Berlin Springer Verlag*, pages 166–192, 2003.

W. Hwang, Y.-K. Kim, and M. E. Rudd. New model for electron-impact ionization cross sections of molecules. *Journal of Chemical Physics*, 104:2956–2966, February 1996. doi: 10.1063/1.471116.

D. S. Intriligator and W. D. Miller. First evidence for a Europa plasma torus. *Journal of Geophysical Research*, 87:8081–8090, October 1982. doi: 10.1029/JA087iA10p08081.

W.-H. Ip. Europa's Oxygen Exosphere and Its Magnetospheric Interaction. *Icarus*, 120: 317–325, April 1996. doi: 10.1006/icar.1996.0052.

S. Jacobsen. *Three-dimensional magnetohydrodynamic simulations of Io's non-linear interaction with the Jovian magnetosphere*. PhD thesis, Institute of Geophysics and Meteorology, University of Cologne, 2011.

S. Jacobsen, F. M. Neubauer, J. Saur, and N. Schilling. Io's nonlinear MHD-wave field in the heterogeneous Jovian magnetosphere. *J. Geophys. Res.*, 341:L10202, May 2007. doi: 10.1029/2006GL029187.

W. L. Jaeger, E. P. Turtle, L. P. Keszthelyi, J. Radebaugh, A. S. McEwen, and R. T. Pappalardo. Orogenic tectonism on Io. *Journal of Geophysical Research (Planets)*, 108:5093, August 2003. doi: 10.1029/2002JE001946.

K. L. Jessup. *Atmospheres under fire: The effects of volcanic and impact induced plumes on the atmospheres of Io and Jupiter, respectively*. PhD thesis, UNIVERSITY OF MICHIGAN, 2002.

K.-L. Jessup and J. Spencer. Spatially Resolved HST/STIS Observations of io's Dayside Equatorial Atmosphere. In *AAS/Division for Planetary Sciences Meeting Abstracts*, volume 45 of *AAS/Division for Planetary Sciences Meeting Abstracts*, page 501.01, October 2013.

K. L. Jessup and J. R. Spencer. Io's Active Eruption Plumes: Insights from HST. In *EPSC-DPS Joint Meeting 2011*, page 1699, October 2011.

K. L. Jessup and J. R. Spencer. Spatially resolved HST/STIS observations of Io's dayside equatorial atmosphere. *Icarus*, 248:165–189, March 2015. doi: 10.1016/j.icarus.2014.10.020.

K. L. Jessup, J. R. Spencer, G. E. Ballester, R. R. Howell, F. Roesler, M. Vigel, and R. Yelle. The atmospheric signature of Io's Prometheus plume and anti-jovian hemisphere: evidence for a sublimation atmosphere. *Icarus*, 169:197–215, May 2004. doi: 10.1016/j.icarus.2003.11.015.

X. Jia, R. J. Walker, M. G. Kivelson, K. K. Khurana, and J. A. Linker. Three-dimensional MHD simulations of Ganymede's magnetosphere. *Journal of Geophysical Research (Space Physics)*, 113:A06212, June 2008. doi: 10.1029/2007JA012748.

X. Jia, R. J. Walker, M. G. Kivelson, K. K. Khurana, and J. A. Linker. Properties of Ganymede's magnetosphere inferred from improved three-dimensional MHD simulations. *Journal of Geophysical Research (Space Physics)*, 114:A09209, September 2009. doi: 10.1029/2009JA014375.

J. H. Johnson. The discovery of the first four satellites of Jupiter. *J. Brit. Astron. Assn.*, 41:164–171, June 1931.

R. E. Johnson. Energetic Charged-Particle Interactions with Atmospheres and Surfaces. *Energetic Charged-Particle Interactions with Atmospheres and Surfaces, X, 232 pp. 84 figs., 28 tabs.. Springer-Verlag Berlin Heidelberg New York. Also Physics and Chemistry in Space, volume 19*, page 84, 1990.

R. E. Johnson. Plasma-Induced Sputtering of an Atmosphere. *Space Science Reviews*, 69:215–253, August 1994. doi: 10.1007/BF02101697.

R. E. Johnson and M. McGrath. Stability of the Io plasma torus/atmosphere interaction. *Geophysical Research Letters*, 20:1735–1738, August 1993. doi: 10.1029/93GL00838.

R. E. Johnson, R. W. Carlson, J. F. Cooper, C. Paranicas, M. H. Moore, and M. C. Wong. Radiation effects on the surfaces of the Galilean satellites. *Jupiter. The Planet, Satellites and Magnetosphere*, pages 485–512, 2004.

R. E. Johnson, M. R. Combi, J. L. Fox, W.-H. Ip, F. Leblanc, M. A. McGrath, V. I. Shematovich, D. F. Strobel, and J. H. Waite. Exospheres and Atmospheric Escape. *Space Science Reviews*, 139:355–397, August 2008. doi: 10.1007/s11214-008-9415-3.

R. E. Johnson, M. H. Burger, T. A. Cassidy, F. Leblanc, M. Marconi, and W. H. Smyth. Composition and Detection of Europa's Sputter-induced Atmosphere. *Europa, Edited by Robert T. Pappalardo, William B. McKinnon, Krishan K. Khurana ; with the assistance of René Dotson with 85 collaborating authors. University of Arizona Press, Tucson, 2009. The University of Arizona space science series ISBN: 9780816528448, p.507*, page 507, 2009.

T. V. Johnson, A. F. Cook, II, C. Sagan, and L. A. Soderblom. Volcanic resurfacing rates and implications for volatiles on Io. *Nature*, 280:746–750, August 1979. doi: 10.1038/280746a0.

K. Kabin, M. R. Combi, T. I. Gombosi, A. F. Nagy, D. L. DeZeeuw, and K. G. Powell. On Europa's magnetospheric interaction: A MHD simulation of the E4 flyby. *Journal of Geophysical Research*, 104:19983–19992, September 1999. doi: 10.1029/1999JA900263.

K. Kabin, M. R. Combi, T. I. Gombosi, D. L. DeZeeuw, K. C. Hansen, and K. G. Powell. Io's magnetospheric interaction: an MHD model with day-night asymmetry. *Planetary Space Science*, 49:337–344, March 2001. doi: 10.1016/S0032-0633(00)00155-0.

L. Keszthelyi, W. L. Jaeger, E. P. Turtle, M. Milazzo, and J. Radebaugh. A post-Galileo view of Io's interior. *Icarus*, 169:271–286, May 2004. doi: 10.1016/j.icarus.2004.01.005.

K. K. Khurana, M. G. Kivelson, D. J. Stevenson, G. Schubert, C. T. Russell, R. J. Walker, and C. Polanskey. Induced magnetic fields as evidence for subsurface oceans in Europa and Callisto. *Nature*, 395:777–780, October 1998. doi: 10.1038/27394.

K. K. Khurana, . M. G. Kivelson, C. T. Russell, R. J. Walker, and S. Joy. Io's Magnetic Field. In *EGS General Assembly Conference Abstracts*, volume 27 of *EGS General Assembly Conference Abstracts*, 2002.

K. K. Khurana, X. Jia, M. G. Kivelson, F. Nimmo, G. Schubert, and C. T. Russell. Evidence of a Global Magma Ocean in Io's Interior. *Science*, 332:1186–, June 2011. doi: 10.1126/science.1201425.

Y.-K. Kim, W. Hwang, N. M. Weinberger, M. A. Ali, and M. E. Rudd. Electron-impact ionization cross sections of atmospheric molecules. *The Journal of Chemical Physics*, 106:1026–1033, January 1997. doi: 10.1063/1.473186.

M. R. Kirchoff and W. B. McKinnon. Mountain Building on Io: An Unsteady Relationship Between Volcanism and Tectonism. In S. Mackwell and E. Stansbery, editors, *36th Annual Lunar and Planetary Science Conference*, volume 36 of *Lunar and Planetary Science Conference*, March 2005.

M. G. Kivelson, K. K. Khurana, S. Joy, C. T. Russell, D. J. Southwood, R. J. Walker, and C. Polanskey. Europa's magnetic signature: report from Galileo's pass on 19 December 1996. *Science*, 276:1239–1241, May 1997. doi: 10.1126/science.276.5316.1239.

M. G. Kivelson, K. K. Khurana, D. J. Stevenson, L. Bennett, S. Joy, C. T. Russell, R. J. Walker, C. Zimmer, and C. Polanskey. Europa and Callisto: Induced or intrinsic fields in a periodically varying plasma environment. *Journal of Geophysical Research*, 104: 4609–4626, March 1999. doi: 10.1029/1998JA900095.

M. G. Kivelson, K. K. Khurana, C. T. Russell, M. Volwerk, R. J. Walker, and C. Zimmer. Galileo Magnetometer Measurements: A Stronger Case for a Subsurface Ocean at Europa. *Science*, 289:1340–1343, August 2000. doi: 10.1126/science.289.5483.1340.

M. G. Kivelson, K. K. Khurana, C. T. Russell, S. P. Joy, M. Volwerk, R. J. Walker, C. Zimmer, and J. A. Linker. Magnetized or unmagnetized: Ambiguity persists following Galileo's encounters with Io in 1999 and 2000. *Journal of Geophysical Research*, 106: 26121–26136, November 2001a. doi: 10.1029/2000JA002510.

M. G. Kivelson, K. K. Khurana, C. T. Russell, and R. J. Walker. Magnetic Signature of a Polar Pass Over Io. *AGU Fall Meeting Abstracts*, December 2001b.

M. G. Kivelson, F. Bagenal, W. S. Kurth, F. M. Neubauer, C. Paranicas, and J. Saur. Magnetospheric interactions with satellites. *Jupiter. The Planet, Satellites and Magnetosphere*, pages 513–536, 2004.

A. Kliore, D. L. Cain, G. Fjeldbo, B. L. Seidel, and S. I. Rasool. Preliminary Results on the Atmospheres of Io and Jupiter from the Pioneer 10 S-Band Occultation Experiment. *Science*, 183:323–324, January 1974. doi: 10.1126/science.183.4122.323.

A. J. Kliore, G. Fjeldbo, B. L. Seidel, D. N. Sweetnam, T. T. Sesplaukis, P. M. Woiceshyn, and S. I. Rasool. The atmosphere of Io from Pioneer 10 radio occultation measurements. *Icarus*, 24:407–410, April 1975. doi: 10.1016/0019-1035(75)90057-3.

A. J. Kliore, D. P. Hinson, F. M. Flasar, A. F. Nagy, and T. E. Cravens. The ionosphere of Europa from Galileo radio occultations. *Science*, 277:355–358, July 1997. doi: 10.1126/science.277.5324.355.

S. Kumar. Sulfur and oxygen escape from Io and a lower limit to atmospheric SO2 at Voyager 1 encounter. *Journal of Geophysical Research*, 89:7399–7406, September 1984. doi: 10.1029/JA089iA09p07399.

I. Kupo, Y. Mekler, and A. Eviatar. Detection of ionized sulfur in the Jovian magnetosphere. *Astrophysical Journal, Letters*, 205:L51–L53, April 1976. doi: 10.1086/182088.

W. S. Kurth, D. A. Gurnett, A. M. Persoon, A. Roux, S. J. Bolton, and C. J. Alexander. The plasma wave environment of Europa. *Planetary and Space Science*, 49:345–363, March 2001. doi: 10.1016/S0032-0633(00)00156-2.

A. Lagg, N. Krupp, J. Woch, and D. J. Williams. In-situ observations of a neutral gas torus at Europa. *Geophysical Research Letters*, 30:1556, June 2003. doi: 10.1029/2003GL017214.

F. Leblanc, R. E. Johnson, and M. E. Brown. Europa's Sodium Atmosphere: An Ocean Source? *Icarus*, 159:132–144, September 2002. doi: 10.1006/icar.2002.6934.

F. Leblanc, A. E. Potter, R. M. Killen, and R. E. Johnson. Origins of Europa Na cloud and torus. *Icarus*, 178:367–385, November 2005. doi: 10.1016/j.icarus.2005.03.027.

E. Lellouch, T. Encrenaz, M. Belton, I. de Pater, and S. Gulkis. Io's atmosphere from microwave detection SO2. *Nature*, 346:639–641, August 1990. doi: 10.1038/346639a0.

E. Lellouch, M. Belton, I. de Pater, G. Paubert, S. Gulkis, and T. Encrenaz. The structure, stability, and global distribution of Io's atmosphere. *Icarus*, 98:271–295, August 1992. doi: 10.1016/0019-1035(92)90095-O.

E. Lellouch, M. A. McGrath, and K. L. Jessup. Io's atmosphere. *Io After Galileo: A New View of Jupiter's Volcanic Moon*, page 231, 2007. doi: 10.1007/978-3-540-48841-5-10.

J. A. Linker, M. G. Kivelson, and R. J. Walker. An MHD simulation of plasma flow past Io - Alfven and slow mode perturbations. *Geophys. Res. Lett.*, 15:1311–1314, October 1988. doi: 10.1029/GL015i011p01311.

J. A. Linker, M. G. Kivelson, and R. J. Walker. The effect of mass loading on the temperature of a flowing plasma. *Geophys. Res. Lett.*, 16:763–766, July 1989. doi: 10.1029/GL016i007p00763.

J. A. Linker, M. G. Kivelson, and R. J. Walker. A three-dimensional MHD simulation of plasma flow past Io. *J. Geophys. Res.*, 96:21037, December 1991. doi: 10.1029/91JA02132.

J. A. Linker, K. K. Khurana, M. G. Kivelson, and R. J. Walker. MHD simulations of Io's interaction with the plasma torus. *J. Geophys. Res.*, 103:19867–19878, September 1998. doi: 10.1029/98JE00632.

A. S. Lipatov and M. R. Combi. Effects of kinetic processes in shaping Io's global plasma environment: A 3D hybrid model. *Icarus*, 180:412–427, February 2006. doi: 10.1016/j.icarus.2005.08.012.

A. S. Lipatov, J. F. Cooper, W. R. Paterson, E. C. Sittler, R. E. Hartle, and D. G. Simpson. Jovian plasma torus interaction with Europa: 3D hybrid kinetic simulation. First results. *Planetary Space Science*, 58:1681–1691, November 2010. doi: 10.1016/j.pss.2010.06.015.

A. S. Lipatov, J. F. Cooper, W. R. Paterson, E. C. Sittler, Jr., R. E. Hartle, and D. G. Simpson. Jovian plasma torus interaction with Europa. Plasma wake structure and effect of

inductive magnetic field: 3D hybrid kinetic simulation. *Planetary Space Science*, 77: 12–24, March 2013. doi: 10.1016/j.pss.2013.01.009.

Y. Liu, A. F. Nagy, K. Kabin, M. R. Combi, D. L. DeZeeuw, T. I. Gombosi, and K. G. Powell. Two-species, 3D, MHD simulation of Europa's interaction with Jupiter's magnetosphere. *Geophysical Research Letters*, 27:1791–1794, June 2000. doi: 10.1029/1999GL003734.

R. M. C. Lopes, L. W. Kamp, W. D. Smythe, P. Mouginis-Mark, J. Kargel, J. Radebaugh, E. P. Turtle, J. Perry, D. A. Williams, R. W. Carlson, and S. Douté. Lava lakes on Io: observations of Io's volcanic activity from Galileo NIMS during the 2001 fly-bys. *Icarus*, 169:140–174, May 2004. doi: 10.1016/j.icarus.2003.11.013.

R. Lopes-Gautier, A. S. McEwen, W. B. Smythe, P. E. Geissler, L. Kamp, A. G. Davies, J. R. Spencer, L. Keszthelyi, R. Carlson, F. E. Leader, R. Mehlman, L. Soderblom, The Galileo NIMS, and SSI Teams. Active Volcanism on Io: Global Distribution and Variations in Activity. *Icarus*, 140:243–264, August 1999. doi: 10.1006/icar.1999.6129.

W. T. Lynn. Simon Marius and the satellites of Jupiter. *The Observatory*, 26:254–256, June 1903.

D. L. Matson, T. V. Johnson, and F. P. Fanale. Sodium D-Line Emission from Io: Sputtering and Resonant Scattering Hypothesis. *Astrophysical Journal*, 192:L43, August 1974. doi: 10.1086/181586.

B. H. Mauk, D. J. Williams, and A. Eviatar. Understanding Io's space environment interaction: Recent energetic electron measurements from Galileo. *Journal of Geophysical Research*, 106:26195–26208, November 2001. doi: 10.1029/2000JA002508.

B. H. Mauk, D. G. Mitchell, S. M. Krimigis, E. C. Roelof, and C. P. Paranicas. Energetic neutral atoms from a trans-Europa gas torus at Jupiter. *Nature*, 421:920–922, February 2003. doi: 10.1038/nature01431.

B. H. Mauk, D. G. Mitchell, R. W. McEntire, C. P. Paranicas, E. C. Roelof, D. J. Williams, S. M. Krimigis, and A. Lagg. Energetic ion characteristics and neutral gas interactions in Jupiter's magnetosphere. *Journal of Geophysical Research (Space Physics)*, 109: A09S12, September 2004. doi: 10.1029/2003JA010270.

T. B. McCord, G. B. Hansen, F. P. Fanale, R. W. Carlson, D. L. Matson, T. V. Johnson, W. D. Smythe, J. K. Crowley, P. D. Martin, A. Ocampo, C. A. Hibbitts, and J. C. Granahan. Salts on Europa's Surface Detected by Galileo's Near Infrared Mapping Spectrometer. *Science*, 280:1242, May 1998. doi: 10.1126/science.280.5367.1242.

W. McDaniel. Atomic Collisions: Electron and Photon Projectiles. 1989.

A. S. McEwen and L. A. Soderblom. Two classes of volcanic plumes on Io. *Icarus*, 55: 191–217, August 1983. doi: 10.1016/0019-1035(83)90075-1.

A. S. McEwen, J. I. Lunine, and M. H. Carr. Dynamic Geophysics of IO. *NASA Special Publication*, 494, 1989.

A. S. McEwen, L. Keszthelyi, J. R. Spencer, G. Schubert, D. L. Matson, R. Lopes-Gautier, K. P. Klaasen, T. V. Johnson, J. W. Head, P. Geissler, S. Fagents, A. G. Davies, M. H. Carr, H. H. Breneman, and M. J. S. Belton. High-Temperature Silicate Volcanism on Jupiter's Moon Io. *Science*, 281:87, July 1998. doi: 10.1126/science.281.5373.87.

A. S. McEwen, L. P. Keszthelyi, R. Lopes, P. M. Schenk, and J. R. Spencer. The lithosphere and surface of Io. *Jupiter. The Planet, Satellites and Magnetosphere*, pages 307–328, 2004.

M. A. McGrath and R. E. Johnson. Magnetospheric plasma sputtering of Io's atmosphere. *Icarus*, 69:519–531, March 1987. doi: 10.1016/0019-1035(87)90021-2.

M. A. McGrath, M. J. S. Belton, J. R. Spencer, and P. Sartoretti. Spatially Resolved Spectroscopy of Io's Pele Plume and SO_2 Atmosphere. *Icarus*, 146:476–493, August 2000. doi: 10.1006/icar.1999.6412.

M. A. McGrath, E. Lellouch, D. F. Strobel, P. D. Feldman, and R. E. Johnson. Satellite atmospheres. *Jupiter. The Planet, Satellites and Magnetosphere*, pages 457–483, 2004.

C. Moore, K. Miki, D. B. Goldstein, K. Stapelfeldt, P. L. Varghese, L. M. Trafton, and R. W. Evans. Monte Carlo modeling of Io's [OI] 6300 Å and [SII] 6716 Å auroral emission in eclipse. *Icarus*, 207:810–833, June 2010. doi: 10.1016/j.icarus.2010.01.004.

C. H. Moore, D. B. Goldstein, P. L. Varghese, L. M. Trafton, and B. Stewart. 1-D DSMC simulation of Io's atmospheric collapse and reformation during and after eclipse. *Icarus*, 201:585–597, June 2009. doi: 10.1016/j.icarus.2009.01.006.

C. H. Moore, H. Deng, D. B. Goldstein, D. Levin, P. L. Varghese, L. M. Trafton, B. D. Stewart, and A. C. Walker. Simulation of Plasma Interaction with Io's Atmosphere. In *American Institute of Physics Conference Series*, volume 1333 of *American Institute of Physics Conference Series*, pages 1163–1168, May 2011. doi: 10.1063/1.3562801.

J. M. Moore, A. S. McEwen, E. F. Albin, and R. Greeley. Topographic evidence for shield volcanism on Io. *Icarus*, 67:181–183, July 1986. doi: 10.1016/0019-1035(86)90183-1.

W. B. Moore. NOTE: The Thermal State of Io. *Icarus*, 154:548–550, December 2001. doi: 10.1006/icar.2001.6739.

W. B. Moore, G. Schubert, J. D. Anderson, and J. R. Spencer. The interior of Io. *Io After Galileo: A New View of Jupiter's Volcanic Moon*, page 89, 2007. doi: 10.1007/978-3-540-48841-5_5.

L. A. Morabito, S. P. Synnott, P. N. Kupferman, and S. A. Collins. Discovery of currently active extraterrestrial volcanism. *Science*, 204:972, June 1979. doi: 10.1126/science.204.4396.972.

A. Moullet, M. A. Gurwell, E. Lellouch, and R. Moreno. Simultaneous mapping of SO_2, SO, NaCl in Io's atmosphere with the Submillimeter Array. *Icarus*, 208:353–365, July 2010. doi: 10.1016/j.icarus.2010.02.009.

D. B. Nash, C. F. Yoder, M. H. Carr, J. Gradie, and D. M. Hunten. Io. *IAU Colloq. 77: Some Background about Satellites*, pages 629–688, 1986.

F. M. Neubauer. Nonlinear standing Alfven wave current system at Io - Theory. *J. Geophys. Res.*, 85:1171–1178, March 1980. doi: 10.1029/JA085iA03p01171.

F. M. Neubauer. The sub-Alfvénic interaction of the Galilean satellites with the Jovian magnetosphere. *J. Geophys. Res.*, 103:19843–19866, September 1998. doi: 10.1029/97JE03370.

F. M. Neubauer. Alfvén wings and electromagnetic induction in the interiors: Europa and Callisto. *J. Geophys. Res.*, 104:28671–28684, 1999. doi: 10.1029/1999JA900217.

M. L. Norman. Introducing ZEUS-MP: A 3D, Parallel, Multiphysics Code for Astrophysical Fluid Dynamics. In S. J. Arthur, N. S. Brickhouse, and J. Franco, editors, *Revista Mexicana de Astronomia y Astrofisica Conference Series*, volume 9 of *Revista Mexicana de Astronomia y Astrofisica Conference Series*, pages 66–71, May 2000.

R. T. Pappalardo, J. W. Head, R. Greeley, R. J. Sullivan, C. Pilcher, G. Schubert, W. B. Moore, M. H. Carr, J. M. Moore, M. J. S. Belton, and D. L. Goldsby. Geological evidence for solid-state convection in Europa's ice shell. *Nature*, 391:365, January 1998. doi: 10.1038/34862.

R. T. Pappalardo, M. J. S. Belton, H. H. Breneman, M. H. Carr, C. R. Chapman, G. C. Collins, T. Denk, S. Fagents, P. E. Geissler, B. Giese, R. Greeley, R. Greenberg, J. W. Head, P. Helfenstein, G. Hoppa, S. D. Kadel, K. P. Klaasen, J. E. Klemaszewski, K. Magee, A. S. McEwen, J. M. Moore, W. B. Moore, G. Neukum, C. B. Phillips, L. M. Prockter, G. Schubert, D. A. Senske, R. J. Sullivan, B. R. Tufts, E. P. Turtle, R. Wagner, and K. K. Williams. Does Europa have a subsurface ocean? Evaluation of the geological evidence. *Journal of Geophysical Research*, 104:24015–24056, October 1999. doi: 10.1029/1998JE000628.

R. T. Pappalardo, W. B. McKinnon, and K. K. Khurana. Europa. *Europa, Edited by Robert T. Pappalardo, William B. McKinnon, Krishan K. Khurana ; with the assistance of René Dotson with 85 collaborating authors. University of Arizona Press, Tucson, 2009. The University of Arizona space science series ISBN: 9780816528448, p.3*, page 3, 2009.

C. Paranicas, R. W. Carlson, and R. E. Johnson. Electron bombardment of Europa. *Geophysical Research Letters*, 28:673–676, 2001. doi: 10.1029/2000GL012320.

C. Paranicas, J. M. Ratliff, B. H. Mauk, C. Cohen, and R. E. Johnson. The ion environment near Europa and its role in surface energetics. *Geophysical Research Letters*, 29:1074, March 2002. doi: 10.1029/2001GL014127.

C. Paranicas, J. F. Cooper, H. B. Garrett, R. E. Johnson, and S. J. Sturner. Europa's Radiation Environment and Its Effects on the Surface. *Europa, Edited by Robert T. Pappalardo, William B. McKinnon, Krishan K. Khurana ; with the assistance of René Dotson with 85 collaborating authors. University of Arizona Press, Tucson, 2009. The University of Arizona space science series ISBN: 9780816528448, p.529*, page 529, 2009.

W. R. Paterson, L. A. Frank, and K. L. Ackerson. Galileo plasma observations at Europa: Ion energy spectra and moments. *Journal of Geophysical Research*, 104:22779–22792, October 1999. doi: 10.1029/1999JA900191.

S. J. Peale, P. Cassen, and R. T. Reynolds. Melting of Io by tidal dissipation. *Science*, 203:892–894, March 1979. doi: 10.1126/science.203.4383.892.

J. Pearl, R. Hanel, V. Kunde, W. Maguire, K. Fox, S. Gupta, C. Ponnamperuma, and F. Raulin. Identification of gaseous SO2 and new upper limits for other gases on Io. *Nature*, 280:755–758, August 1979. doi: 10.1038/280755a0.

J. Perry, R. M. C. Lopes, J. R. Spencer, and C. Alexander. A summary of the Galileo mission and its observations of Io. *Io After Galileo: A New View of Jupiter's Volcanic Moon*, page 35, 2007. doi: 10.1007/978-3-540-48841-5_3.

C. B. Phillips, A. S. McEwen, G. V. Hoppa, S. A. Fagents, R. Greeley, J. E. Klemaszewski, R. T. Pappalardo, K. P. Klaasen, and H. H. Breneman. The search for current geologic activity on Europa. *Journal of Geophysical Research*, 105:22579–22598, September 2000. doi: 10.1029/1999JE001139.

J. H. Piddington and J. F. Drake. Electrodynamic Effects of Jupiter's Satellite Io. *Nature*, 217:935–937, March 1968. doi: 10.1038/217935a0.

C. B. Pilcher and D. F. Strobel. Emissions from neutrals and ions in the Jovian magnetosphere. In D. Morrison, editor, *Satellites of Jupiter*, pages 807–845, 1982.

C. Plainaki, A. Milillo, A. Mura, S. Orsini, and T. Cassidy. Neutral particle release from Europa's surface. *Icarus*, 210:385–395, November 2010. doi: 10.1016/j.icarus.2010.06.041.

C. Plainaki, A. Milillo, A. Mura, S. Orsini, S. Massetti, and T. Cassidy. The role of sputtering and radiolysis in the generation of Europa exosphere. *Icarus*, 218:956–966, April 2012. doi: 10.1016/j.icarus.2012.01.023.

C. Plainaki, A. Milillo, A. Mura, J. Saur, S. Orsini, and S. Massetti. Exospheric O_2 densities at Europa during different orbital phases. *Planetary Space Science*, 88:42–52, November 2013. doi: 10.1016/j.pss.2013.08.011.

M. K. Pospieszalska and R. E. Johnson. Magnetospheric ion bombardment profiles of satellites - Europa and Dione. *Icarus*, 78:1–13, March 1989. doi: 10.1016/0019-1035(89)90065-1.

M. K. Pospieszalska and R. E. Johnson. Monte Carlo calculations of plasma ion-induced sputtering of an atmosphere: SO_2 ejected from Io. *Journal of Geophysical Research*, 101:7565–7574, 1996. doi: 10.1029/95JE03650.

J. A. Rathbun, J. R. Spencer, L. K. Tamppari, T. Z. Martin, L. Barnard, and L. D. Travis. Mapping of Io's thermal radiation by the Galileo photopolarimeter-radiometer (PPR) instrument. *Icarus*, 169:127–139, May 2004. doi: 10.1016/j.icarus.2003.12.021.

K. D. Retherford, H. W. Moos, D. F. Strobel, B. C. Wolven, and F. L. Roesler. Io's equatorial spots: Morphology of neutral UV emissions. *Journal of Geophysical Research*, 105: 27157–27166, December 2000. doi: 10.1029/2000JA002500.

K. D. Retherford, J. R. Spencer, S. A. Stern, J. Saur, D. F. Strobel, A. J. Steffl, G. R. Gladstone, H. A. Weaver, A. F. Cheng, J. W. Parker, D. C. Slater, M. H. Versteeg, M. W. Davis, F. Bagenal, H. B. Throop, R. M. C. Lopes, D. C. Reuter, A. Lunsford, S. J. Conard, L. A. Young, and J. M. Moore. Io's Atmospheric Response to Eclipse: UV Aurorae Observations. *Science*, 318:237, October 2007. doi: 10.1126/science.1147594.

F. L. Roesler, H. W. Moos, R. J. Oliversen, R. C. Woodward, Jr., K. D. Retherford, F. Scherb, M. A. McGrath, W. H. Smyth, P. D. Feldman, and D. F. Strobel. Far-Ultraviolet Imaging Spectroscopy of Io's Atmosphere with HST/STIS. *Science*, 283:353, January 1999. doi: 10.1126/science.283.5400.353.

L. Roth, J. Saur, K. D. Retherford, D. F. Strobel, and J. R. Spencer. Simulation of Io's auroral emission: Constraints on the atmosphere in eclipse. *Icarus*, 214:495–509, August 2011. doi: 10.1016/j.icarus.2011.05.014.

L. Roth, K. D. Retherford, J. Saur, D. F. Strobel, P. D. Feldman, M. A. McGrath, and F. Nimmo. Orbital apocenter is not a sufficient condition for HST/STIS detection of Europa's water vapor aurora. *Proceedings of the National Academy of Science*, 111: E5123–E5132, December 2014a. doi: 10.1073/pnas.1416671111.

L. Roth, J. Saur, K. D. Retherford, D. F. Strobel, P. D. Feldman, M. A. McGrath, and F. Nimmo. Transient Water Vapor at Europa's South Pole. *Science*, 343:171–174, January 2014b. doi: 10.1126/science.1247051.

L. Roth, J. Saur, K. D. Retherford, D. F. Strobel, P. D. Feldman, M. A. McGrath, J. R. Spencer, A. Blöcker, and N. Ivchenko. Europa's far ultraviolet oxygen aurora from a comprehensive set of HST observations. *Journal of Geophysical Research (Space Physics)*, 121:2143–2170, March 2016. doi: 10.1002/2015JA022073.

L. Roth, J. Saur, K. D. Retherford, A. Blöcker, D. F. Strobel, and P. D. Feldman. Constraints on Io's interior from auroral spot oscillations. *Journal of Geophysical Research (Space Physics)*, 122:1903–1927, February 2017. doi: 10.1002/2016JA023701.

M. Rubin, X. Jia, K. Altwegg, M. R. Combi, L. K. S. Daldorff, T. I. Gombosi, K. Khurana, M. G. Kivelson, V. M. Tenishev, G. Tóth, B. Holst, and P. Wurz. Self-consistent multi-fluid MHD simulations of Europa's exospheric interaction with Jupiter's magnetosphere. *Journal of Geophysical Research (Space Physics)*, 120:3503–3524, May 2015. doi: 10.1002/2015JA021149.

C. T. Russell and M. G. Kivelson. Detection of SO in Io's Exosphere. *Science*, 287: 1998–1999, March 2000. doi: 10.1126/science.287.5460.1998.

C. T. Russell, M. G. Kivelson, K. K. Khurana, and D. E. Huddleston. Circulation and Dynamics in the Jovian Magnetosphere. *Advances in Space Research*, 26:1671–1676, 2000. doi: 10.1016/S0273-1177(00)00115-0.

C. T. Russell, X. Blanco-Cano, Y. L. Wang, and M. G. Kivelson. Ion cyclotron waves at Io: implications for the temporal variation of Io's atmosphere. *Planetary and Space Science*, 51:937–944, December 2003. doi: 10.1016/j.pss.2003.05.005.

J. Saur and D. F. Strobel. Relative contributions of sublimation and volcanoes to Io's atmosphere inferred from its plasma interaction during solar eclipse. *Icarus*, 171:411–420, October 2004. doi: 10.1016/j.icarus.2004.05.010.

J. Saur, D. F. Strobel, and F. M. Neubauer. Interaction of the Jovian magnetosphere with Europa: Constraints on the neutral atmosphere. *Journal of Geophysical Research*, 103:19947–19962, September 1998. doi: 10.1029/97JE03556.

J. Saur, F. M. Neubauer, D. F. Strobel, and M. E. Summers. Three-dimensional plasma simulation of Io's interaction with the Io plasma torus: Asymmetric plasma flow. *J. Geophys. Res.*, 1042:25105–25126, November 1999. doi: 10.1029/1999JA900304.

J. Saur, F. M. Neubauer, D. F. Strobel, and M. E. Summers. Io's ultraviolet aurora: Remote sensing of Io's interaction. *Geophys. Res. Lett.*, 27:2893–2896, 2000. doi: 10.1029/2000GL003824.

J. Saur, F. M. Neubauer, D. F. Strobel, and M. E. Summers. Interpretation of Galileo's Io plasma and field observations: I0, I24, and I27 flybys and close polar passes. *Journal of Geophysical Research (Space Physics)*, 107:1422, December 2002. doi: 10.1029/2001JA005067.

J. Saur, D. F. Strobel, F. M. Neubauer, and M. E. Summers. The ion mass loading rate at Io. *Icarus*, 163:456–468, June 2003. doi: 10.1016/S0019-1035(03)00085-X.

J. Saur, F. M. Neubauer, J. E. P. Connerney, P. Zarka, and M. G. Kivelson. Plasma interaction of Io with its plasma torus. *Jupiter. The Planet, Satellites and Magnetosphere*, pages 537–560, 2004.

J. Saur, F. M. Neubauer, and N. Schilling. Hemisphere coupling in Enceladus' asymmetric plasma interaction. *Journal of Geophysical Research (Space Physics)*, 112:A11209, November 2007. doi: 10.1029/2007JA012479.

J. Saur, F. M. Neubauer, and K.-H. Glassmeier. Induced Magnetic Fields in Solar System Bodies. *Space Science Reviews*, 152:391–421, May 2010. doi: 10.1007/s11214-009-9581-y.

J. Saur, P. D. Feldman, L. Roth, F. Nimmo, D. F. Strobel, K. D. Retherford, M. A. McGrath, N. Schilling, J.-C. Gérard, and D. Grodent. Hubble Space Telescope/Advanced Camera for Surveys Observations of Europa's Atmospheric Ultraviolet Emission at Eastern Elongation. *Astrophysical Journal*, 738:153, September 2011. doi: 10.1088/0004-637X/738/2/153.

J. Saur, T. Grambusch, S. Duling, F. M. Neubauer, and S. Simon. Magnetic energy fluxes in sub-Alfvénic planet star and moon planet interactions. *Space Science Reviews*, 552: A119, April 2013. doi: 10.1051/0004-6361/201118179.

J. Saur, S. Duling, L. Roth, X. Jia, D. F. Strobel, P. D. Feldman, U. R. Christensen, K. D. Retherford, M. A. McGrath, F. Musacchio, A. Wennmacher, F. M. Neubauer, S. Simon, and O. Hartkorn. The search for a subsurface ocean in Ganymede with Hubble Space Telescope observations of its auroral ovals. *Journal of Geophysical Research (Space Physics)*, 120:1715–1737, March 2015. doi: 10.1002/2014JA020778.

G. G. Schaber. The geology of Io. In D. Morrison, editor, *Satellites of Jupiter*, pages 556–597, 1982.

P. Schenk, H. Hargitai, R. Wilson, A. McEwen, and P. Thomas. The mountains of Io: Global and geological perspectives from Voyager and Galileo. *Journal of Geophysical Research*, 106:33201–33222, December 2001. doi: 10.1029/2000JE001408.

P. M. Schenk. Thickness constraints on the icy shells of the galilean satellites from a comparison of crater shapes. *Nature*, 417:419–421, May 2002. doi: 10.1038/417419a.

N. Schilling, K. K. Khurana, and M. G. Kivelson. Limits on an intrinsic dipole moment in Europa. *Journal of Geophysical Research (Planets)*, 109:E05006, May 2004. doi: 10.1029/2003JE002166.

N. Schilling, F. M. Neubauer, and J. Saur. Time-varying interaction of Europa with the jovian magnetosphere: Constraints on the conductivity of Europa's subsurface ocean. *Icarus*, 192:41–55, December 2007. doi: 10.1016/j.icarus.2007.06.024.

N. Schilling, F. M. Neubauer, and J. Saur. Influence of the internally induced magnetic field on the plasma interaction of Europa. *Journal of Geophysical Research (Space Physics)*, 113:A03203, March 2008. doi: 10.1029/2007JA012842.

N. M. Schneider, W. H. Smyth, and M. A. McGrath. Io's Atmosphere and Neutral Clouds. *NASA Special Publication*, 494, 1989.

N. M. Schneider, D. M. Hunten, W. K. Wells, A. B. Schultz, and U. Fink. The structure of Io's corona. *Astrophysical Journal*, 368:298–315, February 1991. doi: 10.1086/169694.

G. Schubert, J. D. Anderson, T. Spohn, and W. B. McKinnon. Interior composition, structure and dynamics of the Galilean satellites. *Jupiter. The Planet, Satellites and Magnetosphere*, pages 281–306, 2004.

R. W. Schunk. Transport equations for aeronomy. *Planetary Space Science*, 23:437–485, March 1975. doi: 10.1016/0032-0633(75)90118-X.

R. W. Schunk and A. F. Nagy. Ionospheres: Physics, Plasma Physics, and Chemistry. *Ionospheres: Physics, Plasma Physics, and Chemistry*, 2009. doi: 10.1017/CBO9780511635342.

P. K. Seidelmann and N. Divine. Evaluation of Jupiter Longitudes in System III(1965). In *Bulletin of the American Astronomical Society*, volume 9 of *Bulletin of the American Astronomical Society*, page 474, June 1977.

M. Seufert, J. Saur, and F. M. Neubauer. Multi-frequency electromagnetic sounding of the Galilean moons. *Icarus*, 214:477–494, August 2011. doi: 10.1016/j.icarus.2011.03.017.

V. E. Shaposhnikov, V. V. Zaitsev, H. O. Rucker, and G. V. Litvinenko. On ultraviolet emission observed on the flanks of Io. *Journal of Geophysical Research (Space Physics)*, 118:4248–4252, July 2013. doi: 10.1002/jgra.50360.

V. I. Shematovich and R. E. Johnson. Near-surface oxygen atmosphere at Europa. *Advances in Space Research*, 27:1881–1888, 2001. doi: 10.1016/S0273-1177(01)00299-X.

V. I. Shematovich, R. E. Johnson, J. F. Cooper, and M. C. Wong. Surface-bounded atmosphere of Europa. *Icarus*, 173:480–498, February 2005. doi: 10.1016/j.icarus.2004.08.013.

S. Simon. An analytical model of sub-Alfvénic moon-plasma interactions with application to the hemisphere coupling effect. *Journal of Geophysical Research (Space Physics)*, 120:7209–7227, September 2015. doi: 10.1002/2015JA021529.

S. Simon, J. Saur, H. Kriegel, F. M. Neubauer, U. Motschmann, and M. K. Dougherty. Influence of negatively charged plume grains and hemisphere coupling currents on the structure of Enceladus' Alfvén wings: Analytical modeling of Cassini magnetometer

observations. *Journal of Geophysical Research (Space Physics)*, 116:A04221, April 2011. doi: 10.1029/2010JA016338.

S. Simon, J. Saur, S. C. Treeck, H. Kriegel, and M. K. Dougherty. Discontinuities in the magnetic field near Enceladus. *Geophysical Research Letters*, 41:3359–3366, May 2014. doi: 10.1002/2014GL060081.

E. C. Sittler and D. F. Strobel. Io plasma torus electrons - Voyager 1. *Journal of Geophysical Research*, 92:5741–5762, June 1987. doi: 10.1029/JA092iA06p05741.

E. C. Sittler, J. F. Cooper, R. E. Hartle, W. R. Paterson, E. R. Christian, A. S. Lipatov, P. R. Mahaffy, N. P. Paschalidis, M. A. Coplan, T. A. Cassidy, J. D. Richardson, B. Fegley, and N. Andre. Plasma ion composition measurements for Europa. *Planetary Space Science*, 88:26–41, November 2013. doi: 10.1016/j.pss.2013.01.013.

W. H. Smyth and M. R. Combi. A general model for Io's neutral gas clouds. I - Mathematical description. *Astrophysical Journal Supplement Series*, 66:397–411, April 1988a. doi: 10.1086/191264.

W. H. Smyth and M. R. Combi. A general model for Io's neutral gas clouds. II - Application to the sodium cloud. *Astrophysical Journal*, 328:888–918, May 1988b. doi: 10.1086/166346.

W. H. Smyth and M. L. Marconi. Europa's atmosphere, gas tori, and magnetospheric implications. *Icarus*, 181:510–526, April 2006. doi: 10.1016/j.icarus.2005.10.019.

F. Sohl, T. Spohn, D. Breuer, and K. Nagel. Implications from Galileo Observations on the Interior Structure and Chemistry of the Galilean Satellites. *Icarus*, 157:104–119, May 2002. doi: 10.1006/icar.2002.6828.

D. J. Southwood and M. W. Dunlop. Mass pickup in sub-Alfvenic plasma flow - A case study for Io. *Planetary Space Science*, 32:1079–1086, September 1984. doi: 10.1016/0032-0633(84)90133-8.

D. J. Southwood, M. G. Kivelson, R. J. Walker, and J. A. Slavin. Io and its plasma environment. *Journal of Geophysical Research*, 85:5959–5968, November 1980. doi: 10.1029/JA085iA11p05959.

W. B. Sparks, K. P. Hand, M. A. McGrath, E. Bergeron, M. Cracraft, and S. E. Deustua. Probing for Evidence of Plumes on Europa with HST/STIS. *Astrophysical Journal*, 829:121, October 2016. doi: 10.3847/0004-637X/829/2/121.

J. R. Spencer, J. A. Stansberry, C. Dumas, D. Vakil, R. Pregler, M. Hicks, and K. Hege. History of high-temperature Io volcanism: February 1995 to May 1997. *Geophysical Research Letters*, 24:2451, October 1997. doi: 10.1029/97GL02591.

J. R. Spencer, J. A. Rathbun, L. D. Travis, L. K. Tamppari, L. Barnard, T. Z. Martin, and A. S. McEwen. Io's Thermal Emission from the Galileo Photopolarimeter- Radiometer. *Science*, 288:1198–1201, May 2000. doi: 10.1126/science.288.5469.1198.

J. R. Spencer, E. Lellouch, M. J. Richter, M. A. López-Valverde, K. Lea Jessup, T. K. Greathouse, and J.-M. Flaud. Mid-infrared detection of large longitudinal asymmetries in Io's SO $_2$ atmosphere. *Icarus*, 176:283–304, August 2005. doi: 10.1016/j.icarus.2005.01.019.

T. Spohn and G. Schubert. Oceans in the icy Galilean satellites of Jupiter? *Icarus*, 161: 456–467, February 2003. doi: 10.1016/S0019-1035(02)00048-9.

J. M. Stone, D. Mihalas, and M. L. Norman. ZEUS-2D: A radiation magnetohydrodynamics code for astrophysical flows in two space dimensions. III - The radiation hydrodynamic algorithms and tests. *Astrophys. J. Suppl.*, 80:819–845, June 1992. doi: 10.1086/191682.

D. F. Strobel. Aeronomic Systems on Planets, Moons, and Comets. *Washington DC American Geophysical Union Geophysical Monograph Series*, 130:7, 2002. doi: 10.1029/130GM02.

D. F. Strobel and B. C. Wolven. The Atmosphere of Io: Abundances and Sources of Sulfur Dioxide and Atomic Hydrogen. *Astrophys. Space Sci.*, 277:271–287, June 2001. doi: 10.1023/A:1012261209678.

D. F. Strobel, X. Zhu, and M. F. Summers. On the vertical thermal structure of Io's atmosphere. *Icarus*, 111:18–30, September 1994. doi: 10.1006/icar.1994.1130.

M. E. Summers, Y. L. Yung, and P. K. Haff. A two-stage mechanism for escape of NA and K from Io. *Nature*, 304:710–712, August 1983. doi: 10.1038/304710a0.

K. Szegö, K.-H. Glassmeier, R. Bingham, A. Bogdanov, C. Fischer, G. Haerendel, A. Brinca, T. Cravens, E. Dubinin, K. Sauer, L. Fisk, T. Gombosi, N. Schwadron, P. Isenberg, M. Lee, C. Mazelle, E. Möbius, U. Motschmann, V. D. Shapiro, B. Tsurutani, and G. Zank. Physics of Mass Loaded Plasmas. *Space Science Reviews*, 94:429–671, December 2000.

B. D. Teolis, I. Sillanpää, J. H. Waite, and K. K. Khurana. Surface current balance and thermoelectric whistler wings at airless astrophysical bodies: Cassini at Rhea. *Journal of Geophysical Research (Space Physics)*, 119:8881–8901, November 2014. doi: 10.1002/2014JA020094.

N. Thomas. Optical observations of Io's neutral clouds and plasma torus. *Surveys in Geophysics*, 13:91–164, March 1992. doi: 10.1007/BF01903525.

D. G. Torr. The photochemistry of the upper atmosphere. *The photochemistry of atmospheres: Earth, the other planets, and comets (A86-21076 08-88). Orlando, FL, Academic Press, Inc., 1985, p. 165-278.*, pages 165–278, 1985.

L. Trafton. Detection of a potassium cloud near Io. *Nature*, 258:690–692, December 1975. doi: 10.1038/258690a0.

L. Trafton, T. Parkinson, and W. Macy, Jr. The Spatial Extent of Sodium Emission around IO. *Astrophysical Journal, Letters*, 190:L85, June 1974. doi: 10.1086/181512.

L. M. Trafton, J. J. Caldwell, C. Barnet, and C. C. Cunningham. The Gaseous Sulfur Dioxide Abundance over Io's Leading and Trailing Hemispheres: HST Spectra of Io's C 1B 2–X 1A 1 Band of SO 2 near 2100 Angstrom. *Astrophysical Journal*, 456:384, January 1996. doi: 10.1086/176660.

C. C. C. Tsang, J. R. Spencer, E. Lellouch, M. A. López-Valverde, M. J. Richter, and T. K. Greathouse. Io's atmosphere: Constraints on sublimation support from density variations on seasonal timescales using NASA IRTF/TEXES observations from 2001 to 2010. *Icarus*, 217:277–296, January 2012. doi: 10.1016/j.icarus.2011.11.005.

C. C. C. Tsang, J. R. Spencer, E. Lellouch, M. A. López-Valverde, M. J. Richter, T. K. Greathouse, and H. Roe. Io's contracting atmosphere post 2011 perihelion: Further evidence for partial sublimation support on the anti-Jupiter hemisphere. *Icarus*, 226: 1177–1181, September 2013. doi: 10.1016/j.icarus.2013.06.032.

C. C. C. Tsang, J. R. Spencer, E. Lellouch, M. A. Lopez-Valverde, and M. J. Richter. The collapse of Io's primary atmosphere in Jupiter eclipse. *Journal of Geophysical Research (Planets)*, 121:1400–1410, August 2016. doi: 10.1002/2016JE005025.

F. Tsuchiya, K. Yoshioka, T. Kimura, G. Murakami, M. Yoneda, R. Koga, M. Kagitani, T. Sakanoi, Y. Kasaba, A. Yamazaki, and I. Yoshikawa. Io's volcanic influence on the Io plasma torus: HISAKI observation in 2015. *AGU Fall Meeting Abstracts*, December 2015.

E. P. Turtle, L. P. Keszthelyi, A. S. McEwen, J. Radebaugh, M. Milazzo, D. P. Simonelli, P. Geissler, D. A. Williams, J. Perry, W. L. Jaeger, K. P. Klaasen, H. H. Breneman, T. Denk, C. B. Phillips, and the Galileo SSI Team. The final Galileo SSI observations of Io: orbits G28-I33. *Icarus*, 169:3–28, May 2004. doi: 10.1016/j.icarus.2003.10.014.

V. M. Vasyliūnas. Physical origin of pickup currents. *Annales Geophysicae*, 34:153–156, February 2016. doi: 10.5194/angeo-34-153-2016.

G. J. Veeder, D. L. Matson, T. V. Johnson, D. L. Blaney, and J. D. Goguen. Io's heat flow from infrared radiometry: 1983-1993. *Journal of Geophysical Research*, 99:17095–17162, August 1994. doi: 10.1029/94JE00637.

M. Volwerk, M. G. Kivelson, and K. K. Khurana. Wave activity in Europa's wake: Implications for ion pickup. *Journal of Geophysical Research*, 106:26033–26048, November 2001. doi: 10.1029/2000JA000347.

M. Volwerk, K. Khurana, and M. Kivelson. Europa's Alfvén wing: shrinkage and displacement influenced by an induced magnetic field. *Annales Geophysicae*, 25:905–914, May 2007. doi: 10.5194/angeo-25-905-2007.

A. C. Walker, S. L. Gratiy, D. B. Goldstein, C. H. Moore, P. L. Varghese, L. M. Trafton, D. A. Levin, and B. Stewart. A comprehensive numerical simulation of Io's sublimation-driven atmosphere. *Icarus*, 207:409–432, May 2010. doi: 10.1016/j.icarus.2010.01.012.

A. C. Walker, C. H. Moore, D. B. Goldstein, P. L. Varghese, and L. M. Trafton. A parametric study of Io's thermophysical surface properties and subsequent numerical atmospheric simulations based on the best fit parameters. *Icarus*, 220:225–253, July 2012. doi: 10.1016/j.icarus.2012.05.001.

J. W. Weiss. *Appendix 2: Planetary parameters*, pages 699–706. 2004.

D. A. Williams and R. R. Howell. Active volcanism: Effusive eruptions. *Io After Galileo: A New View of Jupiter's Volcanic Moon*, page 133, 2007. doi: 10.1007/978-3-540-48841-5_7.

D. J. Williams and R. M. Thorne. Energetic particles over Io's polar caps. *Journal of Geophysical Research (Space Physics)*, 108:1397, November 2003. doi: 10.1029/2003JA009980.

D. J. Williams, B. H. Mauk, R. E. McEntire, E. C. Roelof, T. P. Armstrong, B. Wilken, J. G. Roederer, S. M. Krimigis, T. A. Fritz, and L. J. Lanzerotti. Electron Beams and Ion Composition Measured at Io and in Its Torus. *Science*, 274:401–403, October 1996. doi: 10.1126/science.274.5286.401.

D. A. Wolf-Gladrow, F. M. Neubauer, and M. Lussem. Io's interaction with the plasma torus - A self-consistent model. *J. Geophys. Res.*, 92:9949–9961, September 1987. doi: 10.1029/JA092iA09p09949.

B. C. Wolven, H. W. Moos, K. D. Retherford, P. D. Feldman, D. F. Strobel, W. H. Smyth, and F. L. Roesler. Emission profiles of neutral oxygen and sulfur in Io's exospheric corona. *Journal of Geophysical Research*, 106:26155–26182, November 2001. doi: 10.1029/2000JA002506.

M. C. Wong and R. E. Johnson. The effect of plasma heating on sublimation-driven flow in Io's atmosphere. *Icarus*, 115:109–118, May 1995. doi: 10.1006/icar.1995.1082.

M. C. Wong and W. H. Smyth. Model Calculations for Io's Atmosphere at Eastern and Western Elongations. *Icarus*, 146:60–74, July 2000. doi: 10.1006/icar.2000.6362.

J. Zhang, D. B. Goldstein, P. L. Varghese, N. E. Gimelshein, S. F. Gimelshein, and D. A. Levin. Simulation of gas dynamics and radiation in volcanic plumes on Io. *Icarus*, 163: 182–197, May 2003. doi: 10.1016/S0019-1035(03)00050-2.

M. H. G. Zhang, J. G. Luhmann, S. W. Bougher, and A. F. Nagy. The ancient oxygen exosphere of Mars - Implications for atmosphere evolution. *Journal of Geophysical Research*, 98:10, June 1993. doi: 10.1029/93JE00231.

C. Zimmer, K. K. Khurana, and M. G. Kivelson. Subsurface Oceans on Europa and Callisto: Constraints from Galileo Magnetometer Observations. *Icarus*, 147:329–347, October 2000. doi: 10.1006/icar.2000.6456.

Acknowledgements

First of all I thank my supervisor J. Saur for helping and guiding me through my research. His support and the inspirational discussions that we had encouraged me during the time of my research.

I thank L. Roth for his helpful advices. I really enjoyed our discussions at several conferences.

I also thank my second co-supervisor B. Tezkan for his interest in my research.

Special thanks to my colleagues from the space physics and applied geophysics group for the nice time I had during the whole period of my research.

I appreciated the scientific discussions with O. Hartkorn, S. Kabanovic, F. Musacchio, F. M. Neubauer, L. Wennmacher, and S. Simon.

For proof-reading I thank F. Musacchio, O. Hartkorn, and L. Roth.

I acknowledge the financial support by the Verbundforschung Astronomy und Astrophysik through grant 50OR1313 and the technical support by the CHEOPS team.

Finally, I thank my mother.

Versicherung

Ich versichere, dass ich die von mir vorgelegte Dissertation selbständig angefertigt, die benutzten Quellen und Hilfsmittel vollständig angegeben und die Stellen der Arbeit - einschließlich Tabellen, Karten und Abbildungen -, die anderen Werken im Wortlaut oder dem Sinn nach entnommen sind, in jedem Einzelfall als Entlehnung kenntlich gemacht habe; dass diese Dissertation noch keiner anderen Fakultät oder Universität zur Prüfung vorgelegen hat; dass sie - abgesehen von unten angegebenen Teilpublikationen - noch nicht veröffentlicht worden ist, sowie, dass ich eine solche Veröffentlichung vor Abschluss des Promotionsverfahrens nicht vornehmen werde. Die Bestimmungen der Promotionsordnung sind mir bekannt. Die von mir vorgelegte Dissertation ist von Prof. Dr. Joachim Saur betreut worden.

Köln, 26. Juli 2017

Aljona Blöcker

Teilpublikationen

Blöcker, A., Saur, J., & Roth, L. (2016), Europa's plasma interaction with an inhomogeneous atmosphere: Development of Alfvén winglets within the Alfvén wings, *Journal of Geophysical Research (Space Physics)*, *121*, 9794–9828, doi:10.1002/2016JA022479.